12-2015

Quantification of Fast-Neutron Sources with Coded Aperture Imaging

Timothy Donald Jackson
University of Tennessee - Knoxville, tjacks24@vols.utk.edu

To the Graduate Council:

I am submitting herewith a dissertation written by Timothy Donald Jackson entitled "Quantification of Fast-Neutron Sources with Coded Aperture Imaging." I have examined the final electronic copy of this dissertation for form and content and recommend that it be accepted in partial fulfillment of the requirements for the degree of Doctor of Philosophy, with a major in Nuclear Engineering.

Jason P. Hayward, Major Professor

We have read this dissertation and recommend its acceptance:

Steven Skutnik, Xiaodong Zhang, Thomas Handler

Accepted for the Council:

Carolyn R. Hodges

Vice Provost and Dean of the Graduate School

(Original signatures are on file with official student records.)

Quantification of Fast-Neutron Sources with Coded Aperture Imaging

A Dissertation Presented for the

Doctor of Philosophy

Degree

The University of Tennessee, Knoxville

Timothy Donald Jackson

December 2015

Acknowledgements

First and foremost I have to thank my parents and stepparents for their support, mentoring, and incessant belief in me. You've supported me from the very beginning, and have always had faith that I'd make the right decisions even when I've had doubt. Special thanks to my grandparents for always being glad to hear any updates from me and keeping me fed on needed visits out of town. Of course, my cousin Dr. Paul Allen Jackson, you beat me by 6 months to finishing your dissertation, but you had a 4 year head start and our near daily communication has helped me stay focused on the goal.

My friends I've gained at the University of Tennessee, especially the weekly board games with Dr. Michael Sharp, Dr. Eric Strong, Kayla Strong, Nick Sly, and Dr. Matthew Beach.

I wouldn't have been able to develop the skills needed to perform this research or have access to the equipment and materials necessary without the support of many researchers and staff in the NMDC group. Special thanks to my advisor Dr. Jason Hayward for guidance throughout the project. Thanks to Dr. Paul Hausladen, Dr. Matthew Blackston, and Dr. Jason Newby for their understanding of the experimental and operating conditions of coded aperture imagers and tips on improving my various ROOT and Geant codes.

The Bredesen Center brought me to Tennessee due to the ability to combine the facilities and opportunities at ORNL with the University of Tennessee, and deserves a special thanks as well.

I would like to thank the University of Tennessee Nuclear Engineering department, ORNL LDRD, and the DOE NNSA DNN R&D Office for funding this project.

Abstract

Quantification of the mass of plutonium in facilities that process plutonium is important for both nuclear safeguards concerns and safety concerns, and multiple methods to non-destructively quantify plutonium sample characteristics have been proposed, particularly when the sample is located directly adjacent to or within the measurement device. In prior work, coded-aperture fast neutron imaging has been developed to demonstrate the imaging of neutron emitting radiation sources in a qualitative fashion, where the sources may be located meters to tens of meters away. Building upon prior work, this work develops the use of a Maximum Likelihood Expectation Maximization (MLEM) reconstruction technique to simultaneously reconstruct neutron sources measured from different detector positions. Moreover, a modified system response model is developed to accurately but quickly perform forward projections in order to accurately reconstruct and quantify neutron source characteristics including source intensity and location. The system response model incorporates mask transmission, a heterogeneous detector pixel array, scattering within the mask, and scattering within the detector, allowing for the expected detector data from a single source position to be generated in less than a second. The behavior of the MLEM reconstruction technique is discussed, and measurements of Cf-252 sources, acting as a surrogate Pu material, are reconstructed and analyzed. Using the methods developed here, a single 74 μCi [microcurie] Cf-252 point source placed at a distance of 200 cm is reconstructed within 2% of the known position and within 3% of known intensity at distances up to 300 cm. Measurements of more than one source and implications for Pu measurements in facilities are also discussed.

Table of Contents

List of Tables

List of Figures

List of Equations

Chapter 1 Introduction

While the current nuclear fuel cycle in the US consists of a once-through fuel cycle with uranium processing only, future fuel cycles may incorporate reprocessing of spent nuclear fuel or widespread use of mixed-oxide fuel (MOX), both of which require the processing of plutonium. Similar to the needs of uranium processing facilities, it is necessary to be able to non-destructively quantify plutonium in measurement scenarios present in plutonium processing facilities. Increased awareness of the need for measurement techniques that address the challenges in measurement of plutonium at processing facilities that are not addressed by the current measurement regime found in uranium processing facilities has stimulated research in detection techniques to detect and characterize plutonium. Broadly speaking, radiation measurement techniques that may be desirable are either active or passive measurements, with passive measurements studying emissions that are intrinsic to the material being studied while active measurements measure either source radiation that is not modulated by the measured sample (e.g. transmission imaging) or emissions induced by an external source (e.g. induced fission). Detection and quantification by active or passive radiation measurements are limited by distance to the source, heterogeneous background radiation, shielding between the source and the detector system, and acquisition time. One of the central challenges in fast-neutron sensing is the 3D localization and characterization of fast-neutron sources at standoff distances of meters to tens of meters, including the simultaneous localization of multiple neutron sources.

For plutonium processing facilities, gamma-ray measurements are complicated by self-shielding inside of plutonium-containing materials and high-Z materials. Both neutron and gamma-ray measurements are complicated by the difficulty in isolating individual plutonium deposits and the impracticality of contact measurements. The development of 3D fast-neutron imaging technology in this work is motivated by a desire to quantify plutonium holdup in scenarios where results from non-imaging detectors may be ambiguous, their use may be impractical, or gamma-ray imaging techniques may be impractical due to operational considerations.

1.1 Plutonium Quantification

Future nuclear fuel cycles used in the US, as well as current nuclear fuel cycles used internationally, may include reprocessing of spent nuclear fuel or a switch to mixed-oxide (MOX) fuel (Von Hippel, 2001), both of which will require processing of industrial quantities of plutonium (Nuclear Regulatory Commission, 2013). Of notable concern for both Pu and U is the "significant quantity," defined by the IAEA as the approximate amount of nuclear material needed to manufacture a nuclear explosive device. For Pu this quantity is 8 kg for Pu containing less than 80% Pu-238 (IAEA, n.d.). While the goal of nuclear material detection systems is generally to quantify nuclear material at quantities much lower than a significant quantity, it is a convenient mass to test systems against. For passive measurements of Pu metal and compounds, there are a variety of signatures that can be used to detect and quantify Pu. A few notable ones are shown in Table 1.

Table 1. Useful radiation signatures for passive measurements of Plutonium (Reilly, 2007)

Isotope	Technique	Signature (keV)	Intensity ($g^{-1}s^{-1}$)
Pu-239	Passive Gamma	414	34000
		375	36000
		129	140000
	Passive Neutron		0.022
Pu-240	Passive Gamma	642	1044
		160	33700
		45	143600
	Passive Neutron	2000	1000
PuO_2	Passive Neutron	2000	120
PuF_6	Passive Neutron	1000	7300

The neutron emission rate for Pu is dependent not only on the isotopic makeup, but the chemical form due to alpha-particle induced neutron emission in low-mass isotopes. Due to its short half-life (87.7 yr), emissions from alpha decay of Pu-238 may be responsible for much of the neutron emissions in spent nuclear fuel. In addition, spontaneous fission neutrons are emitted with a Watt spectrum, with differences between isotopes being the width and peak energy of the spectrum. Knowledge of not only the isotopic content of the Pu but industrial process knowledge as well is needed to translate a source intensity to a Pu mass from neutron intensity alone. Without more detailed information about the expected material composition, a passive neutron measurement is limited to determination of the neutron emission rate. With spectroscopic information about the emitted neutron energy distribution, the isotopic content and chemical makeup of a fast-neutron source can be determined, as shown in Figure 1.

Since the distribution of emitted fission neutrons differs between each Pu isotope, it is possible to determine the isotopic content of a Pu-containing material from the detected neutron energy distribution if the detector has sufficient energy resolution to distinguish between the different energy spectra. Similarly, the emitted gamma-ray spectrum from each Pu isotope and compound is unique, enabling identification of isotope and compound, such as with the Pu-600 (Luke & Archer, 2000) gamma-ray spectrum analysis technique. Without spectroscopic information, however, only the neutron intensity can be estimated. Since on a per-gram basis the neutron emission rate of Pu-240 is 50,000 times the emission rate of Pu-239, the isotopic content of Pu metal is the primary determinant of neutron emission rate, not the mass, with the exception of high masses.

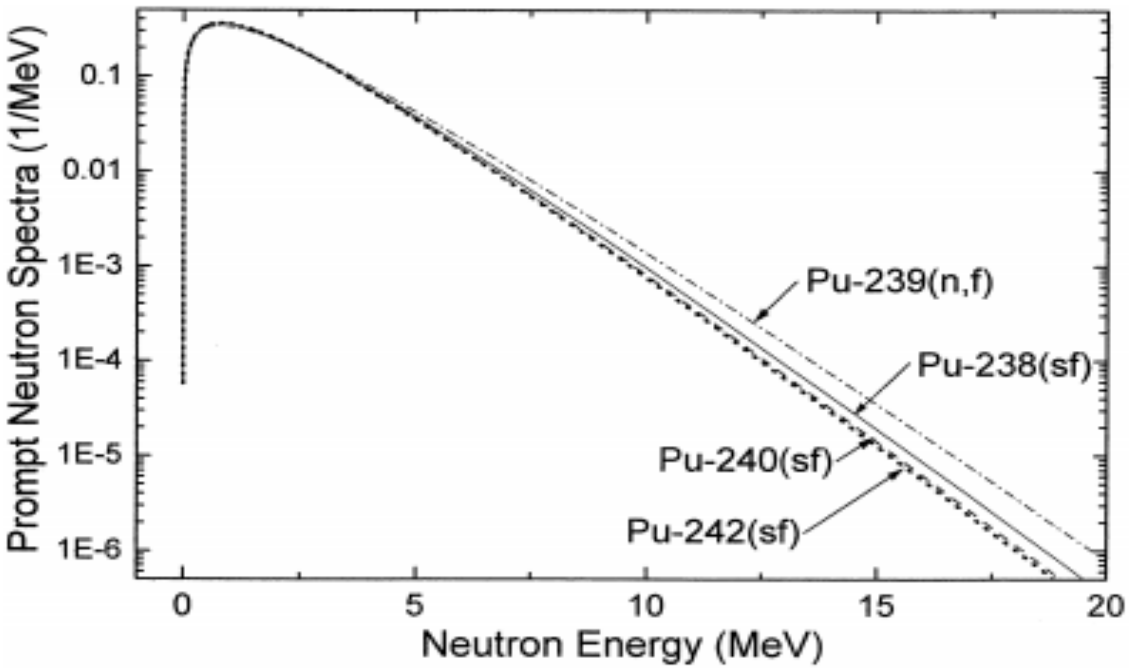

Figure 1. Neutron energy spectrum for various Pu isotopes. From (Oshawa, Horiguchi, & Mitsuhashi, 2000) ©ElSevier 2000.

1.1.1 Plutonium Isotopics

Because Pu is not naturally occurring, the isotopic makeup of Pu samples varies depending on the goal of the Pu production process. The goal can be roughly separated into two goals, power production, where production of Pu is secondary in the operation of a commercial nuclear power plant, and dedicated Pu production for nuclear weapons. Isotopic makeup of Pu varies between the two goals, with Pu for weapons purposes containing <7% Pu-240, and Pu from power production containing generally >18% Pu-240 (Pellaud, 2002).

The isotopic makeup of reactor-produced Pu is complex, dependent on the operating history of the sample, reactor type, and cooling time of the sample, and while the exact concentration of Pu-240 in a sample varies greatly, general trends in the isotopic content of Pu as the burnup (power output through fission) increases are clear and intuitive from an understanding of the underlying physics. Fresh fuel contains zero Pu, and at low burnup nearly all the Pu is the 239 isotope. At increased burnup, Pu-240 and other higher-mass isotopes are produced at increasing concentrations due to relatively low fission cross sections in comparison to the fission cross section of Pu-239. For instance, at 2-4 GWd/MTU (an unit of burnup), the Pu consists of well over 90% Pu-239, but for a common reactor design used in the United States, at 45 GWd/MTU the Pu contains 28% Pu-240 and only 56% Pu-239 (Wagner, et al., 2012). While other isotopes, specifically Pu-238, Pu-241, and Pu-242 make up the bulk of the remaining isotopes, the low spontaneous fission rates of the remaining isotopes result in Pu-240 being the only source of spontaneous fission neutrons considered.

This creates a range of neutron masses that have the same spontaneous-fission neutron emission rate as a Cf-252 source. For instance, a 0.02 mCi Cf-252 source would have the same neutron emission rate as 0.038 S.Q. of Pu with a Pu-240 content of 28% (for a significant quantity (S.Q.)). This same 0.02 mCi Cf-252 source would have the same neutron emission rate as an unrealistically large quantity of pure Pu-239 (ignoring induced fission in pure Pu-239). Allowing for Pu compounds and thus (α,n) reactions and finite sized Pu sources and thus multiplication within the sample, the range of masses that could be represented by a single neutron intensity spans many orders of magnitude. Translating between neutron intensity and

Pu mass can be performed as a post-processing step after the source intensity distribution is reconstructed, so the focus of this work is on estimating the source intensity and its spatial distribution.

Since passive fast-neutron measurements do not provide high resolution spectroscopic data from either gamma-ray intensity distributions or time-distribution of emitted neutrons from induced fission, passive fast-neutron measurements provide more ambiguous information than other measurement techniques. However, fast-neutron imaging has advantages over other measurement technologies that make it attractive for measuring plutonium holdup. Fast-neutrons, while less numerous than gamma-rays, have lower attenuation rates than gamma-rays in materials such as iron and Pu compounds, and, thus, can penetrate equipment and nuclear material that is opaque to gamma-rays (Hausladen, Blackston, & Newby, Measurement Scenarios to Mimic Potential Uses of Passive Fast-Neutron Imaging for Quantifying Holdup at Fuel Cycle Facilities, 2012). Because of this, self-attenuation for fast-neutrons in assemblies containing Pu can generally be ignored, while the high density of Pu (and U) compounds means that self-attenuation of gamma-rays, particularly for the more numerous lower energy gamma-rays, cannot be neglected. In contrast to techniques for measuring thermal neutrons, fast-neutron measurements measure neutron sources directly, while thermal neutron measurements actually measure the moderating material, which provides different information about a sample than what is provided by direct measurement of the source.

1.2 Holdup Measurement

A concern at plutonium processing facilities, as well as uranium processing facilities, is the accumulation of nuclear material deposited in the equipment, defined as holdup. Quantifying holdup is desirable for accountancy, radiation safety, criticality safety, plant efficiency, and other concerns (Reilly, 2007). Holdup accumulates throughout operation, and it can be up to 10% of the nominal throughput of a facility. In subsequent years of steady operation, holdup may approach an asymptotic value and does not increase in quantity.

Measuring holdup in a plutonium processing facility is difficult for a variety of reasons, as shown in Figure 2.

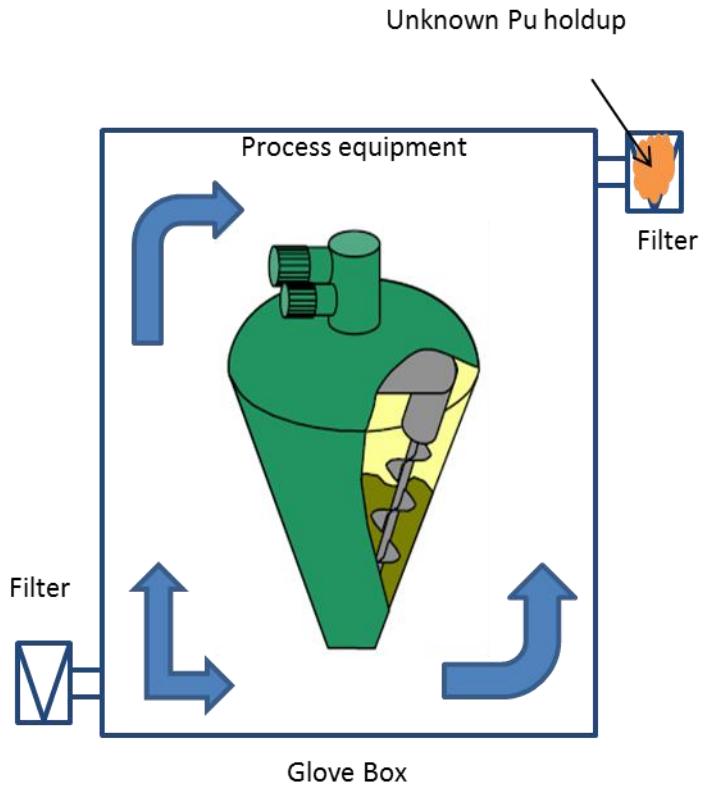

Figure 2. Demonstration of Pu holdup source distribution.

In Figure 2 the desired Pu-containing accumulation to be measured is not contained within the large processing equipment in the glovebox, but one of the smaller filters connected to the glovebox. Measuring holdup within that filter, then, needs to be able to distinguish between radiation emitted from the processing equipment and radiation emitted from the filter. This is especially important, since the total emissions from the processing equipment may be far greater in magnitude than the emissions from the filter. It is not hard to envision a measurement scenario where the equipment being measured is inside of the glovebox, making contact measurements impractical. Traditionally, holdup measurement using gamma-ray

emissions occurs via multiple scans, first a rapid survey with uncollimated NaI detectors operating in counting mode, then quantitative measurements with collimated NaI detectors operating in spectroscopy mode. By collimating the NaI detectors, the viewing area of the detector becomes highly limited, but the detector remains sensitive to emissions from behind the object being inspected due to an inability to distinguish between sources at different distances.

The approach for quantification via neutron measurements (Hagenauer & Mayer, 1991) is similar to that of gamma-rays by first rapidly surveying with uncollimated NaI detectors, then quantifying intensity with neutron measurements. A typical accuracy of ~15% can be expected for neutron measurement of a single glovebox. For the case of a glovebox, such as those used at a MOX fuel facility (Sigg, Casella, Dewberry, & Moore), high-resolution gamma-ray measurements of Pu waste are taken, then Pu content is calculated from the gamma-ray spectra. The method used to quantify Pu holdup (i.e., via use of collimated, non-imaging detectors) requires the conservative estimate of a large source-to-detector distance, high gamma-ray background due to Cs-137, and attenuation within the glovebox. By making conservative estimates and minimizing the total efficiency of the measurement, the method overestimates the source intensity. This ensures that the overall source intensity is below limits set by the facility. Traditional holdup measurement techniques are either based on the sensing and analysis of gamma-rays and, thus, suffer from said shielding in industrial equipment and in the holdup material itself, or measure a single accumulation at a time due to the need for highly collimated detectors.

1.3 Imaging Techniques

Non-imaging sensing techniques do not localize the source of radiation, and, as such, do not inherently distinguish source radiation from background radiation without additional information such as the energy spectrum and intensity of background radiation. In non-laboratory measurement scenarios, radiation background does not just produce statistical uncertainty in detected radiation, but systematic variation as well due to effects such as

shielding of cosmic rays by adjacent buildings (Iyengar, et al., 2015). Non-imaging detectors, especially non-imaging detectors lacking spectroscopic capabilities, are not robust against systematic background variation (Byrd, et al., 2005). On the other hand, some designs of imaging detectors can determine the true background rate by distinguishing between source and background radiation. While non-imaging detectors require collimation to isolate a particular source, imaging detectors may be able isolate the source without collimation, in either 2D or 3D, depending on the imaging technique.

Various imaging techniques have been developed using fast neutrons either as an interrogating source with some induced emission being detected, or as both an interrogating source and detected particle. Fast-neutron imaging techniques developed, each of which will be described in more detail below, include transmission-based imaging (Swift, 2012), neutron scatter cameras (Mascarenhas, et al., 2006), and time-coded apertures (Marleau, et al., 2011).

Transmission-based imaging, implemented, for example, in the Nuclear Materials Identification System (NMIS) system developed at Oak Ridge National Laboratory (ORNL), uses 14.1 MeV neutrons (produced by the D-T reaction) as an interrogation source to identify nuclear material and characterize the morphology of attenuating materials (Swift, 2012). This method consists of performing a radial scan on an object suspected of containing nuclear material and analyzing the spatial and time distribution of the time-tagged detected particle. Detected particles include transmitted 14.1 MeV neutrons and both neutrons and gamma-rays emitted in induced fission of nuclear material. For transmission measurements, reconstruction is performed using a MLEM reconstruction to map the object, as well as a filtered back-projection to determine the overall dimensions of the object and constrain the MLEM. The active measurement with D-T neutrons allows for mapping of the fissionable material geometry (Swift, 2012), and isotopic content of the sample (demonstrated for HEU samples) can be determined by the time distribution of detected neutrons. This transmission-based technique does require 360° access to a measurement object and the use of an active neutron source for characterization, making the transmission based technique more applicable for measurement scenarios where the goal is to verify a declared sample or possibly detect nuclear material in storage containers, than a

blind measurement over a larger volume with one-sided access. Active measurements with one-sided access may require alternative designs, such as a backscatter based imaging system or scatter based imaging.

An alternative passive neutron imaging technique is the neutron scatter camera (Mascarenhas, et al., 2006), based on scatter cameras developed for gamma-ray imaging. The simplest case of a scatter camera is two position-sensitive planar detectors. The energy and position of the recoil proton in the first detector is measured, and the energy of the recoil neutron is measured by the time-of-flight between the position of interaction for the scatter in the first detector and the position of interaction in the second detector, as shown in Figure 3.

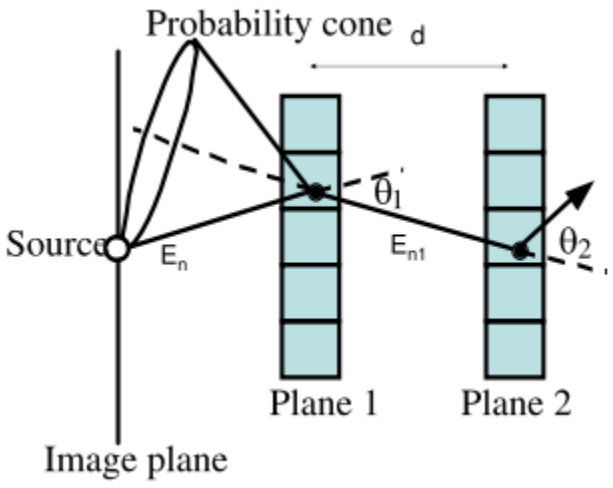

Figure 3. Double-neutron scattering for neutron scatter imaging. (Mascarenhas, et al., 2006) ©IEEE 2006.

Since the time difference between the scattering event in Plane 1 and Plane 2 is known and the distance between the two scattering events can be estimated within the position resolution of Plane 1 and Plane 2, the energy of the scattered neutron can be determined and θ_1 can be estimated from scattering kinematics. Since the angle of the first recoil proton is unknown, and there is finite position resolution (pixel size) in each detector, the calculated incident angle is expressed as a cone when a single neutron interacts in both layers. From neutron kinematics on hydrogen, the most probable scattering angle for non-relativistic neutrons is 45° (Vanier, Diosvegi, Salwen, & Forman, 2009), and reconstructions determined by the reaction kinematics would reconstruct the most probable scattering angle at 45°. Simply assuming all scattering occurs in hydrogen at 45° for detected neutrons can provide a sharper intensity profile, higher signal-to-noise versus determining the scattering angle from peak amplitude and time-of-flight. Over multiple incident neutrons, the probability cones overlap, and, by tallying the number of cone intersections for each incident angle, the source distribution is reconstructed. This technique is similar to the coded aperture technique in that it provides directional information from a single measurement position, but differs from the coded aperture technique in the need for incident neutrons to be detected twice and in the timing resolution required to reconstruct the incident source distribution. The need for incident neutrons to be detected twice within the detector decreases the effective count rate, thus decreasing the statistics of the reconstructed image. Since timing information is recorded and the incident neutron energy is estimated during the reconstruction process, the neutron scatter camera inherently provides spectroscopic information about the neutron source distribution, unlike the coded aperture technique which only provides geometric information about the neutron source distribution.

Figure 4. Time-encoded fast-neutron imager. (Marleau, et al., 2011) ©IEEE 2011.

Various fast-neutron imaging designs have been developed that use a rotational component in the reconstruction of source position (Marleau, et al., 2011), such as the one shown in Figure 4. The time-encoded fast-neutron imager places a 1D mask pattern wrapped into a circle around a single central detector. The mask is spun around the detector while recording neutron count rate incident on the detector and the angle of rotation. Sample data is shown in Figure 5.

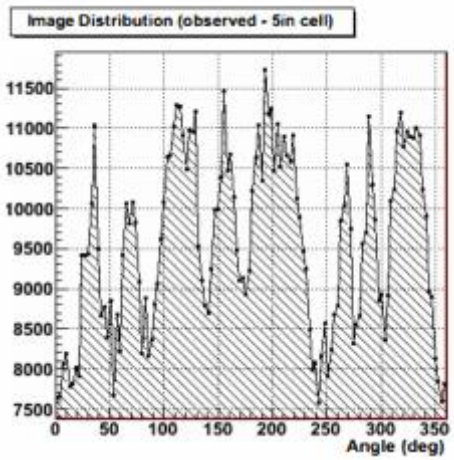

Figure 5. Angular count rate distribution of time-encoded imager. (Marleau, et al., 2011) ©IEEE 2011.

In this setup, the detector itself is completely decoupled from the modulating component, and as long as the mask modulates the incident radiation, a variety of detector materials can be used. Reconstruction is performed using a MLEM reconstruction, resulting in a directional reconstruction of a source position. While this is in many ways similar to the coded aperture technique, and can use the same mask pattern as a 1D coded aperture mask, it differs in that it requires an iterative, statistical reconstruction technique; it does not require a position-sensitive detector; and it uses a moving mask instead of a stationary mask. While the time-encoded imaging technique allows for 360° image reconstruction on a single imaging plane, in

contrast to the limited angular field of view for a coded aperture imager, the technique is not scalable up to a 2D imager, and increasing the size of the imager to increase the range at which the imager is useful (considering faster imaging times) requires increasing the radius of rotation for the mask, making it impractical for large imagers. In contrast, the lack of moving components enables the coded aperture technique to be more readily scaled to larger sizes.

A simple, general imager design is a pinhole imager, which requires the use of a position-sensitive detector. This is the base imaging concept from which coded aperture imaging is derived, and is discussed in more depth in Section 2.1. In a pinhole imager, a uniform mask of moderator material with a single hole is placed between the source and the detector, with the source direction being determined by the position of the detected incident neutron, and the distance to the source determined by the size of the detector area sensing incident neutrons. Because of this simple design, the pinhole imager is scalable to 2D and 3D imaging, and the size of the imager is limited only by the volume of active material available. With only a single pinhole, most of the radiation incident on the mask is not transmitted onto the detector, inefficiently attenuating most of the incident source distribution. Since attribution of detected radiation to a particular distance and direction is limited to the detected pixels and size of the detected pattern, in the absence of information about any heterogeneous background radiation, all detected radiation is attributed to potential source locations. Because of this, sources outside of the space that is modulated by the imaging mask, referred to as the field of view, are erroneously attributed as inside of the field of view. Increasing the number of holes in the mask increases the total throughput of the mask, thus increasing the total detected signal, and the source direction is no longer determined by a single pixel, but by an array of pixels. As the number of holes in the mask increases, the source direction and distance cannot be easily determined by simple analysis of the detected data, and advanced reconstruction techniques are necessary.

1.4 Original Contributions of this Work

The original contributions of this work are as follows:

1. Development of coded aperture fast-neutron imaging for quantifying the intensity of fast-neutron sources.
2. Quantify the improvements of the parallax imaging technique over a single-position imaging technique.
3. Modification of a MLEM reconstruction technique for computational accuracy and speed for the purpose of neutron source attribute quantification.
4. Development of system response model to quickly predict the expected detector count pattern while accounting for significant deviations from idealized coded aperture imaging.

The need of the MLEM technique for an accurate system response model, combined with an understanding of the geometry and dominant physical interactions in the imager, determined the parameters of the system response model. The decisions that led to the development of the system response model were based on a variety of performance objectives, particularly accuracy and computational speed. Modeling of the effects of mask transmission, mask scattering, and the gap between detector elements in the detector pixel array were necessary. Calculations were done analytically and compared to Monte Carlo simulations for mask transmission and detector air gap, while the effect of mask scattering was quantified by analyzing the results of multiple Monte Carlo simulations.

Modification of the MLEM reconstruction technique was necessary to achieve the performance objectives of computational speed and accurate reconstruction of source intensity. Multiple thresholding algorithms were considered prior to settling on a multi-stage reconstruction with thresholding at each stage.

1.5 Overview of Dissertation

This dissertation is organized into six chapters. The subject of fast-neutron imaging is introduced in this chapter along with the background and motivation for this work.

The analytical reconstruction technique and basic coded aperture principles are discussed in Chapter 2. Analytical models for the field of view of the coded aperture imager are introduced, and the principles of the parallax imaging technique are discussed. The difficulty of the analytical reconstruction technique in reconstructing complex source distributions and potential imaging artifacts are discussed. Finally, Chapter 2 includes a description of the coded aperture fast-neutron imager developed at Oak Ridge National Laboratory.

The system response model developed for statistical reconstruction is introduced in Chapter 3. A ray-tracing projection is introduced, and the need to super-sample the detector pixel array is discussed. Possible deviations from ideal coded aperture imaging are discussed, and the way the system response model accounts for mask transmission, mask scattering, and a heterogeneous detector pixel array are developed. Lastly, Chapter 3 shows that the developed system response model effectively models the true system response function by comparing the results of a Monte Carlo simulation of a given source position and the results of the system response model for the same position.

The MLEM statistical reconstruction technique is introduced and developed in Chapter 4. The behavior of the reconstruction process is discussed, and the applicability of the parallax imaging technique with MLEM reconstruction is demonstrated. The MLEM technique is then modified using various thresholding techniques, which are discussed and demonstrated. Lastly, Chapter 4 discusses the differences in reconstructed source distributions using a 24x24 imager and a 40x40 imager of similar size.

Measured source distributions using a 40x40 coded aperture imager are discussed in Chapter 5. Single source measurements both from single measurement positions and demonstrating the parallax imaging measurement technique are reconstructed. Multiple source measurement reconstructions are presented, representing both simultaneous measurements of multiple sources and combined detector data representing measurements of individual sources. The behavior of known source distributions and intensities is discussed as well as unknown source distributions.

Lastly, Chapter 6 presents the conclusions and recommendations for future work. The salient points of previous chapters are summarized.

Chapter 2 Coded aperture Imaging

Originally developed for gamma-ray astronomy (Caroli, Stephen, Di Cocco, Natalucci, & Spizzichino, 1987), coded aperture imaging has been used throughout the radiation detection community as an imaging technique capable of detecting sources and providing directional and distance information for their localization. Imaging consists of two stages: 1) encoding the source information through in imaging mask onto the detector, and 2) reconstructing the source distribution from the encoded data. Traditional coded aperture imaging uses an analytical reconstruction technique. Since coded aperture imaging relies on the geometric modulation of the source distribution and is independent of the particle type or timing information, coded-aperture imaging can be used for a variety of particle imaging applications, including gamma-ray imaging, optical imaging, and neutron imaging.

2.1 Pinhole Imaging

Coded aperture imaging is a modification to the pinhole imaging technique, and understanding of the pinhole imaging technique can inform an understanding of the coded aperture imaging technique. Regions of imaging masks can be grouped into two categories, mask moderator and mask hole elements. Hole elements are open elements of the mask, where the incident particle passes freely through the imaging mask, whereas mask moderator elements are filled with a moderator material that either scatters or absorbs the incident particle. In the absence of a perfect vacuum, mask elements with very low interaction probabilities (e.g. air filled elements) can be treated as mask hole elements. Pinhole imaging consists of a position-sensitive detector and an imaging mask with a single mask hole element. Detector pixels where the line between the source and pixel intersects a mask moderator element are shielded by the mask, while detector pixels where the line intersects a mask hole element are illuminated by the source and detect incident radiation, as shown in Figure 6.

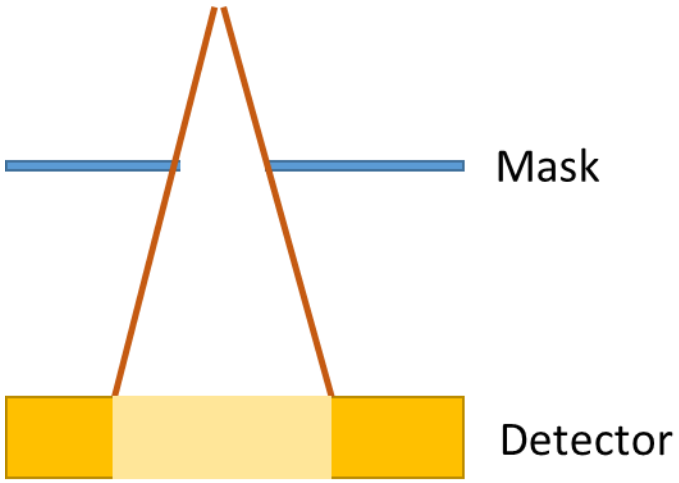

Figure 6. 2D Visualization of the pinhole imaging technique.

Reconstruction of the detected pattern consists of a simple geometric conversion from the size of the illuminated region of the detector through the mask. It is intuitive from Figure 6 that the source-to-mask distance, mask hole width, mask hole thickness, and mask-to-detector distance determine the size of the detector region illuminated by the source. Since both coded aperture and pinhole imaging are geometric imaging techniques, and the position resolution of the detector is independent of the imaging optics, perfect detector position resolution can be assumed in a discussion of the pinhole imaging technique. Assuming an infinitely narrow pinhole, the position resolution of the imaging system itself is zero. However, since the pinhole would have zero width, the total transmission through the imaging mask would be zero and the total count rate in the detector is zero. A finite mask thickness increases the total transmission through the mask, but decreases the resolution of the imager, as shown in Figure 7.

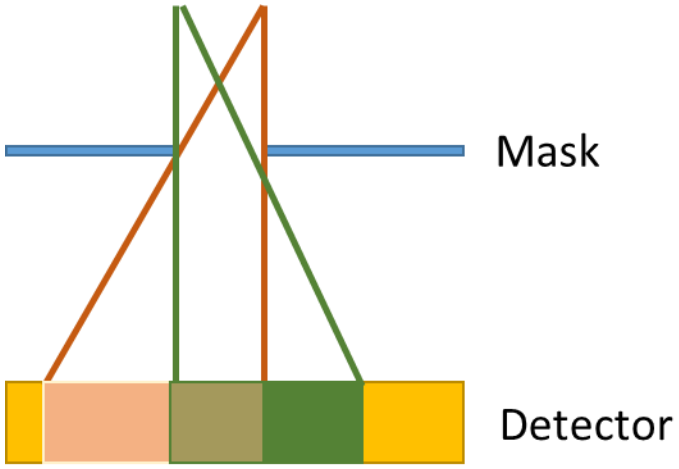

Figure 7. Resolution loss in a finite width mask for pinhole imaging.

While the two sources in Figure 7 independently project on the detector, the detector imperfectly separates the sources in the detected distributions. By increasing the mask width in order to increase the total signal incident on the detector, the region of the detector represented by a given source position increases, thus leading to worse resolution by the

imaging system. For a fixed source position and intensity, increasing the total signal incident on the detector requires increasing the transmission through the mask. Instead of increasing the width of a hole element in the mask, the transmission through the mask can be increased by using a second pinhole in the mask, as shown in Figure 8.

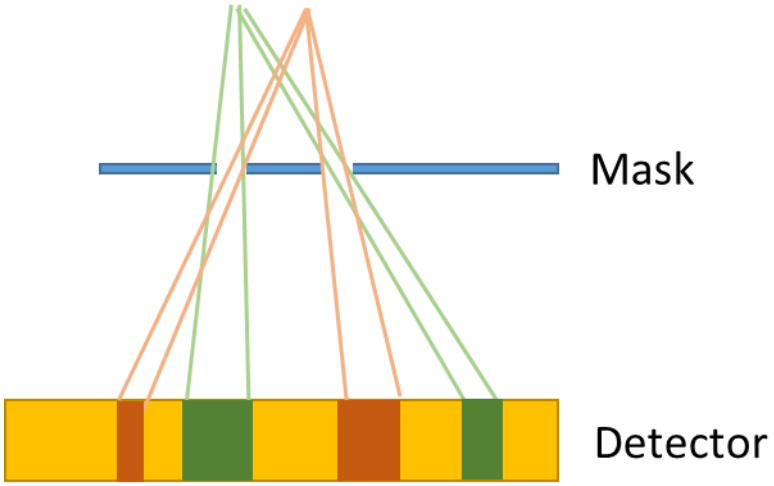

Figure 8. Pinhole imaging with two pinholes.

By increasing the number of pinholes, the distribution of the signal detected is modulated with more complexity than the modulation of a single pinhole. A source position is no longer determined by a single continuous region of the detector but instead by a pattern of detector regions, and a single region of the detector may represent many potential source positions. Increasing the number of mask hole elements and thus increasing the total emission rate results in the a straightforward reconstruction of the source distribution becoming impossible, thus leading to coded aperture imaging. While discussion of pinhole imaging as a concept discussed transmission through one or few mask hole elements, the existence of mask moderator elements surrounded by mask hole elements follows the same analysis and has the same geometric behavior.

2.2 Encoding and Reconstruction

In contrast to the single pinhole that used in traditional pinhole imaging, coded aperture imaging uses a mask with many pinholes placed in mathematically determined patterns that enable an analytical reconstruction of the original source distribution. While many patterns exist that have desirable mathematical properties for coded aperture imaging, physically constructible arrays have been selected as desirable in physically built coded aperture imaging system. The source distribution is projected through the mask onto a position-sensitive detector (Accorsi, 2001). In the far-field assumption, where incident particles can be considered uniformly incident on and normal to the imaging mask, the count pattern on the detector is

$$O \times A = R$$ Equation 1

where *O* is the source distribution, *A* the transmission of the mask (which may take on one or two values, 0 being complete opaqueness, 1 being completely transparent), $\times$ is a non-periodic correlation operator, and *R* is the detector count pattern. Since imaging masks may contain several hundred pinholes, the relationship between *O* and *R* is not immediately intuitive in that a pixel in a reconstructed estimate of *O* is not represented by a single pixel in the detector, but

by the pattern of pixels over the entire detector. The reconstructed estimate of *O*, $\hat{O}$, is generated through the periodic cross-correlation of the detector count pattern *R* and a decoding array, *G*, as

$$\hat{O} = R \otimes G \qquad \text{Equation 2}$$

where $\otimes$ is the periodic correlation operator. In coded aperture imaging, the mask pattern and decoding array selected such that the reconstruction of a perfect projection (*R*=*A*) and the decoding array produces a perfect reconstruction with the reconstructed image $\hat{O}$ being zero except for a single source pixel containing all counts from the source. The choice of the pattern is driven both by the need for mask patterns to be physically realizable and a desire for the autocorrelation of a mask pattern and itself to be either a perfect or near-perfect delta function.

Since reconstructing artifact free images (*R*=*A*) requires a full mask pattern be projected onto the detector, if the imaging mask contains only a single copy of *A* only a single direction can be perfectly reconstructed. But if the pattern used to generate *A* is a cyclic set, meaning that the cross-correlation is perfect regardless of where in the detector the full pattern is centered, the number of directions that can be perfectly reconstructed is limited only by the properties of the mask pattern selected. Due to this, a common pattern is formed by use of a 2x2 tiled Modified Uniformly Redundant Array (MURA) (Fenimore & Cannon, 1981), (Gottesman & Fenimore, 1989). Tiling the mask pattern increases the field of view of the imager, for which a more rigorous discussion is included in Section 2.2.1. In this case, the decoding array is the same as the mask pattern except that where a filled mask element (0) would be expected, the decoding array value is -1. This results in a decoding that produces a zero-valued image except at the location of the source. The MURA is an anti-symmetric array (i.e., a 90° rotation produces the inverse of the pattern) where the mask transmission value of a given pixel (*i,j*) is defined by

$$A_{i,j} = \begin{matrix} 0\, if\ i = 0 \\ 1\, if\ j = 0, i \neq 0 \\ 1\, if\ c_p(i)\, c_p(j) = 1 \\ 0\, otherwise \end{matrix} \qquad \text{Equation 3}$$

where

$$c_p(i) = \begin{matrix} 1 & if\ there\ exists\ an\ integer\ x\ satisfying \\ & the\ condition\ i = mod_p x^2 in\ the\ range\ 1 \leq x \leq p \\ -1 & otherwise \end{matrix} \qquad \text{Equation 4}$$

From Equation 3 and Equation 4, a value of *p* must be chosen to determine the mask transmission value. For MURA patterns, only prime values of *p* are allowable, and the selected value of *p* is referred to as the rank of the MURA pattern. The patterns generated by a MURA are physically constructible arrays and, due to the anti-symmetric property of the array, produce anti-mask data (the inverse of mask data) from a rotation of the mask pattern, as shown in Figure 9.

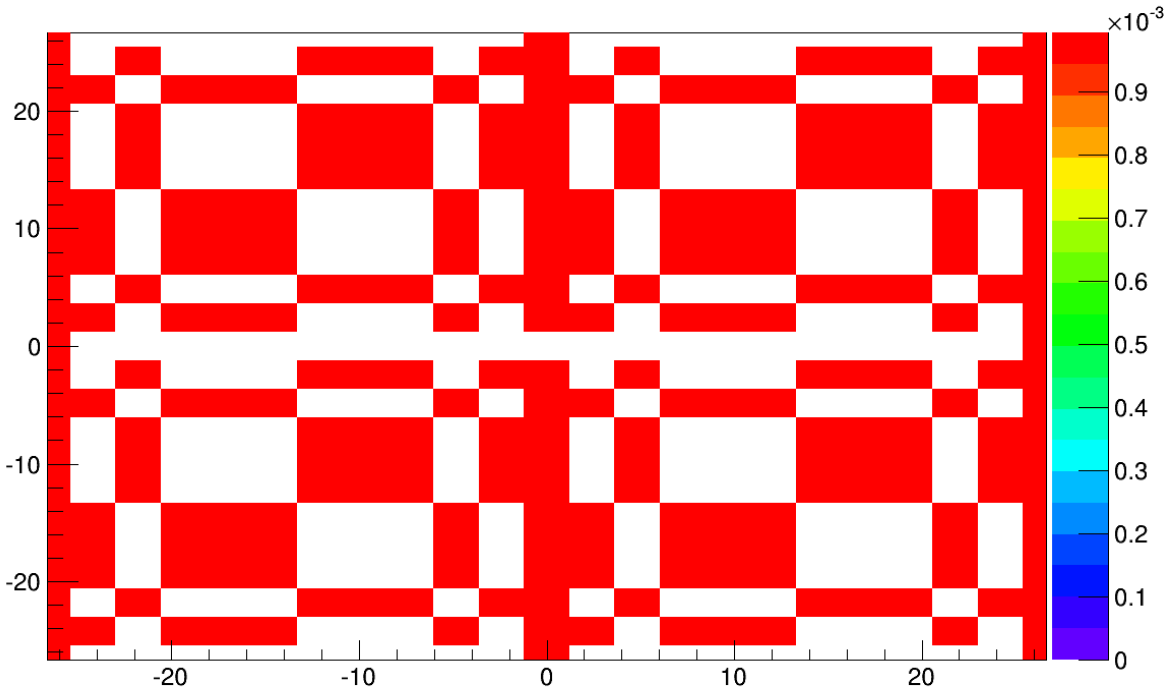

Figure 9. Tiled mask pattern using a 2x2 tiled rank-11 MURA pattern. Mask hole elements are high-value regions of the plot (red color), while mask moderator elements are zero-value regions (white color).

The MURA equations used to generate Figure 9 demonstrates not the mask moderator elements, but the mask transmission elements, meaning that the zero-value regions are where mask moderator elements are located and other regions are where the holes in the mask are located. The MURA pattern itself is tiled into a 2x2 grid, utilizing the cyclic property of the MURA pattern. The ability to a reconstruct from mask and anti-mask data using the same mask is quite attractive, since this enables the removal of mask-independent background influences (e.g. sources located behind or to the side of the imager).

Additionally, the signal-to-noise ratio is increased by the subtraction of anti-mask data from mask data thorough increasing the separation between mask hole elements and mask moderator elements. Consider a measurement of a single source, as shown in Figure 10.

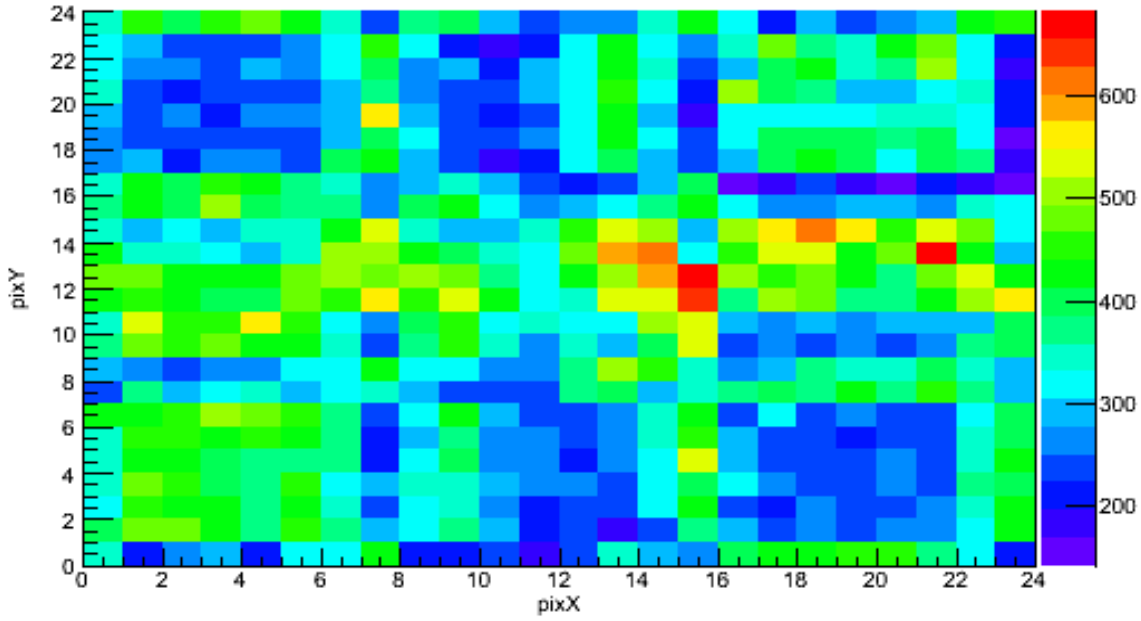

Figure 10. Measured source at 205 cm distance on a 24x24 pixel detector, using a 2" thick tiled rank-11 mask, no anti-mask subtraction.

While the size of the distribution and specific pattern of the detected source distribution is dependent on mask design and position resolution of the detector, the benefits of the anti-mask subtraction for improving the statistics of the modulated data is dependent on the separation between mask hole and mask moderator regions of the detected distribution. From visual inspection, the mask hole regions of Figure 10 are represented by ~415 counts, while the mask hole regions are represented by ~250 counts, corresponding to a contrast of ~165 counts. The data collected using the anti-mask orientation of the imager would have similar values, but

the locations of the mask and anti-mask regions would be reversed due to the change in geometric modulation of the incident source distribution. By subtracting the anti-mask data from the mask data, the separation between the mask moderator and mask hole elements would be increased, as shown in Figure 11.

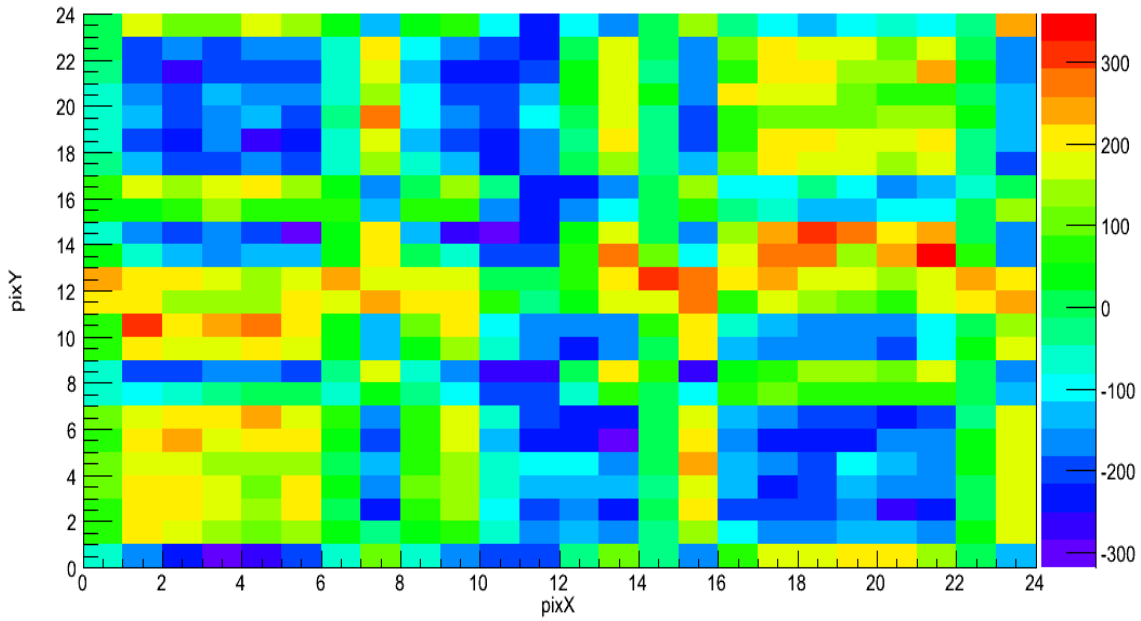

Figure 11. Measured source at 205 cm distance a 24x24 pixel detector, using a 2" thick tiled rank-11 mask, with anti-mask subtraction.

Multiple effects are visible from the subtraction of the anti-mask data. The effective contrast is increased, since the mask moderator regions now have a value of ~-165 and the mask hole regions have a value of ~165, making the effective contrast 330 counts. Also, the distribution of the intensities of the detector data is centered round approximately zero, indicating that the total emissions of the source and background were consistent between the two. The integrated counts in Figure 11 are not representative of the measured counts, then, but the

measured contrast between mask and anti-mask elements. This is confirmed by the near-zero value for the center pixels of the detector, since through rotation of the mask pattern the center mask values are held constant.

While it is not difficult to envision measurement scenarios where the distance to a source is precisely known and measurement consists of verifying a declared radiation source position and intensity, in the more general case, and a particularly relevant case for plutonium holdup measurement, the distance to the source may not be precisely known, and must be estimated from the measured data in some way. Without prior knowledge of expected source distances, a technique is to reconstruct the measured data at multiple source distances, and to then determine the distance to the source based on the reconstructed data. To reconstruct the source at varying mask to source distances, the detector data is sampled corresponding to the physical size of the projected mask pattern at that distance. For a fixed detector pixel size, then, the dimensions of *R* must be equal to the dimensions of the projected mask pattern at that distance, regardless of the true number or size of pixels in the detector. Since the distance to the source for a specific reconstruction distance is determined by sampling the fixed detector data, an infinite number of distances can be reconstructed.

In this way, a 24x24 pixel detector becomes a 22x22 sampled pixel array in the reconstruction process, with individual detector pixels contributing to multiple sampled pixels.

It is intuitive from trigonometry that at infinite source to mask distance, the size of the projected mask pattern is identical to the size of the true mask pattern with a finite detector to mask distance, as well that at some distance for mask patterns smaller in size than the detector, the projected mask pattern is the same physical size as the detector. This latter distance is called the critical distance. Sources located closer than the critical distance do not project full mask patterns, as shown in Figure 12 in comparison to Figure 13.

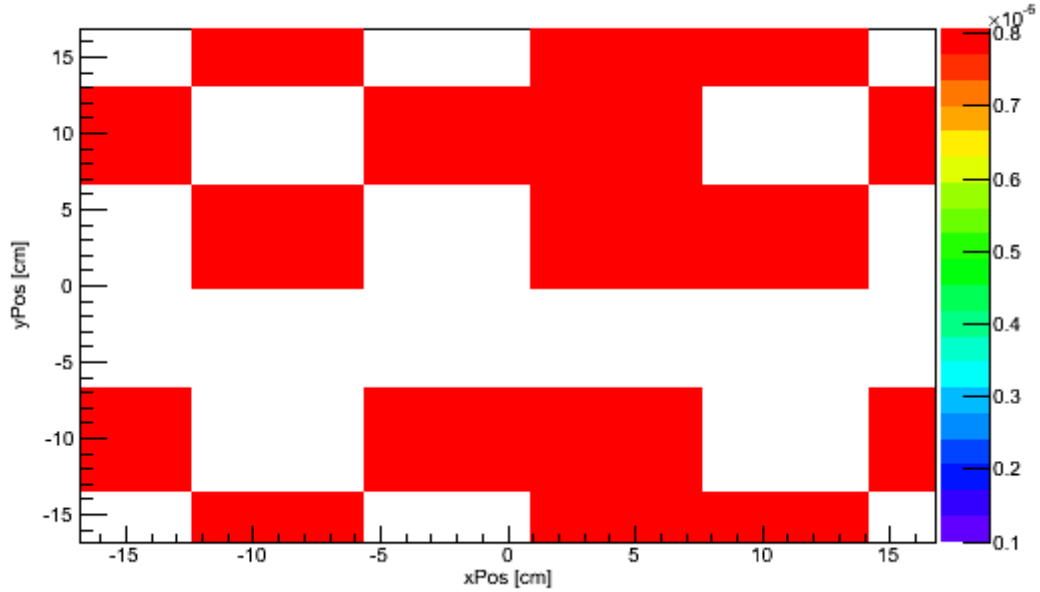

Figure 12. Projected mask pattern incident on detector. Detector design is a24x24 pixel detector, with the mask pattern being a 2x2 tiled rank 11 MURA. Source-to-mask distance is 50 cm for 1.2 cm mask pixels and a 35 cm mask-to-detector distance.

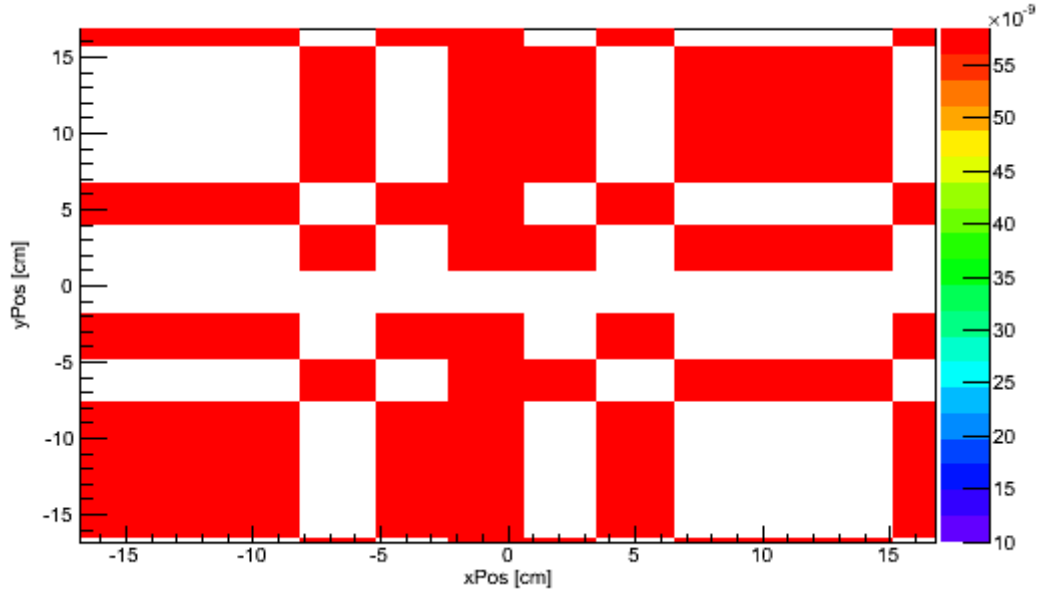

Figure 13. Projected mask pattern incident on detector. Detector design is a24x24 pixel detector, with the mask pattern being a 2x2 tiled rank 11 MURA. Source-to-mask distance is 320 cm for 1.2 cm mask pixels and a 35 cm mask-to-detector distance.

While the absolute values in Figure 12 and Figure 13 differ, this is due to the way the absolute values in the forward projection is determined, specifically accounting for source to detector distance, and the morphological differences are the important characteristics. The same mask pattern is projected from both source positions, and the shape of the pattern in Figure 12 exists within the pattern in Figure 13, and both projections are clearly derived from Figure 9. Since Figure 9 is a 2x2 tiled MURA pattern, any $1/4^{th}$ of Figure 9 centered at any position represents a full mask pattern. As is clear in Figure 12, the projected data does not represent any $1/4^{th}$ of Figure 9, and thus is not a full mask pattern, unlike Figure 13. In order to reconstruct data that does not have a full mask pattern at the proper distance, the size of the sampled distribution would have to be greater than the actual detector. Since this would be non-meaningful, ambiguous and non-meaningful results would be reconstructed, as shown in Figure 14.

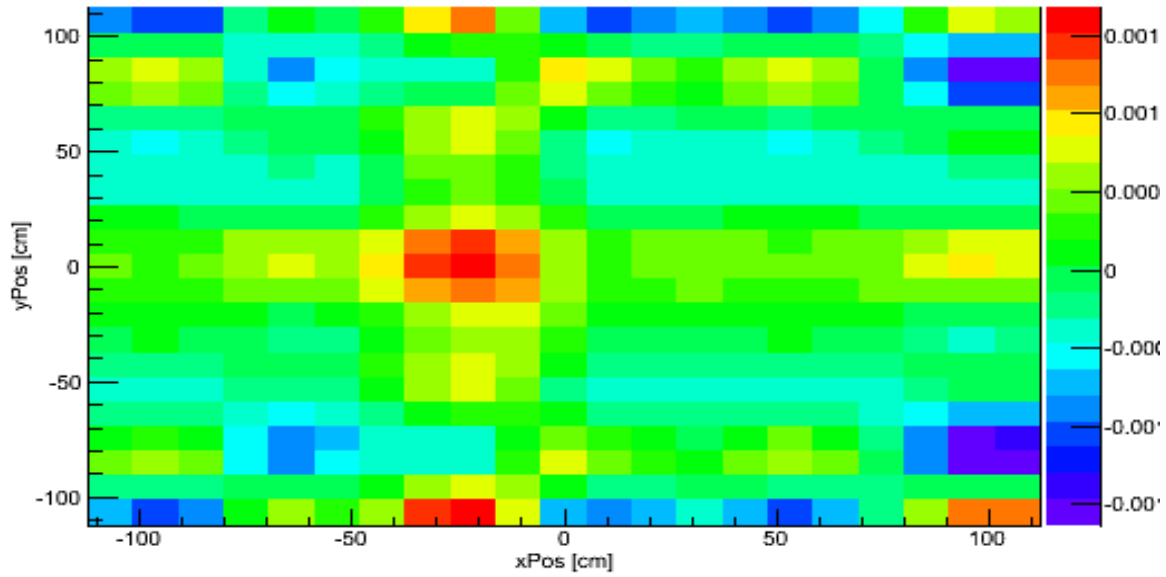

Figure 14. Reconstructed source with projection from Figure 12.

Despite the source being reconstructed at the proper distance and no statistical effects, the source reconstructed in Figure 14 is not reconstructed without large artifacts. While the exact nature of the artifacts reconstructed is dependent on the distance to the source, it is clear from Figure 14 that the reconstructed source distribution at the proper distance is ambiguous. Ambiguity in Figure 14 is defined as the poor separation between the peak intensity and minimum intensity, and the existence of many pixels in the reconstructed image having negative reconstructed intensities, a physically meaningless value.

With a full mask pattern projected on the detector, it is possible to fully reconstruct the source while using the benefits of the MURA pattern and perfect decoding is theoretically possible. In the cross-correlation reconstruction method, it intuitively follows that reconstructing the source at the wrong distance produces artifacts, as shown in Figure 15.D, while reconstructing the source at the proper distance minimizes artifacts, as shown in Figure 16.D.

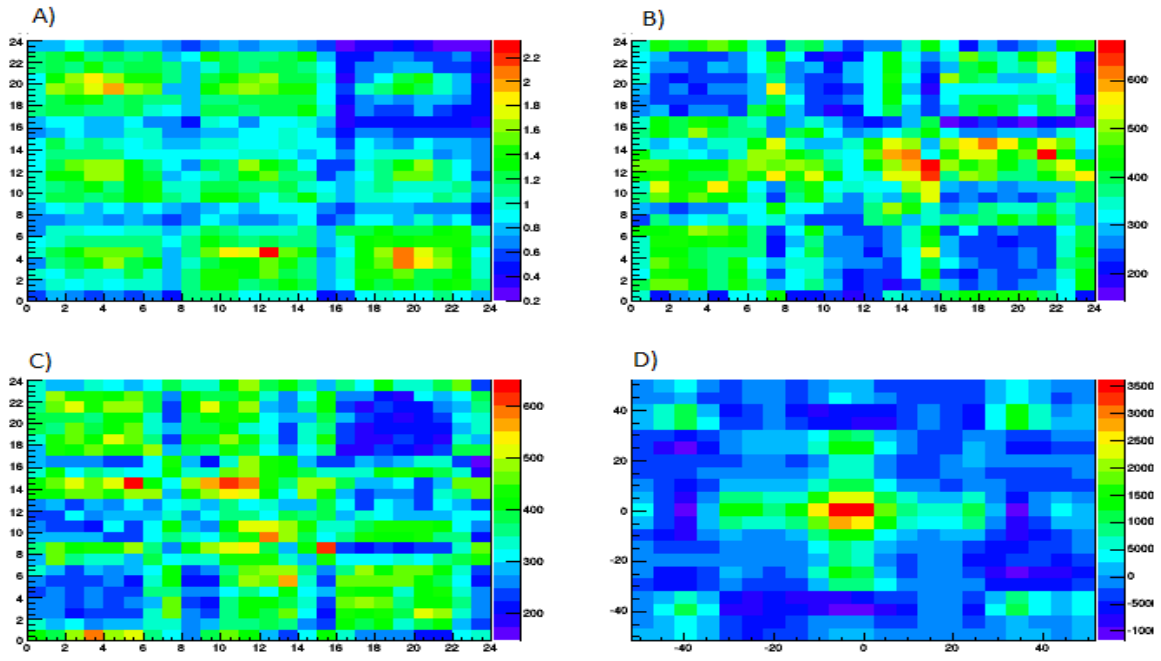

Figure 15. Measured data and reconstructed in focus source using cross-correlation reconstruction. A) No-mask (void) measured data. B) Mask measured data. C) Anti-Mask measured data. D) Reconstructed Image. Data is intentionally reconstructed at the wrong distance.

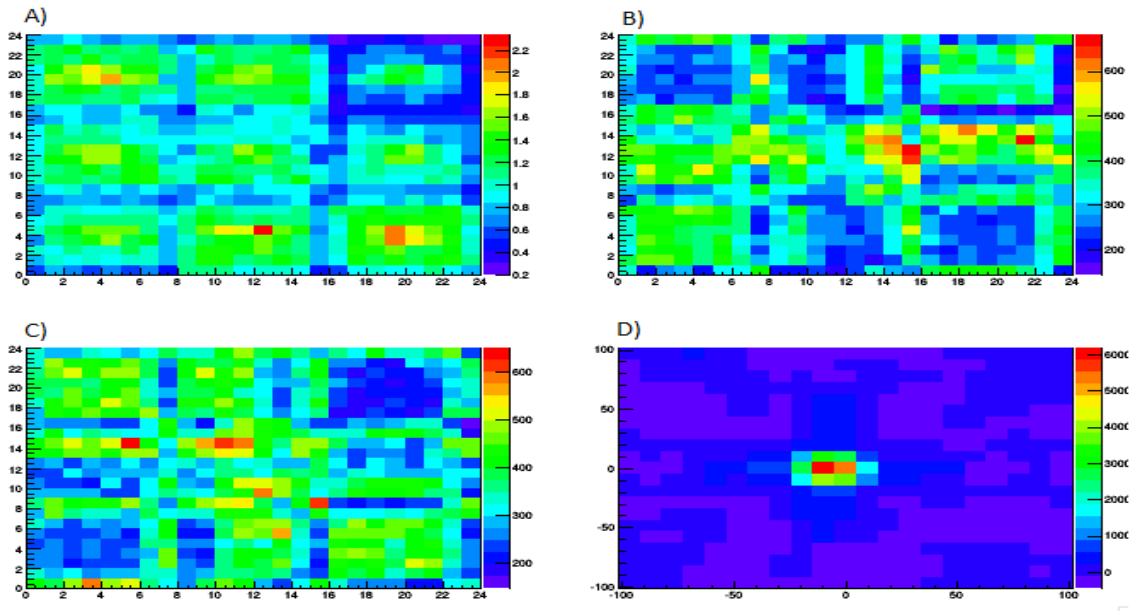

Figure 16. Measured data and reconstructed in focus source using cross-correlation reconstruction. A) No-mask (void) measured data. B) Mask measured data. C) Anti-Mask measured data. D) Reconstructed Image. Data is intentionally reconstructed at the correct distance.

While the measured data in Figure 15 and Figure 16 are held constant, the reconstruction distance varies between the two, resulting in very different reconstructions. Both reconstruction consist of an hour-long measurement at 170 cm using a rank-11 MURA and a 24x24 pixel imager. In Figure 15.B and Figure 15.C some aspects of the MURA pattern in Figure 9 are visible, particularly the anti-symmetry in apparent mask hole and mask moderator locations, with depressed count regions in 15.B corresponding with increased count regions in 15.C, and increased count regions in 15.B corresponding with decreased count regions in 15.C. Figure 15.D, reconstructing the source at the wrong distance causes the production of various artifacts. In particular, the peak source intensity is suppressed (3500 in Figure 15.D and 6000 in Figure 16.D) and, the reconstruction of nonexistent sources diagonal to the source position, and some region of the reconstructed source distribution reconstructed as negative intensity. This is physically unrealistic, and clearly indicates that the reconstruction distance is not the true distance of the source. While 15.A and 16.A are identical images, this is due to them being the same void normalization used to correct for variations of intrinsic efficiency within each neutron block detector, shown in Figure 17.

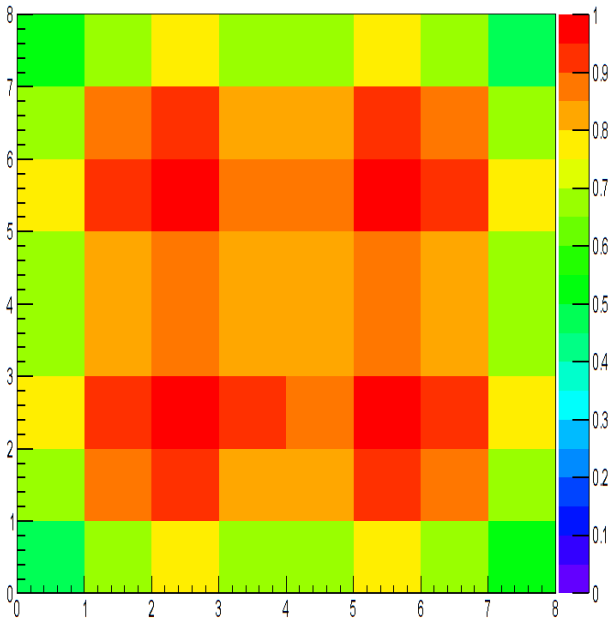

Figure 17. Normalized scintillation light collection efficiency per-pixel for a 24x24 pixel neutron block detector. Data generated by Geant4 simulation of light transport within a block detector.

Because light generated due to scintillation events in different detector pixels has different probability that any individual photon is collected by the PMT's, the raw counts in different pixels are depressed relative to the maximum efficiency pixel. This difference is accounted for by normalizing the detector data with non-mask data.

For a perfect reconstruction, the non-source region of the reconstructed image would be perfectly flat with intensity of zero. This would be expected from the choice of the MURA pattern and the decoding array. While the background of Figure 16.D does contain negative intensity reconstructed pixels and some apparent structure in the non-peak regions, the absolute magnitude of the negative intensity pixels is much lower than Figure 15.D and the peak reconstructed intensity to background ratio is much higher. Considering the measured data, with >5% relative error in many of the detector pixels from Poisson statistics, the

imperfect reconstruction at the proper reconstruction distance can be attributed to statistical noise, and a longer measurement would provide a near-perfect reconstruction.

2.2.1 Field of View and Resolution

Because of both finite detector and mask size and finite pixel size, coded aperture imagers are limited in their field of view (FOV) and resolution. From trigonometry, the magnification of the mask pattern size, *m*, is related to the source-to-mask distance *a* and mask-to-detector distance *b* by:

$$m = 1 + \frac{b}{a}$$ Equation 5

For a cyclic geometry, such as that generally chosen for coded aperture imaging, the field of view is not limited by the overall size of the mask, but by the size of the detector, the field of view is visually represented by Figure 18.

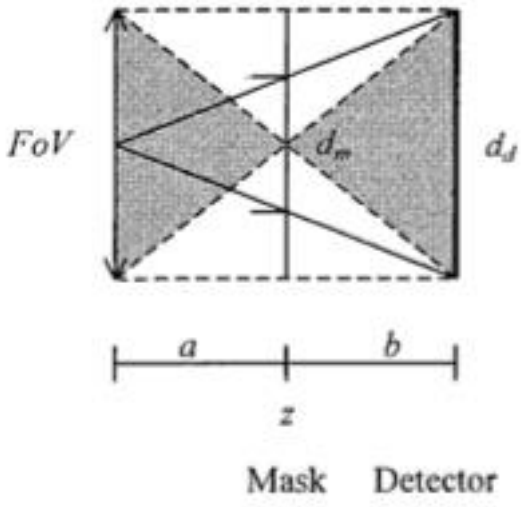

Figure 18. Visual representation of field of view for a cyclic geometry. (Accorsi, 2001) ©MIT 2001.

The field of view for a cyclic geometry is related to the magnification by

$$FoV = \frac{d_d}{m-1} \qquad \text{Equation 6}$$

Where d_d is the size of the detector. From this, it readily follows that increasing the mask-to-detector distance for a fixed detector-to-source a+b distance decreases the field of view, while the inverse is true. Reconstruction typically occurs over multiple distances, thus angular field of view ($\Delta\vartheta$), which is not dependent on the source-to-mask distance a, is more useful, and is determined from considering the geometric relationships in the system to be

$$\Delta\vartheta = \tan^{-1}\left(\frac{d_d}{2b}\right) \qquad \text{Equation 7}$$

Since reconstructed images are fixed in their number of pixels, while covering larger areas for reconstruction distances further away from the source, it is intuitive that the value of resolution is proportional to the field of view. Of course, a low value for resolution (generally referred to by the misnomer "high-resolution") is desirable. Resolution (λ_g), or the width of a reconstructed pixel, can be defined as

$$\lambda_g = \frac{FoV}{n} \qquad \text{Equation 8}$$

where n is the number of pixels in the side of the mask pattern (e.g., 22 for a double sampled rank-11 mask). Resolution can be defined either in physical dimensions (length) or in angular dimensions depending on the needs of the measurement design, but in both cases, it is a constant ratio to the field of view.

The development of an understanding of a field of view for a coded aperture system assumes a tiled mask pattern. This is a somewhat trivial assumption in the case of fast-neutron imaging, since the fast-neutron coded aperture imagers that have been developed all utilize a tiled mask pattern, but the assumption made is due to the properties of a coded aperture type of measurement itself. Reconstruction using the cross-correlation technique requires the projection of a full mask pattern on the detector array. With a mask that has a single mask pattern on it, all improvements in field of view over a single point in the source distribution are due to increases in detector size. By tiling the mask pattern, however, the field of view is increased because one of many full mask patterns can be projected onto the detector. In effect, the allowable angles for a source location to project a full pattern in Figure 9 changes from the center angle only to any angle centered within the inner half of the detector (-13 to 13 on both axes).

Resolution can also be improved by decreasing the physical size of the pixels while maintaining the overall detector size. With decreased pixel size, the number of detector pixels covering each mask element increases, improving the spatial sampling of the incident source projection. Pixels that are too small, however, would require increased measurement time due to the decreased geometric efficiency. Imagers used in this study are all double-sampled, meaning that a 22x22 pixel detector samples a rank-11 mask, the design of which are discussed in Section 2.4.

2.3 Parallax Imaging

For a single coded aperture measurement, distance resolution is limited by pixel size, since the physical size represented by the sampled detector array in the reconstruction process is independent of the physical size of the pixels in the physical detector. Since for common position-sensitive neutron detector designs, the size of pixels in a detector is fixed, reconstruction at varying distances consists of repeatedly sampling detector pixels. If the size of the pixels in the detector array created during the cross-correlation process is smaller than the pixels in the physical detector, the physical meaning of the data cross-correlated with the decoding array is ambiguous, since the angular resolution of the physical detector is larger than

the sampling rate. With very small pixels, the pixel array generated in the cross-correlation process represents many detector pixels, and the data was actually measured. However, with very small pixels, the relative statistical error of individual pixels is decreased in comparison to relatively large pixels due to decreased geometric efficiency. Decreasing the pixel size while maintaining the active volume of the imager improves the distance resolution by maintaining the physical meaning of the sampled detector array, at the cost of increased measurement time due to the decreased statistics. Since this is a limiting factor for a fixed detector pixel array and limited measurement time, it creates a scenario where a coded aperture imager provides mainly directional information of a given source location, and comparatively poor distance information, as seen in Figure 19. The detector data used to generate Figure 19 consists of a source at 250 cm source to mask distance ray-traced through a thin mask at 35 cm mask to detector distance. The data was normalized to an integral of one.

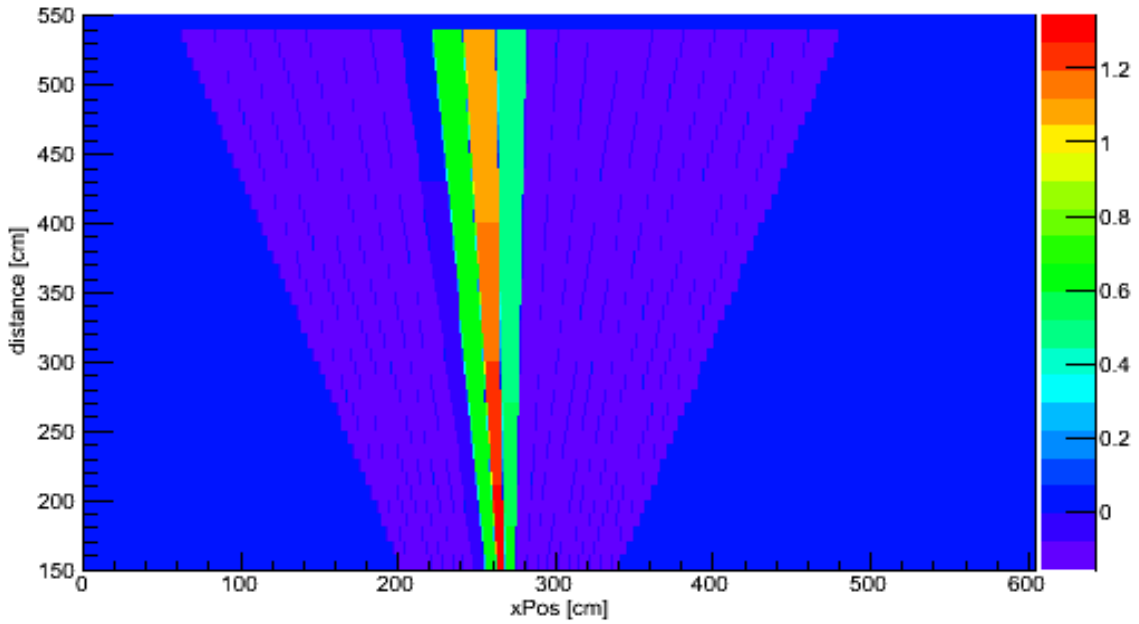

Figure 19. Projection of source reconstruction for a single measurement location. Projected data normalized to an integral of 1.

For reconstruction purposes, the x-axis is parallel to the face of the detector and the orthogonal axis on which the detector moves, the y-axis is vertical from the floor, and the z-axis is parallel to the viewing direction of the detector. When a cross-correlation reconstruction is performed, the zero position on the x-axis is defined as the minimum x-value of the field of view at the maximum reconstructed depth. Due to this, absolute position on the x-axis is less useful than relative position. In Figure 19, a XZ projection of the reconstruction is used, and the addition of the reconstruction from the Y-axis provides no additional distance (Z) information. Distance information that can be determined from the single reconstruction is limited, although angular resolution is possible. Fitting a Gaussian distribution to the vertical slice of this projection containing the maximum intensity pixel, the Gaussian that is fitted has a mean of 241 cm and a standard deviation of 122 cm, indicating very poor distance resolution. In contrast, a Gaussian distribution fitted to a horizontal slice containing the same pixel has a mean of 262 cm and a standard deviation of 8.1 cm.

In the case of no distance resolution but perfect angular resolution, it is intuitive that a second measurement with a field of view rotated 90° but still viewing the source (i.e., a view from a side angle) would allow for more precise localization of the source when the two reconstructions are combined. This is due to the angle between the source and the detector for the second measurement position being changed relative to the first measurement position. Access to potential sources may be limited to only one-sided measurements, so while the extreme example of 90° rotation of field of view represents the largest change in field of view, physically moving the imager along a single axis also changes the field of view of the imager. When reconstructed measurements are combined, a source would be represented not by a single direction, but by the intersection of the reconstructed source direction for each individual measurement. Adding reconstructed data from different measurement positions allows for the use of the superior angular resolution, enabling localization of a source in 3D, as seen in Figure 20.

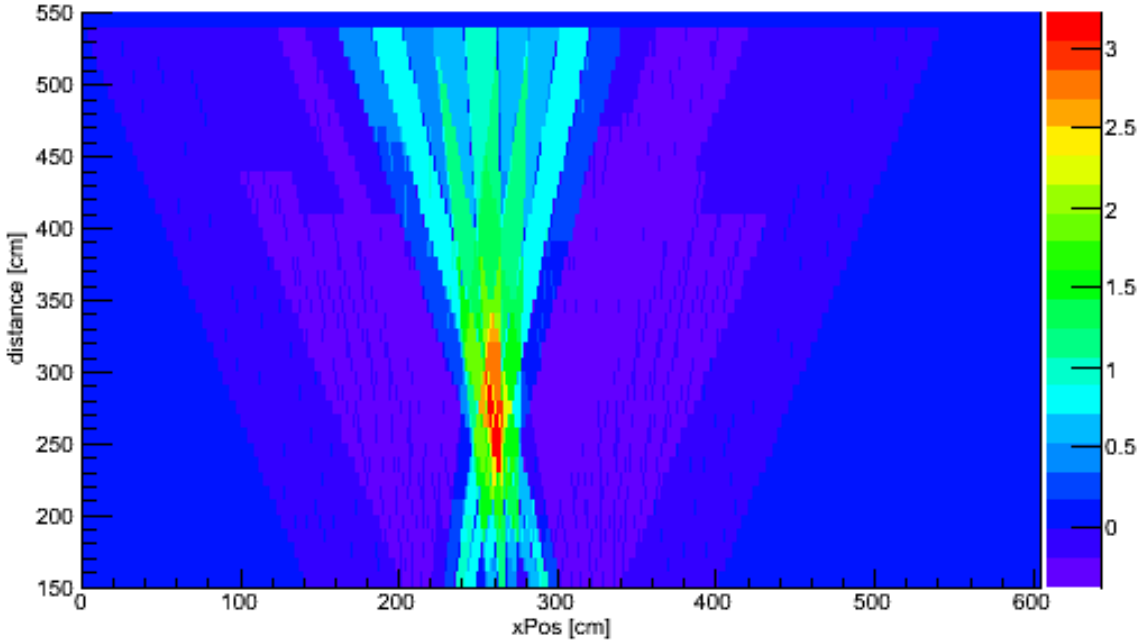

Figure 20. Projection of source reconstruction for three measurement locations. Each detector position is shifted by 30 cm on the orthogonal axis, with the second measurement being directly underneath the source.

The ray-tracing method and normalization used to generate the data reconstructed in Figure 19 was the same as the method used to generate the data reconstructed in Figure 20. The projections from multiple measurement positions were combined by summing the reconstructed projections together. This visualization technique is imperfect, however, since each pixel in the combined reconstructed image is dependent on reconstructed pixel value over each of the reconstructed images. It is a combination of not only the reconstructed source information, but any artifacts produced during the process are included in the averaged projection, which may result in false sources appearing in the projection, or variations in detected source counts that are not accounted for in the reconstruction process.

In contrast to Figure 19, in Figure 20 localization of the source in 3D cannot be determined by fitting a Gaussian distribution to the reconstructed source distribution, since source position is determined by the intersection of the measurement positions. By defining the source as any pixel greater than some threshold (in this case, 2 standard deviations above the intensity of a pixel with the intensity equal to the arithmetic mean of the image), the combined reconstructed source image can be limited to the actual source position, as shown in Figure 21.

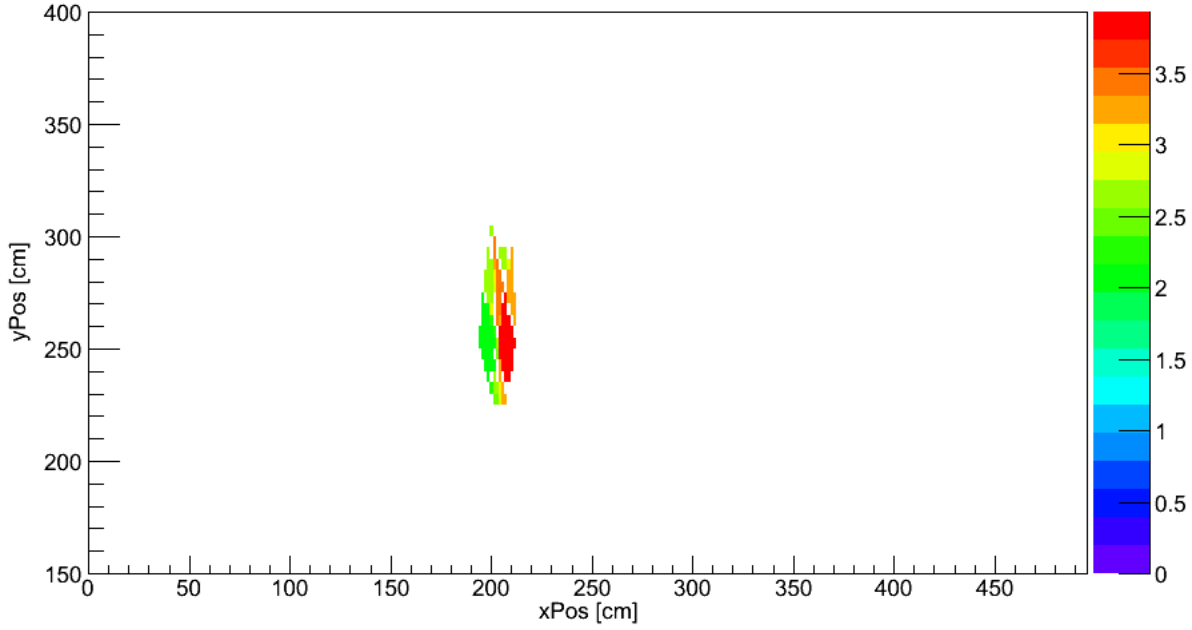

Figure 21. Projection of source reconstruction for three measurement locations, limited to only source pixels in combined reconstruction. Each detector position is shifted by 30 cm on the orthogonal axis, with the second measurement being directly underneath the source

In the case of Figure 21, the source is reconstructed in the overlap of each individual reconstruction, and the shape of this overlap is dependent on the shape of each individual reconstruction. While with certainty it can be said that the source is isolated within this region, it can also be said that the source is located within the peak overlap from a distance of 240 cm to a distance of 280 cm. One of the potential artifacts of interest is sources that are reconstructed to the multiple locations due to the cyclic mask nature, as shown in Figure 22.

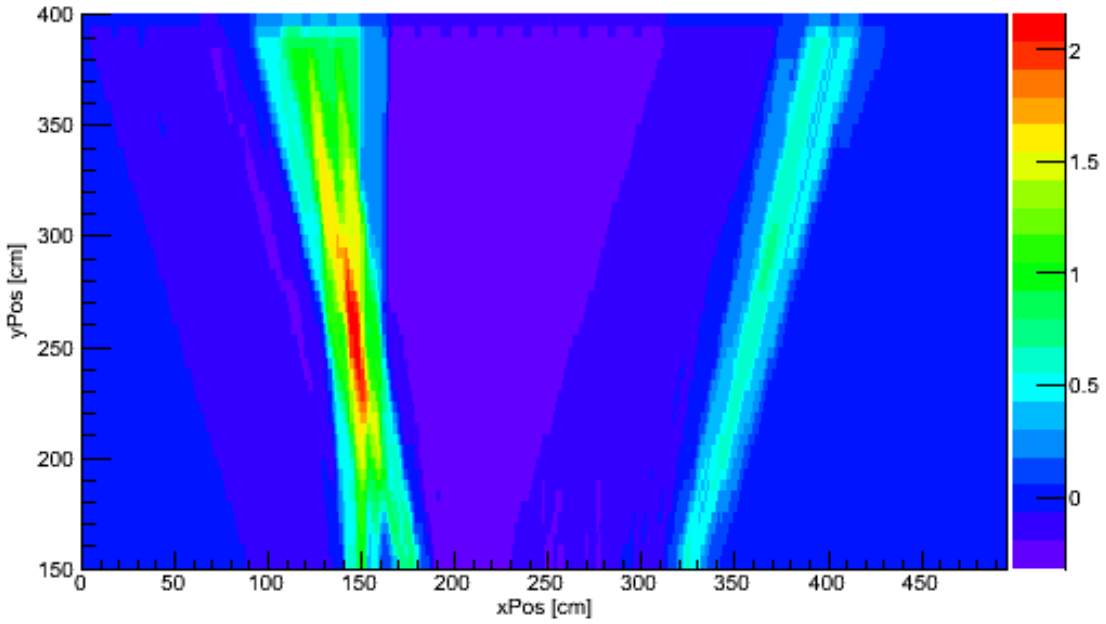

Figure 22. Cross-Correlation reconstruction of simulated data demonstrating a false source located to the right side of the true source.

The simulated data used to generate Figure 22 consisted of a ray tracing from a single source position through an imaging mask at three measurement positions, with the projection normalized to an integral of one for each measurement position, and Gaussian noise added to

the simulated data to blur the reconstructed images and prevent the appearance of discontinuities. While Gaussian noise is continuous and real measurements involve Poisson statistics, the systematic effects of parallax imaging are independent of the total intensity of the source, and normalized sources were used for simulation. This reconstruction demonstrates artifacts common with cross-correlation reconstruction of statistically imperfect data, notably background suppression and the presence of a false-source in the reconstruction. Since each source individually projects data onto each detector position individually, a source located in the suppressed background region between 200 and 300 cm on the ordinate-axis would be reconstructed at a lower intensity due to the decreased background rate, and depending on the source detection algorithm used (e.g. a simple threshold), may not be detected, producing a type II error. An opposite, type I error, is the reconstructed false-source at 350 cm on the ordinate axis. For a single detector position, cross-correlation reconstruction cannot distinguish between sources located on the edges of the fully encoded field of view, and, in fact, it reconstructs a single source to both positions at lower intensity. In signal processing generally, as well as digital imaging, this inability to distinguish two different signals is referred to as aliasing. With a sufficiently intense source, the false-source may meet whatever source detection threshold is used, or with an insufficiently intense source, the reconstructed source at both positions may not meet a source detection threshold due to the depressed reconstructed source intensity, despite the source intensity being physically greater than the threshold.

In more complex imaging scenarios, such as those with limited statistics, noticeable collimation within the imaging mask, unknown variance in detector position, multiple sources, and other scenarios, reconstruction techniques that account for non-ideal encoding and prevent artifact formation may provide more accurate and less ambiguous information on source intensity, location, and shape. The use of multiple measurement locations does enable the use of coded aperture imagers with poor distance resolution to localize sources in 3D, but any artifacts generated during the reconstruction process are carried through to the final reconstructed image, which still doesn't inherently signify that a source is present and requires either operator analysis or further analytical analysis to determine source location and intensity.

2.3.1 Measurement Positions

In a parallax imaging measurement, measurement resolution is limited by the angular resolution of the imager. Only considering the angular resolution of the imager, it is apparent that for a perfect imager, the source location on the distance axis can be determined exactly for even minute changes in detector position. Alternatively, a detector with no angular resolution is very poor determining the source position regardless of the distance between measurement positions. No angular resolution is strictly necessary, since the source position can be estimated from the relative count rates in the detector, but the possibility of heterogeneous background radiation or the need to detect multiple sources simultaneously makes imaging preferable to source position determination by non-imaging techniques.

For a coded aperture imager, the field of view is a finite value, and if the step between measurement positions is larger than the field of view of the imager, the source would be outside of the field of view for at least one of the measurement positions. Conversely, since the angular resolution is limited, minute changes in detector position would not necessarily provide significantly different viewing angles of the source and parallax imaging may not provide significant additional distance information, as shown in Figure 23.

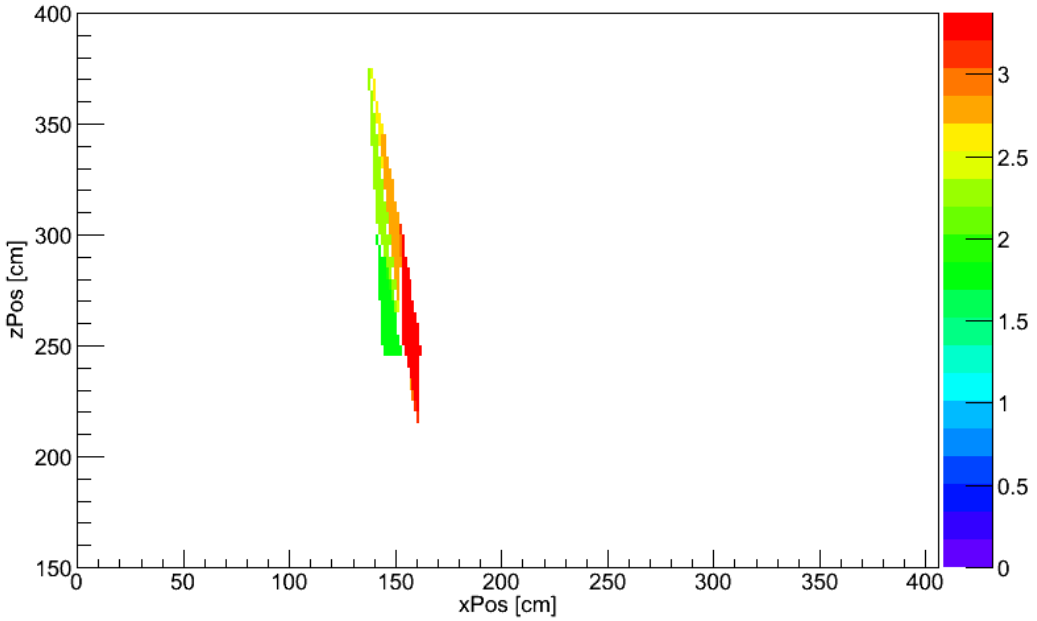

Figure 23. Simulated reconstruction of a source at 250 cm with a 30 cm difference in detector position on the x-axis.

The process to create the reconstructed data in Figure 23 was the same process as Figure 22 and similar previous reconstructions, with a source located at a distance of 250 cm and a 30 cm step between measurement positions on the ordinate axis.

While some distance information is gained by the addition of the second detector position, such as the maximum bin and thus the source itself being located between 220 cm and 300 cm distance away, this is poor distance resolution in comparison to Figure 20. This is logical when the distance resolution of an individual is neglected in analysis, and only angular resolution is considered. Specifically, the overlap between the reconstructed source distributions is greater when the angles of the reconstructed source distributions are similar. By increasing the difference between the angles of the reconstructed source distribution, the resolution of the reconstruction on the distance axis is improved, as shown in Figure 24.

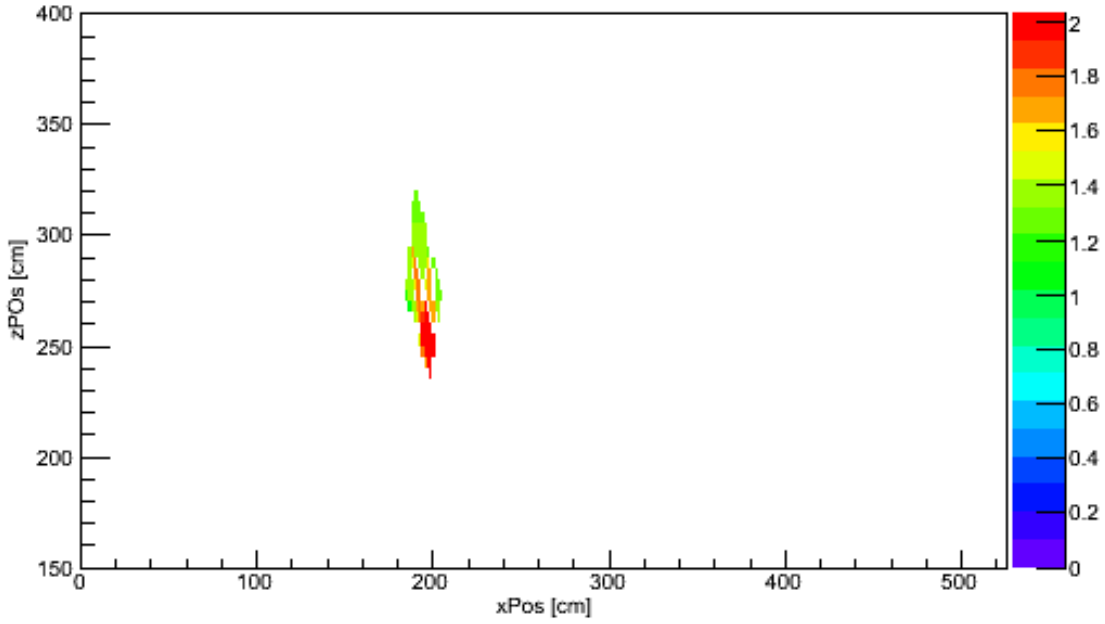

Figure 24. Simulated reconstruction of a source at 250 cm with a 70 cm difference in detector position on the ordinate axis.

Due to the decreased overlap between the reconstructed source distributions, the source is constrained within a smaller region Figure 24 than in Figure 23. While both reconstructions have good resolution on the ordinate axis, this is expected due to the good angular resolution of the technique. The increase in angle between the reconstructions decreases the distance covered by both reconstructions, leading to the peak overlap being between 240 and 270 cm, an improvement of 50 cm distance resolution over Figure 23.

Increasing the separation between the two detector positions would not have the effect of further constraining the source, however, since as is apparent in Figure 24 and Figure 22, increasing the separation would induce artifacts related to the reconstruction of sources outside of the field of view.

2.4 The Deployable Fast-Neutron Coded Aperture Imager

ORNL has developed multiple fast-neutron imagers since 2010 for a variety of purposes, including the quantification of plutonium (Hausladen, Blackston, & Newby, Position-Sensitive Fast-Neutron Detector Development in Support of Fuel-Cycle R&D MPACT Campaign, 2010). Previous imagers used various designs, including a computed tomography based imager (Hausladen, Blackston, & Newby, Demonstration of Emitted-Neutron Computed Tomography to Quantify Nuclear Materials, 2011), a plastic-scintillator coded aperture imager with no gamma-ray discrimination (Hausladen & Blackston, 2009), and a liquid-scintillator (EJ-309) based coded aperture imager (Hausladen P. , et al., 2012). Two imagers have been built based on the experimental scintillator EJ-299-34 (Zaitseva, et al., 2012) (Newby, Hausladen, Blackston, & Liang, 2013). One imager employs a 24x24 pixel detector array (P24), while the other imager employs a 40 x 40 pixel detector array (P40), where each detector array is based on previously developed block detector designs (Hausladen, Newby, Liang, & Blackston, 2013). A photograph of the 24x24 pixel imager is shown in Figure 25.

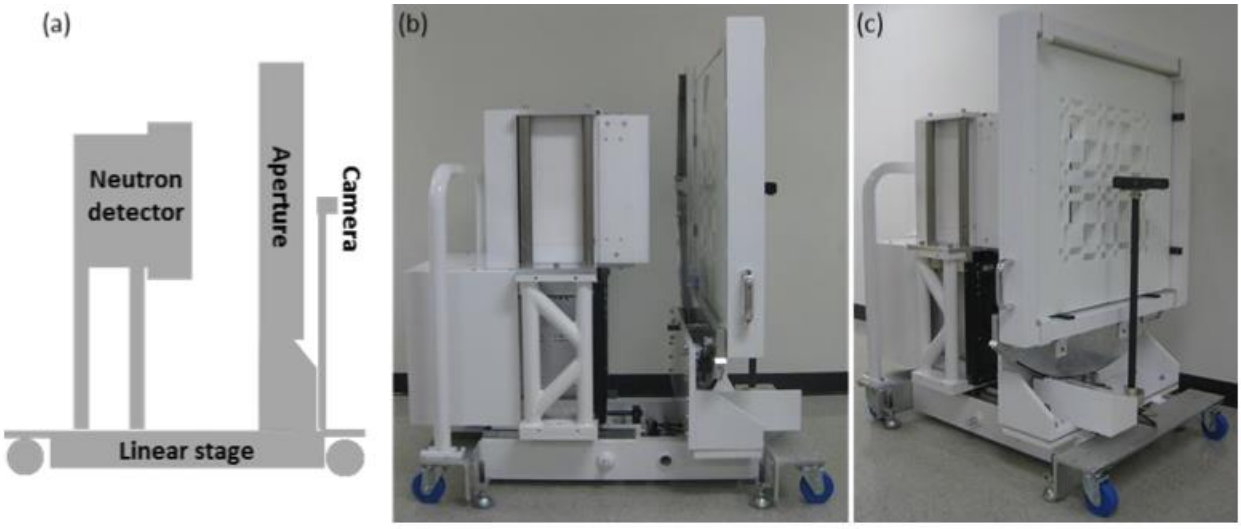

Figure 25. The 24x24 pixel fast-neutron imager: (a) schematic diagram of imager, (b) photograph of imager, and (c) imager from the front, showing the aperture mask. (Hausladen, Newby, Liang, & Blackston, 2013)

For the 24x24 imager, the detector array consists of a 3x3 array of 8x8 pixel block detectors, where the active volume of each block detector is 108 × 108 × 5 mm^3. Each block detector pixel is surrounded on 5 sides by a negligible thickness (<1 mm) of 3M Vikuiti reflector. The plastic pixels, each 13.5×13.5×50 mm^3 in dimension, in each block detector are viewed by the photosensor through a 28 mm thick segmented PMMA (poly(methyl methacrylate)) light guide. The interaction located is determined using Anger logic, considering the shared response of four 51 mm Hamamatsu R7724-100 photomultiplier tubes (PMTs) to determine the relative position of the scintillation event. The PMTs are read out by a custom board designed at ORNL. A photograph of the scintillator pixel block, light guide, and assembled detector module (before encapsulation) is shown in Figure 26.

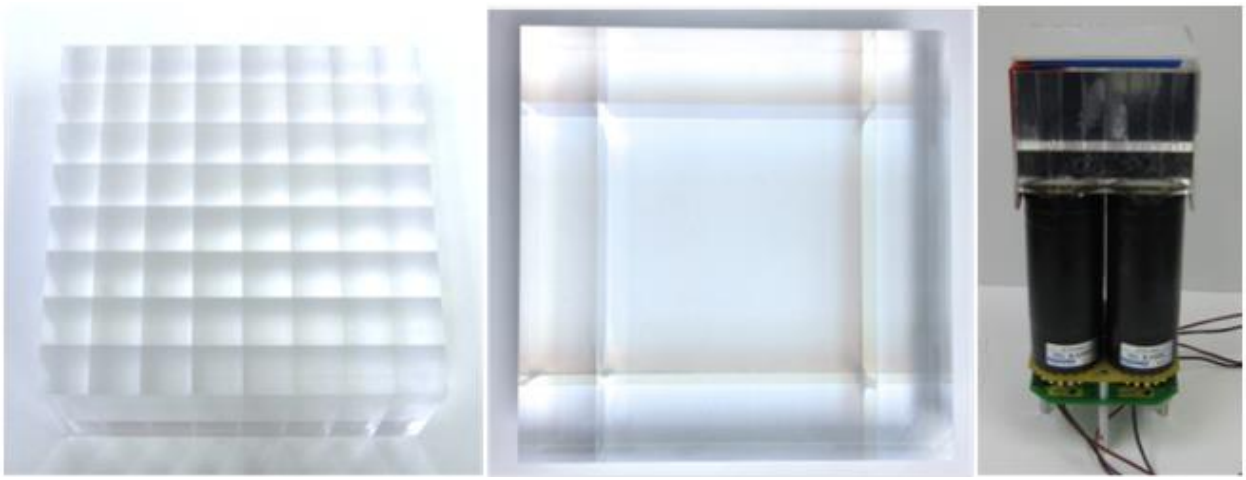

Figure 26. EJ-299-34 segmented pixel array (left), segmented light guide (middle), assembled detector module (right).

Based on a design similar to the 24x24 pixel array, the 40x40 pixel array consists of a 4x4 array

of 10x10 pixel block detectors. The size of each EJ-299-34 scintillator pixel is 10.7 x 10.7 x 50mm^3. In contrast to the 8x8 block detectors, the 10x10 block detector has a two-piece light guide of total length 29.21 mm. The two piece light guide is split into two-pieces, one piece with a length of 5.25 mm, the second piece meeting the rest of the total length. The scintillation event position is determined in the same manner as the 24 x 24 pixel imager. For both P24 and P40, each block detector is wrapped in 2-3 mm of aluminum on five sides, with electronics readout on the sixth side.

The imaging mask for each imager consists of a 2x2 tiled MURA pattern made of high density polyethylene (HDPE). The 24x24 pixel imager has a rank-11 mask pattern, and the 40x40 pixel imager has a rank-19 mask pattern. Each element size of the rank-11 mask is 1.2 cm. Three copies of a 1" thick mask are available, allowing for mask thicknesses of 1", 2", or 3" when those masks are stacked next to each other. Furthermore, three versions of the rank-19 mask exist, with mask element sizes of 1.2, 1.6, and 2.0 cm, thereby allowing for more control of the size of the field of view and thus angular resolution at a given distance compared to the case where only one element size is available. Moreover, thicknesses of 0.5" and 1" are available for the rank-19 masks, allowing for more control of the total mask thickness, up to 3" in total for a given mask element size. The combined imager assembly consists of a neutron detector array; an automated rotating aperture, which holds the selected mask; and a linear stage allowing for controlled variation of focal length (i.e., detector-mask separation).

For both imagers, pulse-shape discrimination (PSD) is performed using standard tail-to-total ratio techniques, in order to discriminate between gamma-ray induced scintillations and fast-neutron induced scintillations.

2.5 Chi-Squared Analysis

The encoding process of coded aperture imaging filters a source projection through an imaging mask onto a discretized detector pixel array, inducing scintillation, the light of which is collected by PMT's, as well as any scintillation light due to multiple scattering within the detector. Traditional cross-correlation decoding filters the detector data through a decoding array that's been resized for various distances, with artifacts potentially being introduced in decoding due

to assumptions such as a homogenous detector array, two-valued imaging mask, and a lack of multiple scattering within the detector. The ideal imaging system assumed in cross-correlation reconstruction consistently of an infinitely thin, opaque mask, and a homogenous detector array, is not true in the case of fast-neutron coded aperture imaging. Due to low interaction cross sections in HDPE, masks must be thick, leading to collimation effects and scattering within the mask in the direction of the detector. Additionally, the neutron block detectors used in coded aperture imaging are discrete sized pixel arrays with discontinuities between pixels. Cross-correlation reconstruction makes erroneous assumptions, leading to artifacts in reconstructed source distributions, in addition to the generation of artifacts inherent to the cross-correlation reconstruction process. These artifacts may potentially obscure true sources, produce noise that may exceed whatever source detection threshold is used, depress the reconstructed emission rate of true sources, or falsely inflate or depress the reconstructed source intensity. Thus, a better understanding of, and the ability to quantify the effects of, deviations from the assumed ideal measurement conditions and imaging systems in measurements where quantification of sources is desired.

One technique to quantify how well a particular system response model or source distribution represents the measured detector data is a goodness-of-fit test, fitting validated simulation data to the measured data. The goodness-of-fit test used is a reduced Chi-squared test.

$$\chi^2 = \frac{1}{\eta - 1}\sum_{i=1}^{\eta}\frac{(A_i - M_i)^2}{\sigma_{m_i}^2} \qquad \text{Equation 9}$$

where *i* is pixel number, η is the total number of observations (pixels) for the analysis, A_i the simulated detector data in each pixel, and M_i the pixel's measured data with variance $\sigma_{m_i}^2$. The reduced chi-squared value is dependent on the accuracy of the system response model used to generate the simulated data. While the Chi-squared test can be used to quantify the goodness-of-fit for radiation detector data, it is a general test used for a variety of situations

where the goodness-of-fit for a model representing statistically imperfect data is desired. The system response model may vary from a very simple model to a full Monte Carlo simulation that incorporates all potential physical effects from source particle emission to detection. The value of reduced chi-squared should be expected to reach a relative minimum where a measurement parameter, such as mask thickness or source position, is properly modeled, and over a number of chi-squared analyses reach an absolute minimum when the detector data is properly modeled, accounting for all relevant components. When the source position is known or imaging parameters are unknown, relative minima would be found when a modeled effect represents the measured data well in comparison to other parameter distributions within the local region of the parameter space. For a "good fit" that fully accounts for the non-statistical variation within the data, the reduced chi-squared value should be close to one. Reduced chi-squared values less than one either fit the statistical noise in the measured data, or possibly represent improper quantification of the variance in a measurement.

A chi-squared analysis consists of varying system parameters, and determining which set of parameter values has the minimum reduce chi-squared value. System parameters may include source information, such as source position and intensity, as aspects of imager design, or aspects of the measurement design. For a known imager and measurement design, then, performing a chi-squared analysis on source position may effectively characterize the source distribution. However, a chi-squared analysis blindly analyzes source and imager parameters and does not converge to the ideal distribution of parameters. Since source position is a parameter that can be analyzed using a chi-squared analysis, it should be possible to determine source position using a chi-squared analysis, but since a chi-squared analysis relies on the distribution of parameters being analyzed and does not inherently converge to the ideal distribution of parameters, it does not perform a true reconstruction. However, a chi-squared analysis is useful for comparing projected data against measured data, and can be used to determine whether a given system model accurately represents the measured data, and to vary system models in order to determine the optimum distribution of parameters.

Since a chi-squared analysis studies the effect of varying system parameters in comparison to the entire measured dataset simultaneously, it provides a tool with which to consider the behavior of a projected source distribution against the entire measured dataset. In contrast to Figure 20, a chi-squared analysis over source position would represent a source position by a minimum value instead of a maximum value. This is seen in Figure 27.

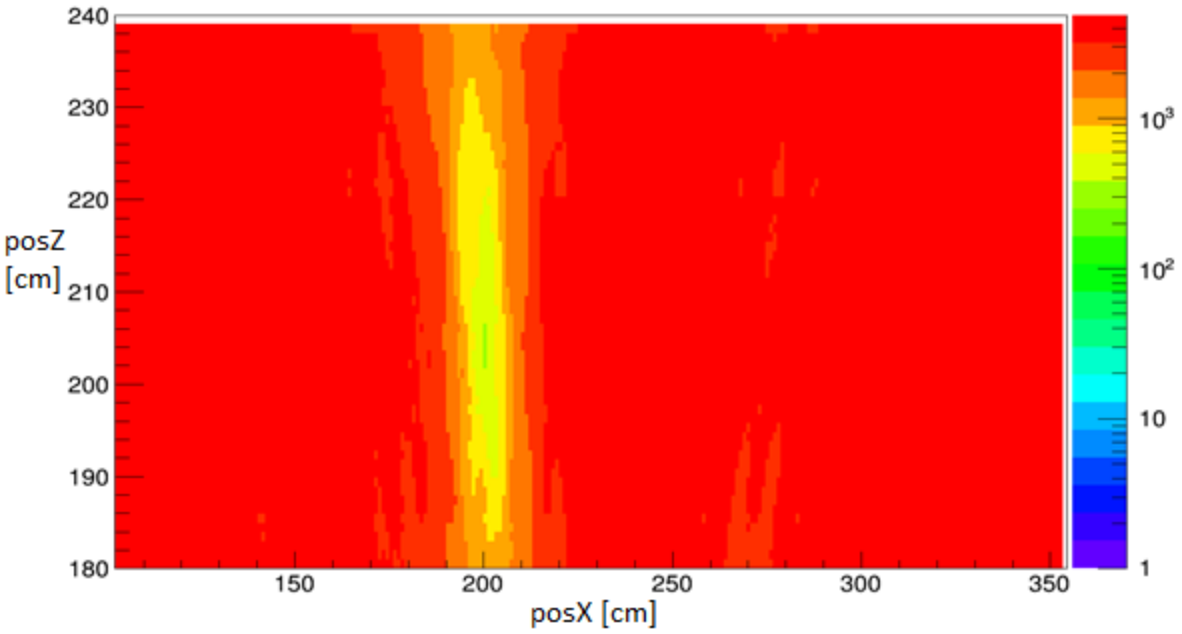

Figure 27. Chi-Squared analysis for simulated data, considered from three detector positions, with no statistical variance at x = 200 cm, z = 205 cm, shown on a logarithmic scale.

While it appears that the source is located within a relatively large region, comparable to the size of the region in Figure 22, the sharp minimum found in Figure 27 indicates a much smaller region containing the source. Due to the lack of statistical effects being included and the variance in each detector pixel being near zero, the reduced chi-squared value is not exactly

one, and indeed if the source detection threshold is one or near one, a source would not indicated. The utility of combining data from multiple measurement positions has different effects when considering the data simultaneously instead of independently, with limited distance resolution from a single detector position, as seen in Figure 28.

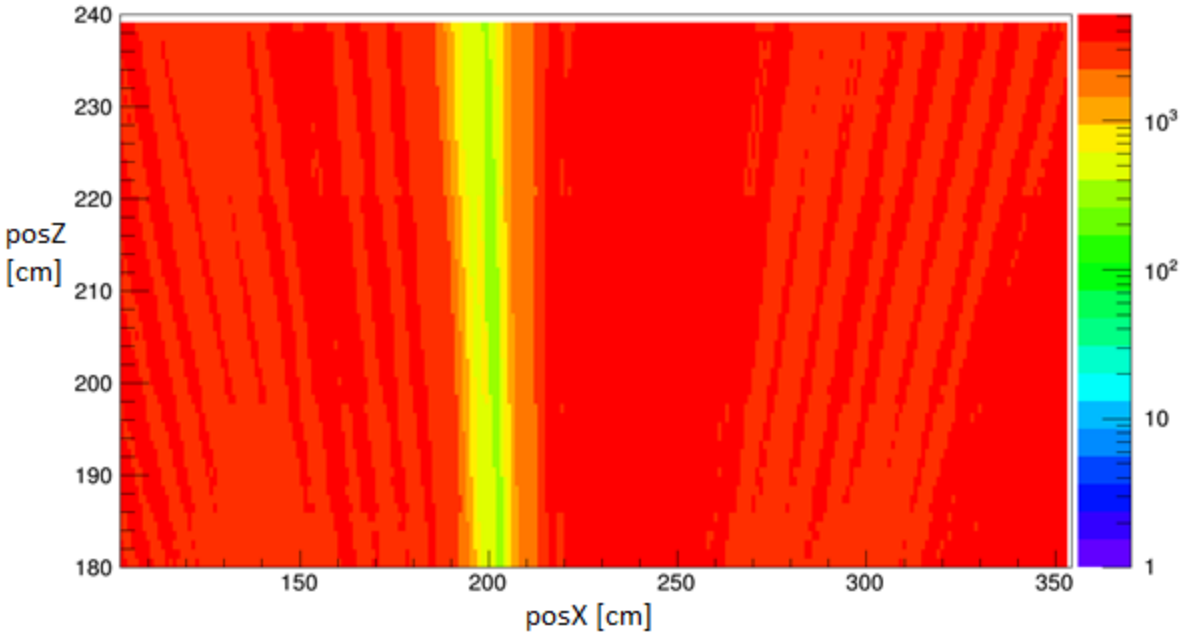

Figure 28. Chi-squared analysis of a single measurement position for statistically perfect data, shown on a logarithmic scale.

With the chi-squared technique, the improvement in distance resolution due to the use of multiple measurement positions is still seen in the contrast between Figure 27 and Figure 28. Figure 28 does demonstrate improvement over the cross-correlation reconstruction of a single measurement position. Based on this chi-squared analysis, one can conclude that distance resolution based on the measured data is improved when using the parallax imaging

measurement technique, much like the distance resolution based on the cross-correlation reconstructed data is improved. In addition to quantifying improved resolution with the parallax imaging measurement technique over a single detector position, with a chi-squared analysis, it is possible to quantify how much deviances from ideal imaging effect reconstructed source distributions, in both position and intensity, and quantify how well complex system models represent actual imaging measurements.

Reconstructing a measured source distribution by using a cross-correlation technique and averaging the reconstructed values over multiple measurement positions induces artifacts in the finalized reconstruction. Understanding how deviations from ideal imaging scenarios, such as a heterogeneous detector and thick mask, impact the reconstruction of a source distribution is important for the quantification of source intensity, and a chi-squared analysis of a system model is useful in quantifying the contribution of various deviations. Since cross-correlation analysis assumes a simplified system model, a simplified system model is an effective baseline from which other system models can be compared. As seen in Figure 27 and Figure 28, for a known system model, a single source can be localized using the chi-squared technique. Experimental data, in addition to not being statistically significant, does contain artifacts from the encoding process. A 22 kBq Cf-252 source was positioned 210 cm away from the P24 imager with a 30 cm mask-detector distance, mask thickness of 5.08 cm, and measured for an hour each mask and antimask measurements. The measurements were performed at three separate detector positions with a separation of 56cm between measurements. A simplified detector model, assuming a uniform detector pixel array, no mask transmission, no background radiation, which was equivalent to the model assumed in cross-correlation reconstruction, and normalized to the measured data (equal integrals of center measurements) was used as the model for a chi-squared analysis of the measured data. This analysis is shown in Figure 29, and the reconstructed source distribution image generated with the cross-correlation technique is shown in Figure 30.

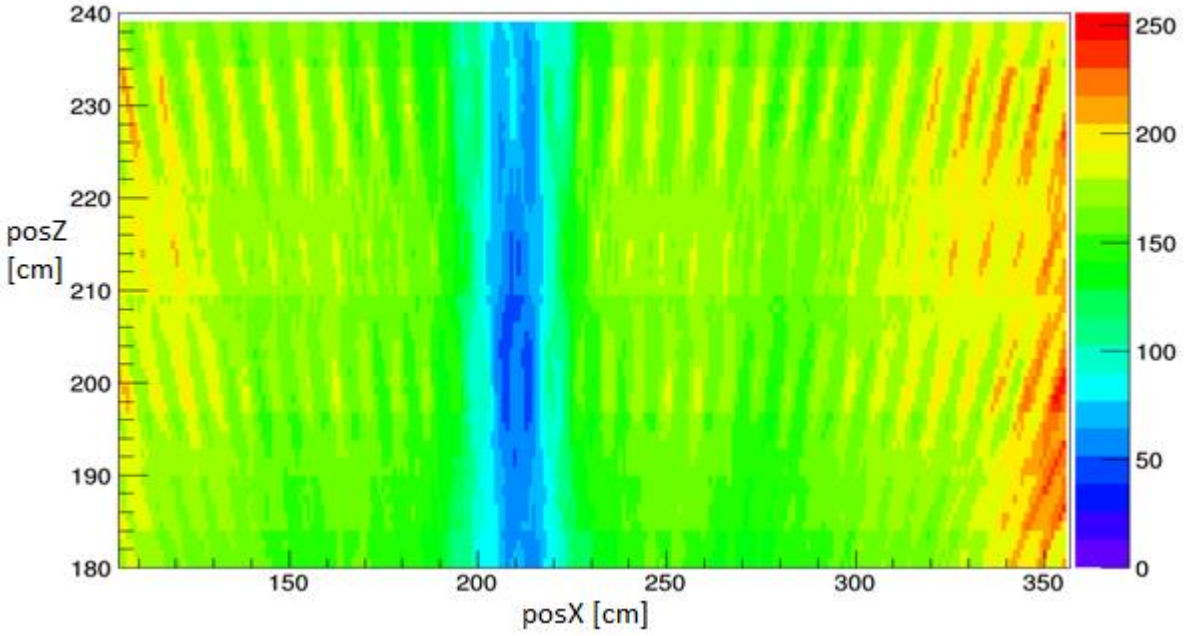

Figure 29. Chi-squared analysis of real data from 3 detector positions using simplified detector model, each measurement one hour.

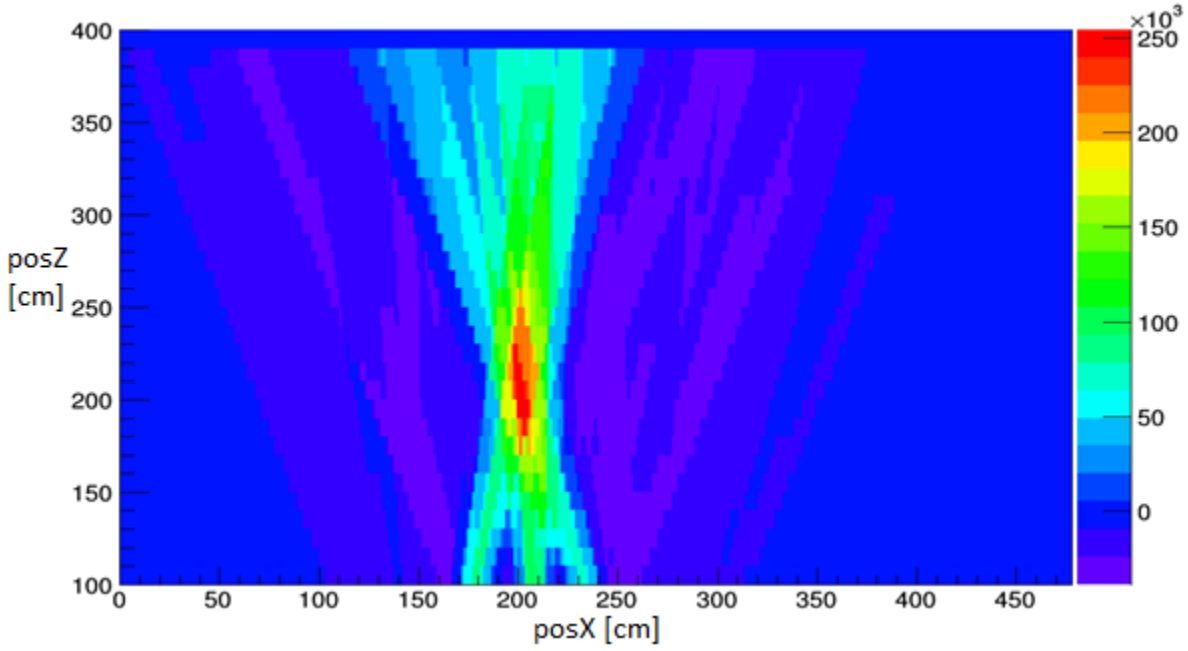

Figure 30. Cross-correlation reconstruction of the data used in Figure 29.

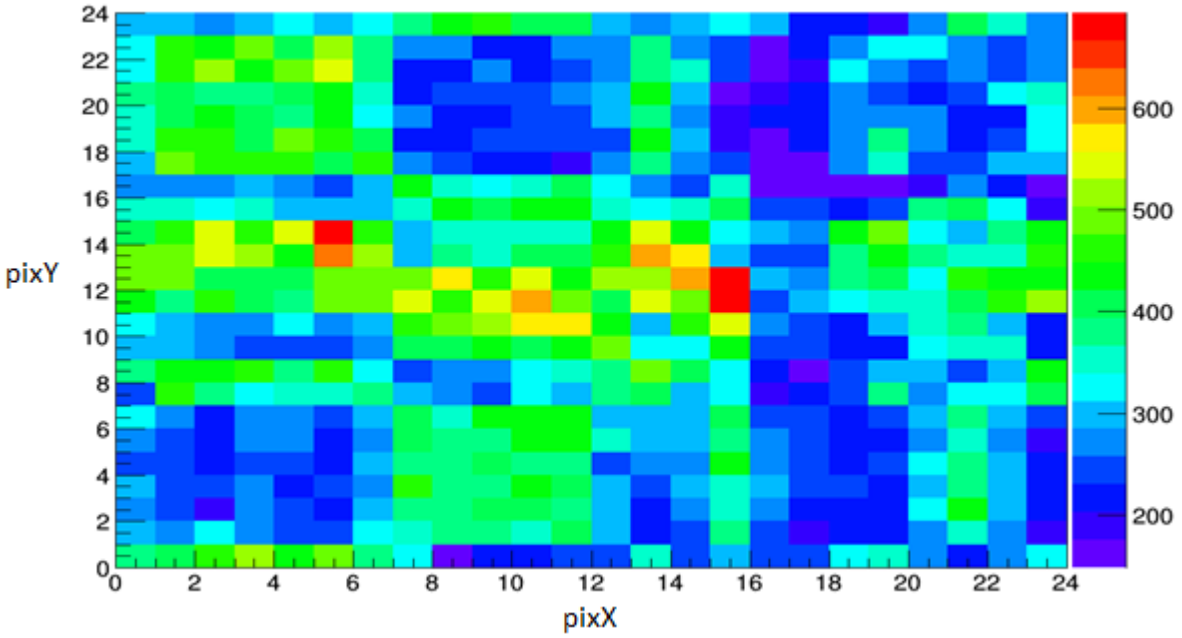

Figure 31. Measured data 1hour measurement. Source intensity is 70 µCi, at a distance of 220 cm. Imager used is P24.

After an hour measurement, the measured data signifies statistical error of less than 5% for mask hole element representative regions (7-12 x axis, 1-7 y axis), and less than 6.5% for mask moderator element representative regions (7-12 x axis, 17-23 y axis). The chi-squared analysis of experimental data indicates that while it is possible to localize a source with a simplified system model, a simplified system model does not accurately explain experimental data, potentially indicating that a more complex model would potentially accurately represent the system model. One of the notable features in Figure 29 is that the chi-squared value approaches a local minimum in the same general region as the absolute maximum in the reconstruction in Figure 30, suggesting that the data generated by the simplified system response model near the true source position more accurately represents the measured data than generated data at positions far from the true source position, but the high relative minima indicates the measured data was generated by a complex system which requires more accurate modeling to fully represent. One of the components of a simplified system model is the lack of transmission through the mask in the source distribution measured by the detector. When normalized to identical integrals, the projected data overestimates the contrast between the mask holes and mask. Adding a flat background term to each pixel (0.5 used for example) would decrease the contrast between mask hole and mask moderator elements, more accurately representing the measured data, as seen in Figure 32.

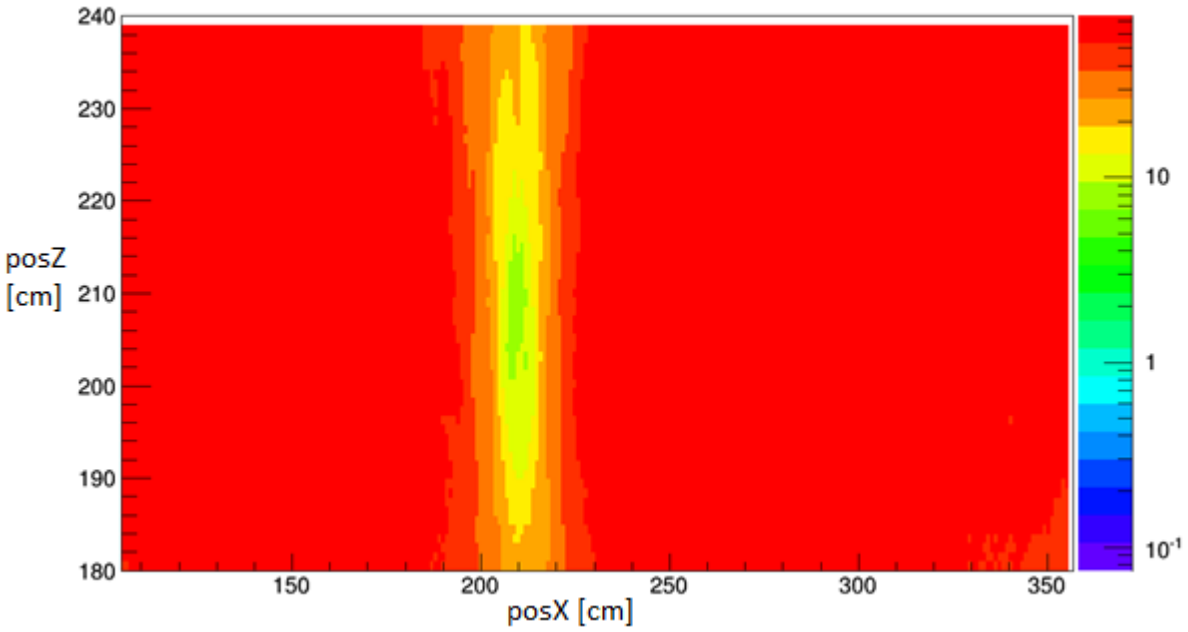

Figure 32. Chi Squared analysis of measured data. 0.5 Added to each pixel to simulate background. Log scale.

This small increase of complexity in the system model used to generate projected data in the chi-squared analysis does improve the fit between measured data and projected data at all positions, particularly near the actual source position, while the absolute minimum reduced chi-squared value is greater than one. This indicates that an increased complexity system model, instead of a simplified system response model, is necessary to sufficiently accurately represent the measured data.

2.6 Complex Source Distributions

As seen in Figure 20, in a cross-correlation reconstruction a source is represented not by a single pixel, but by a pattern of elevated regions and depressed background regions, with the center source position determined by the position of the maximum value pixel. This is because the source position is defined as the intersection of the reconstructed source distributions from individual measurement positions. Outside of the intersection region, however, there is either an elevated or depressed background region. Since each measurement position is reconstructed individually, sources sit on top of the local background. Automated methods to detect sources and calculate their individual intensities may overestimate the source intensity for sources located in elevated background regions, and underestimate source intensity in depressed background regions, an issue common in radiation quantification applications (Lo Presti, Weier, Kouzes, & Schweppe, 2006). In addition, tiled MURA patterns are cyclic sets, meaning that the MURA pattern is repeated throughout the mask, with uniqueness of a projection not guaranteed, resulting in aliasing of sources on or near the edges of the field of view when using a cross-correlation reconstruction technique. This results in identical sources imaged from the same Z distance but in different parts of the field of view appearing as very different sources after reconstruction, as shown in Figure 33. One source in Figure 33 is positioned at 250 cm distance and at 200 cm on the ordinate axis, while the second source is positioned at the same Z distance but at 255 cm on the ordinate axis.

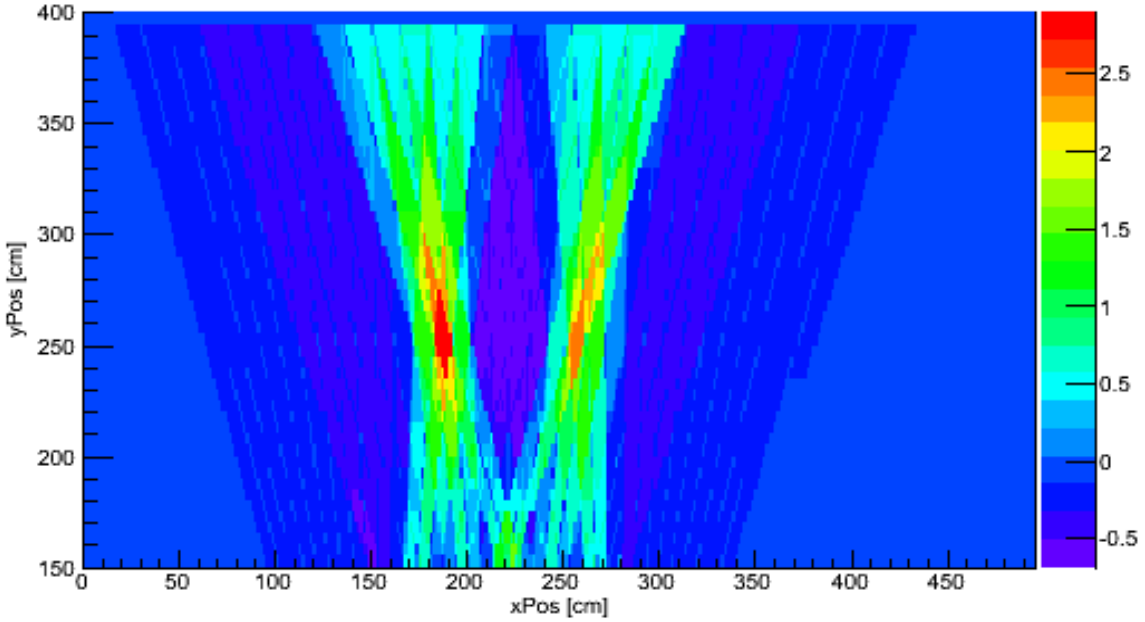

Figure 33. Reconstruction of two identical intensity sources at different x positions using a cross-correlation reconstruction.

While both sources have the same intensity, the second source (x=255) appears lower in intensity than the first source. Using the cross-correlation technique for sources that are on the edge of the field of view for some detectors results in not one, but two sources of depressed intensity appearing, and combining this reconstruction, which still contains useful source information, with other reconstructed data that contains only one source, causes artifacts in reconstruction. The depression in intensity is logical due to detected radiation being attributed to not one source position but two source positions. Statistically imperfect data would be even worse, since the contrast between the mask moderator element and mask hole elements would be less uniform.

Performing a chi-squared analysis of multi-source data demonstrates the need for reconstruction techniques capable of considering not only the entire detector dataset simultaneously, but the entire source distribution simultaneously as well. For measurements of multiple sources, no individual source position in a chi-squared analysis fully represents the measured data, but the source positions at the true source locations are partially represented by an individual source position. A chi-squared analysis, then, would have a local minima at each true source position, but the absolute minimum would be higher than were each source measured individual, as shown in Figure 34.

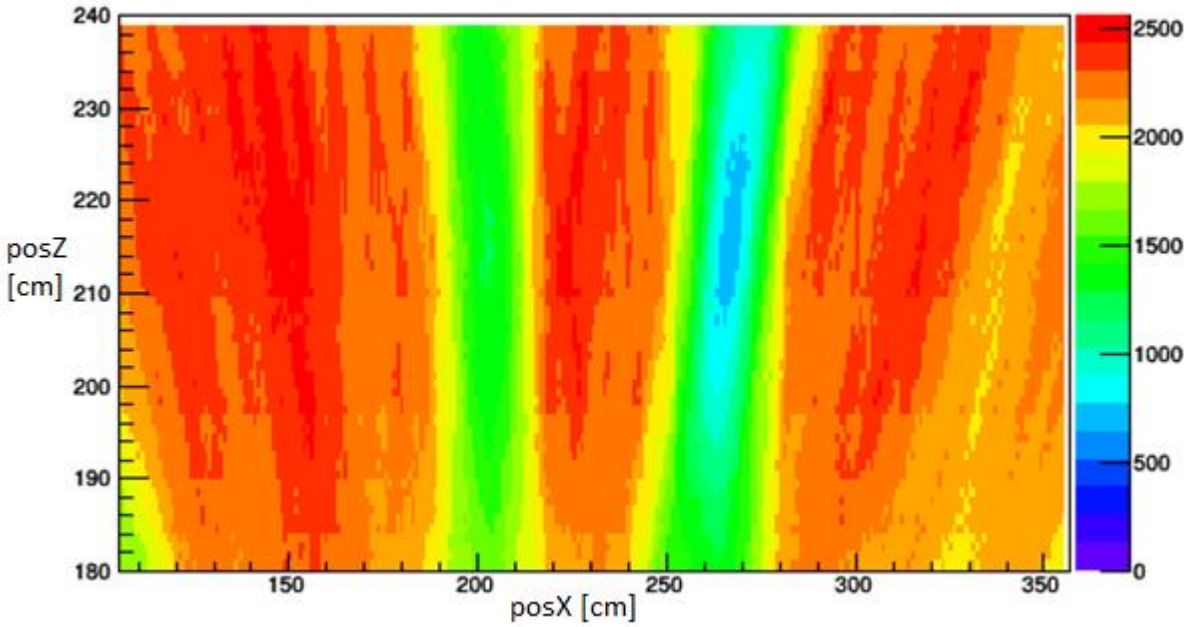

Figure 34. Chi-squared analysis of simulated data from two equal intensity sources placed at different x positions.

Figure 34 demonstrates predicted behavior for a chi-squared analysis of two sources, specifically the local minima at the locations of the actual sources, and that the reconstructed minima is less statistically significant than the reconstruction for a single source (Figure 28). Quantification of complex source distributions, then, requires the simultaneous modeling of all sources instead of modeling each source individually. This is computationally expensive to do for a brute force calculation, however, and becomes more computationally expensive the more sources involved, requiring alternatives to blind reconstruction. The difficulty in choosing what needs to be modeled (number of sources, scattering materials within the field of view, etc) does limit the use of a blind chi-squared analysis. A chi-squared analysis is useful, however, in validating and quantifying the expected impact of deviances from an ideal imaging system when source position is already known, thus providing an analysis tool to quantify understanding of coded aperture imaging systems. While a chi-squared analysis can test whether a given source distribution or imaging parameter matches experimental data, it does not inherently converge to an optimal distribution of parameters, making it more useful as an tool to analyze the accuracy of current projections of the measured data than a reconstruction technique itself.

Chapter 3 System Model

Statistical reconstructions require a system response model from which projected data for each source position can be determined. While ideally a full physics simulation of coded aperture fast-neutron imaging system would be performed for each source position, a full physics simulation for each potential source position is computationally expensive. Due to potential variations in shielding geometry and measurement geometry, such as limited positions where the imager can be placed or varied detector to mask distance, the system response model for each source position may have to be generated during or immediately prior to a measurement and reconstruction. Because this may be computationally expensive, a simplified system model that is sufficiently accurate can make reconstruction using a statistical reconstruction technique feasible in the event of previously unknown measurement conditions.

In the simplest simulated measurement, with an assumption of no scattering and a perfect detector, ray tracing through an infinitely thin mask onto a detector pixel array should accurately represent the measured data. With no additional physics and an idealized detector, the only modulation of the detected source distribution is due to the geometry of the mask and geometry of the detector. This simplified system would match measurement scenarios considered by (Accorsi, 2001). In a far more complex measurement, such as the imaging of low energy gamma-rays emitted from distributed sources within a human or animal body, mask thickness may need to be accounted for (Mu & Liu, 2006), attenuation within the source region is non-negligible, scattering occurs within the mask and potentially within the detector, and a full physics simulation for each possible source location may be necessary to accurately reconstruct the source distribution. In general, a system response model that accounts for the major systematic effects without requiring a full physics simulation should be capable of accurately representing the measurement, and would be useful in a reconstruction technique capable of using a complex system model.

3.1 Ray-Tracing Projection

From geometry, it is simple to trace a line between an arbitrary pixel and a position in space, and determine the position where that line intersects the mask. Beginning with a detector

array that is the same size, but at higher position resolution, as the true detector array, one can perform a ray tracing that determines the expected mask projection (at a given distance) that is incident on the detector, as shown in Figure 35.

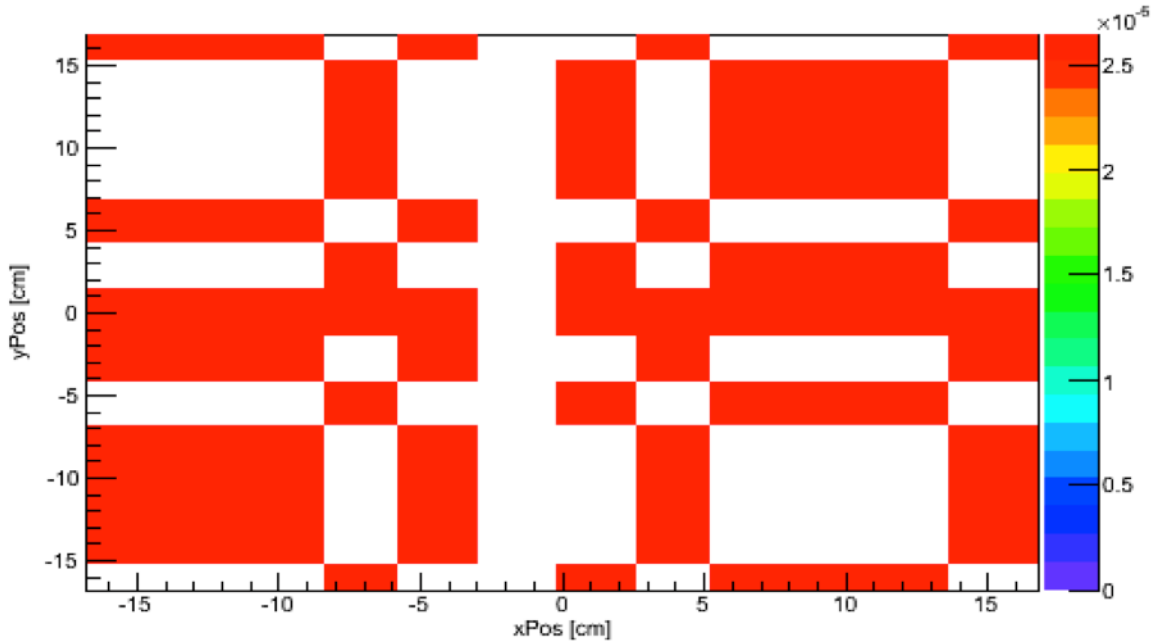

Figure 35. Projected mask pattern for an ideal mask onto space represented by a detector. Source to mask distance is 200 cm, and the detector to mask distance is 35 cm.

While the projection in Figure 35 represents the modulated source distribution incident on the detector, the position resolution of the neutron block detector is limited to its pixel size. Since this projection is equivalent to the projection that would be measured if the position resolution of the neutron block detector was one-half, one-fourth, or some smaller fraction of the position resolution of the neutron block detector, this projection is referred to as the supersampled projection. Rebinning the pattern on the incident detector into an array with pixels the same size as the detector pixels in the imager represents the actual values recorded by the detector

array, as demonstrated in Figure 36. While some mask elements are projected perfectly onto a detector pixel, other mask elements are only partially projected onto a detector pixel, resulting in only partial coverage of mask elements in the measured distribution.

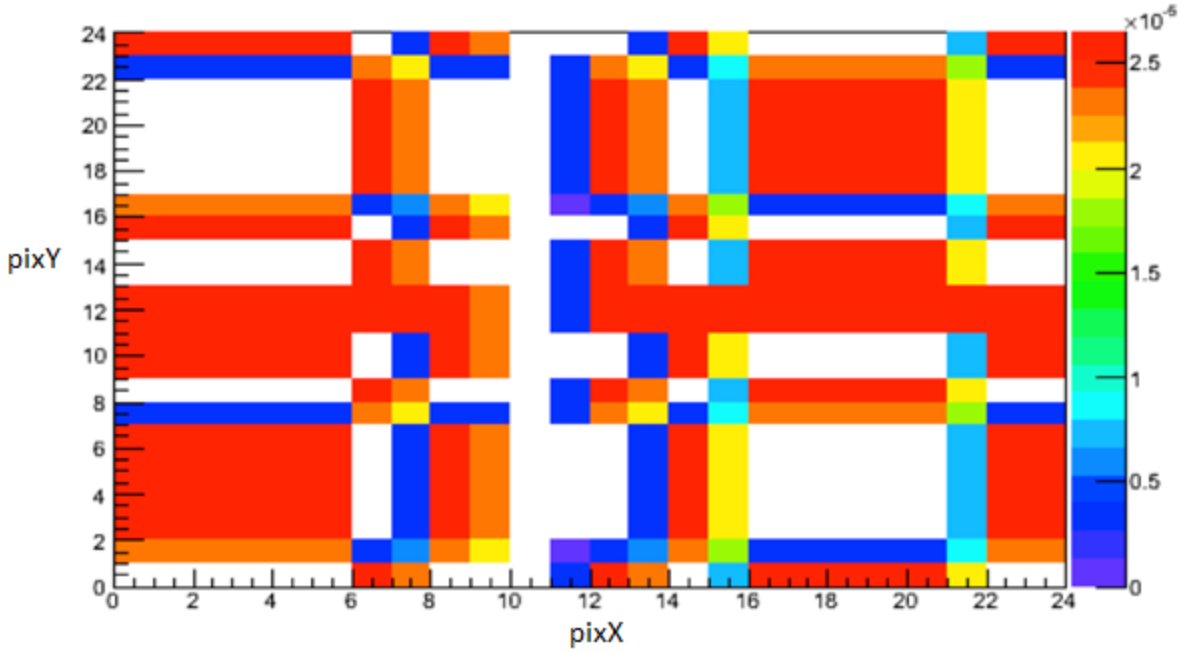

Figure 36. Projected mask pattern onto detector for an ideal mask, with rebinning of supersampled projection. Supersampled projection is equal to the supersampled projection in Figure 35.

As shown in Figure 36, the sampling of the incident source distribution imperfectly represents the true source distribution. This is due to mask element boundaries not exactly corresponding with detector pixel boundaries. Since the system response model discretizes the true incident source distribution, the sampling rate for the ray-tracing must be sufficiently high so as to accurately represent the true incident source distribution.

3.2 Sampling Rate

In an actual measurement or full physics simulation, such as one performed by Geant4, a continuous, non-uniform source distribution is incident upon a position-sensitive detector array. In a simplified system response model utilizing a modified ray-tracing technique, the incident signal is discretized. This intuitively leads to the consideration of whether or not the incident signal simulated by the simplified system model is sufficiently similar to the continuous signal for accurate reconstruction with statistical reconstruction techniques. The effect of undersampling the incident signal can be demonstrated in 1D for a known signal, and easily extrapolated to 2D with complex coded aperture data. Consider a 1D signal defined by

$$f(x) = \cos(4x)\cos(6.5x) + 2 \qquad \text{Equation 10}$$

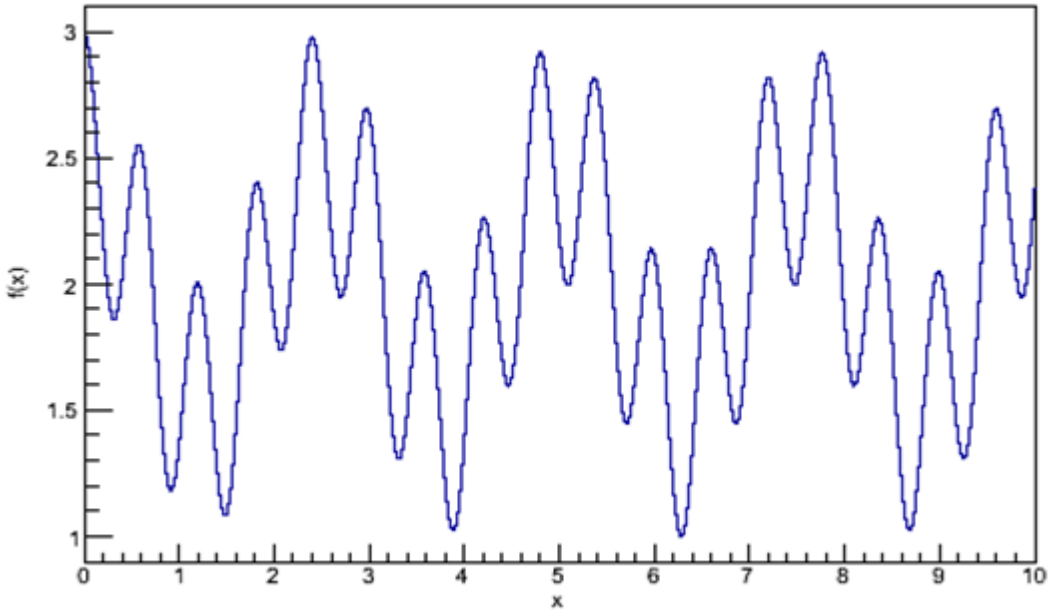

Figure 37. True signal for super-sampling demonstration.

In a measurement or sufficiently complex simulation, this signal is sampled by the detector at a fixed resolution. With a fixed ten pixels, Figure 37 would be discretized, as shown in Figure 38.

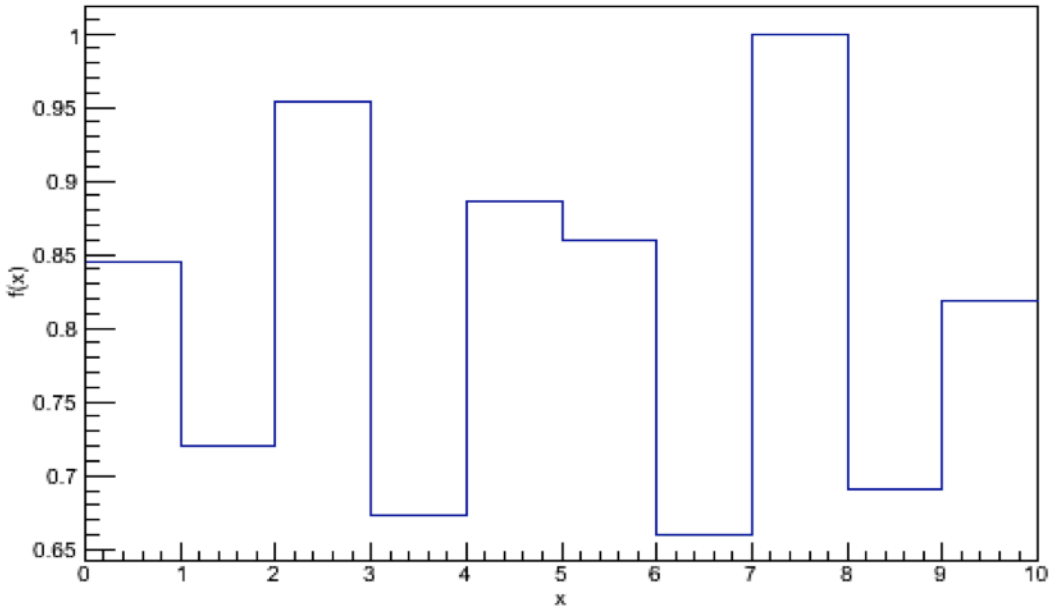

Figure 38. Sampled projection sampling Equation 10.

While the true signal in Figure 37 contains features that are not present in Figure 38, and accurately representing Figure 37 with a discrete sampling rate is defined by the Nyquist criteria (sampling rate at least twice the highest frequency component of the signal), the physical limitation of a fixed detector pixel size may require imperfect sampling of the incident source distribution by the detector pixel array. Determining whether or not the system response model sufficiently models the incident source distribution depends on the how closely the measured detector pattern and simulated detector pattern correlate, not how well the incident source distributions correlate. At the extreme minimum, sampling the true source distribution only once per detector pixel, the modeled source distribution for a true source distribution with

features smaller than pixel size is not representative of the true source distribution, as shown in Figure 39.

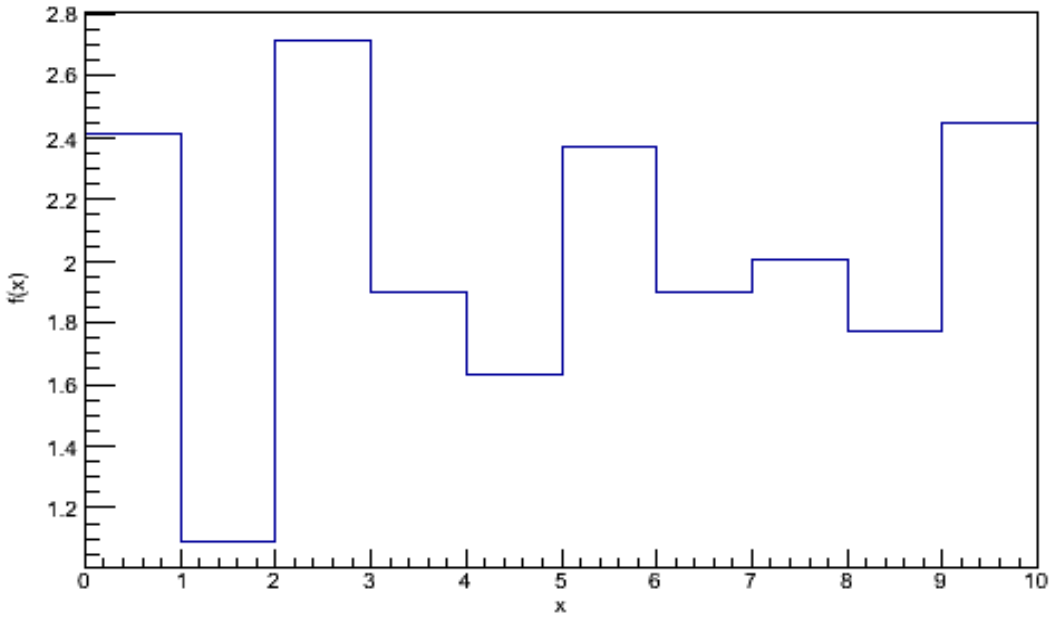

Figure 39. Distribution representing Equation 10 at a sampling rate of once per detector pixel.

While the true distribution is too complex for only a single sampling point per pixel in the system response model to sufficiently represent the source distribution, as the sampling rate increases, the modeled distribution approaches the true distribution, as shown in Figure 40.

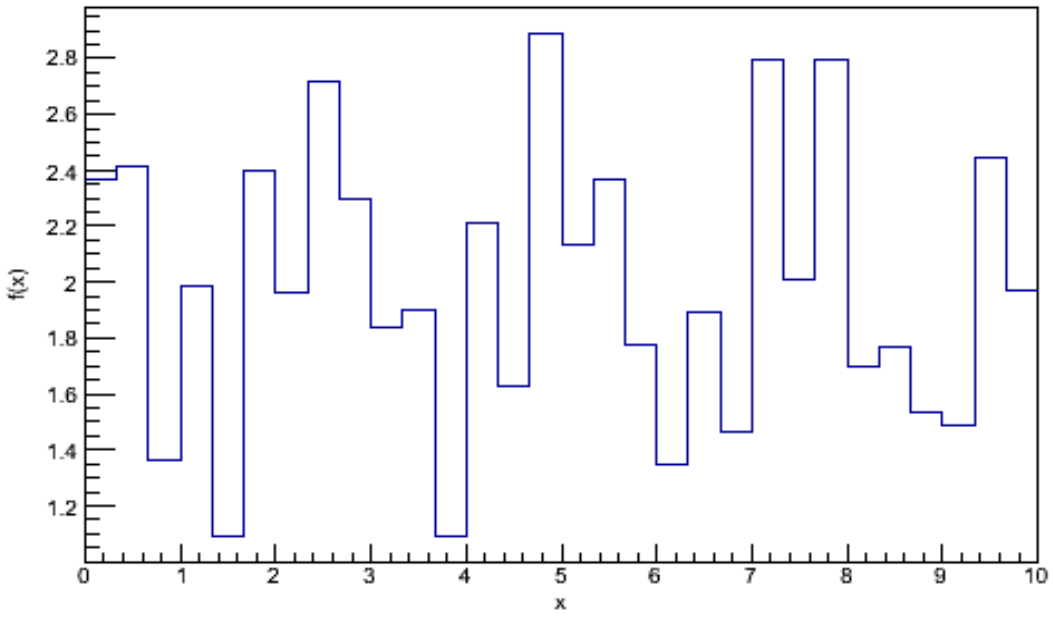

Figure 40. Distribution representing Equation 10 at a sampling rate of 4 times each axis per detector pixel.

Since the modeled source distribution approaches the true source distribution as the sampling rate increases, it follows that the distribution measured by the detector approaches the distribution measured by the detector for the true source distribution as the sampling rate increases, as shown in Figure 41. This does come at the cost of increased computational time, with geometric growth in the size of the projected source distribution and, thus, increased calculations that must be performed, so when computational speed is a consideration, it is

desirable to minimize the sampling rate as much as possible while maintaining accuracy in reconstruction.

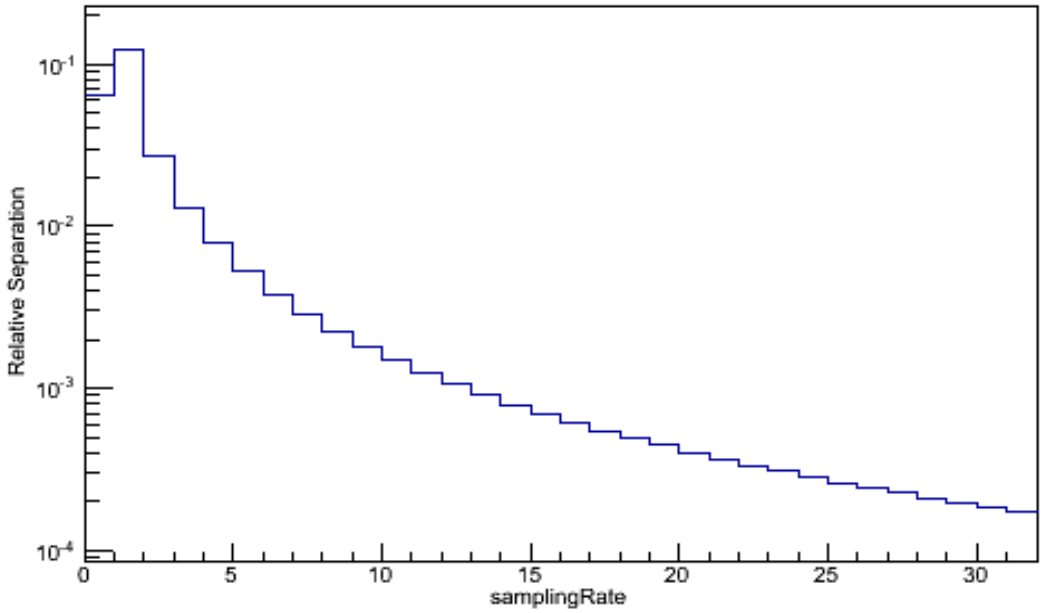

Figure 41. Relative separation between true projected data and modeled data.

Since the total separation between the true source distribution and the modeled source distribution, as determined by the projected detector data, drops below 1% error after sampling four times, this is determined to be a sufficient sample rate. It should be noted that the sampling rate of 4 times is does not indicate each detector pixel 4 times, but sampling each pixel 4 times per axis, meaning 16 total sampling positions per detector pixel.

For coded aperture data, which has a more complex, less uniform and regular source distribution, sampling requires that the major components of the source distribution incident on the detector be represented. As shown in Figure 35 and Figure 36, even when accounting only for the optical projection of the mask pattern through an infinitely thin mask, the measured data is not equivalent to the two-valued mask projection due to projected mask element boundaries not exactly matching the detector pixel boundaries. At a sampling frequency of only once per detector pixel, this effect would not be accounted for, leading to a system response model that does not represent the true system response model. Other effects, such as transmission through the mask, may influence even smaller regions of the detector pixel array, requiring a sampling rate smaller than the detector pixel size.

3.3 Mask Transmission

In the understanding of how mask thickness creates artifacts in projected data, a simple pinhole mask provides an example of how a single mask element affects a projection, which can be extrapolated to the entire pattern. In the ideal case, an infinitely thin mask with no transmission through mask moderator elements has a uniform point spread function (PSF), i.e., having perfect transmission within the mask hole elements, and zero otherwise. While the ideal case may be true in the case of low-energy photons or other particles, masks used in fast-neutron imaging are unlikely to be perfectly opaque. Instead, masks in use are sufficiently thick to cause a non-uniform point spread function, with the incident angle of the neutron changing the thickness of the mask, and thus changing the probability of interaction within the mask. In this case, the assumption of a two-valued mask pattern independent of source location in the cross-correlation reconstruction technique may only provide an approximate reconstruction,

and in extreme cases (i.e., sources on the edge of the field of view), a system model accurately accounting for transmission in the mask is necessary.

Accounting for the transmission of neutrons through an imaging mask, two effects to the PSF are expected. Specifically, one expects: 1) an increased contrast between the mask hole and mask moderator element due to increased mask thickness, and 2) a broadening of the region with increased transmission due to the mask hole element. A ray tracing of the expected PSF for various mask thicknesses and incident angles is included in Figure 42.

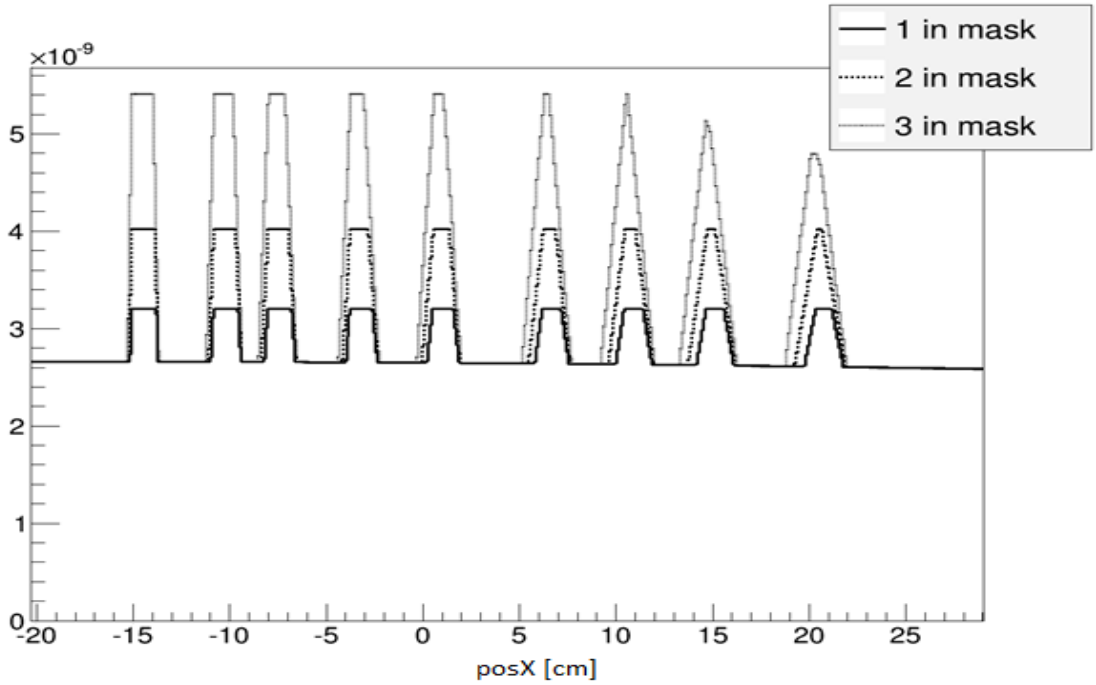

Figure 42. Pinhole PSF for varying mask thicknesses (see legend) and incident angles. Values given are unitless.

To generate Figure 42, a modified ray tracing was performed with 8 square mask hole elements in a line with a 35 cm mask to detector distance. Mask thickness was accounted for by

performing a ray tracing for multiple horizontal slices in the mask, and for each slice recording the total distance traveled through the mask moderator for a given slice. Each point in the detector that was sampled was normalized by a nominal transmission value multiplied by the total distance traveled through the moderator. The nominal transmission value used was equivalent to the expected transmission for a 1-MeV neutron traveling through the mask thicknesses studied.

In Figure 42 multiple aspects are apparent. The leftmost peak corresponds to a mask hole element location directly underneath the source, which is centered at –15 cm, and the difference between mask thicknesses only demonstrates the decreased transmission through the moderator elements of the imaging mask. At the rightmost pixel, mask thickness effects become more pronounced, and the two-valued mask assumption no longer is valid for a 3-inch thick mask, and is not strictly valid for a 2-inch thick mask. Notably, the region influenced by the pinhole is broadened for all mask thicknesses, and for a 3-inch thick mask, the peak transmission through the mask is decreased at high angles between the detector pixel and source because there is no point of the pinhole that is not partially or wholly covered by the moderator element. While the baseline mask transmission value appears flat, it does decrease slightly towards the right of Figure 42, indicating increased moderation due to increased distance travelled in the mask. Extrapolating to a full detector, as the angle between the source and detector pixel deviates from orthogonal, the effective mask thickness increases and, thus, a square PSF is no longer a valid assumption for thick masks and high-angle transmission. When reconstructing an image with the cross-correlation technique, not only would the angular resolution on the edges of the field of view be expected to be decreased, but for thicker masks, the reconstructed count rate would vary depending on the source position within the field of view.

This allows for varying effective mask thickness due to transmission through the imaging mask at oblique angles, as shown in Figure 43.

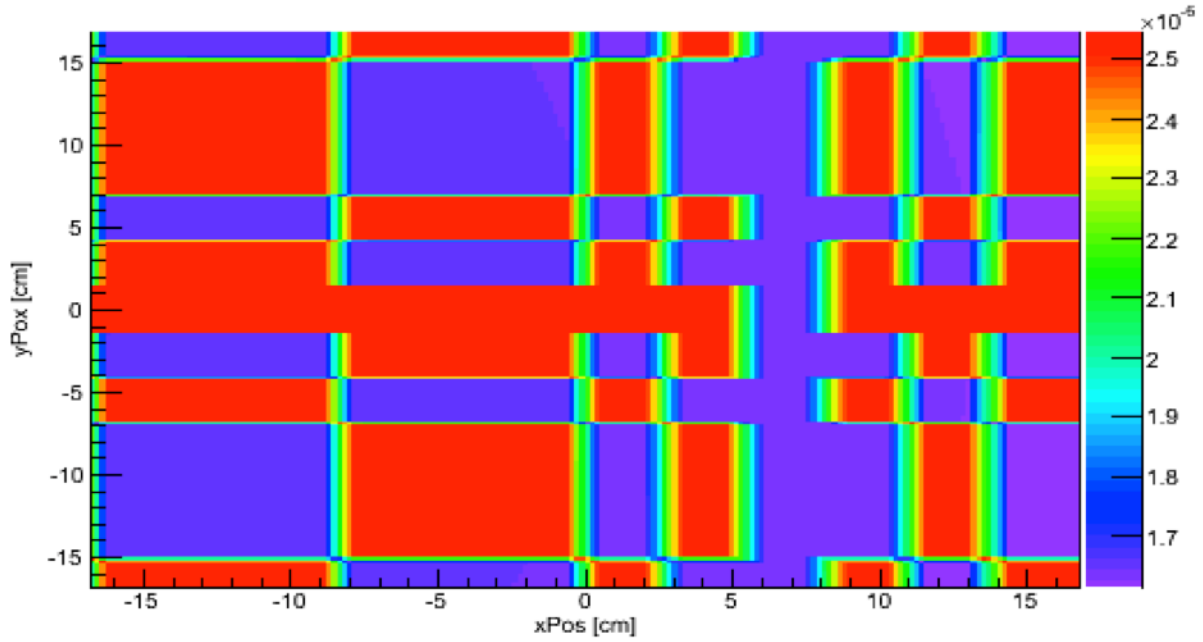

Figure 43. Projected mask pattern incident on detector, incorporating mask thickness. Scale is the normalized counts for that specific sampling point.

Both effects attributed to mask thickness are visible in Figure 43, which displays a source from a position with a higher angle between the source and detector, at a position of -15 cm on the x axis but centered on the y-axis, in order to more visibly display mask thickness effects. In regions fully covered by a mask moderator element in all projections, the intensity of the source distribution incident on the detector is consistently lower than mask hole elements, but as the position on the abscissa of the detector increases, the total distance travelled through mask moderator elements increases, and the effective mask opacity increases. As expected, the region effected by a mask hole element increases, such as the region from 10.5 to 14.1 on the x-axis in comparison to the less extreme angle for the region from -0.5 to 3 on the x-axis, due to decreased effective mask thickness within that region. While the open fraction for every mask hole element in Figure 43 is greater than zero and, thus, perfect transmission is possible through every mask hole element,, increasing the incident angle or mask thickness would be expected to have some mask hole element that has no full transmission.

Only considering the geometric variation in effective transmission between masks of different thickness, it is more visually effective to consider the difference between an infinitely thin mask and a mask that has a physical thickness. As shown in Figure 42 deviation from an ideal projection would be expected with increased angle between the mask and source location, so the effects of mask thickness would be increased for a source near the edge of the field of view. This is demonstrated in Figure 44 and Figure 47.

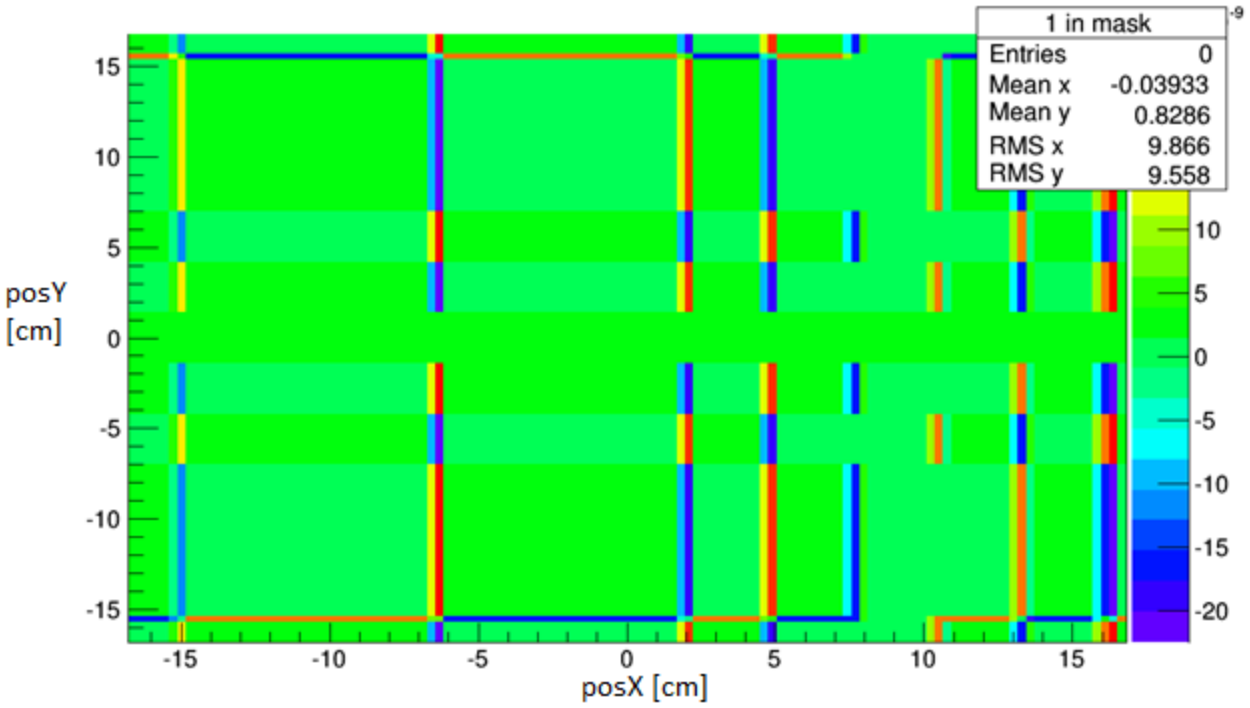

Figure 44. Separation from a thin mask for a 1-inch mask thickness.

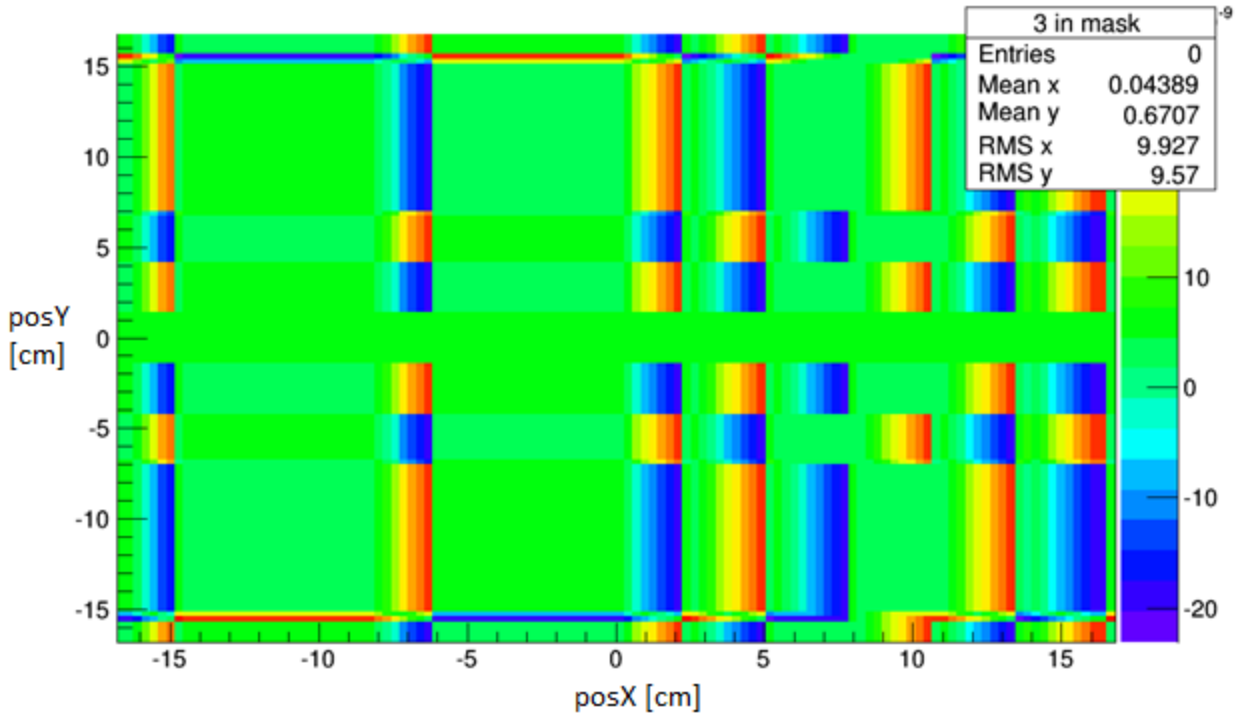

Figure 45. Separation from a thin mask for a 3-inch mask thickness.

As expected, as mask thickness is increased, the separation between the projections of an infinitely thin mask and an actual mask thickness increases with increased mask thickness. Not accounting for this separation from the thin mask model would depress the reconstructed source intensity in the reconstructed pixel containing the source as well as increase the count rate in pixels near the reconstructed source pixel, thus blurring the source location. For all detector positions the further away a pixel is from the source, the less contrast there is between mask hole and moderator, lowering the reconstructed source intensity. Over multiple detector positions, this error in reconstructed source intensity produces a systematic effect dependent on angle between the source and detector independent of the variation in distance, and for thick masks where collimation is non-negligible, this would have the effect of making the source appear further away from the detector and blurring the reconstructed image for each distance and detector position, as seen in Figure 46.

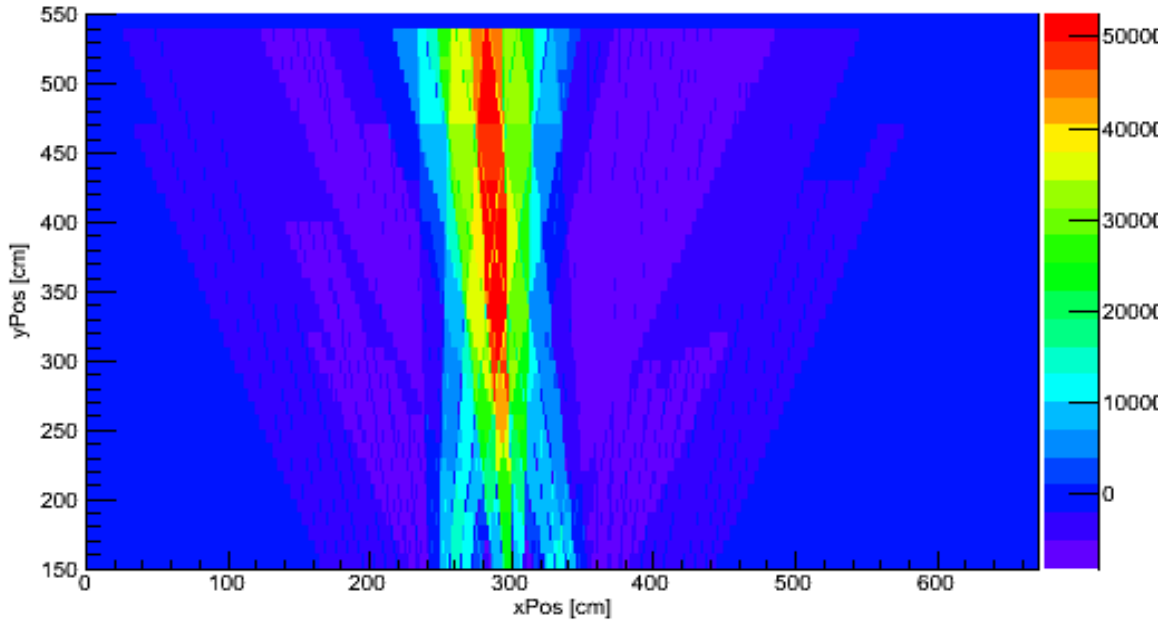

Figure 46. Cross-correlation reconstruction of simulated data for a 10 inch thick mask.

Reconstruction algorithms that do not account for mask thickness, thus making the assumption of an infinitely think mask, would systematically reconstruct sources as further away from the detector than their actual location, as seen in the difference between Figure 46 and Figure 20. Since estimates of source intensity are especially dependent on the reconstructed distance to the source ($1/r^2$ effect), this error in reconstruction due to deviance from the idealized imaging case strongly induces error in estimate of source intensity due to the error in the estimate of Z and position due to the blurring of the reconstructed image.

3.4 Detector Air Gap

While an ideal pixel array for a coded aperture imager consists of a single continuous array, detectors using the block detector designs developed for fast-neutron imaging consist of reconfigurable arrays of multiple position-sensitive block detectors. In contrast to the negligible thickness of reflector between pixels, the discontinuity due to the aluminum covering of each block detector and any additional space due to an imperfect fit between block detectors has a thickness within an order of magnitude (~1 mm – 1 cm) of a pixel size. Since the active volume in each detector in the array consists of only approximately 92% of the area of the detector face, neglecting the discontinuities in the detector array during reconstruction would induce error in the reconstructed image. Simply scaling the measured data or reconstructed image by the active fraction (92%) would be inappropriate, since the effect of the gap between detector elements is a discontinuity in the detector array. For a detector array with a 5mm gap, the projected source distribution incident on the detector active volume would be non-continuous as shown in Figure 47.

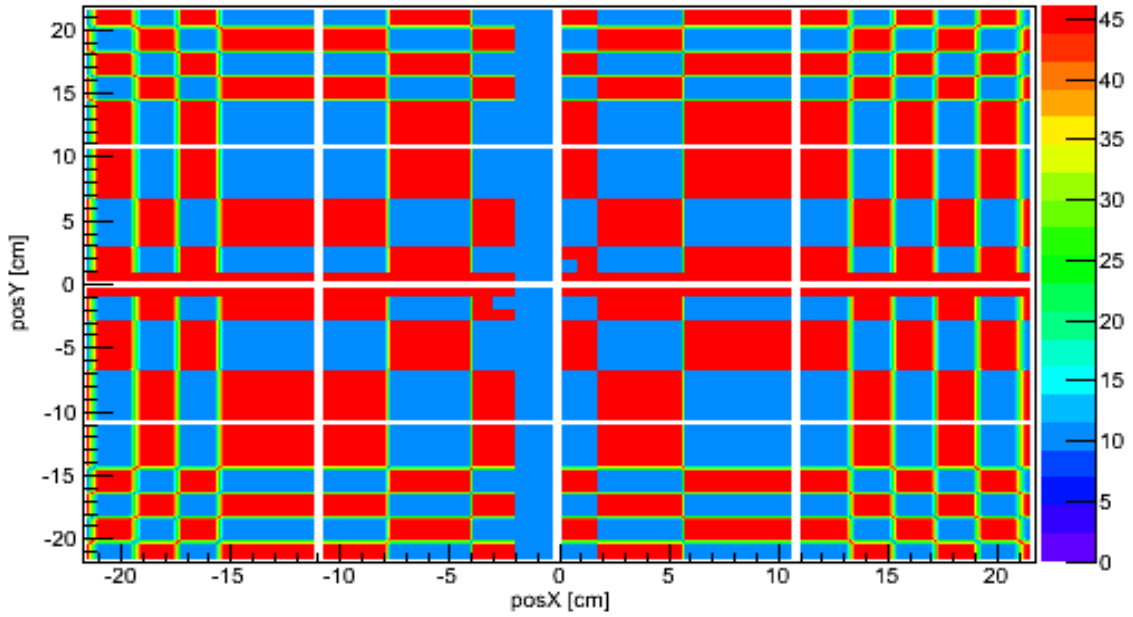

Figure 47. Projected source distribution incident on detector for a 5 mm gap between block detectors. Detector design is a 40x40 pixel detector with 10x10 pixel block detectors.

Since the imager modeled in output shown in Figure 47 is a 40x40 imager consisting of a 4x4 array of 10x10 pixel detectors and a rank-19 mask, the three vertical and three horizontal discontinuities within the detector active volume represent the gaps between individual detectors. For the ray-tracing model used to generate Figure 47, the source intensity was arbitrarily chosen such that the maximum value of the source distribution incident on the detector was 46, which corresponds to the number of slices through the mask sampled. In a true measurement or complex physics simulation of a coded aperture measurement, the entire detector pixel array is contained within the detectors, so the detected data generated by the system response model must exclude the regions containing the detector gap, as shown in Figure 48.

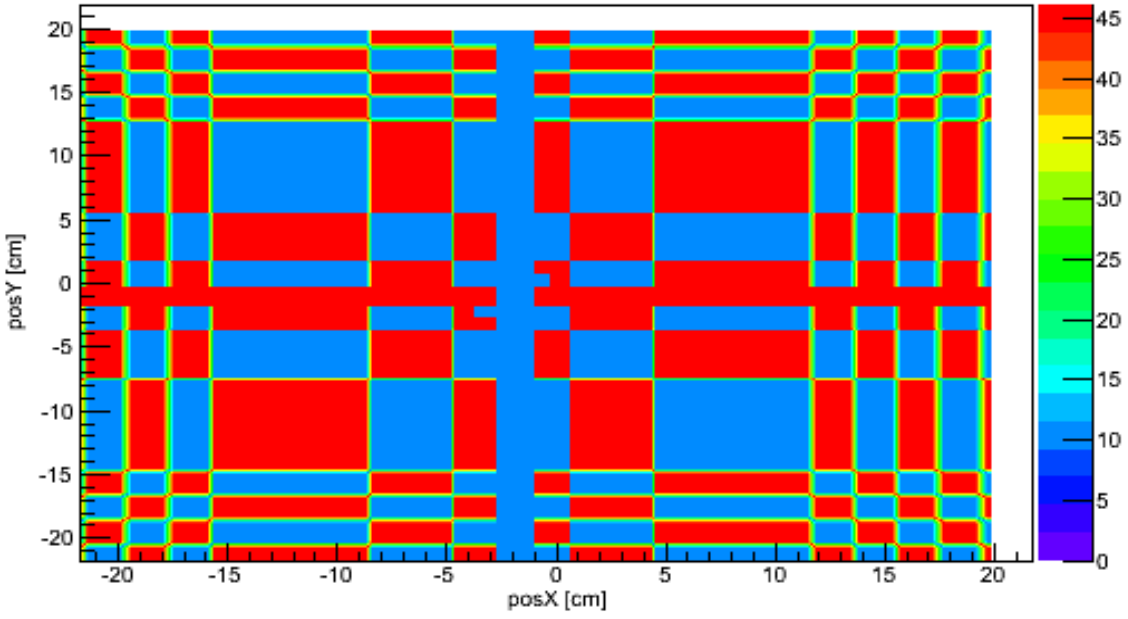

Figure 48. Projected source distribution incident on detector active material with a 5 mm gap.

While the same general pattern of Figure 47 is present in Figure 48, by rejecting the regions covered by the air gap, the remaining source distribution actually incident on the detector active volume is a continuous region, from which the measured data can be sampled, as shown in Figure 49.

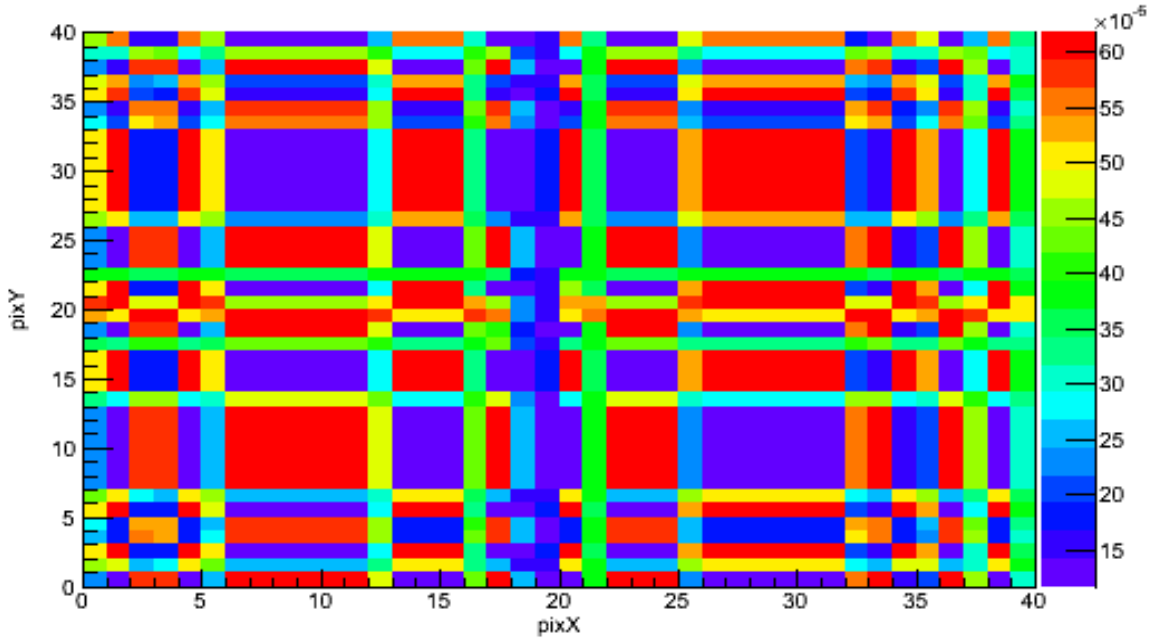

Figure 49. Measured data for a 5 mm gap as determined by ray-tracing model.

Due to the way the source distribution is sampled and projected mask pixel boundaries not exactly matching the pixel boundaries of the detector, an imperfect projection is detected. Features of the rank-19 mask pattern are apparent in Figure 49, such as the relative location of mask hole and mask moderator elements. With the data properly normalized to account for solid angle, the measured values represent the detection probability of each individual pixel. While for a 5 mm gap, the difference between a continuous array and an array with block detectors is rather small and the features of the detected information are visually similar to the

projected pattern without a gap, increasing the size of the gap between detectors necessarily increases the size of the discontinuities within the detector. Due to this, the mask features apparent in Figure 49 in are less readily apparent with an increased gap between block detectors, as shown in Figure 50.

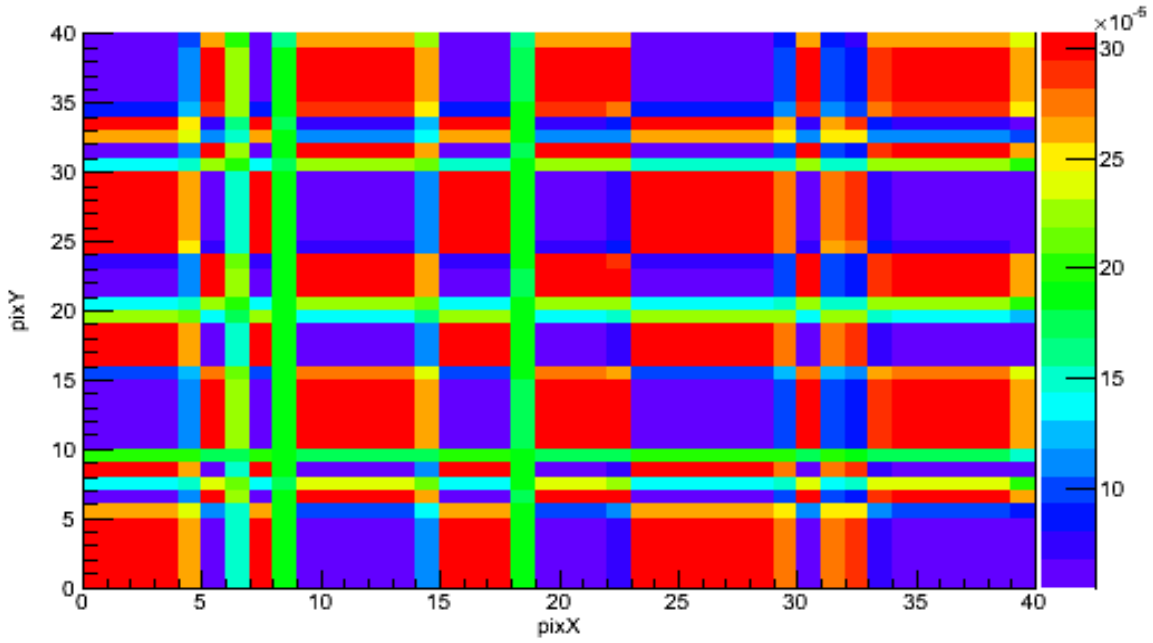

Figure 50. Measured data for a 50 mm gap as determined by ray-tracing model.

With a relatively large gap between detectors in the detector assembly, the measured data in Figure 50 bears no obvious similarities to the measured data in Figure 49. This would be expected, since the physical regions represented by each block detector in the detector pixel array in the forward projection would be separated by distances much larger than the size of an individual pixel. It is intuitive that due to the large discontinuities in the measured data,

reconstruction with the cross-correlation technique would provide ambiguous results, thereby requiring statistical reconstruction instead.

To study the effect of the gap between individual detector blocks, the measured data used in Section 5.3 was reconstructed with a detector gap of varying width. From the design of the imager, it was anticipated that there was 92% active volume in the detector assembly, corresponding to a 5 mm air gap between individual detectors in the assembly. Directly measuring the air gap was determined to be impractical due to the instrument design, but it was assumed that the imager design was accurate. Building on the results of Section 5.3, a 2 inch mask thickness with a mask transmission of 0.35 was selected for a chi-squared analysis. Detector air gaps were determined by adding a dead space of varying thickness at the positions within the detector affected by the air gap. A dimension of 1 cm was selected as the maximum detector air gap, since air gaps greater than 1 cm were considered to be highly improbable due to the tight packing of detectors in the array. The minimum reduced chi-squared value in each analysis is displayed in Figure 51.

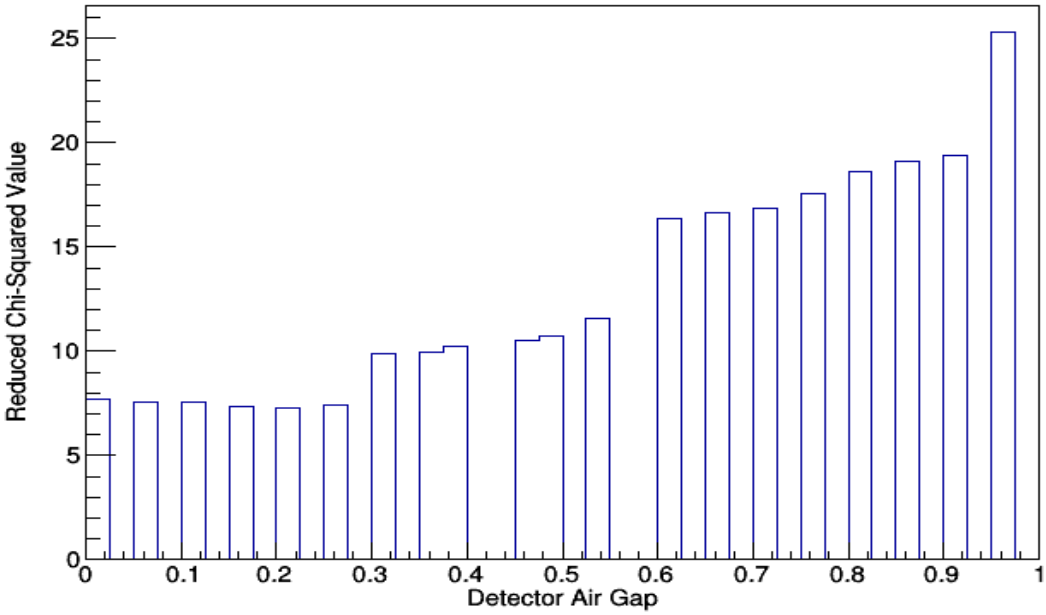

Figure 51. Minimum value of a chi-squared analysis as a function of detector air gap in cm with a fixed mask thickness.

Due to the imager design, it was anticipated that the most probable detector air gap would be a thickness of 5 mm, which is confirmed by the results shown in Figure 51. The calculated air gap that best represents the projected data was 2.5 mm, or 0.025 cm. Considering that the definition of the air gap in the system model is the thickness on either side of the center of the gap, such as the gap between the 10^{th} and 20^{th} pixels, so this 2.5 mm air gap corresponds to a 5 mm air gap in the physical detector. Unexpectedly, this was a rather small improvement in the system response model, with the reduced chi-squared value being above 7 for all considered detector air gap thicknesses, leaving some unaccounted for deviation from the geometric components of the system model. From consideration of the most probable interactions of fast-neutrons within the imaging system, the likely unaccounted for deviation is scattering events within the mask that do not remove neutrons from the source distribution incident on the detector, which is discussed in Section 3.5, and scattering within the detector that results in an imperfect encoding of the incident source distribution, discussed in Section 3.6.

3.5 Mask Scattering

The moderator elements of the mask are intended to either absorb fast neutrons or scatter them away from the detector so that they are not recorded. The material selected for the mask, HDPE, has a cross section that is scattering-dominated, since fast-neutron absorption results in secondary particle production.

While scattering may occur in any material along the path of a neutron, in an imaging system without any special environmental conditions there are two elements where scattering is of particular interest, specifically scattering within the detector itself and scattering within the mask. Neglecting scattering within the measurement room, scattering within the mask where the scattered neutron is scattered away from the direction of the detector assembly effectively removes the neutron from the source radiation incident on the detector. Neutron scattering in the direction of the detector, on the other hand, does not fully remove the neutron from the incident source distribution; instead, it modifies the source distribution incident on the detector according to the angular distribution of the scattered neutrons and scattering cross section at a given neutron energy. Since the angular distribution of neutron scattering

interactions at fission energies is anisotropic, and the distribution is dependent on both the incident neutron energy and the isotope with which the neutron scatters, scattering within the mask occurs in a complex manner that is not easily accounted for through analytical techniques.

3.5.1 Kinematics of Neutron Scattering

In general, scattering of neutrons off nuclei is anisotropic, and with limited exceptions at energies of interest the neutron loses, but does not completely lose, kinetic energy in scattering reactions. From classical mechanics, consider the kinetic energy of a scattered neutron, given by

$$E' = \frac{E}{(A+1)^2}\left[cos\vartheta + \sqrt{A^2 - sin^2\vartheta}\right]^2 \qquad \text{Equation 11}$$

where ϑ is the scattering angle, *A* the atomic mass of the nuclei, *E* the incident neutron energy, and *E'* the scattered neutron energy. Various consequences of Equation 11 are immediately clear: 1) perfect backscatter would result in the minimum scattered neutron energy, 2) perfect forward scatter would result in the maximum scattered neutron energy, and 3) the scattered neutron energy is dependent on the isotope off of which the neutron scatters. Since scintillation-based neutron detectors with pulse-shape discrimination (PSD) have a minimum neutron energy they can detect, if the incident neutron is near the cutoff energy for detection, scattering events may result in effective removal of the neutron, despite the neutron potentially scattering into and interacting within the detector. Due to the requirement for linear momentum to be conserved, scattering for high energy neutrons is forward biased, and increasingly biased as the neutron energy increases, as shown in Figure 52.

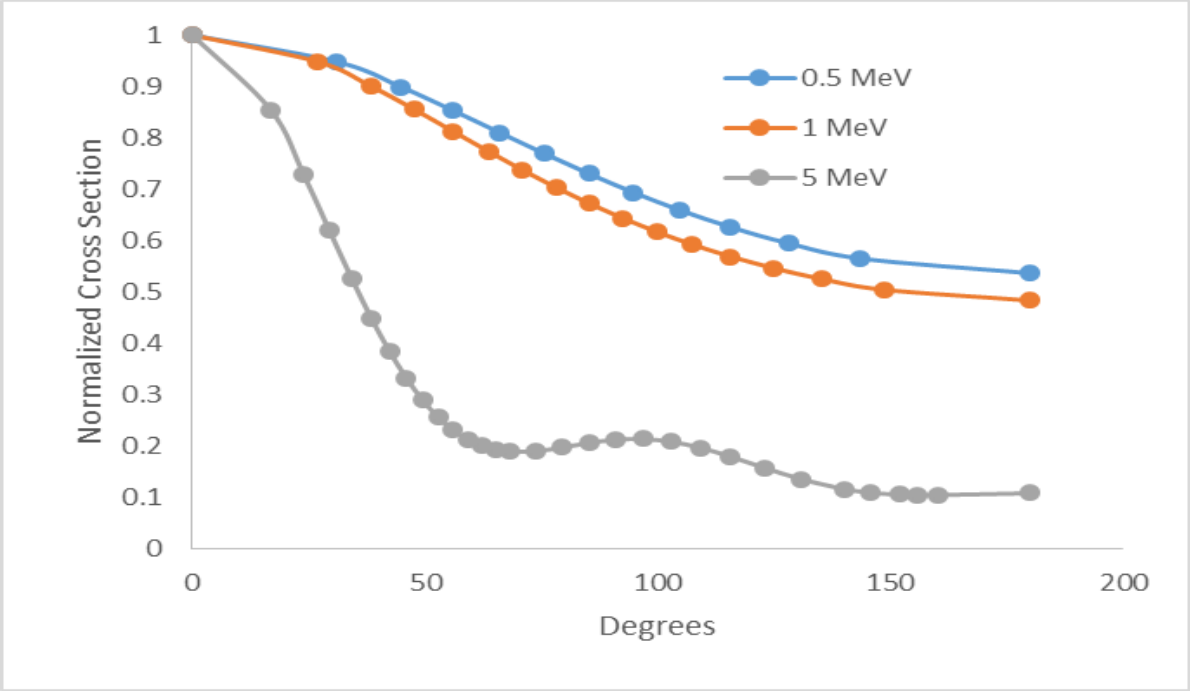

Figure 52. Angular distribution of elastic scattering off C-12 by neutrons. Cross sections are from ENDF/B-VII.1.

While there is structure in the differential angular cross section at 5 MeV that is not present at 1 MeV or 0.5 MeV, this is due to 5 MeV meeting the threshold for elastic scattering resonances, which for C-12 a resonance is at 2.0 MeV. The general trend of increased forward-bias in the elastic scattering cross section is shown, however, indicating that scattered neutrons are unlikely to be completely removed from the source distribution incident on the detector, but that their angle be changed. This has the expected effect of blurring the apparent moderator elements projected on the detector, as shown in Figure 53.

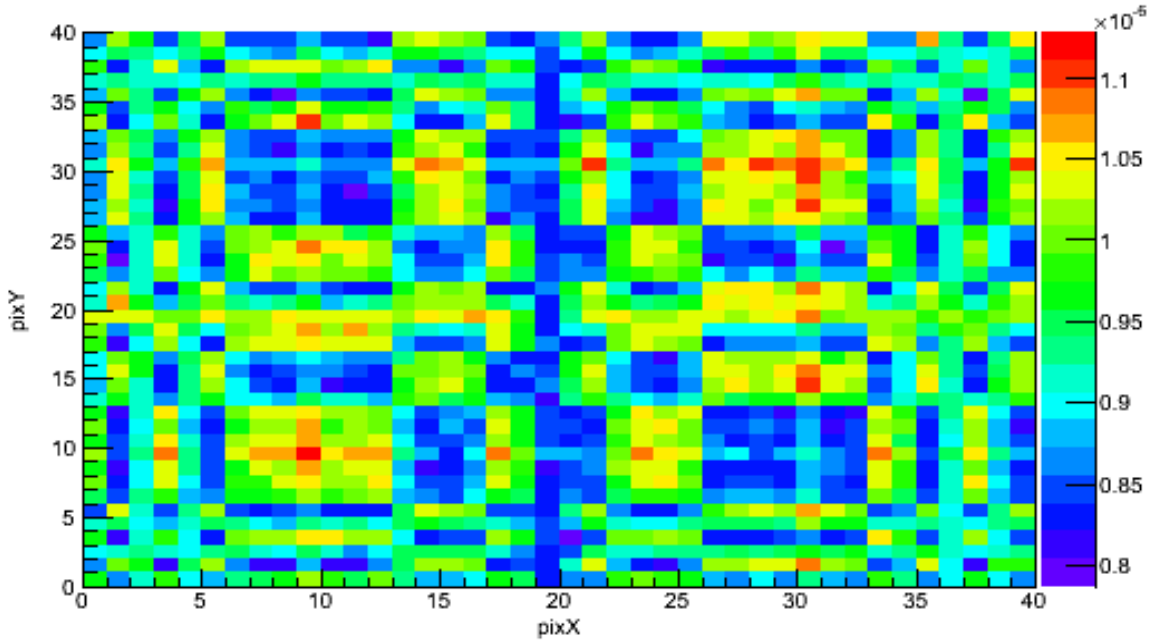

Figure 53. Normalized simulated projected mask data with mask scattering. Simulation consisted of 4E9 Cf-252 spontaneous fission spectrum neutrons emitted isotropically and transported through a rank-19 mask. Simulation performed in Geant4 (Agostinelli, 2003).

The Geant4 simulation used to generate Figure 53 consisted of 4E9 neutrons isotropically at a distance of 300 cm from an imager of the same design as P40 with a detector-to-mask distance of 45 cm and a 2" thick, rank-19 mask with 1.6 cm mask pixel width. The energy distribution of the emitted neutrons was the same as the energy distribution of neutrons emitted from spontaneous fission of Cf-252 (Smith, Fields, & Roberts, 1957). The standard deviation of the measured counts in each pixel was determined by Poisson statistics to be the square root of the number of counts, and the pixel values contained in Figure 53 are normalized to the total number of emissions. Neutrons were determined to have been detected if they scattered within a scintillator region of the detector, thus ignoring any misattribution of neutrons and thresholding of deposited energy. Since the number of initial particles per simulation requires a 4-byte integer, the maximum value of which is 2,147,483,647, the results of two simulations of 2E9 initial particles were added, one with an initial random number generator seed of 5678910, the other 348908. The standard deviation for each recorded detector pixel of the summed simulation was determined by error propagation to be

$$\sigma_{1+2}{}^2 = \sigma_1{}^2 + \sigma_2{}^2 \qquad \text{Equation 12}$$

Where σ_{1+2} is the standard deviation of the summed simulation, and σ_1 and σ_2 the standard deviation of each individual simulation. For each simulation, simultaneously recorded was the measured data when source particles that scattered within the mask were rejected, with the same statistical treatment of the no-scatter data, the results of which are shown in Figure 54.

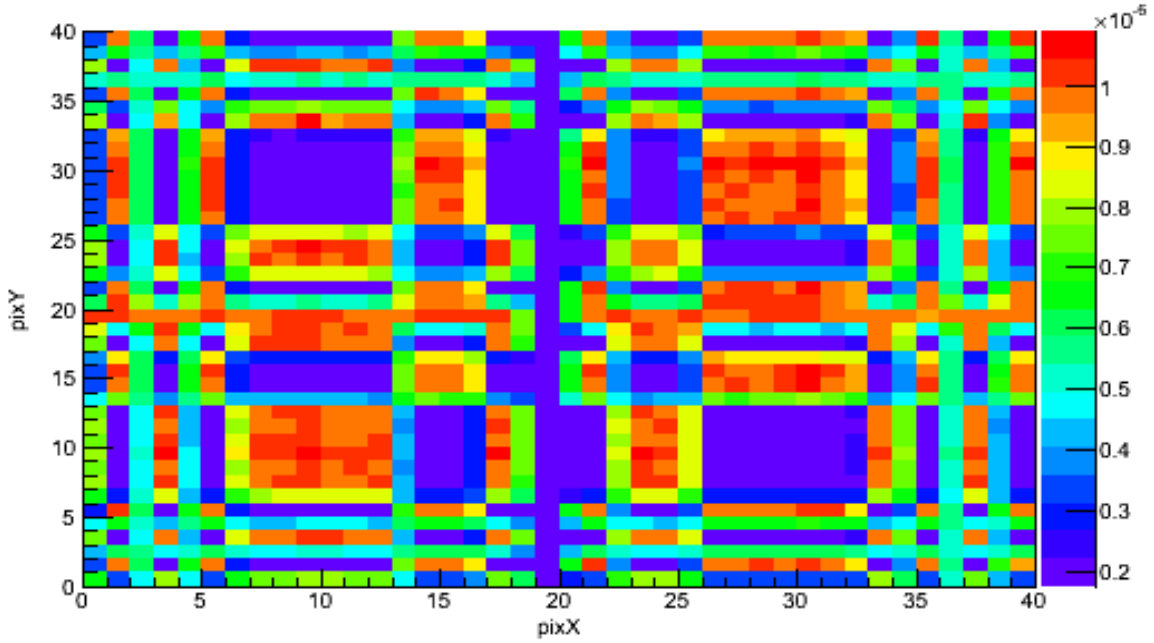

Figure 54. Normalized simulated projected mask data with no mask scattering. Simulation consisted of 4E9 Cf-252 spontaneous fission spectrum neutrons emitted isotropically and transported through a rank-19 mask. Simulation performed in Geant4.

Each pixel of the detector data with scattering within the mask included had a relative error of < 1.8%, and the maximum relative error of the data with scattering rejected was 3.8%. The minimum error for the scattering and no-scattering datasets were 1.48% and 1.52%, respectively. The higher relative error for the data with scattering rejected was expected, due to lowered total measurement efficiency. In both datasets, the region defined by pixels 6-13 on the x-axis and pixels 26-33 on the y-axis represent a mask moderator element, and the region defined by pixels 26-33 on the x-axis and pixels 26-33 on the y-axis represent a mask hole element. The effects of incorporating scattering within the mask are apparent when considering mask hole regions and mask element regions. The average value of a pixel within the mask element region in Figure 54 is less than half of the average pixel value within the corresponding region in Figure 53. This would be expected with a forward-biased scattering distribution, since the majority of scattered neutrons would be scattered in the direction of the detector pixel array. The forward-bias, but non-unidirectional scattered neutron distribution is supported by the mask hole region Figure 53 being slightly higher in the average pixel value than the same region in Figure 54. With non-unidirectional forward biased-scattering, some neutrons that scatter within mask elements will scatter into detector regions representative of mask hole elements, thus increasing the counts within detector pixels that would otherwise be unaffected by mask moderator elements.

The source distributions incident on the detector that generate Figure 53 and Figure 54 are both modulated by the geometric pattern of the mask, with additional modulation due to the effects of scattering within the mask. Since the underlying structure of Figure 53 and Figure 54 are equivalent, by treating the detector data as a 2D image, it is possible to convert between one dataset and the other by manipulating the values of each pixel. By creating a frequency histogram consisting of the number of pixels defined by a particular bin value, the range of values for both figures can be represented by a 1D figure. Due to the large range of possible values and the relatively small number of detector pixels, the shape of this histogram is not immediately meaningful, but the content of the histogram is useful. Defining the cumulative histogram as the cumulative integral of an individual image's histogram, the cumulative

histograms of the mask scatter and no mask scatter simulations are shown in Figure 55 and Figure 56.

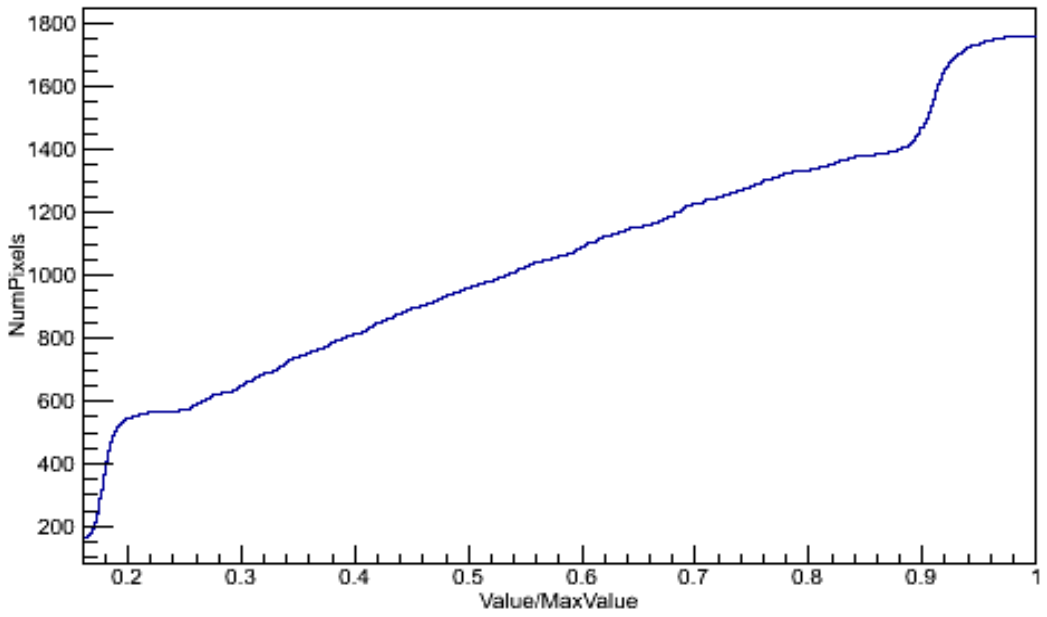

Figure 55. Cumulative histogram of simulated data without scattering in the mask

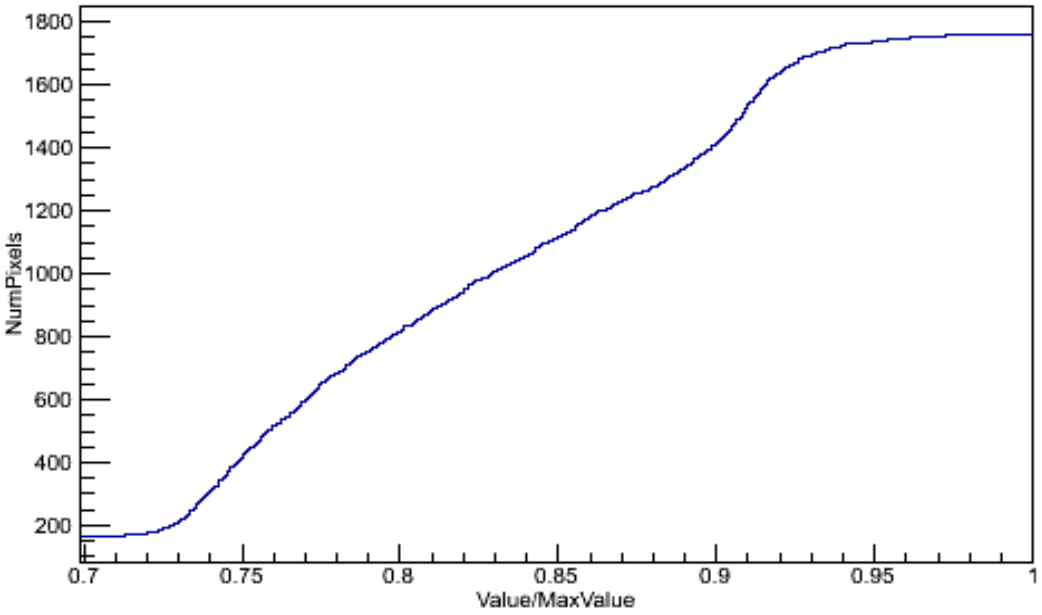

Figure 56. Cumulative histogram of simulated data with scattering in the mask

In both the scattering and non-scattering histograms, the cumulative histogram is monotonically increasing to the same number of pixels, but the rate of increase and the behavior at the maximum values differs between the two histograms. Since the projected data with scattering has less contrast between regions of the detector data representative of mask moderator elements and mask hole elements, the slope of the histogram in Figure 56 is higher than in Figure 55. Likewise, since there is scattering from mask moderator elements into detector pixels that represent mask hole elements, the absolute maximum pixel value is higher in the data represented by Figure 56, but the values in Figure 56 are normalized and thus do not reflect this. Both histograms in Figure 55 and Figure 56 have the same minimum value and the same maximum value of pixels, as would be expected since the number of pixels is the same in both. From the histograms, one can generate a transfer function that translates the pixel values of a no-scatter projected distribution to the pixel values of a distribution incorporating mask scatter, as shown in Figure 57.

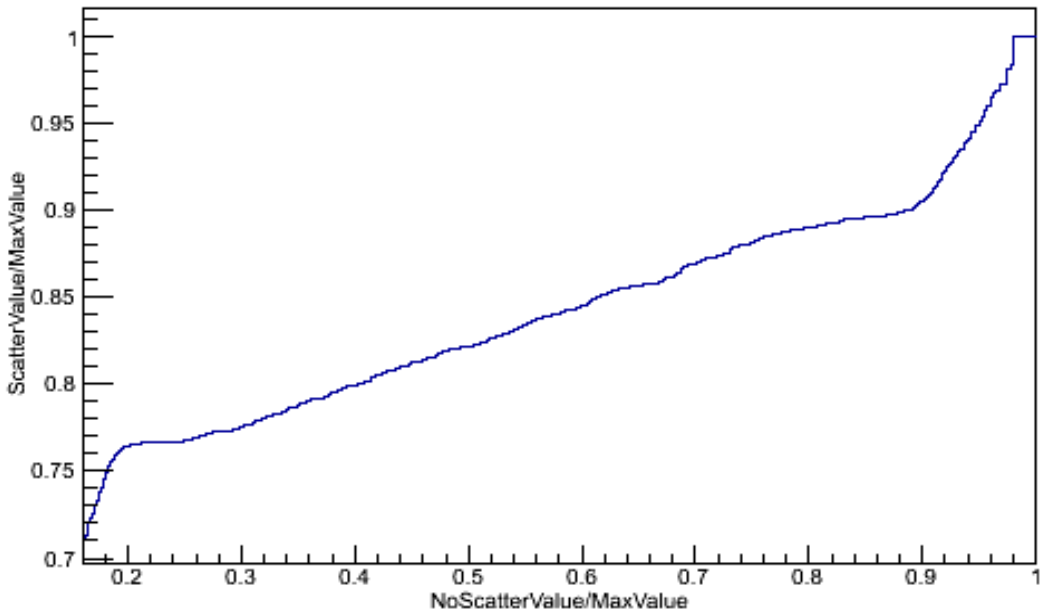

Figure 57. Transfer Function from simulation excluding scattering within the mask to simulation including scattering within the mask

By changing the pixel values of the no-scatter detector data with the transfer function in Figure 57, one can be assured that the distribution in pixel values is consistent between the two projected distributions. If two distributions have equal histograms, the transfer function between the two would be a straight line with a slope of 1 that intersects the origin, which is not the case for Figure 57. Instead, the transfer function consists of increasing the value of the regions affected by mask moderator elements either completely or partially and modifying the regions of the detector data that are partially affected by a mask moderator element, as shown in Figure 58.

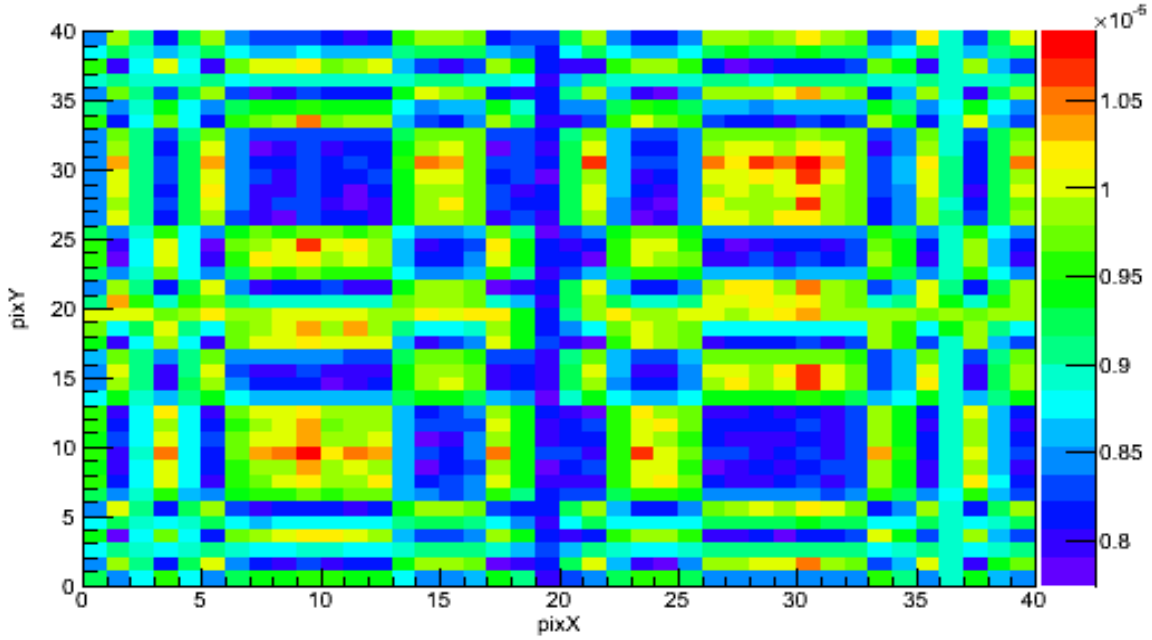

Figure 58. Simulated no-mask-scatter projected incident neutron distribution after histogram equalization, normalized per initial neutron.

Figure 58 clearly more closely resembles the simulated data that incorporates mask scatter than does the simulated data that does not incorporate any scatter at all. For 10^8 total

emissions, the reduced chi-squared value between the no-scatter simulation and the scatter simulation is 87.77, clearly indicating that there is poor agreement between the two distributions. By translating the projected no-scatter data with the transfer function, however, the reduced chi-squared value is 0.11, which is expected due to the no-scatter distribution being the distribution used to generate the transfer function. Applying this technique to the modified ray-tracing system response model, the initial projection for 10^8 total emissions is shown in Figure 59.

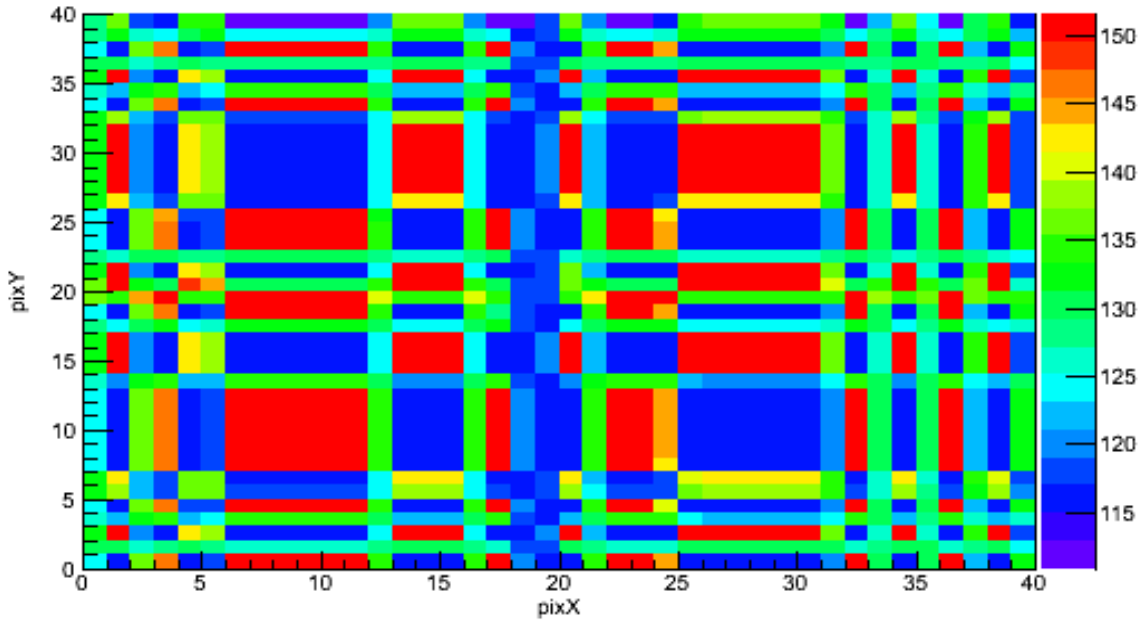

Figure 59. Modified ray-tracing projection for 10^8 total emissions, scattering accounted for by transfer function.

While there is no agreement between the no-scatter simulation and the ray-tracing model after a pointwise operation has been performed on the ray-tracing model, there is agreement between the scattering-corrected ray-tracing model and simulation incorporating mask scatter (reduced chi-squared = 0.37). While a reduced chi-squared of 0.37 generally suggests over-fitting the measured data, the relatively high relative error after 10^8 emissions (6-8%) suggests high statistical error as the cause of the low reduced chi-squared value. Increasing the emissions to 10^9 results in a reduced chi-squared of 3.7, strengthening the assumption of high relative error. However, using a pointwise translation prevents the need for a complex translation that approaches a true neutron transport, and the forward projection is able to be generated in less than a second instead of over the multiple hours necessary for a Geant4 simulation for a single source position.

3.6 Detector Scattering

For scintillation detectors, scattering within the detector is desirable, since that is the mechanism by which neutrons are detected. Neutrons that are scattered and do not interact again within the detector array are detected only once, and the effect of them being scattered are only of interest due to the scintillation effect enabling the neutron to be detected. Neutrons that scatter in the detector and are detected again are either easily discriminated against or are counted as two independent events. If a second detection occurs within the same detector element as the first detection, two scintillation events occur. With sufficiently quick timing resolution, one can potentially separate the two events, but with a large timing window per event such as those desired for measurements requiring PSD between neutrons and gamma-rays, timing-based discrimination between scintillation events may be impractical. Additionally, neutrons that scatter into other detectors within the detector array are indistinguishable from new neutrons that enter the detector array, and are counted. For a given neutron, what happens after the neutron enters the detector array has a variety of outcomes, including:

1. No Interaction
2. Single scatter in initial pixel, no energy deposited

3. Single scatter in other pixel, no energy deposited
4. Single scatter, scintillation event attributed to wrong detector pixel
5. Single scatter, scintillation event attributed to correct detector pixel
6. Single scatter, event rejected by electronics or data processing
7. Double scatter in same detector
8. Double scatter in separate detectors

If no interaction occurs or a scattering event does not deposit energy, the neutron cannot be detected by the electronics. Likewise, if the amount of energy is too low to be detected or the scintillation event is rejected at some point in the electronics or data processing (e.g. light transport places it between pixels, PSD properties indicate gamma-ray, etc.) the neutron cannot be detected either. Attribution to the wrong pixel is prevented by proper optical design and PMT gain-matching, as reported in (Newby, Hausladen, Blackston, & Liang, 2013), which would prevent systematic misattribution of scintillation events. A necessary aspect of the data processing for quantification of neutron sources is the rejection of gamma-ray events from the desired neutron distribution of neutron events. With the knowledge that the distribution of the tail-to-total ratios of individual scintillation light spectra differ between neutrons and gamma-rays for PSD-capable scintillators, the threshold to be determined to be a neutron event was > 5σ outside of the gamma-ray distribution and within 2σ of the previously-calculated neutron distribution. This systematically rejects at least 4.5% of neutrons from the measured data, but additionally rejects nearly all gamma-ray events.

With a known neutron energy, it is trivial to calculate the probability that it interacts within a pixel, and from a given incident angle it is trivial to calculate the probability of interaction within multiple pixels. After a first interaction this becomes more complex, logically requiring a full physics simulation. This enables calculation of the effects of multiple scatters, as well as the intrinsic efficiency of the detector, since the number of neutrons that are incident in a detector and the number of neutrons that scatter and deposit energy within the detector are not equal. Since this is independent of any mask modulation outside of any shifts in the energy distribution of the incident neutrons, the neutron energy spectrum incident on the detector

was assumed to be identical to the neutron energy spectrum of spontaneous fission of Cf-252. From neutron kinematics, scattering at fission-spectrum energies is forward-biased, and high-angle (e.g. 90°) scattering off hydrogen greatly decreases the energy of the scattered neutron in comparison to the incident neutron energy. With the decrease in neutron energy, as a general trend the interaction cross section is increased and thus the probable distance to the next scattering interaction decreased. Due to both the decreased probable distance to the next scattering event after a high-angle scattering event and the forward-bias of scattering events, it is highly unlikely that secondary scatters occur far away from the initial scattering event, and thus the behavior of single and multiple scattering events at the center of a detector pixel array would be representative of the behavior throughout the detector.

To account for detector scattering, which indirectly accounts for the intrinsic efficiency of a detector, a Geant4 simulation of a pencil beam neutron source in the direction of a detector pixel array of the same design as P40, with unscattered neutrons incident on the detector face at an angle normal to the detector. The energy spectrum of the initial neutrons was equal to the energy spectrum of neutrons emitted from spontaneous fission of Cf-252, the source was located at a distance of 100 cm from the center of the detector, and 2E6 initial neutrons were simulated. Since the simulation assumed air and the presence of the Al shield on the detector face, some neutrons were scattered away from the pencil beam, and the spatial distribution of neutrons incident on the detector pixel array is shown in Figure 60.

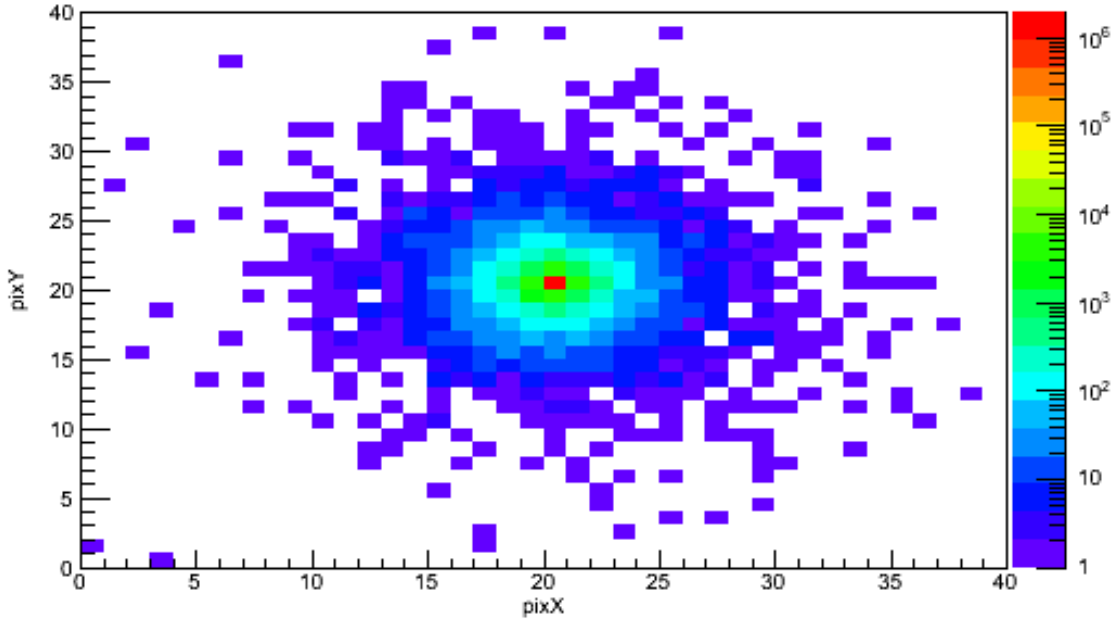

Figure 60. Spatial distribution of $2x10^6$ Geant4 simulated Cf-252 energy spectrum neutrons with a pencil beam angular distribution centered on the center detector pixel incident on detector pixel array.

Due to scattering in the air medium and aluminum face of the detector, not all incident neutrons are contained within a single pixel in the center of the detector, the distribution of incident neutrons rapidly drops off as the distance from the center of the detector increases, with a 4 order of magnitude decrease over 3 pixels in the detector. With increased scattering cross section at lower energies, neutrons that are scattered are likely to be of lower energy than non-scattered neutrons. For scattering events of low-energy neutrons, less energy is transmitted to the recoil nucleus, and thus fewer scintillation photons collected by the PMT's, increasing the probability that the photon collection threshold is not met.

Since neutrons must scatter and transfer energy to recoil nuclei in the scattering event to be detected, the spatial and energy distribution of recoil nuclei and incident neutrons are not identical, as shown in Figure 61.

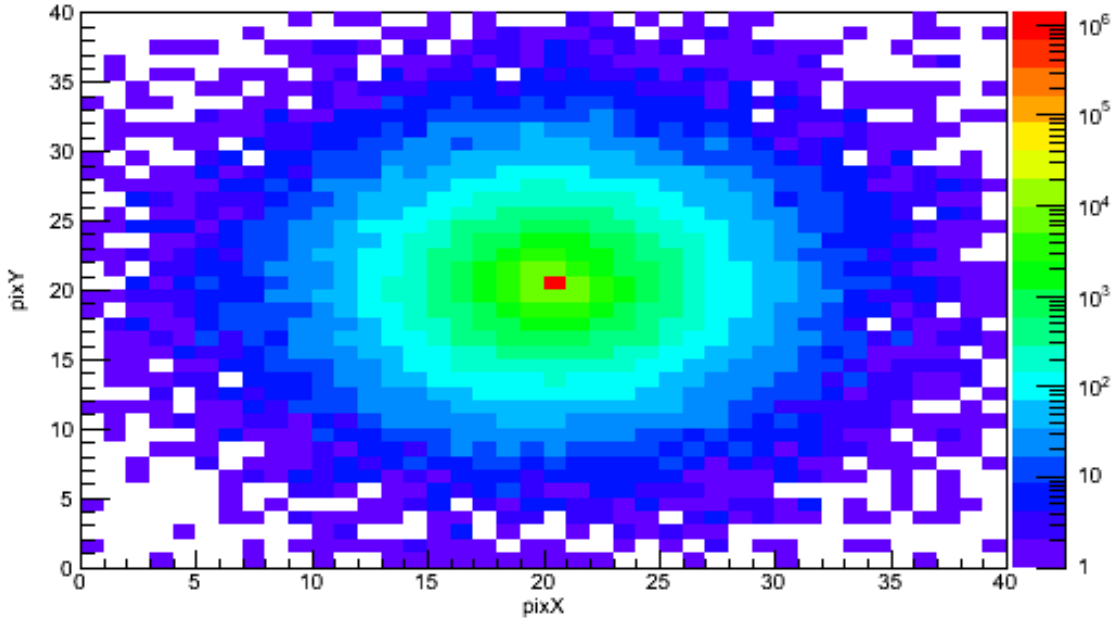

Figure 61. Spatial distribution of Geant4 simulated recoil nuclei after the first scattering event of 2×10^6 Cf-252 energy spectrum neutrons with a pencil beam angular distribution centered on the center detector pixel in a detector pixel array.

Since Figure 60 and Figure 61 quantify different aspects of the same simulation, the difference between the two figures can directly determine the effect on the spatial distribution by inclusion of scattering within the detector. Due to the decrease in energy after a scattering event, neutrons that scatter prior to entering the detector scintillator material have increased probability to scatter within the detector.

To be representative of a true detector, however, the amount of scintillation photons collected by the PMT's must meet a collection threshold. Low energy recoil nuclei produce comparatively fewer scintillation photons than high energy recoil nuclei, so incident neutrons that deposit only a small amount of energy within a neutron block detector must be rejected, requiring an understanding of the energy spectrum of recoil nuclei, as shown in Figure 62.

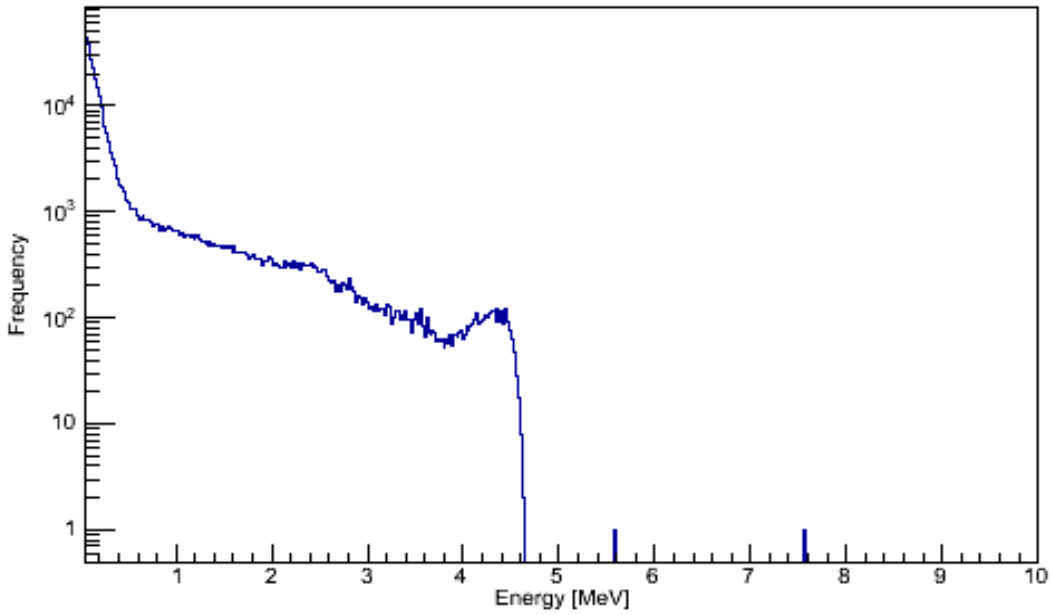

Figure 62. Total kinetic energy of recoil nuclei created by scatter of Cf-252 energy neutrons in a detector pixel array. 2×10^6 total simulated incident neutrons simulated using Geant4.

Since PSD between neutrons and gamma-rays requires discrimination between the time distributions of the scintillation light, it is insufficient to simply determine that a scintillation event occurred. At a low number of collected scintillation photons, distinguishing between the different time distributions of scintillations due to incident gamma-rays and neutrons is difficult, requiring a minimum amount of collected scintillation light to perform PSD. The photon collection threshold is set so that the amount of scintillation light produced is equivalent to the amount of light produced by scintillation of an electron of fixed energy. Light collection thresholds, while related to the total energy deposited, depend on the incident particle type, and are in the unit of MeVee, for Mega-electron-volt energy equivalent. This equates the amount of scintillation light produced by a scattering event with a particle to the amount of light produced by an electron of a given energy. For the detector design used, a photon collection threshold was set to be equivalent to the scintillation light produced and collected by a 100 keV electron. From (Lawrence, et al., 2014), the experimentally derived light yield in MeVee as a function of total deposited energy from neutron interactions within one detector block is

$$E_{MeVee} = 0.75E_{dep} - 0.32(1 - e^{-0.22E_{dep}}) \quad \text{Equation 13}$$

Where E_{dep} is the total deposited energy from neutron interactions, and E_{MeVee} is the light output. With a threshold of 0.1 MeVee, this is equal to 0.150 MeV deposited in the scintillator by the neutron. By thresholding the recoil nuclei data, the resulting distribution of recoil nuclei is shown in Figure 63.

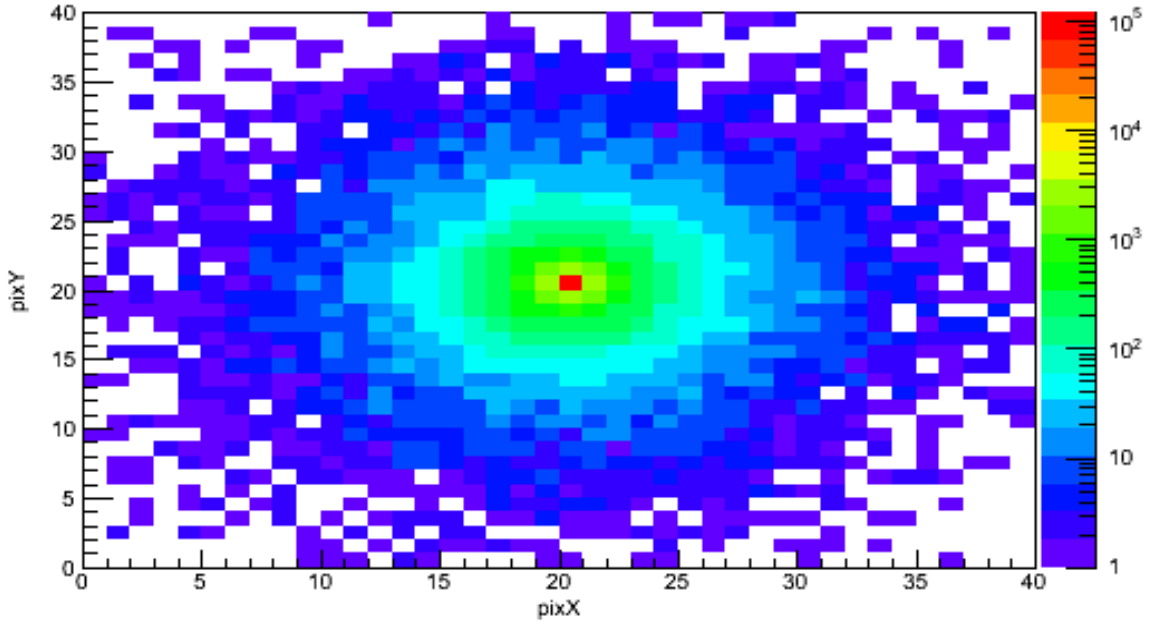

Figure 63. Spatial distribution of $2x10^6$ Geant4 simulated recoil nuclei after the first scattering event of Cf-252 energy neutrons in a detector pixel array. Data is thresholded requiring a total of 0.15 MeV deposited in the scintillator per initial neutron.

The use of thresholding in Figure 63 changes the resultant distribution of recoil nuclei from Figure 61. The total integral is decreased, and there is less contribution from pixels not located in the center of the detector. Figure 63 represents neutrons that are emitted from the simulated neutron source, scatter in the scintillator material, and in the scattering event transfer enough energy to the recoil nuclei to meet the photon collection threshold (0.1 MeVee) of the detector. This data can be used to calculate the intrinsic efficiency of the detector. From Figure 60 and Figure 61, the total number of neutrons incident on the detector pixels is 1.95 $x10^6$, and the number of neutrons that scatter in the detector is 1.51 $x10^6$. The probability that incident neutrons scatter in the scintillator element of the detector is then 0.77. The integral of Figure 63, however, is 1.61 $x10^5$, corresponding to an intrinsic efficiency of 0.087 ± 0.0002.

Since the calculation of intrinsic efficiency required not just an understanding of the physics of the imaging system but an understanding of the operational characteristics of the imaging system, the total intrinsic efficiency of the system was verified by measurement. Using P40, a 92.5 μCi Cf-252 neutron source located at a distance of 260 cm from the detector, and measured for 600 seconds. The integrated neutron counts was 33768, with a background of 1500 neutrons attributed to misattribution of gamma-rays and neutron sources in storage, for a calculated intrinsic efficiency of 0.067 ± 0.0004. Since the Geant4 calculation is 6.43 standard deviations separated from the measured data, despite being separated by a relative distance of 3.86%, the calculated estimate of intrinsic efficiency is not statistically consistent with the measured estimate. Since the threshold was selected to be equivalent to 0.1 MeVee, this threshold directly impacted the calculation of intrinsic efficiency. A slightly higher threshold, such as 0.125 MeVee, allows fewer neutrons to be counted by the system, while decreasing the misattribution rate. For a threshold of 0.125 MeVee, the calculated intrinsic efficiency of the detector using a Geant4 simulation was 0.067 ± 0.0001, which is consistent with the measured data. A slightly higher threshold could be attributed to a desire to reduce contamination of the neutron data by gamma-rays, and a desire to reject low-energy neutron interactions.

Using the understanding of the detector efficiency and the spatial distribution of scattering within the detector, the detected distribution from a neutron incident on a single pixel can be calculated. Since the source distribution incident on the detector is a delta function, the normalized detected distribution has an integral equal to the intrinsic efficiency of the detector. Instead of a delta function, the detected distribution is more complex, as shown in Figure 64.

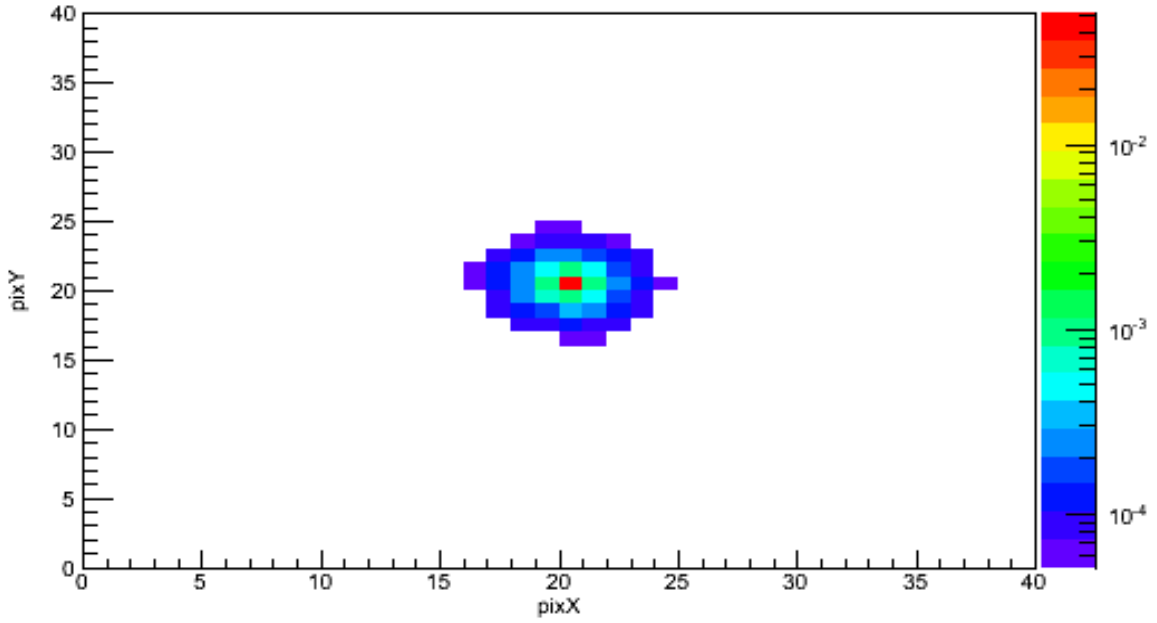

Figure 64. Detected distribution per neutron incident on the center pixel. Data is thresholded requiring a total of 0.125 MeVee deposited in the pixel, data generated by simulating 2×10^6 Cf-252 spontaneous fission spectrum neutrons in Geant4.

In Figure 64, over 75% of the detected events are contained within the initial incident pixel, and over 85% of the detected events are contained within either the incident pixel or the pixels

surrounding the incident pixel. From this, it is clear that as the distance from the center pixel increases, the contribution of the pixel to the detected data decreases, and the distribution of pixels that contribute to the detected data is only the pixels near the incident pixel. Considering that measurements with $1x10^4$ neutrons detected per detector pixel are impractical due to the long measurement time required, $1x10^4$ detected neutrons in a single pixel can be viewed as the maximum potential value. With this as a maximum value for the number of detected neutrons in a pixel, the minimum value for a pixel in Figure 64 is the maximum value scaled by 10^{-4}. The effective distribution is limited to only pixels near the incident pixel, allowing for a filter to created, as shown in Figure 65.

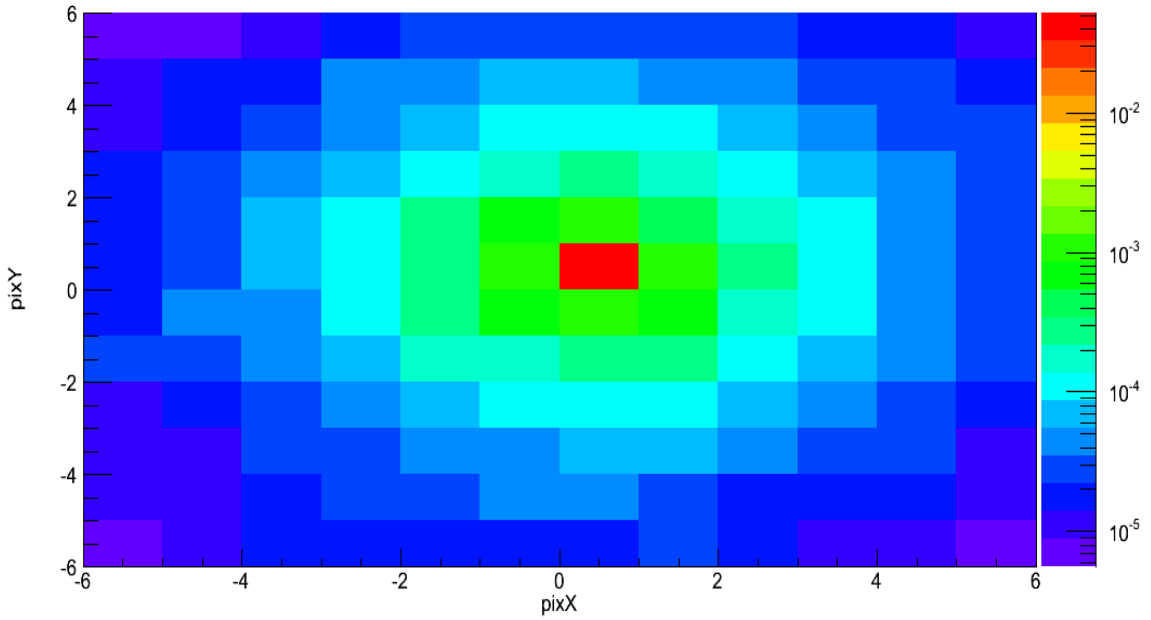

Figure 65. Detected neutrons per incident neutron centered on pixel (0,0). Filter generated by Geant4 simulation of $2x10^6$ Cf-252 spontaneous fission spectrum neutrons with 0.125 MeVee threshold.

In the system model, when scattering in the detector is neglected the intrinsic efficiency model for the detector is effectively perfect transmission within a single pixel. Since this model was used to develop an understanding of the effects of imager geometry and scattering within the mask, applying the detector scattering correction as a final processing step accounts for the detector scattering model independently. The detector scattering correction consists of a creation of a new array to store the detector data, with array elements consisting of the transfer function scaled by the original bin content. A Geant4 simulation consisting of 8.7×10^8 neutrons sampled from a Cf-252 spontaneous fission neutron energy spectra were simulated at a distance of 255 cm from the detector pixel array, centered on the center of the detector, with a mask to detector distance of 45 cm, a mask pixel width of 1.6 cm, and a mask thickness of 5.08 cm, with the source distribution incident on the detector and the distribution detected after a 0.125 MeVee threshold were recorded, as shown in Figure 66 and Figure 67.

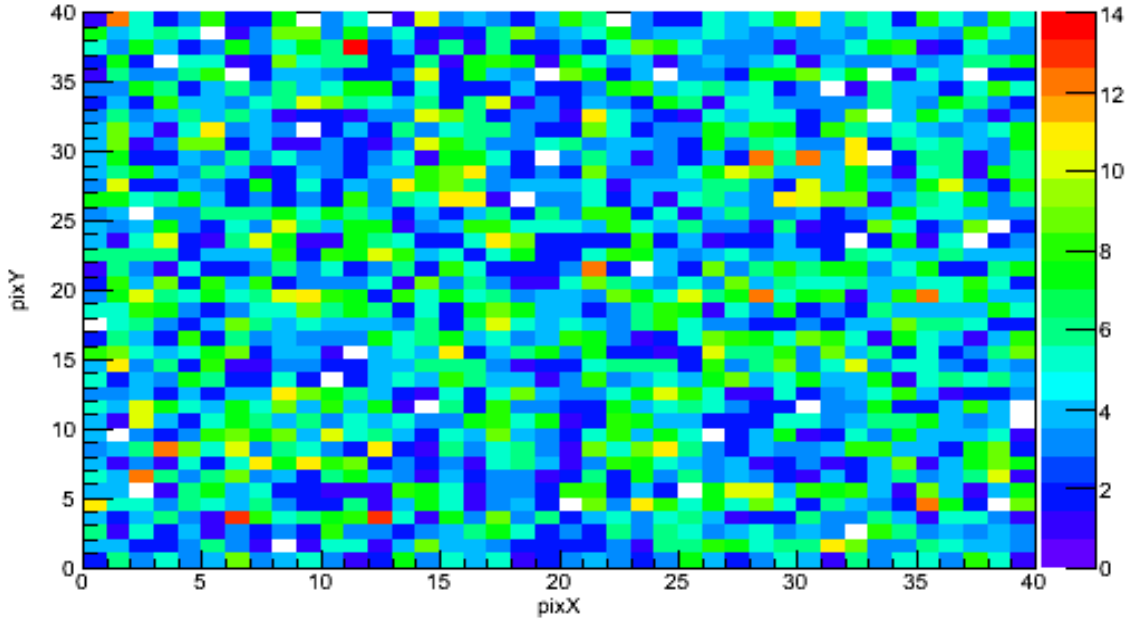

Figure 66. Simulated detector data of 6.36×10^7 neutrons with an energy threshold of 0.125 MeVee, a Cf-252 spontaneous fission neutron energy spectra were simulated at a distance of 255 cm from the detector pixel array, centered on the center of the detector, with a mask to detector distance of 45 cm, a mask pixel width of 1.6 cm, and a mask thickness of 5.08 cm.

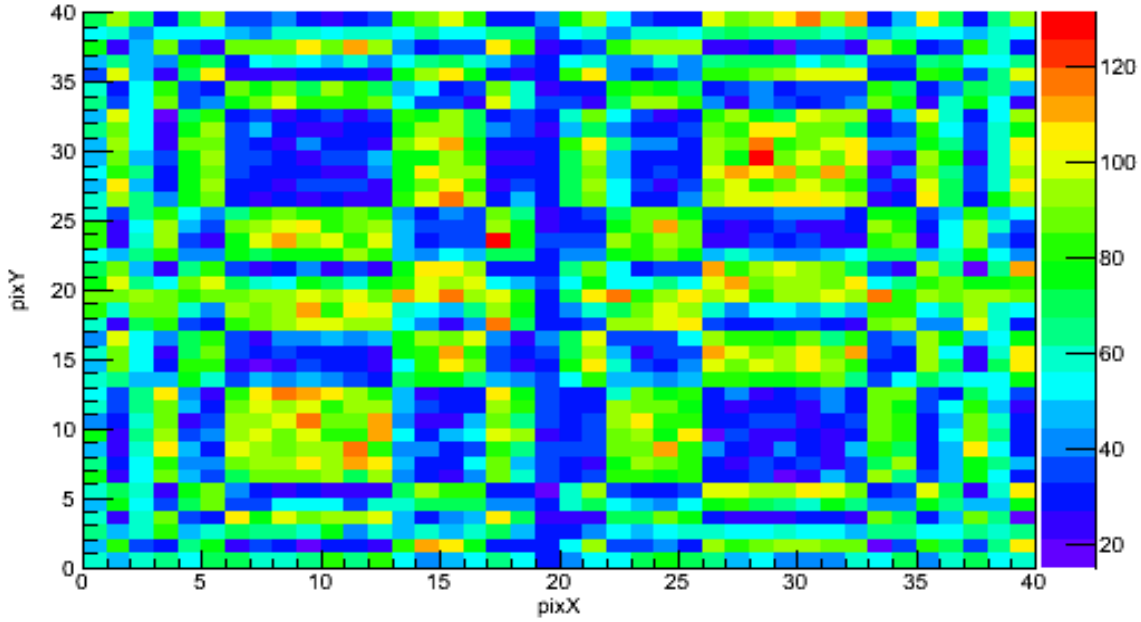

Figure 67. Projection of 6.36×10^7 neutrons isotroptically emitted sampled from a Cf-252 spontaneous fission neutron energy spectra were simulated at a distance of 255 cm from the detector pixel array, centered on the center of the detector, with a mask to detector distance of 45 cm, a mask pixel width of 1.6 cm, and a mask thickness of 5.08 cm.

Since Figure 67 consists of the source distribution incident on the detector and Figure 66 the actual measured distribution, Figure 67 was used in conjunction with Figure 65 to generate an estimate of the measured data from the incident distribution.

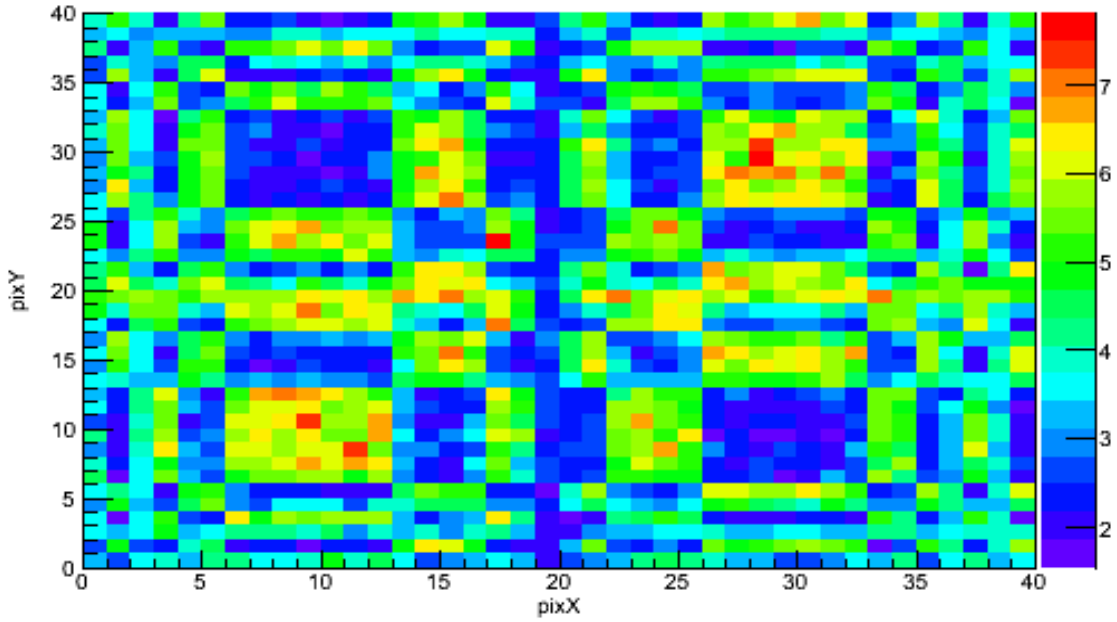

Figure 68. Estimate of measured data generated from a projection of 6.36×10^7 neutrons isotroptically emitted sampled from a Cf-252 spontaneous fission neutron energy spectra were simulated at a distance of 255 cm from the detector pixel array, centered on the center of the detector, with a mask to detector distance of 45 cm, a mask pixel width of 1.6 cm, and a mask thickness of 5.08 cm.

Despite the low number of counts per pixel, there is good agreement between the data after applying the correction for scattering in the detector and the Geant4 simulated data accounting for the scattering within the detector. The reduced chi-squared value for Figure 66 and Figure 68 is 0.49, indicating a good fit.

3.7 System Model Validation

To determine whether this simplified system response model was sufficient for reconstruction purposes, a Geant4 (Agostinelli, 2003) model of the P40 imaging system was built to perform a physics simulation incorporating scattering within the mask, detector, and a minimlum threshold of energy deposited in the scintillator. A quantify of 7.61×10^8 neutrons selected from a Cf-252 spontaneous fission neutron energy spectra were simulated at a distance of 255 cm from the detector pixel array, centered on the center of the detector, with a mask to detector distance of 45 cm, a mask pixel width of 1.6 cm, and a mask thickness of 5.08 cm. The energy threshold was selected to be 0.125 MeVee, corresponding to a detector intrinsic efficiency of 0.067, based on the study of scattering within the detector. In order to incorporate the effects of detector scattering and mask scattering, data was recorded representing secondary protons that met the energy threshold of 0.125 MeVee.

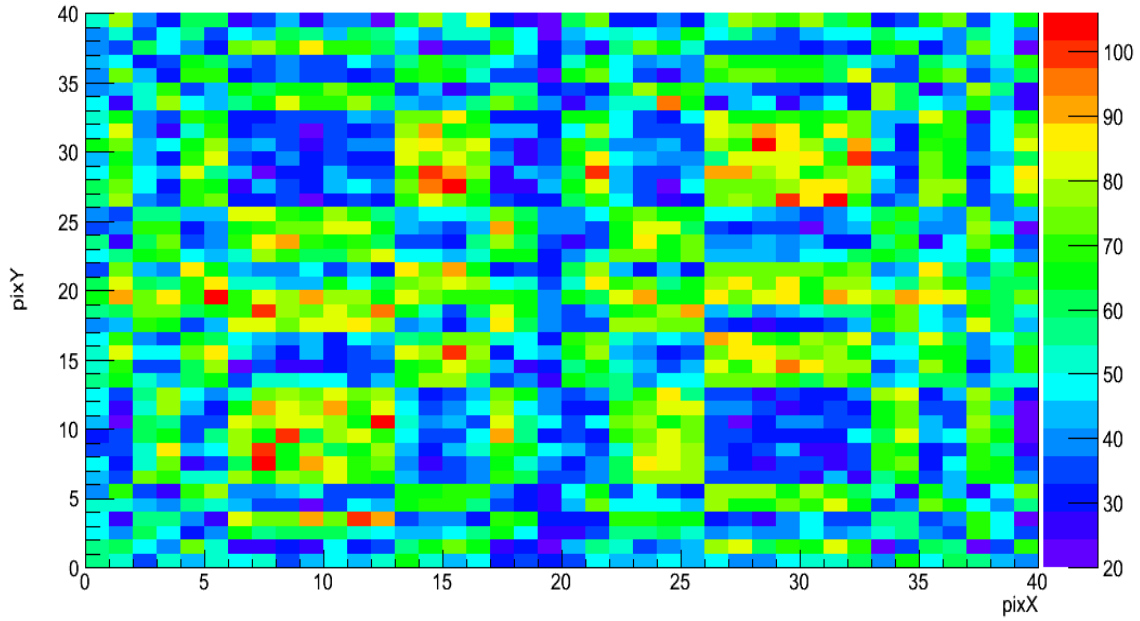

Figure 69. Simulated distribution detected by the detector of 7.61×10^8 neutrons with an energy threshold of 0.125 MeVee, a Cf-252 spontaneous fission neutron energy spectra were simulated at a distance of 255 cm from the detector pixel array, centered on the center of the detector, with a mask to detector distance of 45 cm, a mask pixel width of 1.6 cm, and a mask thickness of 5.08 cm.

The simulation design information was used to generate an expected detector data distribution from the same position and geometry using the modified system response model, incorporating corrections for mask scattering and detector scattering.

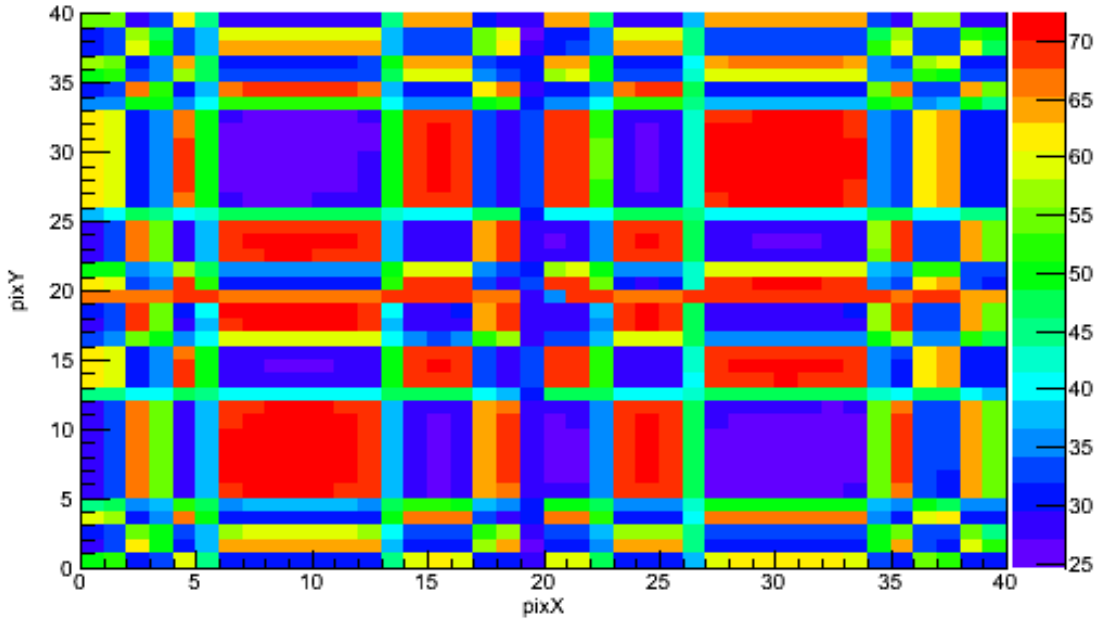

Figure 70. Simulated neutron distribution detected by the detector with an energy threshold of 0.125 MeVee, a Cf-252 spontaneous fission neutron energy spectra were simulated at a distance of 255 cm from the detector pixel array, centered on the center of the detector, with a mask to detector distance of 45 cm, a mask pixel width of 1.6 cm, a mask thickness of 5.08 cm, and scaled by 7.61×10^8 neutrons.

The Geant4 simulated data was compared to the projection data using a chi-squared test in order to determine their similarity. The reduced chi-squared value between Figure 69 and Figure 70 was determined to be 0.55, indicating that the modified system response model accurately represents the data measured in a Geant4 simulation.

Chapter 4 Maximum-Likelihood Expectation Maximization Reconstruction

An alternative reconstruction approach fits possible source distributions to the measured data in a statistical reconstruction technique instead of the analytical technique used by the cross-correlation reconstruction technique. Statistical techniques vary over a set of parameters and converge on the optimal distribution of parameters. Based on the maximum-likelihood algorithm, and derived from Bayesian analysis in the Appendix, the Maximum-Likelihood Expectation Maximization (MLEM) reconstruction fits estimated projected data to the measured data, converging on a single estimate of the source distribution.

4.1 Statistical Reconstruction Techniques

Since cross-correlation reconstruction does not fully incorporate the physics involved in neutron imaging and provides ambiguous results when combined with the parallax imaging technique, alternative reconstruction techniques are desirable. Techniques roughly fall into two categories, modified analytical techniques and statistical reconstruction. Many coded aperture reconstruction techniques have been developed for single photon emission computed tomography (SPECT) imaging, and may or may not be applicable for parallax imaging.

Recalling Equation 1, the measured data R is the convolution of the source distribution O and mask function A, the data can be reconstructed in the frequency domain by

$$\mathcal{O} = \frac{\mathcal{R}}{\mathcal{A}}\mathcal{S} \qquad \text{Equation 14}$$

where $\mathcal{O}$, $\mathcal{R}$, and $\mathcal{A}$ are the Fourier transforms of O, R, and A, respectively, and $\mathcal{S}$ is a low-pass filter (Chen, Wu, & Jin, 2005). Since high-frequency statistical noise is amplified by the division of $\mathcal{R}$ by $\mathcal{A}$, $\mathcal{S}$ is necessary to degrade the high-frequency component. Note that, while $\mathcal{A}$ can be selected such that it is the Fourier transform of the true mask pattern, alternative formulations of $\mathcal{A}$ can be selected such that they are exact solutions to the true model, not an approximate solution. This does not, however, allow for the use of multiple datasets during

reconstruction, and suffers from the same issue of independently reconstructing each measurement position as the cross-correlation technique.

An alternative technique consists of backprojecting the measured data through every mask hole element in the detector, and over multiple measurements accumulating an estimate of the source (Horn, Lanza, Bell, & Koshe, 2010). Sources are not determined by an individual detector, but by the intersection of the backprojected source distribution, similarly to the cross-correlation reconstruction. This technique, then, treats individual events in each detector position independently, while allowing for a full system response model to be applied. Intuitively, backprojecting improves with an increased number of measurement positions, since the separation between the backprojected source vectors for individual pixels within a detector is lower than the separation between backprojection vectors over different detector positions. This makes this technique especially applicable for moving detectors over many detector positions, although this technique does cause many potential artifacts from the intersecting backprojections.

An iterative technique proposed by (Hammersley, 1986) consists of iteratively removing the projection of the maximum intensity source from cross-correlation reconstructions until all sources have been accounted for. This technique inherently assumes that any sources measured are point sources, which may be an accurate assumption for astronomy applications of coded aperture imaging. Combining this with parallax imaging would result in shadow sources being removed from later iterations of the source distribution, and since sources are continually removed from subsequent estimates of the source distribution, many of the artifacts inherent to combining the parallax technique with cross-correlation reconstruction would be prevented. While complex system models can be used in the model of projected detector data of the highest intensity source, each iteration requires a cross-correlation reconstruction, which provides erroneous results for fast-neutron measurements.

4.2 MLEM Technique

As discussed in previous sections, cross-correlation image reconstruction assumes an idealized imaging system, which for real detectors and particularly for the case of fast neutron imaging

from multiple positions, is a non-valid assumption. Reconstructing using this analytical method potentially results in ambiguity in the reconstructed image due to various artifacts. Likewise, a blind chi-squared analysis that iterates over all possible source distributions is not a true reconstruction technique, and is impractical for source quantification due to the computational complexity of the problem. An alternative reconstruction technique, which has been used successfully in medical imaging and various other emission imaging applications, is maximum likelihood expectation maximization (MLEM). In MLEM, for each source voxel *b*, the probability that an emitted particle will be detected in detector pixel *d* is calculated, and during the MLEM reconstruction the expected source intensity is iterated in such a way as to guarantee the maximum likelihood (Shepp & Vardi, 1982). For Poisson distributed counts in a detector pixel and an emission source, commonly used in radiation detection, the conditional probability of detecting the measured data P^* is given by:

$$Prob(P^*|\bar{S}) = \prod_{i=1}^{m} \frac{(\bar{P}_i)^{P_i^*}}{P_i^*!} \exp(-\bar{P}_i) \qquad \text{Equation 15}$$

Where $\bar{S}$ is the source distribution, in detector counts, that can be attributed to a particular source voxel, *m* the number of detector pixels, and $\bar{P}_i$ the expected counts in pixel *i* (Ito & Fujimura, 1996). The use of P^* prohibits the use of subtracted mask/anti-mask data (purely modulated data) due the need for P^* to follow a Poisson distribution. It does allow, however, for the use of anti-mask data as an extension of the detector data, increasing the number of data points used in the reconstruction. Knowing the source distribution,$\bar{S}$, $\bar{P}_i$ would be equal to:

$$\bar{P}_i = \sum_{j=1}^{n} p_{ij}\, \bar{S}_j \qquad \text{Equation 16}$$

Where *j* is the source voxel and p_{ij} the probability that a particle emitted in source voxel *j* is detected in detector pixel *i*. A MLEM reconstruction, therefore, requires the development of p_{ij} for each detector pixel and source voxel. The MLEM algorithm can be derived from multiple frameworks, including from taking a log-likelihood approach to Equation 15, and optimizing the results using the sufficient conditions of the Kuhn-Tucker conditions (Kuhn & Tucker, 1951). The MLEM algorithm has been previously determined (Ito & Fujimura, 1996), and from an initial estimate of $\bar{S}^0$, the source distribution for each voxel is iterated by:

$$S^{new}(b) = S^{old}(b) \sum_{i=1}^{m} \frac{P^*{}_i \, p_{ib}}{\sum_{b'=0}^{n} S^{old}(b') p_{ib'}} \qquad \text{Equation 17}$$

From Equation 17, it is apparent that the reconstructed voxel value is not the source intensity, but the detected counts that can be attributed to that voxel. The choice of a $\bar{S}^0$ close to the true distribution can decrease the number of iterations necessary to reconstruct the image, but without a priori knowledge of the expected source distribution, generally a uniform constant is used as the initial estimate, as shown in Figure 71.

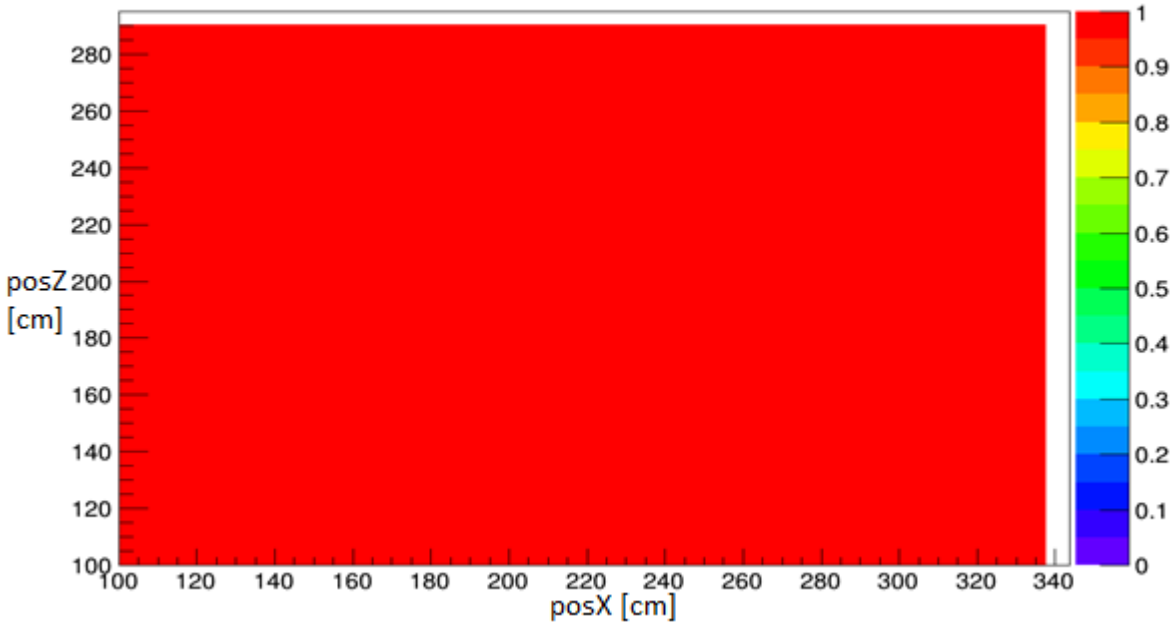

Figure 71. First iteration of source distribution for MLEM reconstruction, seeded with a uniform source distribution across all source voxels.

After a number of iterations, for a single point source, the reconstruction converges to a parameter distribution, as seen in Figure 72 and Figure 73.

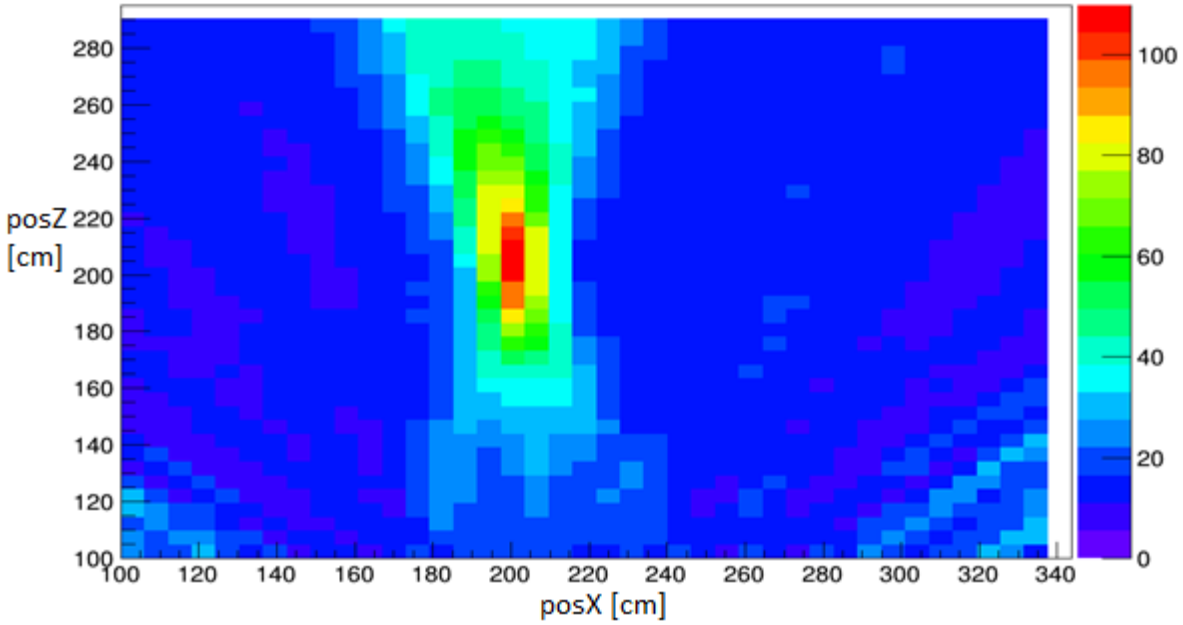

Figure 72. Ninth iteration of source distribution for MLEM reconstruction of a source localized at 200 cm on the x axis, 210 cm on the distance axis, for three measurement positions shifted by 60 cm per measurement position. The center of the second measurement position is centered at 210 cm on the x axis.

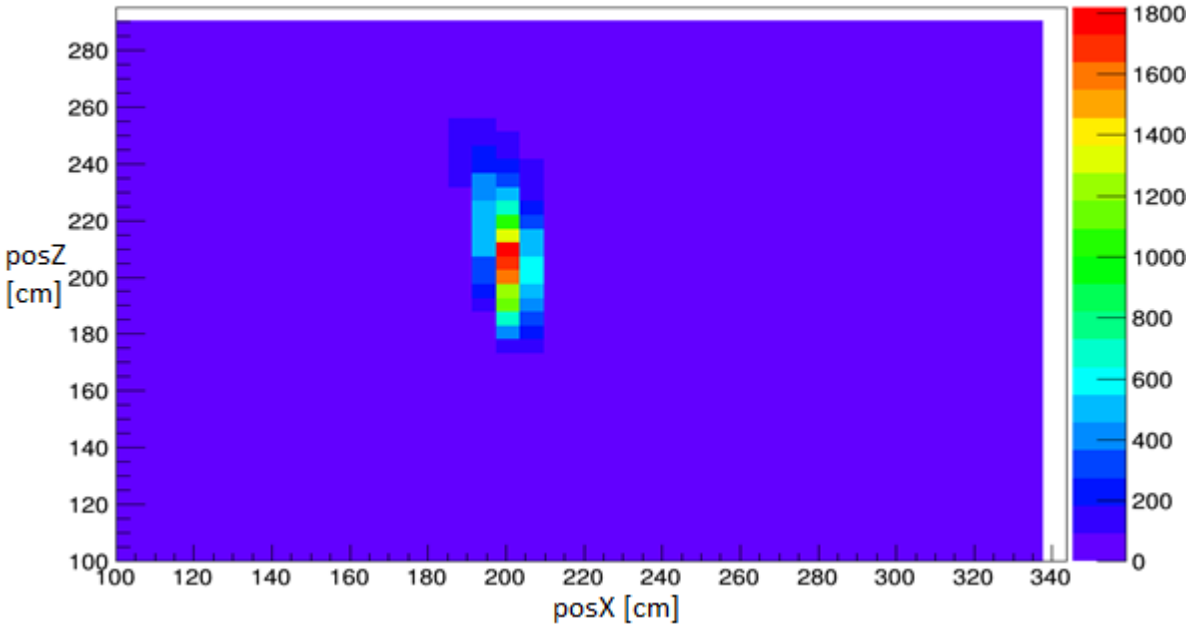

Figure 73. 45th iteration of source distribution for MLEM reconstruction of a source localized at 200 cm on the x axis, 210 cm on the distance axis, for three measurement positions shifted by 60 cm per measurement position. The center of the second measurement position is centered at 210 cm on the x axis.

A notable comparison to reconstructions generated by the cross-correlation technique is the relative lack of imaging artifacts. While early iterations such as Figure 72 and Figure 73 demonstrate artifacts similar to the cross-correlation technique, such as the source apparently extending behind and in front of the source location, the later reconstruction shows a tighter distribution, reconstructing the source at a distance of 210 cm with a FWHM of 40 cm, the general behavior of which would be expected for a point source. MLEM reconstruction allows for the use of a complex system response model, desirable in fast-neutron imaging, as well as the use of various datasets, ranging from an individual pixel to every pixel in each measurement position for parallax imaging. Attractive for parallax imaging, MLEM reconstruction reconstructs the source distribution considering each detector pixel simultaneously, so the reconstructed source distribution is not generated from individual reconstructions of each detector position, but the entire measurement as a whole.

Since the MLEM reconstruction iterates over each voxel, it was a question whether the order of voxels made a significant impact on the reconstruction once the reconstruction converged on a source distribution. From Equation 17, each voxel in an iteration is dependent on the measured data, which is fixed, and the previous reconstruction, which for a given iteration is fixed. Due to this, the order of voxels in the reconstruction does not matter.

While reconstructed images demonstrated reconstructed source intensity distributions, Equation 17, indicates that source intensity is not reconstructed, but the measured counts that can be attributed to a given source voxel. Since the forward projections used to generate the source distribution in terms of detected counts is well known, converting between detected emissions and total emissions consists of backprojecting the reconstructed distribution of detector counts. Intuitively, for a uniform reconstructed source distribution in detector counts, the reconstructed source intensity distribution is biased towards source voxels at increased distance due to the backprojection considering the inverse of the geometric efficiency.

4.3 Parallax MLEM

Since the MLEM technique is statistical reconstruction that fits the projected data from a source position to the measured detector, it should be possible to reconstruct a source from a

single detector position. As previously discussed, the distance resolution of the coded aperture technique is inferior to the angular resolution, so parallax imaging has been proposed to improve the distance resolution of a measurement by taking advantage of the comparatively high angular resolution from multiple measurement positions. This was demonstrated for cross-correlation reconstruction, and the improvement on statistically fitting a source distribution was demonstrated with a chi-squared analysis in previous sections. A source of 10^8 intensity was simulated at a distance of 250 cm from the detector using a simplified system response model, and first reconstructed with a single detector position, and then reconstructed with three detector positions with a movement of 56 cm between detector positions, with both reconstructions using a system response model identical to the one used to simulate the data. Reconstruction was performed using the standard MLEM algorithm, and ended after 50 iterations.

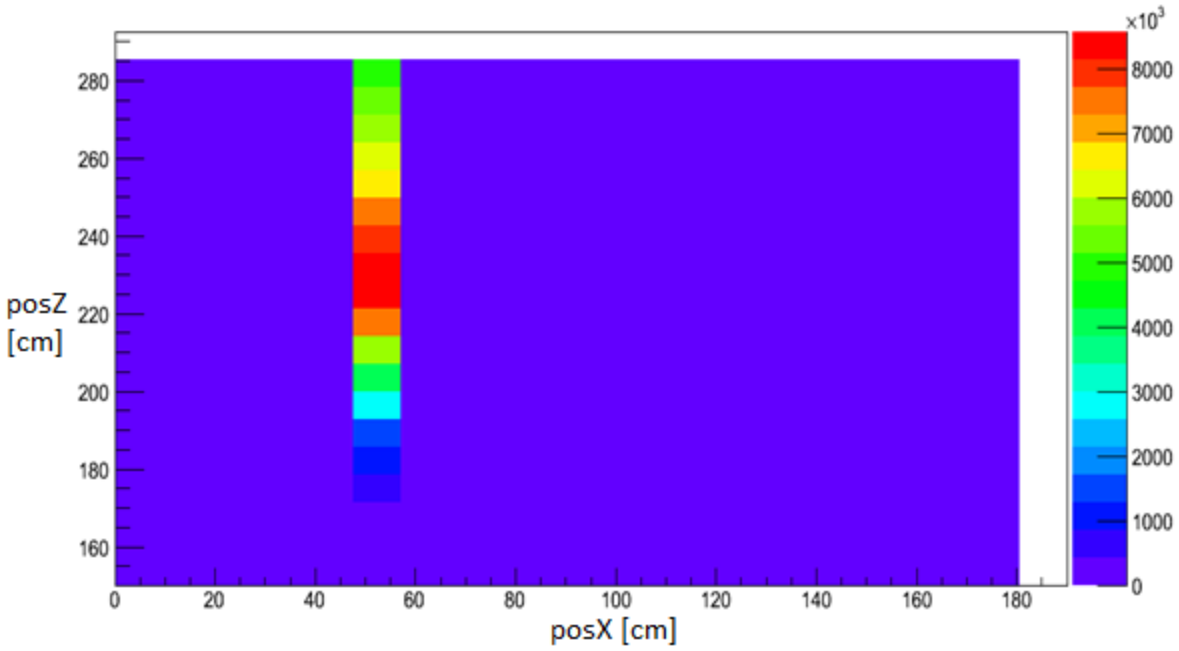

Figure 74. MLEM reconstruction of a single source at 250 cm distance with a single detector position.

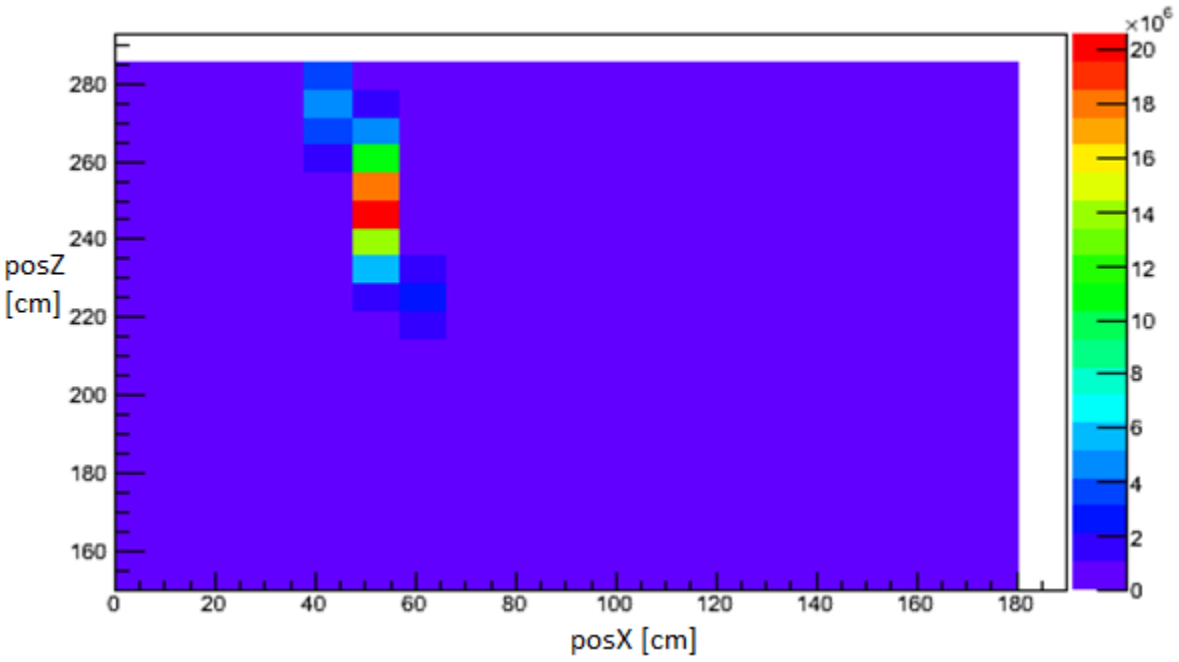

Figure 75. MLEM reconstruction of a single source at 250 cm distance with three detector positions separated by 56 cm.

From Figure 74 and Figure 75, it is apparent that distance resolution is improved by using three detector positions versus using only a single detector location. After 50 iterations, the single measurement source is reconstructed at 230 cm with a FWHM of 100 cm, while the three measurement source is reconstructed at the proper distance of 250 cm with a FWHM of 30 cm. This indicates that the MLEM reconstruction of a single detector position does not reconstruct the source distribution uniformly, but is biased towards reconstructing the source at the closest voxel representative of the measured data. While 50 iterations is too few to determine the absolute resolution of the measurement techniques, and more voxels and more iterations would likely improve resolution for both reconstructions, after 50 iterations it's already clear that combining multiple measurement positions provides superior resolution and more accurate estimation of detector position than a single measurement position. In addition to having inferior distance resolution, the single detector position reconstruction reconstructs the source to the wrong distance. This can be attributed to the poor distance resolution of the coded aperture imaging technique itself. The poor distance resolution is demonstrated to a lesser amount in the reconstruction with multiple measurement positions, with the extension of the source angularly in front of and behind the source location. While convergence has not been completed after 50 iterations and more iterations may better isolate the source, the behavior of the convergence is apparent in that a single source is reconstructed with more accurate and improved resolution for parallax imaging in comparison to a single measurement position.

4.4 MLEM Stopping Rules

One of the challenges with MLEM reconstructions is determining the number of iterations necessary to sufficiently reconstruct a source distribution without inducing error from over-reconstructing the source distribution. While it may be sufficient to determine that the source of a given intensity is isolated within a 10x10 cm voxel or region of voxel for instance, in a more general case, it is useful to have a statistical test based on the reconstruction to determine that the current reconstruction is sufficient. Multiple statistical stopping rules have been proposed (Bouallegue, Crouzet, & Mariano-Goulart, 2013), notably a chi-squared stopping rule using the same statistic discussed in Section 2.5, which is attractive due to its relatively unambiguous

indication of when the reconstruction best represents the measured data. Since the first iteration, with the exception of the unexamined case where a uniform source distribution is an accurate estimate of the true source distribution, will have a reduced X^2 value >>1, and as the number of iterations approaches infinite, the reconstructed source distribution will over-fit the measured data and X^2 will approach zero. Two potential reconstruction behaviors with respect to the reduced chi-squared value are possible: 1) a minimum value is met or asymptotically approached that is >1; 2) a minimum value is met or asymptotically approached that is <1. A minimum value >1 indicates that the reconstruction conditions do not exactly match up with the measurement, such as the need for more source voxels or a modified system model. Setting a stopping rule that when the reduced X^2 statistic is equal to 1 or has surpassed a minimum value prevents overfitting the measured data with a given system response model.

To demonstrate this, a source of $5\text{x}10^8$ total emissions was projected through a rank-11 mask onto a 24x24 pixel detector the same geometry as P24 at a mask to detector distance of 35 cm. The source was positioned at a source-to-mask distance of 250 cm, and the data for two measurement positions was recorded, one position with the x position of the source +50 with respect to the detector center, and the other -10. With no thresholding, a single-stage MLEM reconstruction was performed with 30 voxels on the x-axis, and 40 voxels on the distance axis. The reduced chi-squared value was recorded for each iteration, as shown in Figure 76.

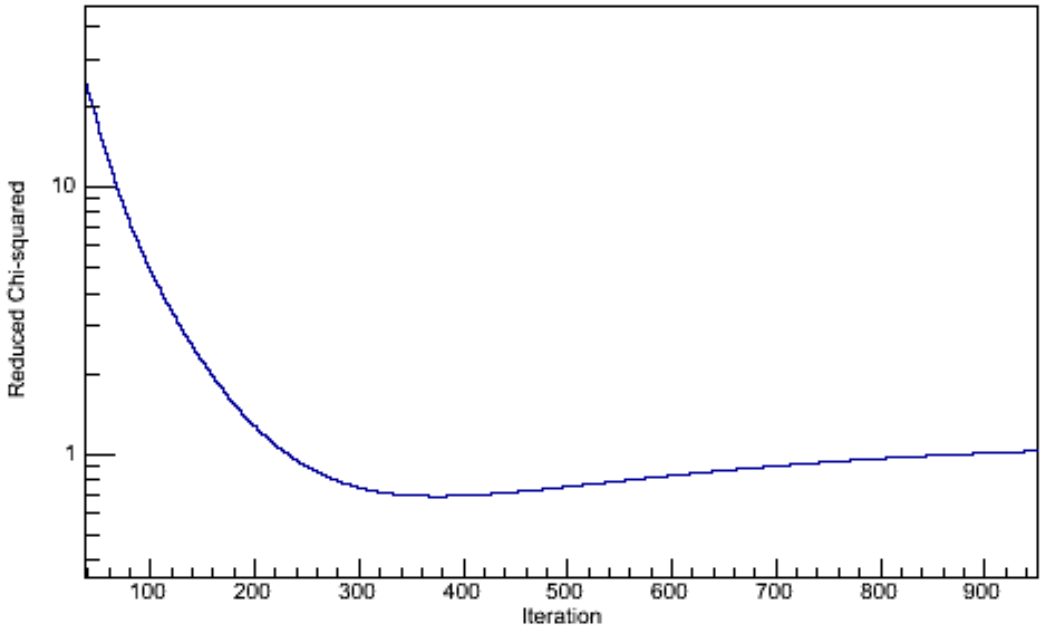

Figure 76. Reduced chi-squared value for each iteration of a MLEM reconstruction. Source intensity is $5x10^8$, with no statistical sampling of the projected detector data.

Since there is no thresholding involved, further iterations are dominated by the behavior of non-source voxels, which is indicated by the chi-squared value increasing after 380 iterations. After 220 iterations, however, the reduced chi-squared value decreases below 1, indicating a good fit. Since the simulated measured data is statistically perfect, a reduced chi-squared value of exactly zero represents a perfect reconstruction of the initial source distribution. As the reconstruction does not reach a reduced chi-squared value of exactly zero, then, the reconstruction imperfectly reconstructs the initial source distribution.

An imperfect reconstruction could have multiple potential causes, including either the use of a system response model that does not accurately represent the physics of the measurement or a MLEM reconstruction that does not contain the exact parameters that represent the measured data. Intuitively, the source position may not be contained at all within the parameter space being reconstructed, or the source position may not be exactly represented by a possible distribution of parameters. At no iteration in reconstruction, then, would the measured distribution be exactly represented. Additionally, without thresholding non-source voxels are reconstructed with positive intensity, despite their true zero intensity, erroneously contributing to the reconstructed distribution. Determining that a reconstruction is sufficient is dependent on the needs of the measurement.

4.4.1 Statistical Effects

Since reconstruction requires determining the source distribution that accurately represents the measured data, it would be expected that properties of the measured data impact the performance of the reconstruction algorithm. As measurement time increases, the counts in each detector pixel increases, with the statistical error for a Poisson distribution being equivalent to the square root of the number of counts. From this, relative error at 100 counts is 10%, at 10000 counts 1%, and so on. Due to transmission through the mask, scattering within the mask, and scattering within the detector, at low counts the separation between mask moderator elements of the detector data and mask hole elements may be less than the statistical error in the measurement. For low counts with high relative error, a reduced chi-squared analysis may indicate a good reconstruction despite the reconstruction being

inaccurate of having not yet converged. Conversely, the separation between small shifts in source location may be enough that at very high statistical accuracy measurements, a reduced chi-squared analysis indicates a poor reconstruction.

To verify this, the system response model was used to simulate a measurement of a Cf-252 source located at 22 cm on the orthogonal axis at a distance of 250 cm, with a source to mask distance of 47.5 cm, and a step between measurements of 60 cm. The MLEM reconstruction consisted of 1500 iterations with a threshold equal to the mean voxel value, 25 voxels on the distance axis from 200 cm to 400 cm, and 25 voxels on the orthogonal axis from -50 cm to +50 cm from the center of the first measurement position, as shown in Figure 77.

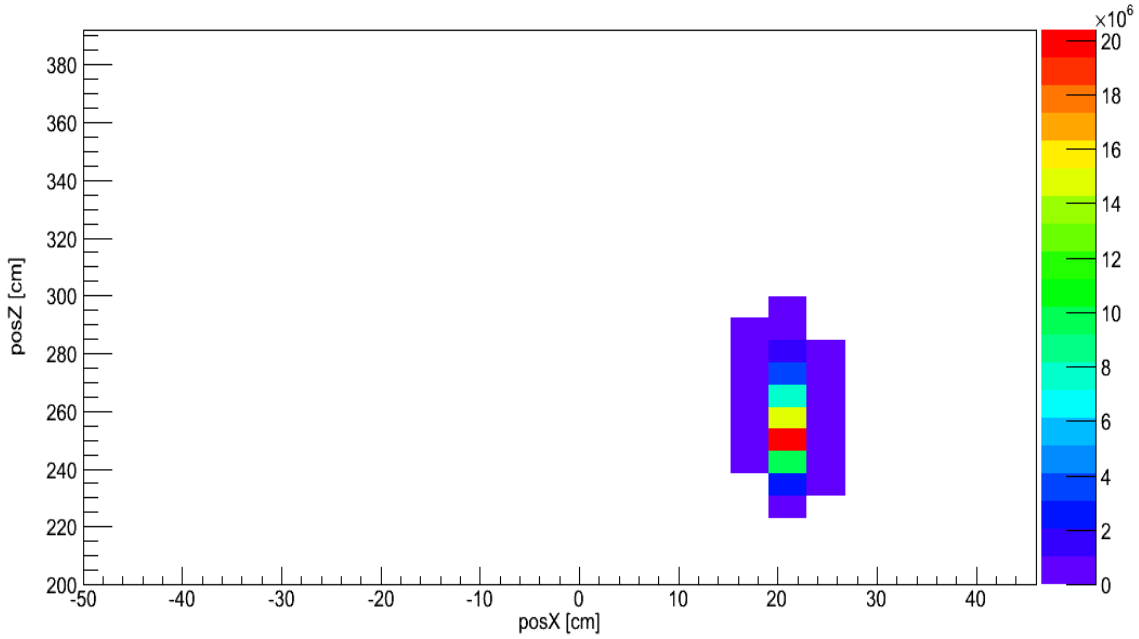

Figure 77. MLEM reconstruction of simulated measurement of a Cf-252 source located at 22 cm on the orthogonal axis at a distance of 250 cm, with a source to mask distance of 47.5 cm, and a step between measurements of 60 cm. The integrated projection was selected such that the average pixel contained 82 counts, equaling a relative error of 10.9%.

The same reconstruction was performed integrated counts ranging from an average pixel count of 4 to 135000. The reconstructed projected data was compared to the simulated measured data using a chi-squared test, the results of which are shown in Figure 78.

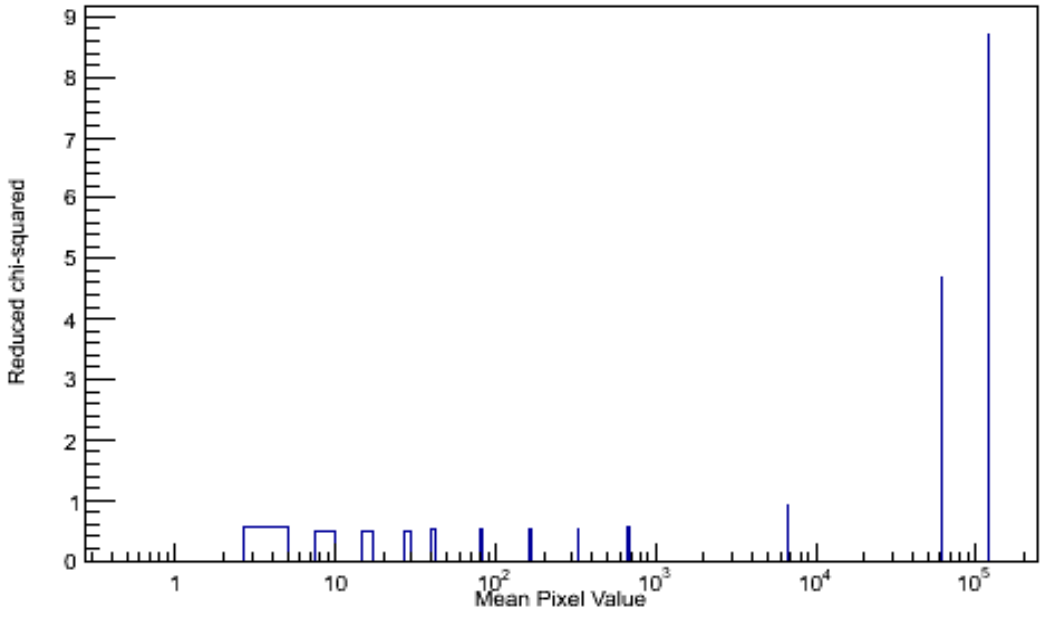

Figure 78. Reduced chi-squared for MLEM reconstructed data for a range of mean pixel values.

While each reconstruction reconstructed the source to the proper voxel and had equivalent resolution, the center of the voxel containing the source does not exactly match the source position. At relative errors >1%, the reduced chi-squared value is consistently below 1, but at increased counts, the reduced chi-squared value is consistently high. For the reduced chi-

squared value to be below 1, smaller size voxels are necessary for measurements with high statistical accuracy.

4.5 Thresholding

In a MLEM reconstruction, prior to the first iteration of a reconstruction, $\bar{P}_i$ for each source voxel must be generated. In the case of 3 detector positions and a 24x24 detector, over 1700 values must be generated and stored for each voxel, and accessed each iteration. For a large number of voxels or large number of measured data points, this can become prohibitively expensive. Furthermore, after multiple iterations, some reconstructed voxels approach a small but non-zero value, indicating the absence of source radiation at that detector position, but a physically accurate reconstruction represents them as declining to zero. Since these erroneously nonzero voxels contribute to the reconstruction of true source voxels, they reduce the accuracy of the reconstruction (Chuang, et al., 2005). By first reconstructing a low-resolution (large voxel size) source distribution, positions where source radiation is not present can be determined, and those positions can be ignored for repeated, higher-resolution reconstructions. The new original estimate of source distribution $\bar{S}^0$, for later, higher resolution reconstructions does not represent not a discretized but continuous field covering the entire range of possible source positions, but only those voxels that have passed previous reconstructions. This decreases the number of voxels reconstructed for higher-resolution reconstructions, representing advancement in computational time and accuracy of reconstruction. Further improvements in computational time for later reconstructions can be made by seeding the new $\bar{S}^0$ not with a uniform source distribution, but with the source distribution from the previous reconstruction. Early in the reconstruction, convergence has not stabilized, and removing voxels may result in the removal of meaningful voxels, while beginning the thresholding too late in the reconstruction does not result in substantial improvement over the non-threshold reconstruction.

Selecting a threshold value for reconstruction is of interest, since a threshold too high would exclude voxels that actually contain source radiation, while a threshold too low would include unnecessary non-source voxels in the reconstruction, not have significant improvement in

computational speed, and have measured data falsely attributed to non-source voxels. The threshold value selected is dependent on the characteristics of the expected source distribution itself. For a reconstruction of a single point source with no background radiation, for instance, all the detector pixel counts should be attributed to a single voxel or a small region of voxels if the voxel center is not equal to the source position, making a relatively high threshold, since most reconstructed voxels are not source voxels and thus should be rejected, appropriate. Conversely, with reconstructing a source distribution with low separation between source and background voxels, nearly all voxels in the reconstruction contain source radiation, but a high threshold would eliminate meaningful information from the reconstruction and overestimate remaining source voxel intensities. Unless otherwise noted, the arithmetic mean voxel value was selected as the threshold. This is due to the use of physically small sources that are equivalent to point sources in measurements, with the source constrained to a small area of the region covered by the voxels in reconstruction. This threshold becomes more conservative near the end of the reconstruction for low-background reconstructions, since most reconstruction voxels have zero counts.

A demonstration of this principle was performed using three reconstructions: a three-stage reconstruction eliminating non-source voxels from $\bar{S}^0$ from the second and third reconstructions as well as removing non-source voxels from $\bar{S}^n$ after the 15th and later iterations, a single-stage reconstruction that removes non-source voxels from $\bar{S}^n$ after the 15th and later iterations, and a single-stage reconstruction with no voxel removal. The size of the source distribution for the three stage of the three-stage reconstruction was selected to be the same as the $\bar{S}^0$ for the single-stage reconstructions, a 30x30 voxel array prior to any voxel removal. Voxels were removed if their value was determined to be less than a certain amount, arbitrarily selected to be mean value of the reconstructed source distribution. The results of the final iteration (50 iterations) of this test are shown in Figure 79, Figure 80, and Figure 81, and summarized in Table 2. A low number of iterations was selected in the interest of reconstruction time and to demonstrate general behavior of the thresholding technique, and the accuracy of the reconstructed distributions is considered to be low. The simulated source used to generate the

measured data was sampled from a simplified system response model, which was used as the system model in the MLEM reconstruction.

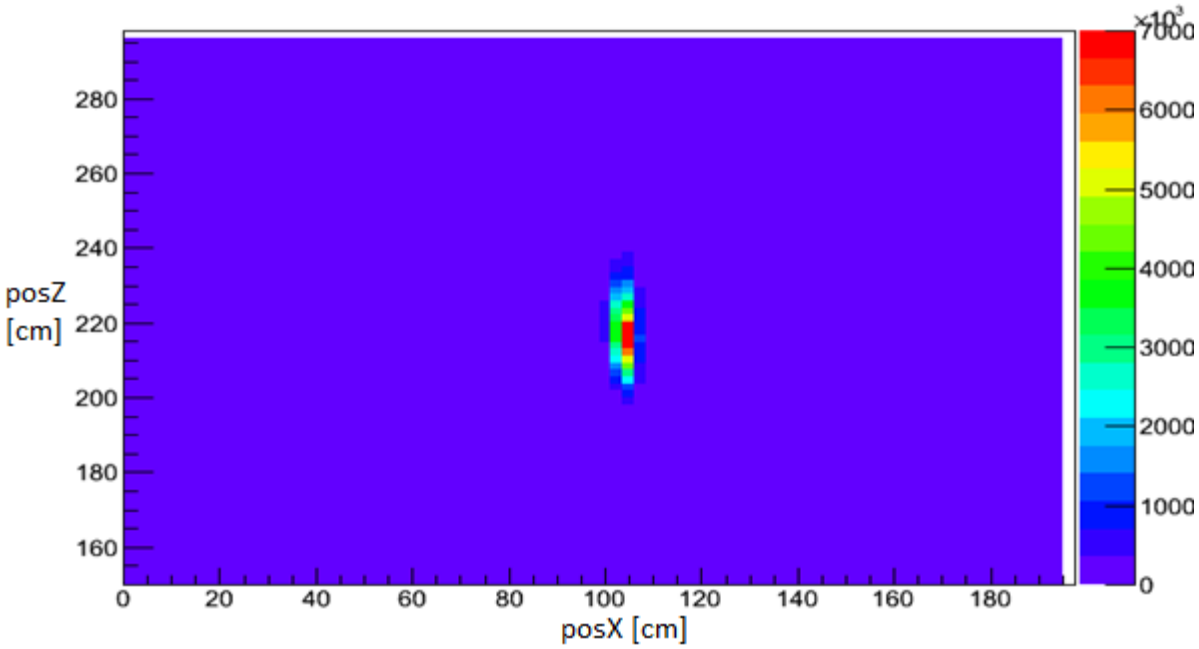

Figure 79. 50th iteration of a single source located at (105,220) reconstructed with a MLEM reconstruction with no voxel removal.

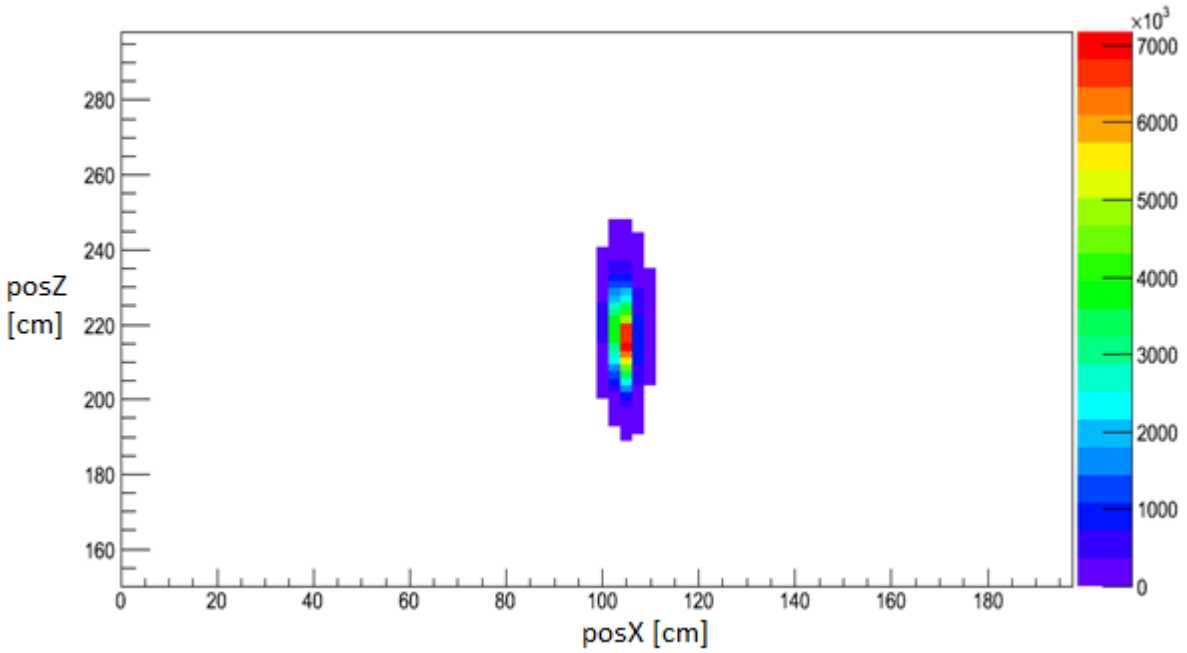

Figure 80. 50th iteration of a single source located at (105,220) reconstructed with a single-stage MLEM reconstruction with voxel removal.

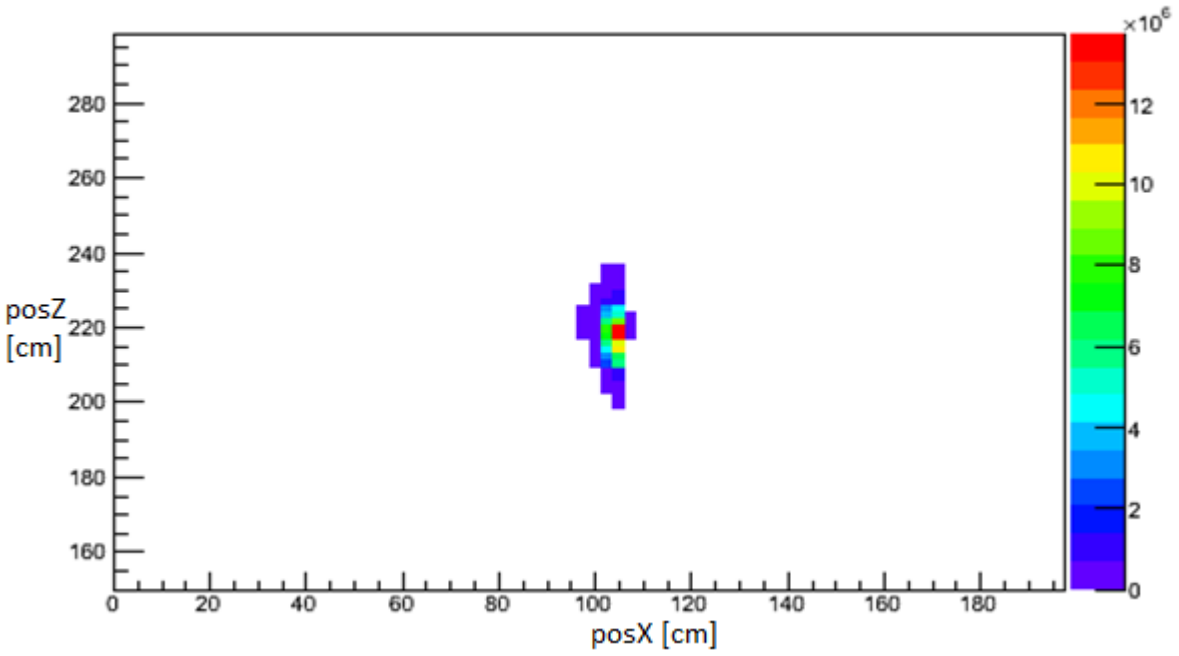

Figure 81. 50th iteration of a single source located at (105,220) reconstructed with a three-stage MLEM reconstruction with voxel removal.

Table 2. Reconstruction summary for MLEM reconstructions of simulated data

Reconstruction Type	Time
Single-stage, no voxel removal	133m24s
Single-stage, with voxel removal	71m39s
Three-stage, with voxel removal	7m33s

As expected, both iterations with voxel removal require less time to iterate than the single-step reconstruction without voxel removal and the source is localized in the same region in all three reconstruction techniques. This is expected when considering the reconstruction process itself, with initially a forward projection for each voxel, then iterating over each voxel for each source iteration. A multi-stage reconstruction with thresholding has to perform fewer calculations of the system response than a single-stage reconstruction, since at each stage the source distribution is constrained by a priori knowledge gained in previous stages, as well as iterating over fewer voxels during each iteration. The improvements in reconstruction speed for a single-stage reconstruction with voxel removal in comparison to a single-stage reconstruction without voxel removal only occur for later iterations, requiring the same number of forward projections as the reconstruction without voxel removal. Both iterations with thresholding reconstruct the source at higher resolution than the reconstruction without thresholding, demonstrating the effect of zero-intensity voxels being reconstructed as low-intensity voxels in the non-thresholding reconstruction. This improvement is particularly noticeable for the resolution on the distance axis, and negligible over the orthogonal axis of the reconstructed image. This is not surprising, since all of the reconstructions have very good x-axis resolution, constraining the source within two or three voxels.

4.5.1 Local Region Thresholding

A simple thresholding algorithm consists of conditionally forcing the voxel value to zero if the value is less than a threshold value. This treats voxels that potentially contain meaningful source information identically to voxels that are quickly determined to not contain source information. This may result in non-source voxels near the source being removed by the same criteria as voxels far from the source, resulting in an image such as Figure 82.

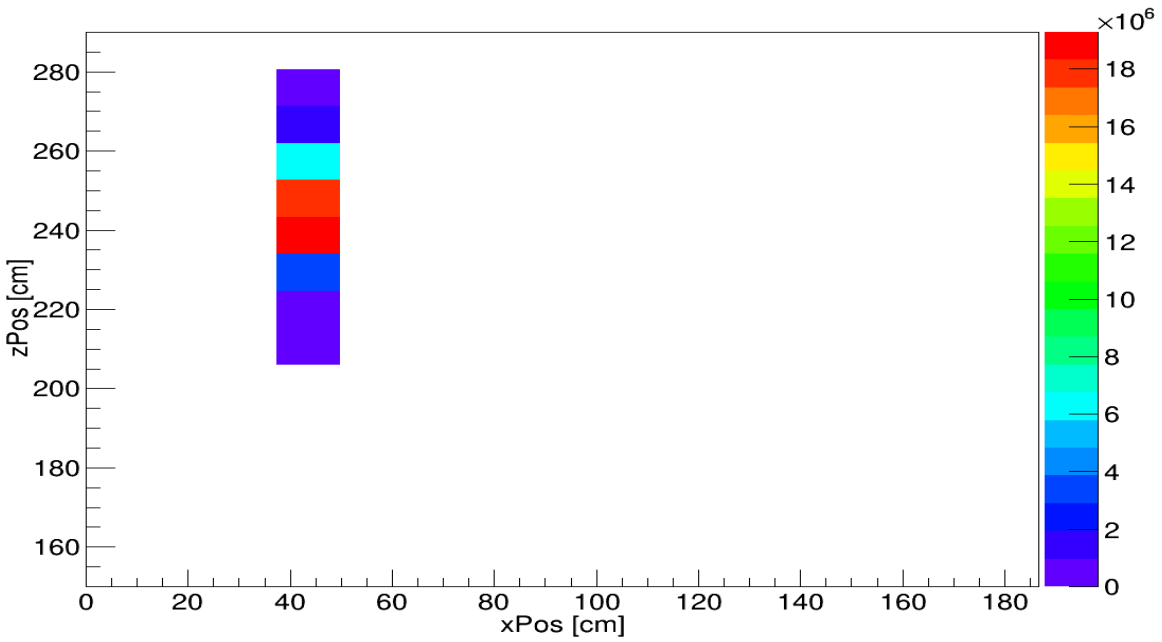

Figure 82. Reconstructed simulated source using a simple thresholding algorithm and a single stage reconstruction

While it is possible that the source truly is located within the few remaining voxels in Figure 82 the source may not be a point source and extend partially outside of one of the source voxels or another reconstruction error may occur. Using this as an initial source distribution estimate for a second stage in a multi-stage reconstruction may result in not reconstructing over meaningful

voxels. Modifying the thresholding algorithm prior to the final stage in the reconstruction to prevent misattributing potential source voxels consists of using information about the region of the voxel, in addition to the voxel value itself. For example, the middle voxel in Figure 83 does not meet the arbitrarily selected threshold value of 14.

0	18	21
0	5	22
0	0	13

Figure 83. Voxel values for demonstrating local region based thresholding.

Under a simple thresholding algorithm, the middle voxel would be forced to zero due to not meeting the threshold, despite being the voxel immediately adjacent to the highest value voxel in the image, and the physical space represented by the middle voxel may contain the source position. The 4-connected voxel region, which share at least one edge with the center voxel, contains two voxels that not only exceed the threshold value, but also exceed double the threshold value. If the conditional threshold were changed so that a pass consists of exceeding the threshold value or two of the 4-connected voxels exceed the threshold value, the middle voxel would be conserved. Requiring two 4-connected voxels does not conserve a voxel that is diagonally on the edge of a line bounding the source distribution. Were the local region of the voxel instead that of Figure 84, the middle voxel would not be conserved, despite being on the edge of a high value continuous region of voxels.

0	13	21
0	5	22
0	0	18

Figure 84. Voxel values for demonstrating local region based thresholding

Expanding the 4-connected region to an 8-connected region, where all voxels share either an edge or a corner with the middle voxel, the middle voxel of Figure 84 has three neighbors fulfilling the threshold condition. Extrapolating the 8-connected region to 3D, the equivalent connectivity region is a 26-connected region, and the 4-connected region in 2D is extrapolated to 6-connected region in 3D. Expanding the local region under consideration from a 4-connected region to an 8-connected region ensures that any voxels that represent local maxima in the reconstructed image are completely surrounded by voxels, such as in Figure 85.

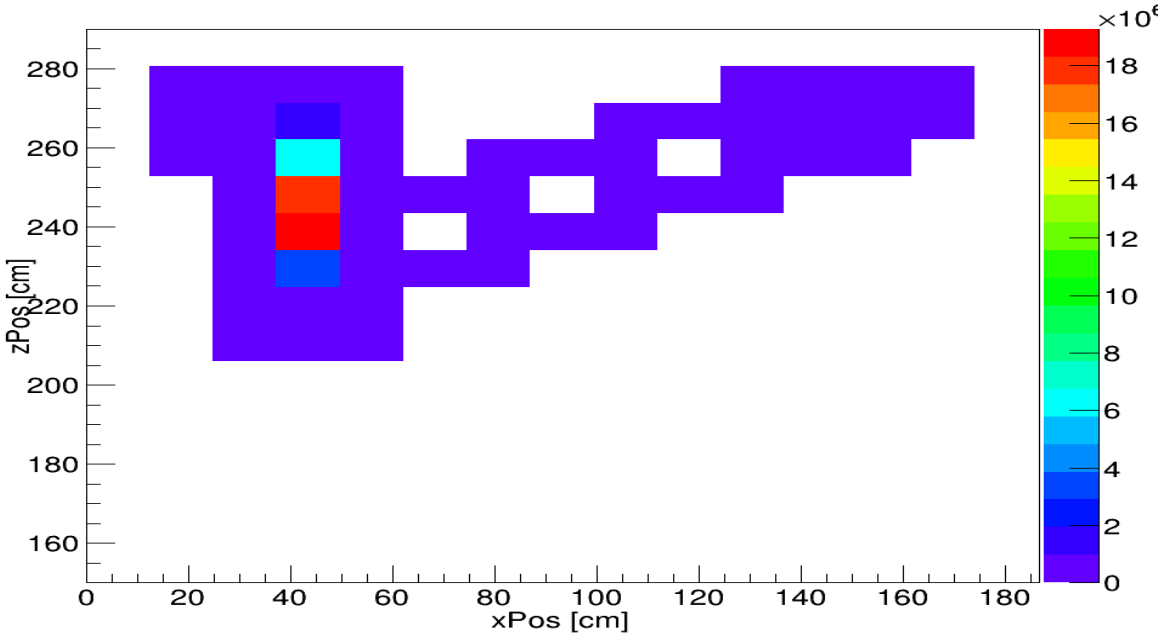

Figure 85. Reconstructed simulated source using an 8-neighbor thresholding algorithm and a single stage reconstruction

While the source in Figure 85 is located in the same region as the source in Figure 82, and is entirely surrounded by other voxels, a region of voxels extends outside of the source region throughout the entire image. This slows down the reconstruction process, since forward projections for each of the remaining voxels must be generated. When applying a simple threshold in the final stage of the reconstruction, however, these non-source voxels are removed and only voxels containing the source or near the source remain, as shown in Figure 86.

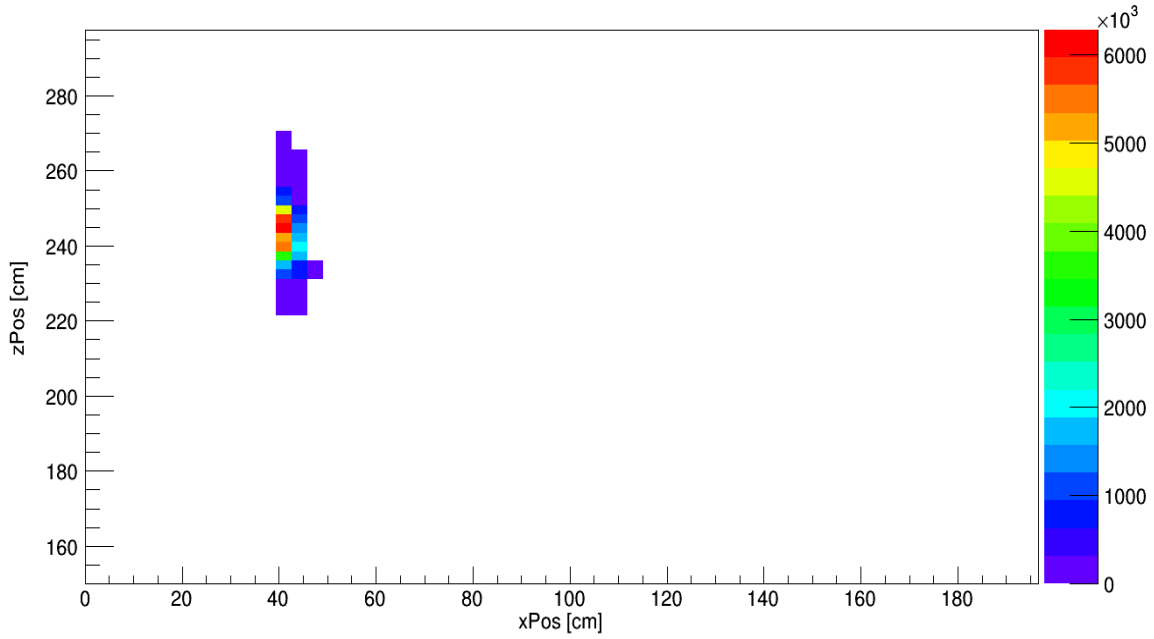

Figure 86. Reconstructed simulated source using an 8-neighbor thresholding algorithm and a three-stage reconstruction

4.6 Voxel Size

It is intuitive that small voxels provide a more accurate reconstruction than large voxels, but at the cost of increased computational time due to both the increased number of forward

projections that must be calculated and the number of voxels per iteration of the reconstruction. Excluding systematic effects due to the coded-aperture imaging technique, MLEM resolution is limited by the voxel size and the rate of convergence depends on the total number of voxels and the contrast in the forward projections between voxels, a small number of voxels may misattribute a single source to the wrong voxel, eliminating the true source voxel after thresholding, and converging to the wrong source position in the final stage of the reconstruction. In addition, since the true source position may not be located at the center of any particular voxel, the reduced chi-squared statistic may not reach a minimum indicating a perfect representation of the measured data, requiring more voxels for an accurate reconstruction.

A source was simulated using Geant4 at a distance of 250 cm, centered on -10 cm on the ordinate axis, with two measurement positions, the first position centered on 0 cm on the ordinate axis and the second at 40 cm on the ordinate axis, with a focal length of 50.5 cm. This data was reconstructed over possible distances ranging from 150 cm to 350 cm, and possible positions on the ordinate axis ranging from -20 cm to 100 cm. Reconstruction was performed with a three stage process, splitting after 400 iterations and again after 800 total iterations, and used a simple threshold of the mean voxel value. Multiple reconstructions were performed, with the total number of equal sized voxels for the first stage of the reconstruction equaling 16, 36, 64, 100, 225, 400, 625, and 1600, the results of which are shown in Figure 87, Figure 88, and Figure 89.

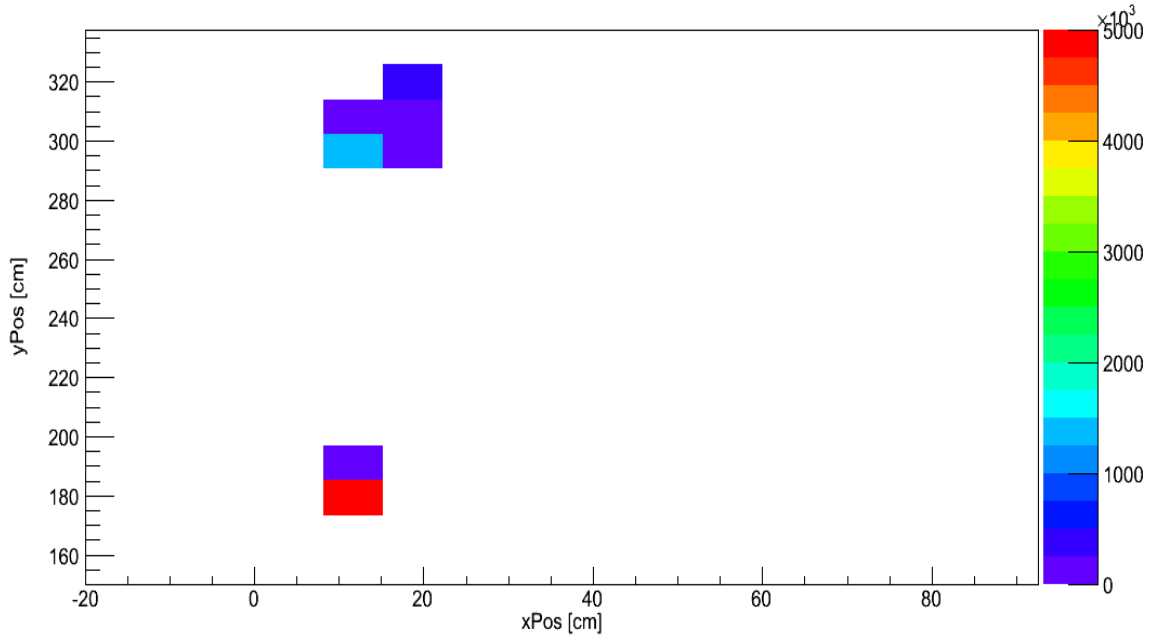

Figure 87. Reconstructed source distribution with an initial 4x4 voxel array, splitting into 8x8 after 400 iterations and 16x16 after 800 iterations.

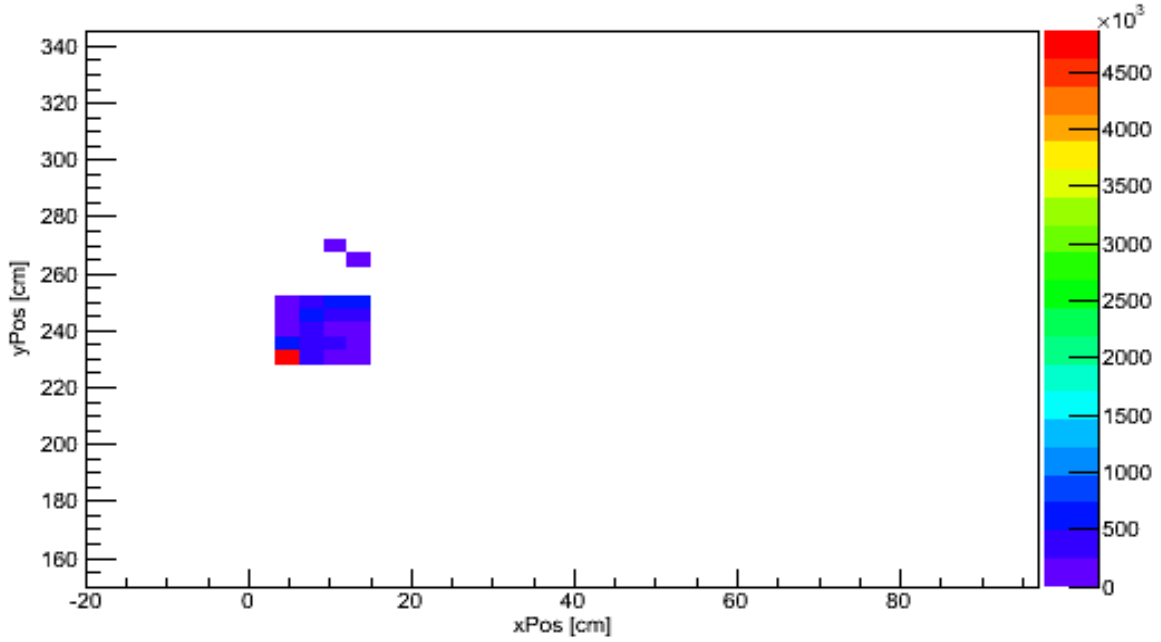

Figure 88. Reconstructed source distribution with an initial 10x10 voxel array, splitting into 20x20 after 400 iterations and 40x40 after 800 iterations.

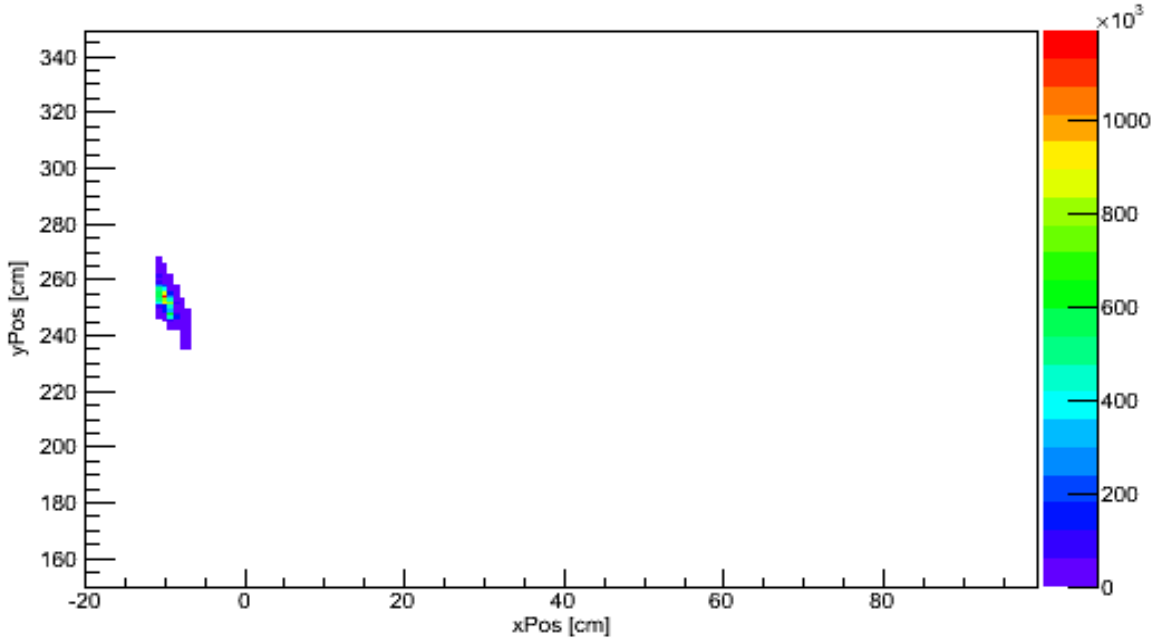

Figure 89. Reconstructed source distribution with an initial 40x40 voxel array, splitting into 80x80 after 400 iterations and 160x160 after 800 iterations.

It is logical that with increased number of voxels, reconstruction would more accurately reconstruct the source position. With a small number of voxels, and thus each voxel representing a large physical volume, the source is reconstructed to the wrong position, while for a larger number of voxels, the source is more accurately reconstructed to the proper position. Since it logically follows that increasing the number of voxels increases the number of necessary calculations and thus computational time, it is desirable to limit the number of voxels used in reconstruction. Quantifying the number of necessary voxels to reconstruct depends on the requirements of the measurement, the contrast between voxels in the system response model, and on the statistical accuracy of the measurement. Measurements requiring small voxel sizes, such as those separating closely spaced sources, require more voxels than measurements with less position-sensitive goals, so a more accurate reconstruction may be necessary.

4.7 MLEM Intensity

In addition to the position and resolution of a reconstructed source, the accuracy of the reconstructed source intensity is of interest, since quantification of plutonium mass requires quantification of the emission rate. Specifically, the reconstructed number of emissions should be consistent with the actual number of emissions. Considering the difference between a reconstruction without thresholding and one with thresholding: a thresholding MLEM reconstruction forces non-source locations to zero, and thus should more quickly reach a value that is consistent with the total number of emissions, and since non-source regions of the reconstructed source distribution are excluded, the reconstructed intensity should be more accurate than a non-thresholding reconstruction. For simulated data that has no statistical variance and an accurate response model used in the reconstruction process, one would expect the reconstructed intensity to match the true intensity after an infinite number of iterations over infinitely many infinitesimal voxels, but of interest is that the reconstructed intensity should be greater than the true intensity prior to reconstructing to the true intensity. This is because the reconstruction is biased to reconstruct sources at distances greater than the true source position, which is expected when considering the geometry of the projection process.

As the distance increases, the separation between the projections at given distances decreases, so the MLEM algorithm is slower to distinguish between source positions.

In order to distinguish between the reconstructed intensity of a thresholding MLEM reconstruction and a non-thresholding MLEM reconstruction, a reconstruction was performed of a statistically perfect projection from a source of 10^8 intensity. For the thresholding reconstruction, the source distribution was split into double the number of voxels in both the x and z axes after 50 iterations, and after the 100th iteration the split was performed again. The final 50 iterations of the thresholding reconstruction have the same voxel size and positions as the non-thresholding reconstruction.

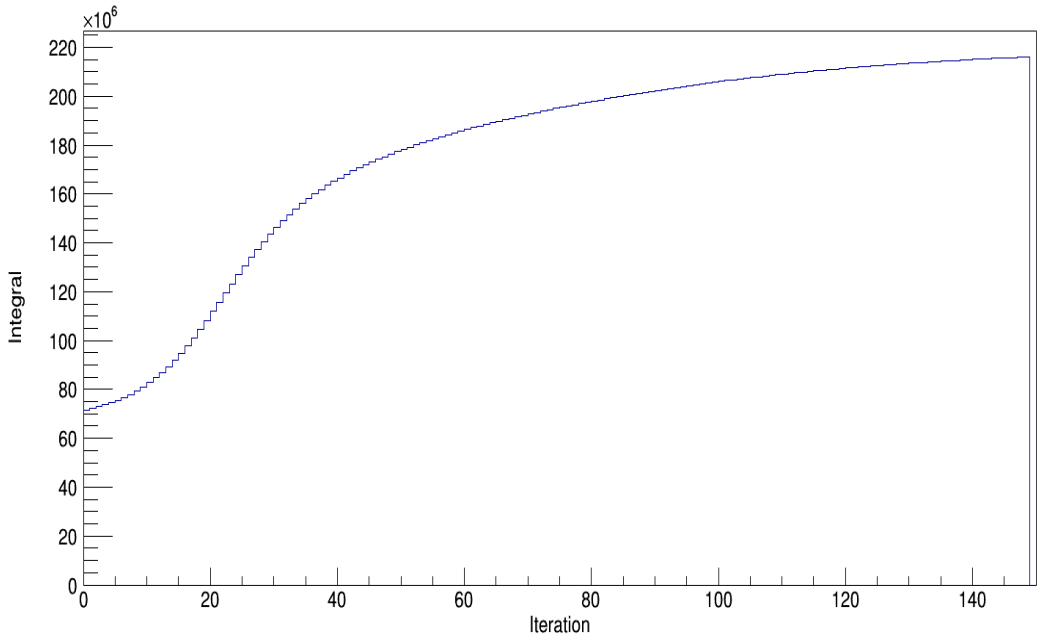

Figure 90. Reconstructed intensity for a non-thresholding MLEM reconstruction. Source intensity is 10^8.

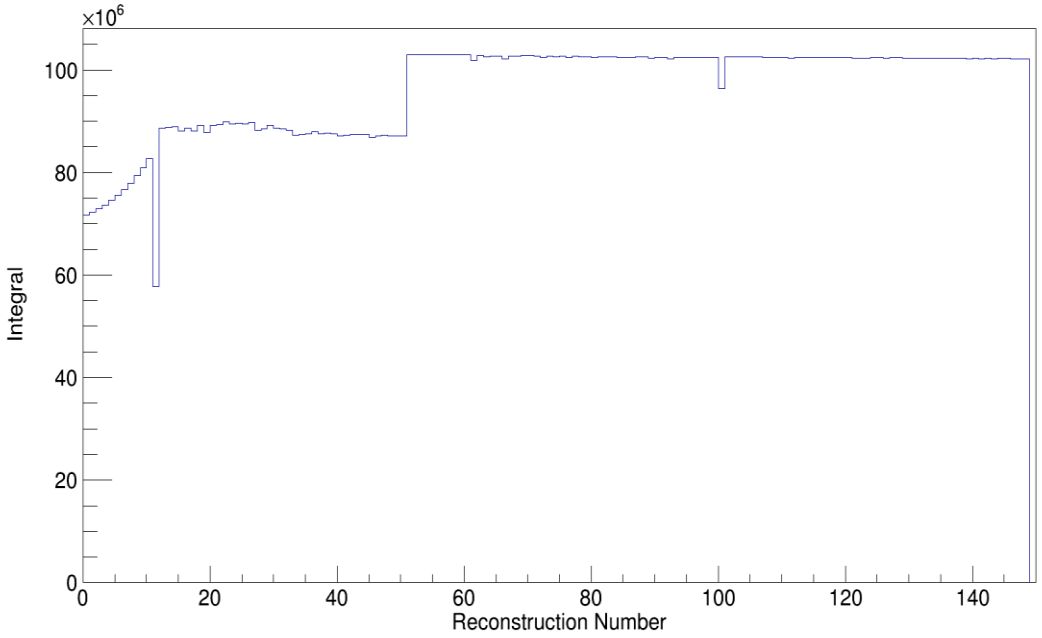

Figure 91. Reconstructed intensity for a thresholding MLEM reconstruction. Source intensity is 10^8.

The difference between the thresholding reconstruction and the non-thresholding reconstruction are clear from Figure 90 and Figure 91. The non-thresholding reconstruction converges to an intensity slower than the thresholding reconstruction, and does not reconstruct to an intensity near the true intensity. In contrast, the thresholding reconstruction reconstructs to an intensity near the true intensity after less than 80 iterations. This is expected, since by restricting the source distribution, the rate of convergence is increased, and non-source regions to not contribute to the total reconstructed intensity. The thresholding reconstruction does display structures that are not included in the non-thresholding reconstruction, notably sharp decreases after 10 and 110 iterations. These decreases, as well as the noise in otherwise flat iterations, can be attributed to the thresholding process itself, since voxels that do not meet the threshold value are forced to zero, and for one iteration those zero voxels are not accounted for. Interestingly, the first iterations in the thresholding reconstruction, prior to the expansion of the number of source voxels, appears to reconstruct a source at 15% lower intensity than the true intensity. Given that the non-thresholding reconstruction converges to an intensity greater than the true intensity, the first iterations likely reconstruct with too large a voxel size and insufficient number of voxels. Since all the projected source is contained within a single voxel, this is not a problem for this reconstruction, but a more complex source distribution, or potentially even a reconstruction that is not statistically perfect could erroneously remove voxels that contain meaningful source radiation, requiring more initial voxels.

Determining whether or not a MLEM reconstruction with thresholding provided a more accurate estimate of source intensity than a reconstruction without thresholding consisted of a single source from a known position. To determine whether or not a thresholding MLEM was consistent with simulated data over multiple source positions or whether the selected position was unique, projected data from multiple source positions was reconstructed, each position with the same 10^8 total number of emissions, and the relative error between the reconstructed intensity and the true intensity was recorded.

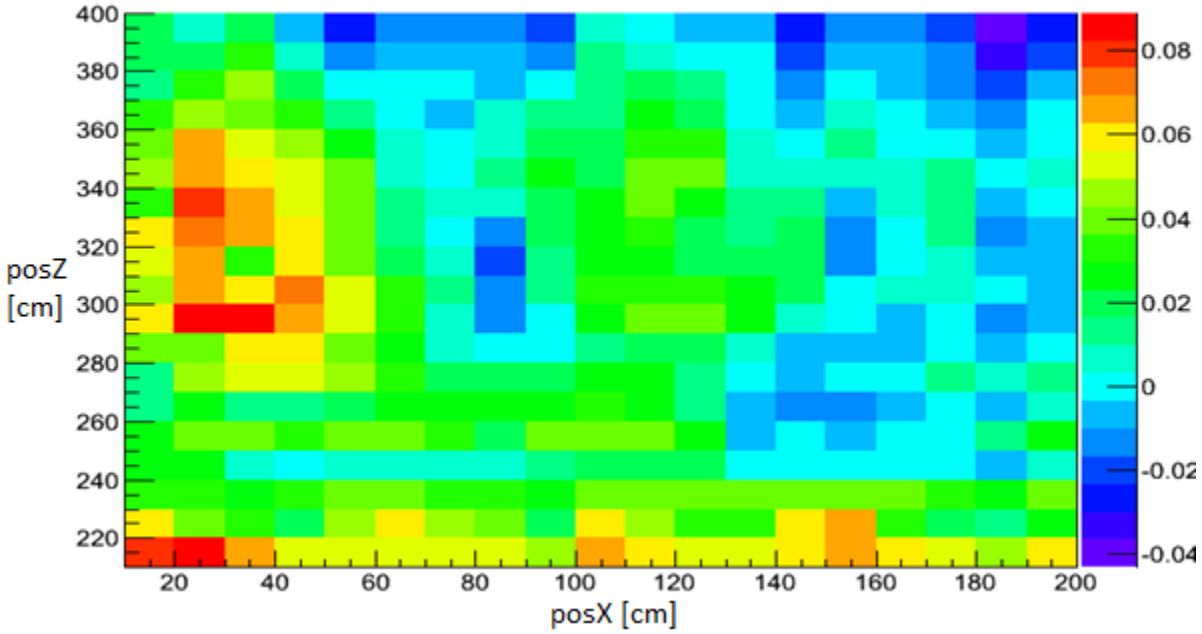

Figure 92. Relative deviation in intensity for source located at the center of a voxel.

For a range from 200 cm – 400 cm in the distance axis, and 0 cm – 200 cm on the x axis, the reconstructed source intensity is within 10% error versus the total source intensity. The first pixel in the first detector is at 0 cm, and each detector is moved 56 cm, so the range of source positions selected includes the entire field of view of detector position, transitioning from first within only the field of view of the leftmost detector position, transitioning to only within the field of view of the detector position furthest along the x-axis. The variation dependent on source position does have some structure to it, and is biased to overestimate the source intensity. While the bias can be attributed to the limited distance resolution of the imaging system reconstructing behind the source position more than in front of the true source position, the structure in the x-axis is likely due to the source only partially projecting a mask pattern onto a detector at a specific position, with a relative decrease in accuracy due to the system model chosen assuming mask moderator elements outside the mask pattern. The most accurate reconstruction position is between 60 cm and 100 cm, which corresponds to the region that is within the field of view of all three detector positions. The reconstruction would be expected to be more accurate at positions within the field of view of each detector, since the measured data has meaningful information for all detector pixels. This makes sense from the coded aperture concept, since imaging without a mask would only differentiate pixels based on geometric efficiency, which is a negligible difference between pixels at a given detector position.

4.8 Multiple Sources

In contrast to a single source measurement, imaging multiple sources adds complexity requiring analysis of the reconstructed image. In the thresholding reconstruction of a single source or sufficiently separated sources, non-source voxels are zero, and a source position and intensity can be easily determined by integrating continuous non-zero voxels. In contrast, complex reconstructed images need some ability to distinguish between a source and background and between individual sources, such as the reconstructed image in Figure 93.

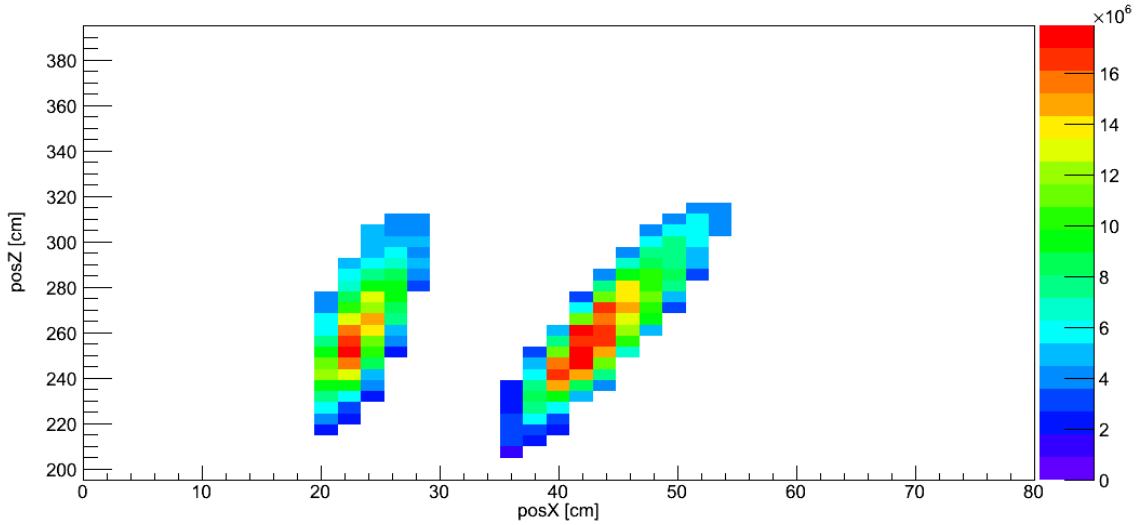

Figure 93. MLEM reconstruction of two simulated sources, one located at (45,250) and the other at (25,250) with an average value threshold.

While Figure 93 is a relatively simple two-source image with clear separation between the two sources and clear reconstruction of the sources with no attribution of source radiation to non-source voxels, techniques that can determine the presence of both sources in this image and independently determine their intensity and position can also be applied to reconstructed images with background, as well as images with less separation between sources. The main challenge of individually quantifying each source in an image is determining which regions of the image can be determined to be dominated by each source. This is analogous to performing signal detection in a 1D distribution, since a peak in an image can be expressed as a local maximum or minimum sitting atop of a non-uniform background. The derivative of this distribution in background regions, were there non-source background regions, would be of random value, but relatively low magnitude. In contrast, the derivative in the region of the source would be high magnitude approaching the peak, with zero magnitude at the peak itself, as shown in Figure 94.

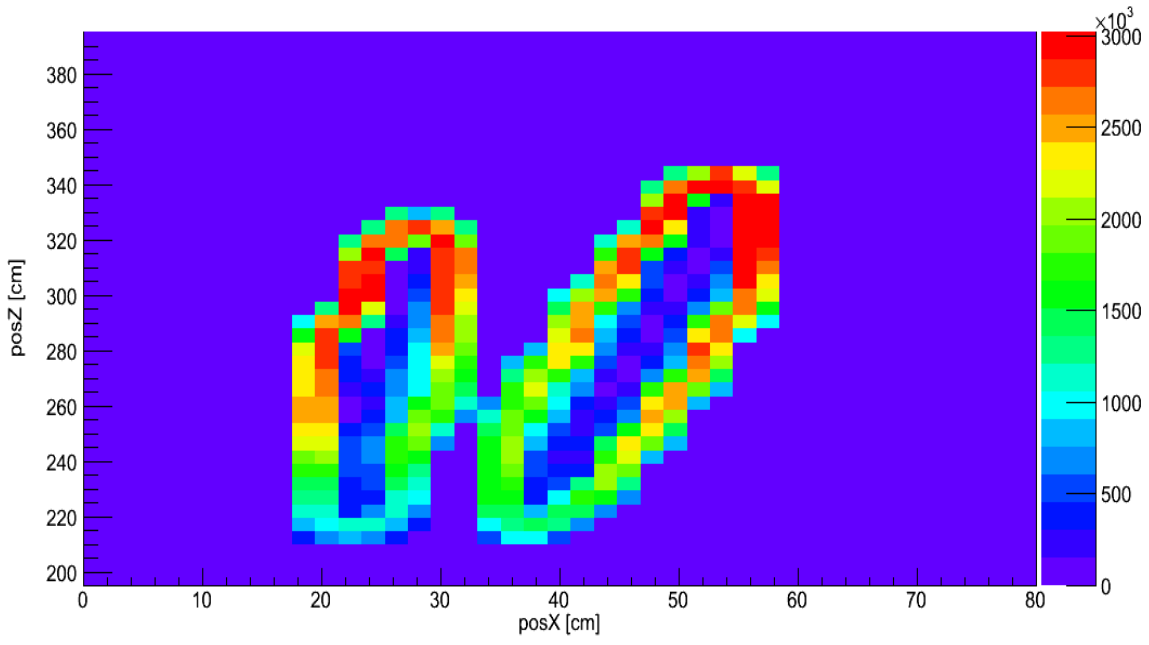

Figure 94. Gradient of MLEM reconstruction of two simulated sources, one located at (45,250) and the other at (25,250) with an average value threshold.

Sources in the gradient image are not represented by a single high intensity pixel or elevated region, but by the depressed gradient surrounded by high value regions. By performing a flood fill starting from source centers, the two sources can be segmented from the gradient and categorized into individual sources, as shown in Figure 95.

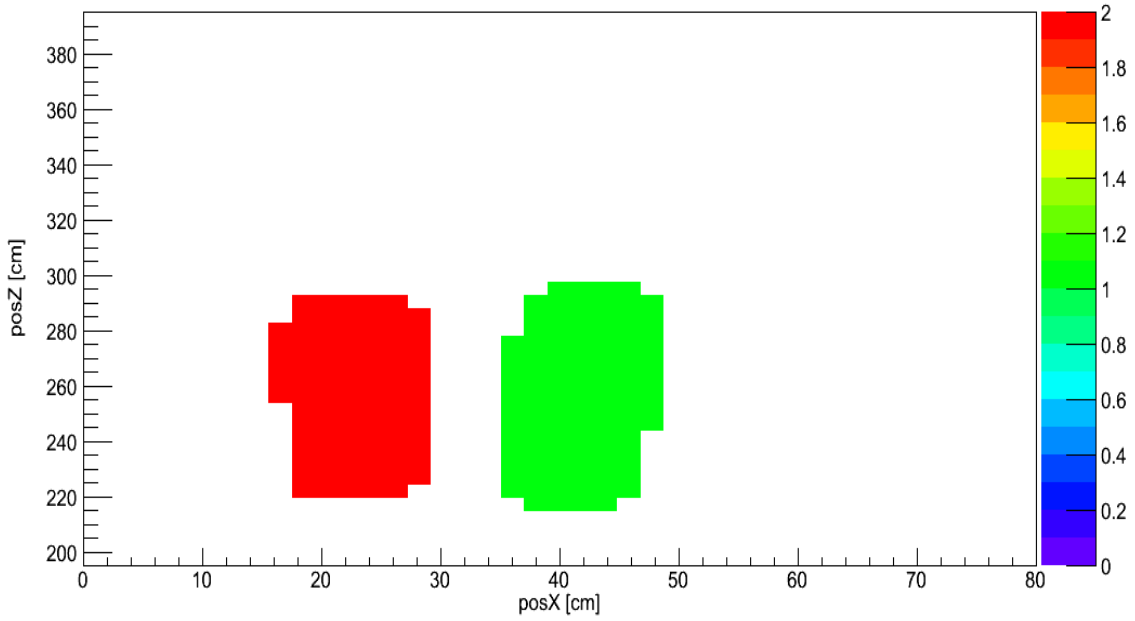

Figure 95. Source objects created from flood fill of gradient image in Figure 94.

The values of non-zero regions in Figure 95 are radically different than the values of non-zero regions in both the gradient image and the source reconstruction itself. That is because Figure 95 is a mapping of individual voxels in the reconstruction to individual sources. From this, it is

trivial to limit the reconstructed source distribution to an individual source for quantification, as shown in Figure 96.

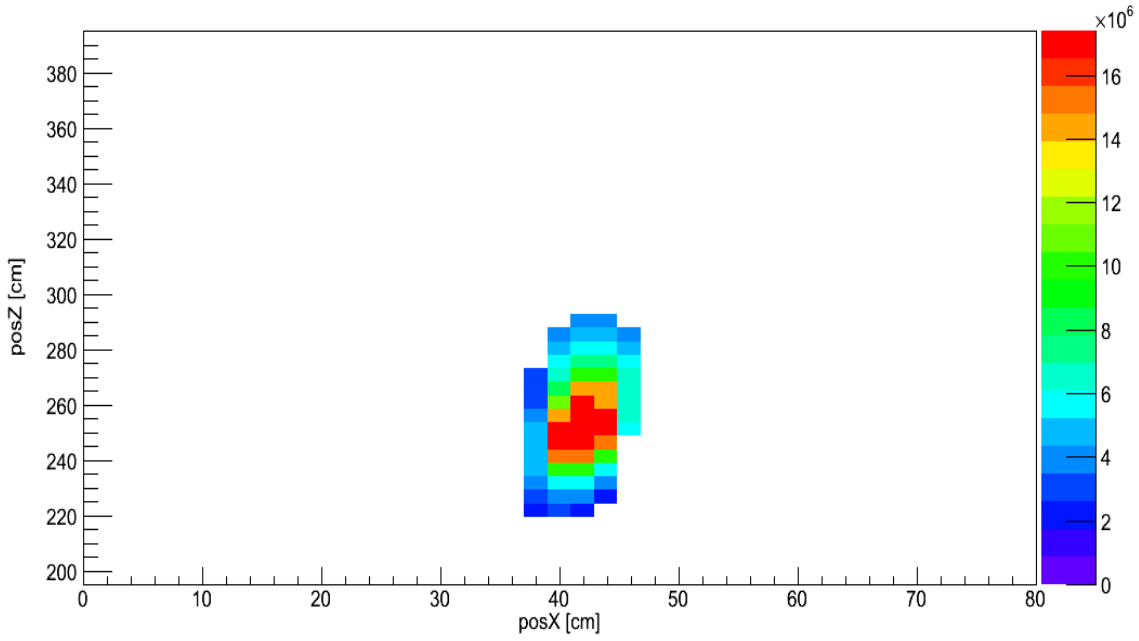

Figure 96. Reconstructed voxels in Figure 93, limited to voxels contained within source 1.

With only a single source reconstructed in an image, it is trivial to quantify the source intensity since the total number of emissions is simply the integral of each individual source's reconstructed image. This does not remove the need to reconstruct the entire source distribution simultaneously, but simplifies the selection of individual regions of the reconstructed source distribution as containing individual sources, and the quantification of those individual sources. The use of an automated source quantification process removes the

need for operator selection of individual sources, and removes that as a potential source of error in reconstructed estimates of source position and intensity.

4.9 Imager Selection

Since the MLEM technique and expected deviations from the assumptions made for ideal image reconstruction are based on common traits either inherent to the coded aperture imaging technique itself or common detector design characteristics between the 24x24 pixel imager and the 40x40 pixel imager, it is expected that both imagers would have comparable results imaging the same source distribution. Slight differences in both final result and the behavior of the reconstruction process itself are expected, in part due to the larger size of the 40x40 imager and the higher angular resolution of the 40x40 imager. Reconstructions of measurements by the 40x40 imager would be anticipated to make longer to perform, since the number of measured pixels is larger. To compare the reconstructions of the 40x40 imager and the 24x24 imager and determine whether the modeled imagers were consistent with each other, a simulated 5E7 emission source, including statistical variation within each detector pixel, was reconstructed using a three-stage MLEM reconstruction with thresholding. 500 iterations of each stage were reconstructed, with a threshold value of the mean value in each voxel, including zero intensity voxels.

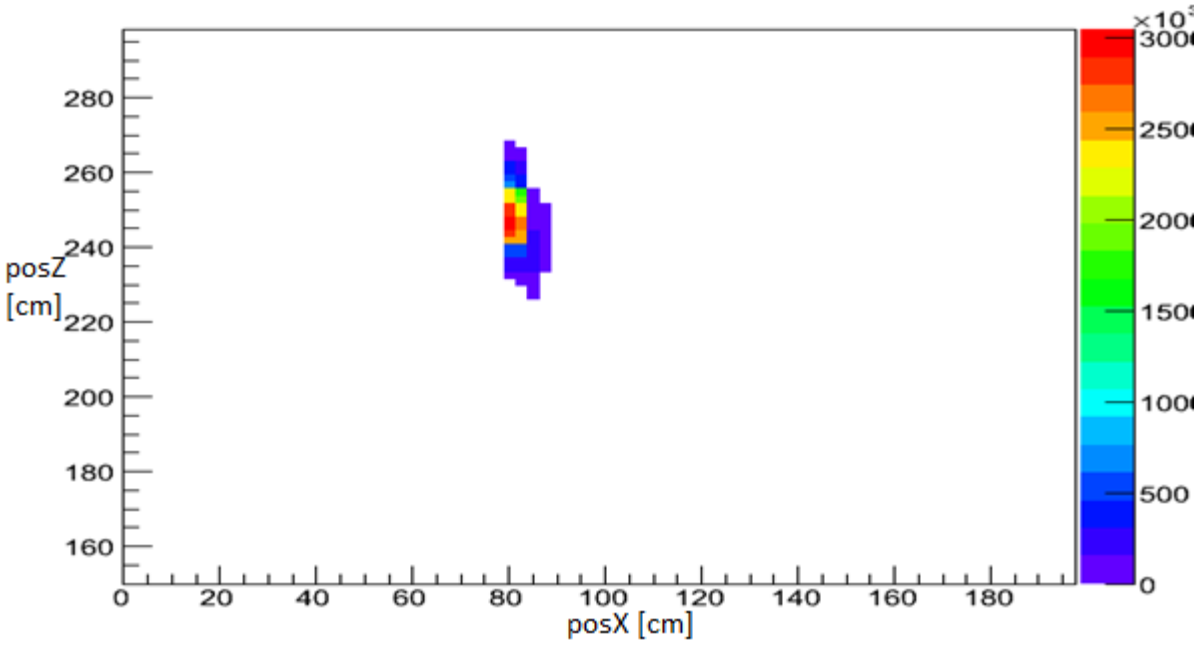

Figure 97. MLEM Reconstruction of simulated single source incident on 24x24 pixel imager.

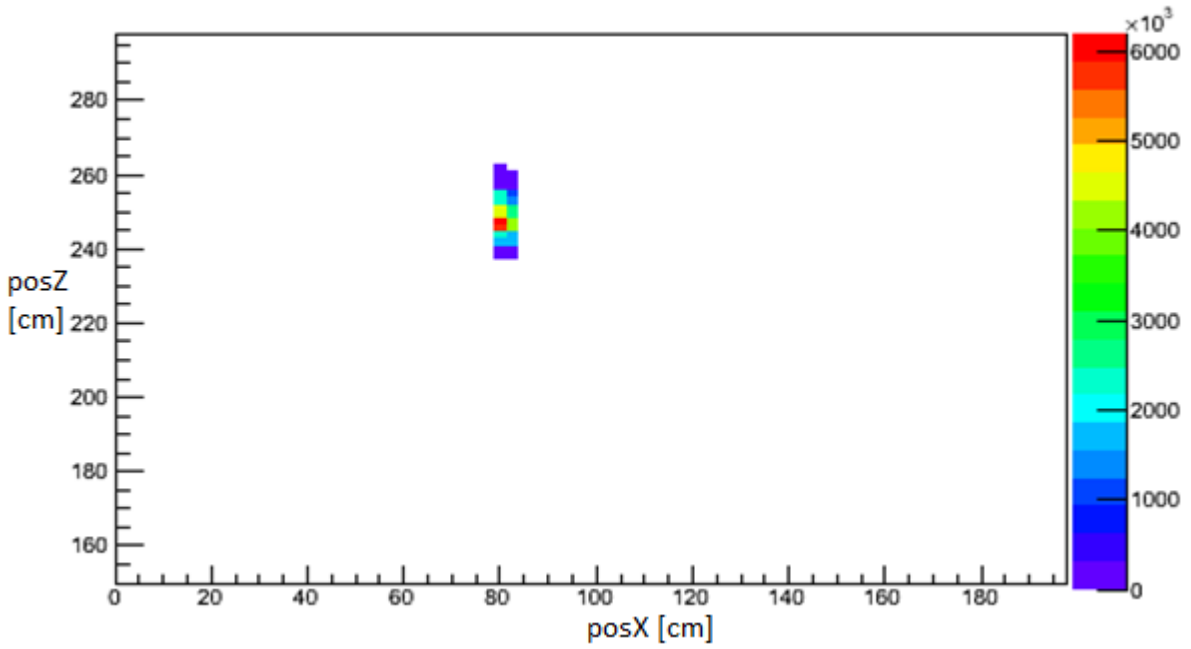

Figure 98. MLEM Reconstruction of simulated single source incident on 40x40 pixel imager.

The simulated source is reconstructed by both detectors at the same position on the x-axis, and while they are reconstructed at different positions on the distance axis, both reconstructions are consistent with the true source position (250 cm). The 40x40 pixel imager reconstructs the source within a smaller area than the 24x24 pixel imager, likely due to the improved angular resolution. While the 24x24 pixel imager reconstructs the source within 2% of the true intensity (4.90E7), the 40x40 pixel imager reconstructs the source more accurately (4.93E7), the difference in reconstructed intensity are within 0.5%, well within the statistical error of a single pixel, with the minimum pixel of the 40x40 pixel imager having a value of 25.

Chapter 5 Source Quantification

Real sources provide statistical uncertainty in the measurement, involving the detection of both neutrons and gamma-rays, as well as the simultaneous detection of neutrons from both the source and any background sources of radiation, resulting in uncertainty in the reconstruction in addition to any systematic effects. In addition, simultaneous quantification of multiple sources requires analysis more complex than simply integrating the reconstructed source distribution.

5.1 Single Source Reconstruction

Reconstruction and quantification of sources relies on the projected data incident on the detector, and the poor distance resolution of cross-correlation reconstruction without any additional measurement designs is shared by MLEM reconstruction. To demonstrate this, a measurement of a single 3.706 μCi source, equivalent to the neutron emission rate of 0.0071 S.Q. of Pu, was measured for 90 min with no second detector position (described in Measurement 1 of Appendix B) was reconstructed using both a cross-correlation reconstruction (Figure 99) and a MLEM reconstruction consisting of 1000 iterations with a threshold equal to the average voxel value.

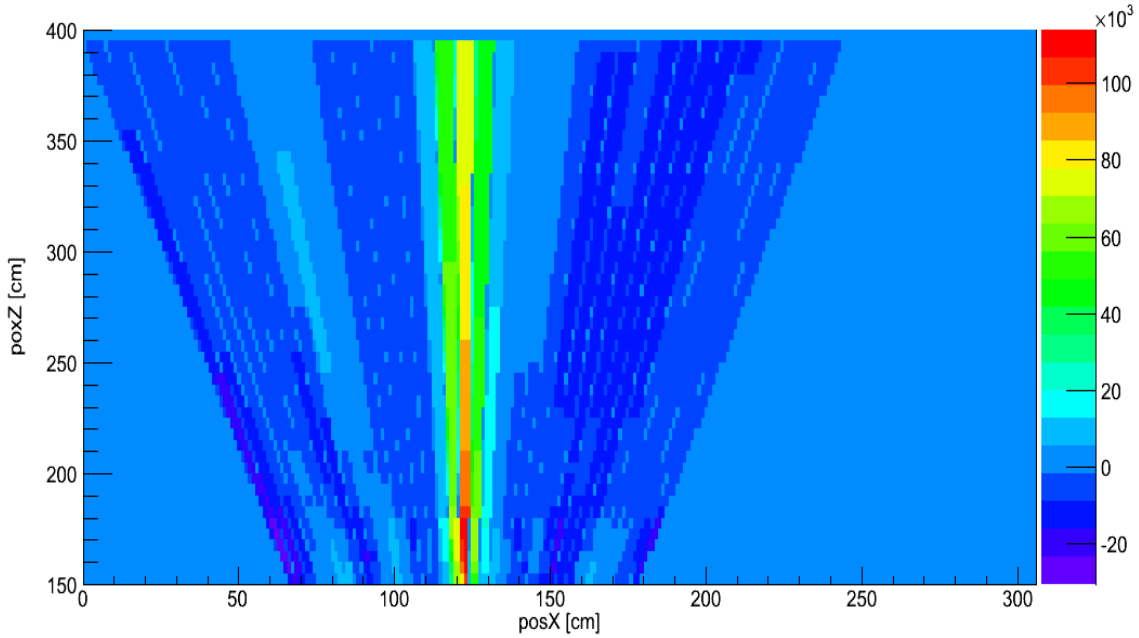

Figure 99. Cross-correlation reconstruction of data from Appendix B, Measurement 1.

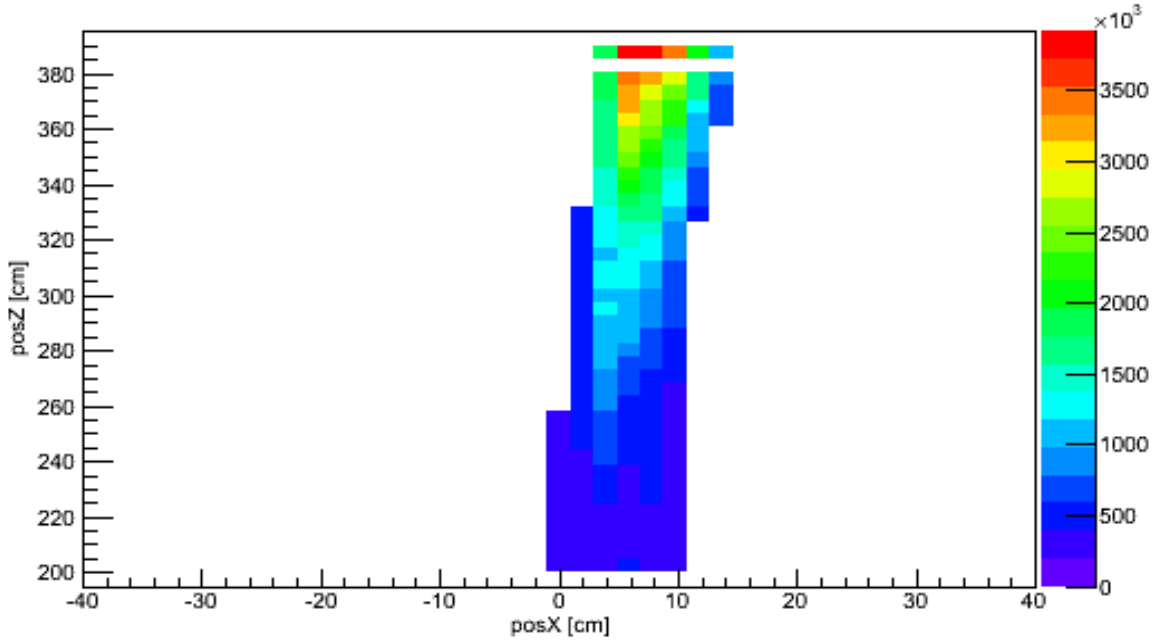

Figure 100. MLEM reconstruction of 1000 iterations with an average voxel threshold of data from Appendix B, Measurement 1.

The immediate similarities between the cross-correlation reconstruction and MLEM reconstruction is that they both reconstruct the single source on a one-dimensional axis, both failing to reconstruct the source at the true distance of 260 cm with poor distance resolution in comparison to the angular resolution (FWHM > 50 cm and 10 cm, respectively) Differences are also apparent, such as the position on the orthogonal axis differing, which is due to the differences in origin definition between the reconstruction processes, as well as the different distances to the maximum bin between the two reconstructions. Due to this, the source is reconstructed with an intensity of 2.05×10^8 emissions, in contrast to the total number of emissions at 8.58×10^7. This increase over the true emission rate is not unexpected, since with the poor localization of the source position on the distance axis results in it being located at an increased distance once the reconstructed source voxel contributions to measured data is converted to source intensity. As discussed in previous sections, poor distance resolution in comparison to angular distribution from a single measurement position is inherent to the coded aperture technique itself. With the use of the parallax imaging technique, distance resolution and accuracy of the estimated source position in the reconstructed image is improved over a single measurement position in both the MLEM and cross-correlation reconstruction techniques.

5.1.1 Distance Variation

Neglecting any effects of dead time in the detector, measurements of a single source are only affected by the source position, intensity, background radiation, and any statistical or systematic effects of the MLEM reconstruction process. Using P40, a measurement of a single 74 µCi Cf-252 point source, equivalent to 0.14 S.Q. of Pu at 28% Pu-240 content, was performed for 90 min for both a mask and anti-mask measurement. The measurement was repeated after moving the source 56 cm on the orthogonal axis of the detector to perform a parallax measurement. The source was placed at a distance of 200 cm from the mask, at a distance of 5 cm on the orthogonal axis, and 44 cm mask to detector distance. The imaging measurement was repeated for source distances of 220 cm, 260 cm, 300 cm, and 340 cm.

For the reconstruction of each source position, 50 voxels covering a total range of 160 cm on the orthogonal axis and 25 voxels covering a range of 120 cm on the distance axis were used, with the system response model developed in Section Chapter 3 used as the system model. The thresholding technique developed in Section 4.5.1 was used with a threshold value equal to the mean value of an image voxel. The total number of neutrons emitted for each measurement was 1.66×10^9. The reconstruction of 200 cm is shown in Figure 101, 220 cm in Figure 102, 260 cm in Figure 103, 300 cm in Figure 104, and 340 cm in Figure 105.

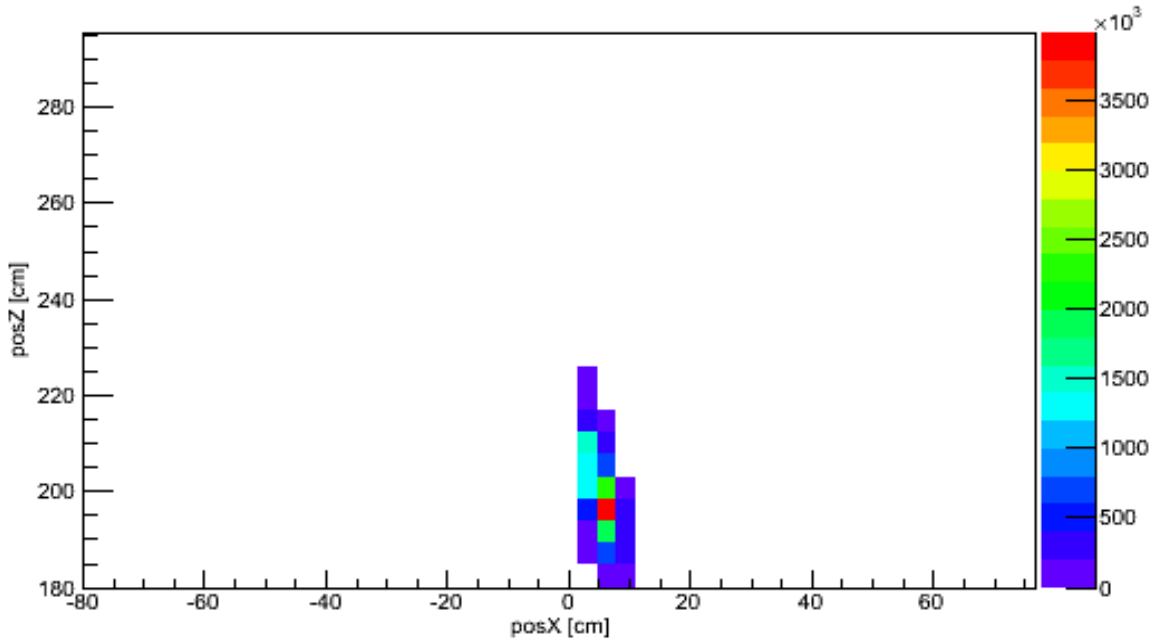

Figure 101. Reconstruction of 90 minute measurement of 74 µCi Cf-252 source located at 5 cm on the orthogonal axis at a distance of 200 cm.

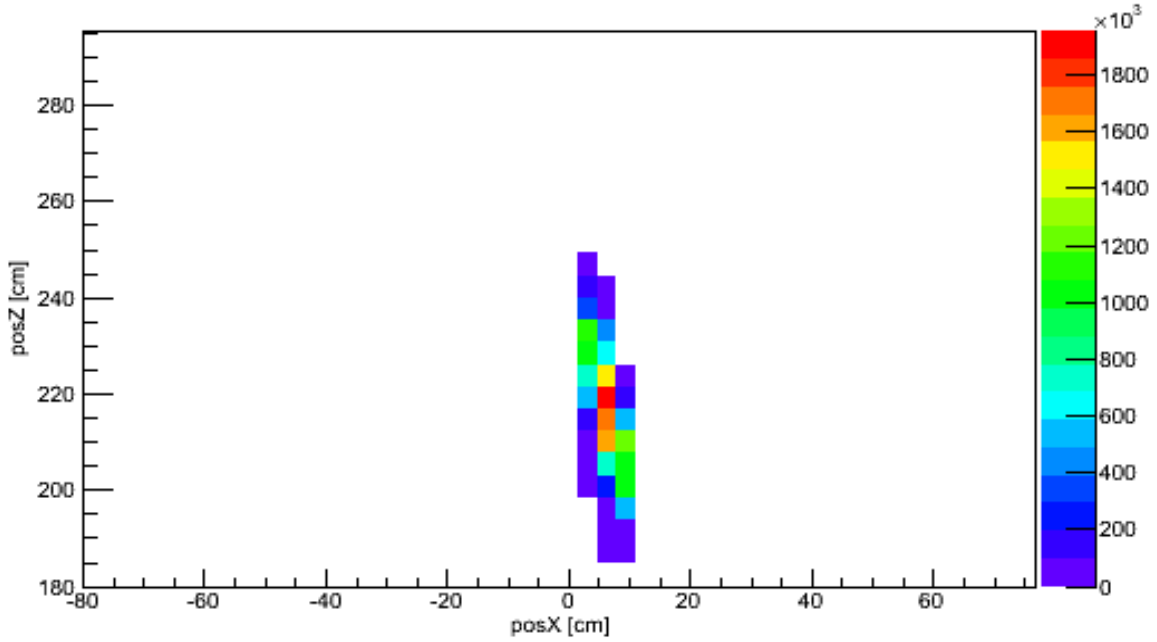

Figure 102. Reconstruction of 90 minute measurement of 74 µCi Cf-252 source located at 5 cm on the orthogonal axis at a distance of 220 cm.

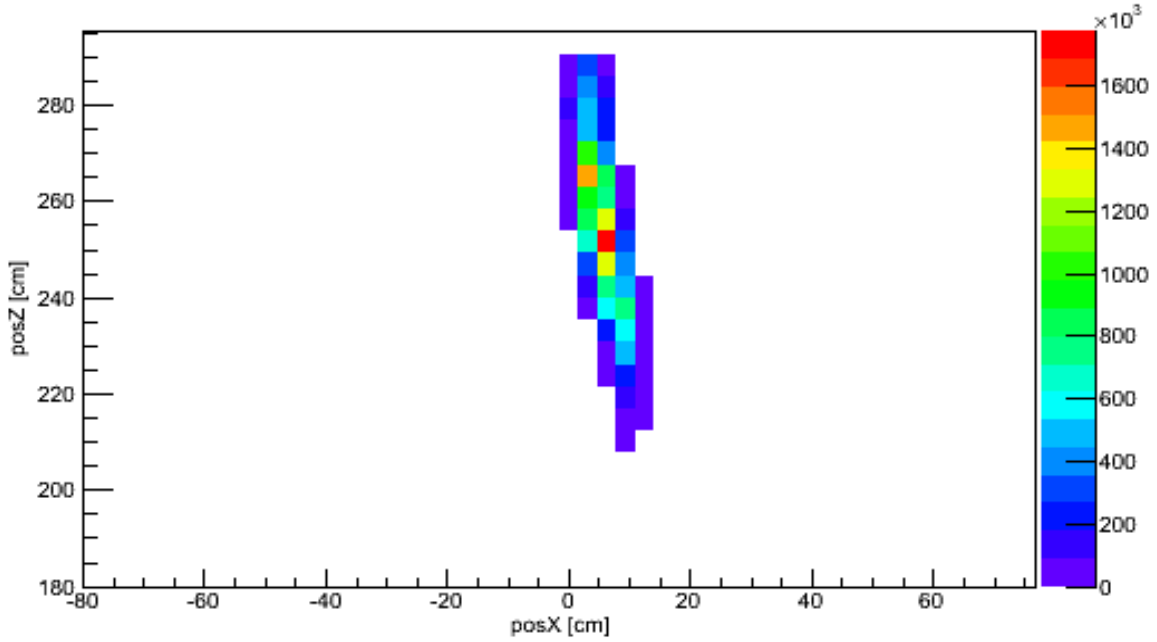

Figure 103. Reconstruction of 90 minute measurement of 74 µCi Cf-252 source located at 5 cm on the orthogonal axis at a distance of 260 cm.

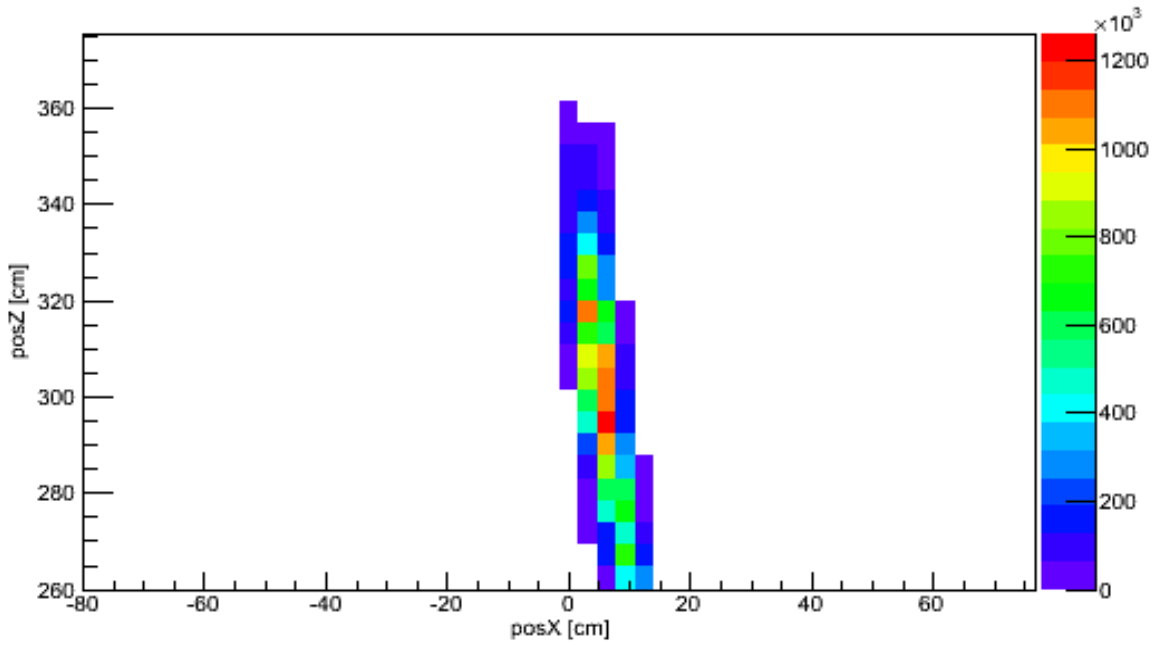

Figure 104. Reconstruction of 90 minute measurement of 74 µCi Cf-252 source located at 5 cm on the orthogonal axis at a distance of 300 cm.

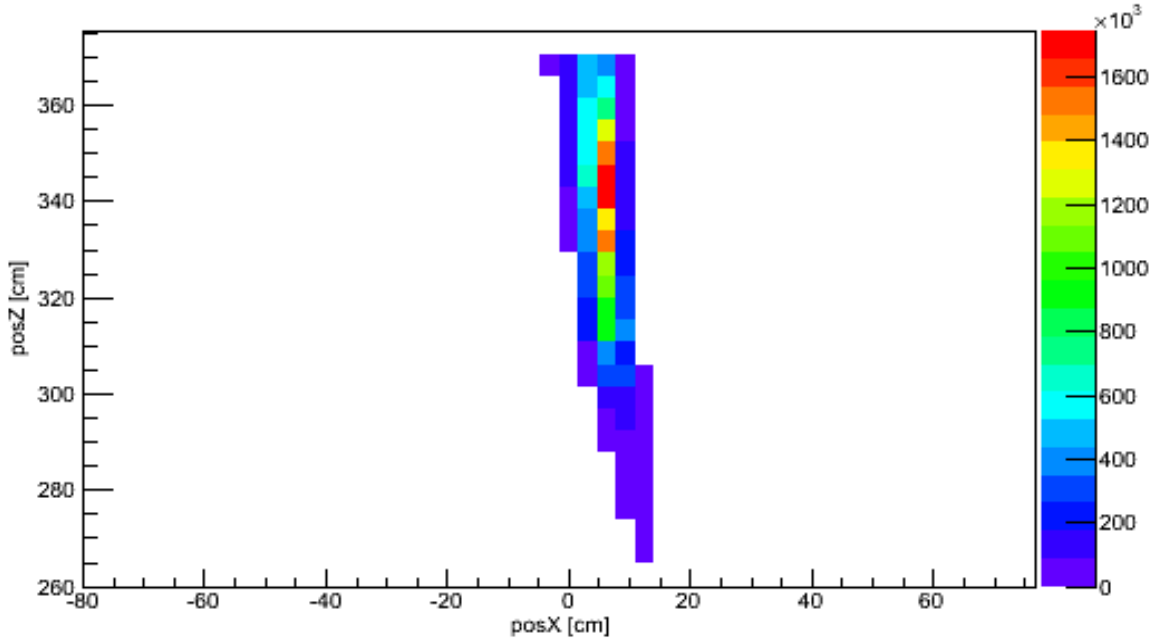

Figure 105. Reconstruction of 90 minute measurement of 74 µCi Cf-252 source located at 5 cm on the orthogonal axis at a distance of 340 cm.

Each measurement reconstructs the source in the correct position on the orthogonal axis, but the behavior of the reconstructions differ on the distance axis. At a true source distance of 200 cm, the source is reconstructed at 195 on the distance axis, which is within 2% of the true position, in addition to being only a single voxel offset from the true source position, with a FWHM of 10 cm, indicating that the true source position was contained within one standard deviation of the reconstructed source position. At 340 cm, the source is reconstructed at a peak location of 340 cm, which is consistent with the true source position, but with a FWHM of 42.5 cm. While this may be indicative of the need for more iterations in the MLEM algorithm, poor resolution on the distance axis may be more indicative of the high statistical and systematic noise in the measured data, a mask orientation of the first detector position is shown in Figure 106.

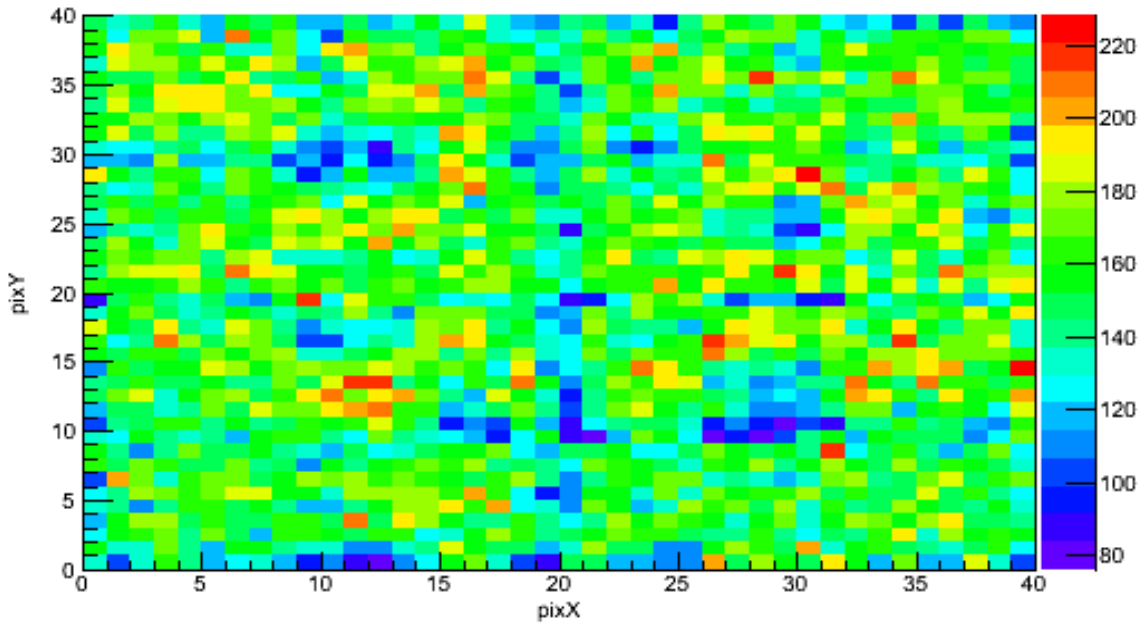

Figure 106. Measured data for mask orientation of 90 min measurement of 74 µCi Cf-252 source located at 5 cm on the orthogonal axis at a distance of 340 cm.

After 90 minutes, regions of the measured detector data representative of mask transmission elements (26-32 x, 26-32 y) have an average of 170 counts, while regions representative of mask moderator elements (8-14 x, 26-32 y) have an average of 110 counts. While the separation between these two regions is certainly > 2σ, the relatively low number of counts in each pixel and thus high statistical uncertainty makes for a poor reconstruction, since the reconstruction is dependent on small changes in the overall projected distribution. At a much closer distance, however, there is more structure apparent in the measured data, as shown in Figure 107, which is the measured data from 200 cm of the same mask orientation and position on the orthogonal axis as Figure 93.

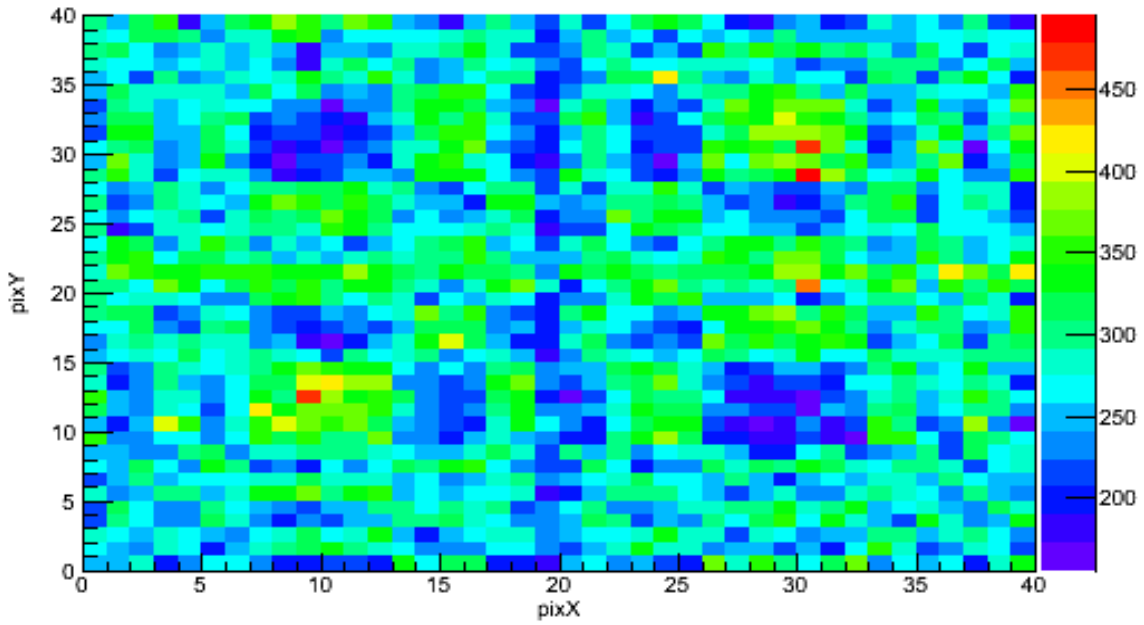

Figure 107. Measured data for mask orientation of 90 minute measurement of 74 µCi Cf-252 source located at 5 cm on the orthogonal axis at a distance of 200 cm.

In comparison to the measured data from 340 cm, the number of counts in each detector pixel is higher at 200 cm, which is attributable to the $1/r^2$ relationship between distance and

geometric efficiency. Due to this increased number of counts, structures in the measured data separated by low percentages become apparent, and the MLEM method results in a more precise reconstruction, as shown by the FWHM of 10 cm (2 voxels) at 200 cm, and 42.5 cm (10 voxels) at 340 cm. Since estimates of source intensity depend on the estimate of source position due to the $1/r^2$ relationship between geometric efficiency and distance, it intuitively follows that source quantification of either weak sources or sources at increased distances require longer measurements than strong sources or sources at close distances for a fixed accuracy of the measurement. This is born out in the intensity reconstructed, with the measurement at 200 cm reconstructing the source at 1.74×10^9 emissions, 220 cm at 1.76×10^9 emissions, 260 cm at 1.67×10^9 emissions, 300 cm at 1.70×10^9 emissions, and 340 cm at 1.51×10^9 emissions. While distances at 300 cm and below reconstruct the source within 3% of the true intensity, at 340 cm the intensity reconstructed is only within 12% of the true intensity. For the 340 cm measurement, the maximum pixel value was only 240 counts, while the minimum value pixels contained less than 100 counts. For a 90 minute measurement, this low counting rate results in a low source-to-background rate than at 200 cm, and background radiation detected is attributed to the source, falsely increasing the reconstructed source intensity.

5.2 Multiple Source Quantification

One of the challenges of measuring multiple sources is that the signal encoded by the detector is independently encoded, and in image reconstruction the contribution from each source is simultaneously extracted from the measured data. Two 11.1 μCi Cf-252 point sources at a distance of 165 cm were measured for 90 minutes each mask orientation and detector position, and reconstructed using the MLEM reconstruction technique and complex system response model. The reconstructed source intensity distribution is shown in Figure 108.

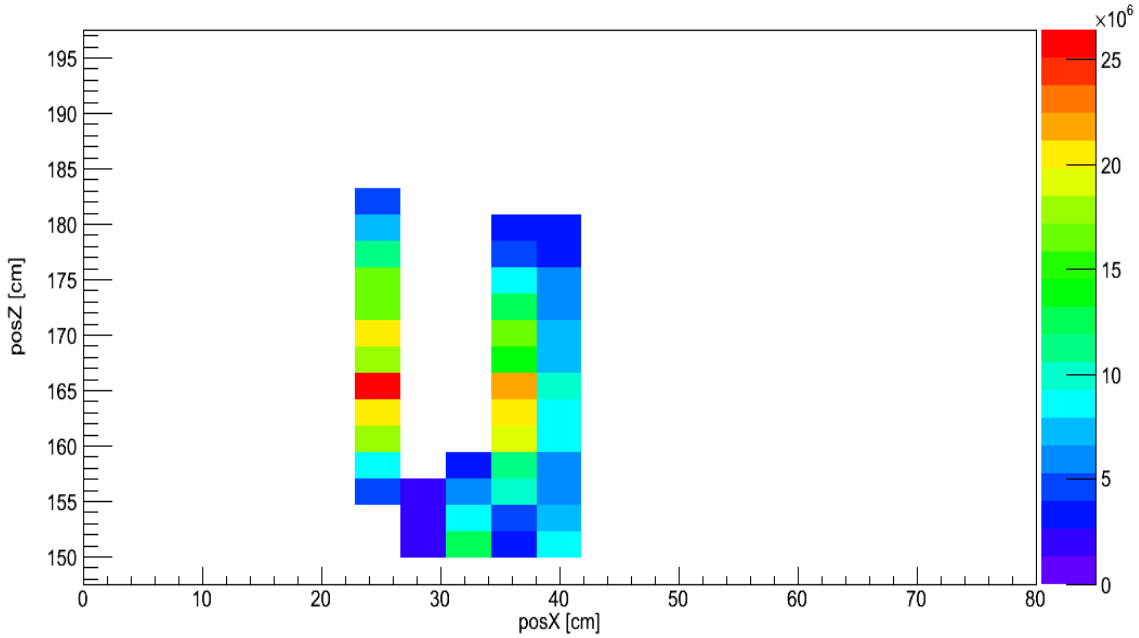

Figure 108. MLEM Reconstruction of two 11.1 µCi Cf-252 point sources, one at (22.8,165), the other at (33.8,165) from 90 minute measurements with a shift between measurements on the orthogonal axis of 69 cm.

One of the weaknesses of Figure 108 is that the second source is reconstructed at the wrong distance on the orthogonal axis, despite both sources being properly reconstructed on the distance axis. Both sources are well constrained on the orthogonal axis, with FWHM's at most the size of a single voxel, and with comparable FWHM's on the distance axis of 7 cm and 12 cm for the source reconstructed at 25 cm on the orthogonal axis and 37 cm, respectively. Two sources are reconstructed, with the source at 25 cm reconstructed with an intensity of 1.81 x 10^8 emissions and the source reconstructed at 37 cm reconstructed with an intensity of 2.68 x 10^8 emissions. In comparison to the true rate of 2.57 x 10^8 total emissions (0.0074 significant quantities of Pu), the source at a position of 25 cm underestimates the true intensity by 29%, and the source at 37 cm overestimates the true intensity by 4%. The number of counts in an average pixel that can be attributed to a single source is 84.5 counts, corresponding to a statistical error of 10.1%. Because of this, the source at 37 cm is well characterized by the MLEM reconstruction, but the source at 25 cm is underestimated. This may be due to the low statistical accuracy of the measurement attributing source counts to the source at 37 cm that belong at 25 cm, and with a more intense source both sources would have been accurately resolved. A more intense source would be more preferable to increased measurement time, since at 90 minutes per mask orientation the total measurement time needed to generate Figure 108 is 6 hours, increasing the measurement time is impractical.

In measurements with low detector dead time and low background radiation rates, radiation from each source is independently counted by the detector, and the sum of measurements of single sources is equal to the simultaneous measurement of multiple sources at the same positions as single sources. In addition to the consideration where sources are separated on the orthogonal axis, but not on the distance axis, identical positions on the orthogonal axis but different positions on the distance axis provides a situation where at one measurement position both sources are located on the same imaging axis. Using data from measurements discussed in Section 5.1.1, data from a measurement of a 74 μCi Cf-252 point source at a distance 200 cm and a 74 μCi Cf-252 point source at a distance of 300 cm were combined to represent data generated by measuring two 74 μCi Cf-252 point sources, one at each distance,

which was reconstructed using a MLEM reconstruction with the system response model developed in Chapter 3, the results of which are shown in Figure 109.

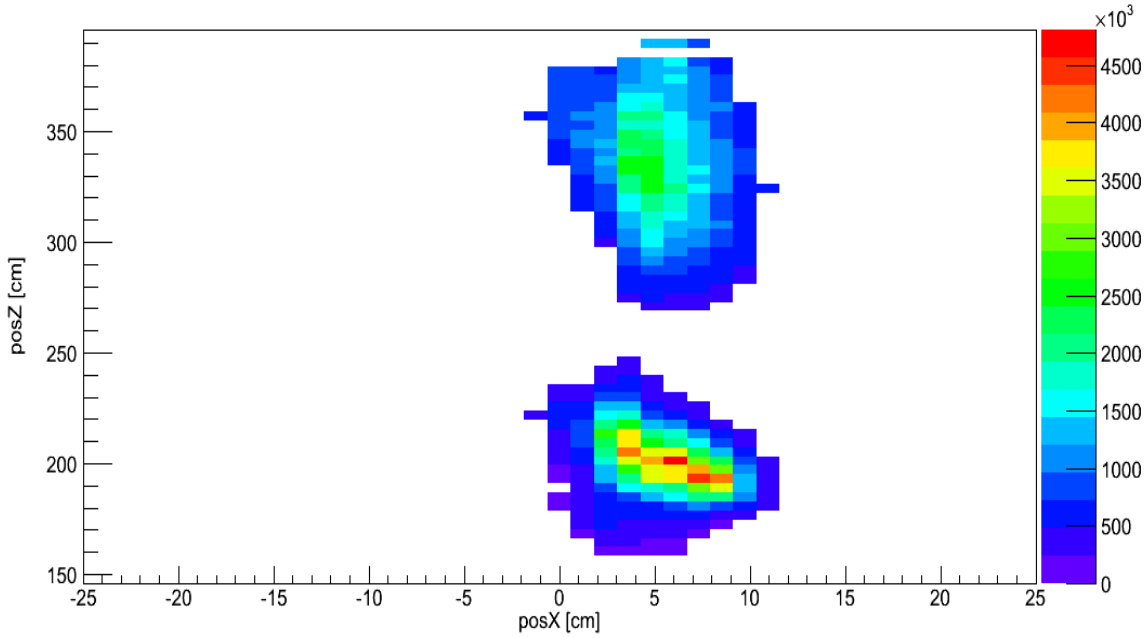

Figure 109. MLEM reconstruction of two 74 µCi Cf-252 point sources, one at (5,200), the other at (5,300), with a mean value threshold and splitting after 1500 iterations.

While both sources are reconstructed within a single FWHM of the true position (5 cm) on the orthogonal axis, the region bounded by the FWHM of the source at a distance of 200 cm is centered on 200 cm with a FWHM of 36 cm, and the source at 300 cm is centered at 340 cm with a FWHM of 40 cm. While the FHWM of both sources does contain the true source position, the source at 200 cm is reconstructed with a more accurate and precise distribution than at 300 cm. With a perfect reconstruction, the total number of emissions would be 3.42×10^9, equally shared by the two sources. This does not occur in the multi-source reconstruction, with the source at 200 cm being reconstructed at an intensity of 2.67×10^9 emissions (156% of the true rate) and the source at 300 cm reconstructed at 1.01×10^9 emissions (61% of the true rate), with the total number of emissions being overestimated by 7.3%, attributed to the source at 300 cm being reconstructed extending beyond the true 300 cm distance. This is in contrast to the reconstruction of each source from data representing individual measurements, with both sources being reconstructed within 3% of the true intensity.

Part of the difference between the reconstructions of measurements of each source individually and multi-source measurements can be attributed to imperfect angular resolution of the coded aperture technique, while part can be attributed to the poor distance resolution of coded aperture imaging from a single measurement position. Only a single detector position is able to distinguish between the two sources, and because of imperfect angular resolution, the separation between the two sources in the data is limited. Since most of the measured counts in both sets of detector data can be attributed to the nearest source, the reconstructed source distributions are biased towards the nearest source. The imperfect angular resolution of the second measurement position is insufficient to completely counter this nearest source bias, but is sufficient in allowing some reconstruction of the second source.

Chapter 6 Conclusions And Future Work

A system response model for use in coded aperture, parallax-based imaging has been designed, used, and tested with a modified MLEM reconstruction algorithm that allows for accurate quantification of source distribution and intensity. The system response model incorporates mask transmission, mask scattering, a heterogeneous detector pixel array, scattering within the mask, and scattering within the detector, allowing for the expected detector data from a single source position to be rapidly generated. From the development of this model and the reconstruction technique, a number of conclusions can be drawn, and avenues for further research are apparent.

6.1 Conclusions

While cross-correlation reconstruction is capable of reconstructing a source distribution from measured data without the influence of measured data that is outside of the imaging field of view, cross-correlation-based reconstruction is limited in its distance resolution, and cross-correlation-based reconstruction inherently assumes a two-valued, infinitely thin mask with a homogenous detector array. For quantification of fast-neutron sources, these assumptions are invalid, and the subtraction of anti-mask data from mask data in cross-correlation-based reconstruction results in the removal of meaningful source information.

In order to enable imaging with both angular and distance resolution, the parallax imaging measurement technique, consisting of imaging from multiple detector positions, is proposed and reconstructed with cross-correlation reconstruction and MLEM reconstruction. Since coded aperture imaging from a single detector position has much better angular resolution than it does distance resolution, imaging from multiple detector positions enables the estimate of distance resolution for a set of measurements to be dominated by the angular resolution of the imager, rather than the distance resolution of the imager. When combining multiple measurement positions with the parallax imaging technique while reconstructing using the cross-correlation reconstruction technique, each measurement position is treated independently. This results in reconstruction artifacts if a source is on the edge of or outside of the field of view. Additionally, the apparent source may be extended in front of and behind the

true source position. These artifacts may obscure the true source position and limit the resolution of the reconstruction.

Reconstructing with a MLEM reconstruction technique, however, allows for the simultaneous reconstruction of multiple measurement positions and the use of a system response model that accurately reflects the physics involved in fast-neutron coded aperture imaging. This reconstruction technique iterates over each detector pixel for each potential source position. In this work, the traditional MLEM technique is modified to isolate the reconstructed source intensity distribution to only the positions potentially containing the source distribution through using both a simple thresholding technique and a thresholding technique that accounts for the behavior of the local region. In addition, a threshold is applied to reconstructions where the source is spread out over multiple voxels, improving the estimate of the source position distribution and allowing for an increase in reconstruction speed.

System model development accounts for major systematic effects, such as mask transmission, a heterogeneous detector array, mask scattering, and scattering within the detector. While mask transmission and a heterogeneous detector is modeled by modifying a ray-tracing model, scattering in the mask is more complex, requiring a Monte Carlo simulation and, thus, orders of magnitude more computational time than a ray-tracing model. To save time, scattering is accounted for by precomputing a transfer function created using two Monte Carlo simulations. One simulation accounts for mask scattering in the direction of the detector; the other removes scattered neutrons from the distribution of neutrons incident on the detector. Then a pointwise transformation is applied on the system model data based on this generated transfer function. Accounting for scattering within the detector in the system response model consists of creating a detector response to an incident neutron. This system model was capable of producing projected detector data in less than a second on an Intel® Core™ i7-2640M CPU @ 2.8GHz, compared to a timescale of hours for a Geant4 simulation on the same machine, with a reduced chi-squared value of 0.55 between the system model projected data and Geant4 simulated data, in the case of reconstruction a Cf-252 source that emits for 7.61×10^8 neutrons from a distance of 255 cm.

The MLEM reconstruction iterates over every source voxel, requiring a forward projection for each source voxel, and each source voxel contributes to all other voxels in each iteration. Since non-source voxels approach a small but positive intensity estimate during repeated iterations of the MLEM reconstruction, this results in reconstructing over non-meaningful voxels, and, at the same time, non-meaningful voxels contribute to the reconstruction of meaningful voxels. Even with the use of a simplified system response model, creating a forward projection for each source voxel is still computationally expensive (in comparison to iterating over a source voxel in the MLEM reconstruction), so it is desirable to minimize the number of forward projections that must be created. In this work, it was found that by thresholding each source voxel after a set number of iterations, non-source voxels were eliminated and, thus, did not negatively contribute to later iterations. Furthermore, by splitting the reconstructed voxels after a set number of iterations, the number of voxels that needed to be reconstructed was minimized.

The MLEM method incorporating a modified system response model was used to reconstruct measured Cf-252 sources of varying intensity and location. In the measured dataset, sources were positioned as single sources or as multiple sources in the imager's field-of-view. To demonstrate the need for the parallax imaging measurement technique, a single source equivalent to 0.0071 S.Q. of Pu was measured from a single detector position for 90 min, at a source to detector distance of 260 cm. This source could not be accurately localized in either angle or distance by either the cross-correlation or the MLEM reconstruction technique. A single 74 μCi Cf-252 point source, equivalent to 0.14 S.Q. of Pu at 28% Pu-240 content, was imaged, demonstrating the capability of the parallax imaging technique, with a distance between measurement positions of 56 cm, and reconstructed using both the cross-correlation and MLEM reconstruction technique. The distance to the source varied over repeated measurements, including 200 cm, 220 cm, 260 cm, 300 cm, and 340 cm. The MLEM reconstruction reconstructed the source within 2% of the true source position on the distance axis, and it reconstructed the intensity within 3% at a distance of 200 cm, or within 12% at a distance at 340 cm for 90 minutes per mask orientation at two detector positions.

Measurements of multiple sources were performed, as well as reconstructions of summed single source measurements to represent the difficult case of multiple sources in less favorable radiation background conditions. Data measured in the single source measurements with sources located at 200 cm and at 300 cm were combined and reconstructed using the MLEM reconstruction technique. The source at 200 cm was well localized well within one FWHM of the true position, while the source at 300 cm was barely within one FWHM of the true source position. While the total integrated emissions from the combined sources were reconstructed accurately, the intensity of the source at 200 cm was estimated at 156% of the true emission rate and the source at 300 cm was estimated at 61% of the true emission rate, despite the reconstruction of the sources from individual measurements within 3%. This difference between the two reconstructions is attributed to imperfect angular resolution and the presence of both sources on the same imaging axis for one of the detector positions.

6.2 Future Work

Many questions and recommendations for further study arose as a result of the work presented here. Some of the points relate to the design of the coded aperture imaging system, while others are directed to reconstructing the data detected by the coded aperture imaging system and analyzing reconstructed images.

6.2.1 Imager Design

As discussed in Section 2.4, the detectors used in fast-neutron coded aperture imaging at ORNL are neutron block detector based. The detector pixel size is fixed by the reflector boundary of each pixel. Pixel size for an imaging system is determined in the design process by balancing the competing goals of high light collection efficiency and high position resolution. One alternative method, developed for gamma-ray imaging systems, consists of a monolithic scintillator, with an internal optical photon coded aperture mask placed between the scintillator and a position-sensitive phototransducer (Ziock, Blackston, & Van Vuure, 2011). Since coded aperture imaging requires only 2D position resolution within a scintillator, no depth-of-interaction resolution within the scintillator itself is necessary. From this, it should be possible to create variable-sized detector pixels for reconstruction. Combining this with the

MLEM reconstruction technique, the size and resolution of the measured data can be selected as a variable size, allowing for smaller features of the measured source distribution to be represented in the measured data. This is particularly attractive, since the decreased size pixels would actually represent measured data, and not just rebinning of fixed pixel sizes. While design of a detector with this design would require an understanding of multiple scatter effects and position response within the detector, the use of single scintillator block detectors instead of pixelated block detectors makes this advanced design an attractive possibility. Since the detector pixel size used in reconstruction is more physically meaningful than varied detector pixel sizes in imaging with pixelated detector arrays, this additional ability is expected to increase both the distance and the angular resolution of the imager.

6.2.2 Dual Imaging Reconstruction

Since the coded aperture fast-neutron imagers are designed for fast-neutron imaging, it would be expected that their ability to reconstruct gamma-rays is inferior to their ability to reconstruct fast-neutrons. This is obvious from considering the design of the imager and the high quantity of hydrogenous material, and the lack of high-Z material in the imaging mask. But coded aperture imaging requires only geometric modulation of the source distribution incident on the mask, and even the imperfect modulation (60% transmission of 1 MeV gamma-rays for 2" HDPE) of gamma-rays by the mask provides sufficient modulation to form an image. Since Cf-252 and other fission sources emit both gamma-rays and neutrons, it is possible to reconstruct both the gamma-ray and fast-neutron emissions, as further discussed in Appendix F. Additionally high Z material in the mask, ideally lowering the transmission to less than 10% at 1 MeV, would further improve the ability to generate gamma ray images.

6.2.3 Background Radiation Effects

Measurements in this study consisted of Cf-252 neutron sources and relatively low, homogenous background rates. In the analysis, all of the detected counts are attributed to the source distribution. Measurements with relatively low source to homogenous background rates would falsely increase the detected source intensity, and, intuitively, heterogeneous background would decrease the effectiveness of the reconstruction by adding additional false

neutron source counts. Cross-correlation reconstruction accounts for this by subtracting anti-mask data from mask data, but the resulting distribution does not maintain a constant integrated source distribution and is not Poisson in nature, making it incapable of being used for MLEM reconstruction. Preliminary work by (Brubaker, 2013) suggests that by increasing the size of the source distribution and system response model in the MLEM reconstruction, it is possible to reconstruct the data that is not modulated by the mask, at the cost of more than doubling the number of calculations necessary per iteration. Further work is necessary to quantify the effects of this change to the MLEM algorithm and combine this technique with a complex system response model that incorporates the major physical effects involved in the detection and source encoding process.

6.2.4 Three-Dimensional Imaging

While measurements and simulations in this work have considered only variations of source position on the orthogonal axis of parallax imaging measurements and the distance axis, measurements of complex source distributions such as those potentially occurring at nuclear fuel reprocessing facilities may require truly 3D imaging. While for 2D coded apertures with 2D detector pixel arrays, cross-correlation-based reconstruction inherently produces 3D reconstructed data, MLEM reconstruction iterates over discrete source positions, and 3D reconstruction is not strictly necessary. Adding consideration of a third axis in the MLEM parameter space represents a large increase in the number of potential source positions, increasing the amount of forward projections necessary and the number of voxels in the reconstruction. For MLEM reconstruction, the use of an original reconstruction over large voxels and later reconstruction over small voxels, as well as applying the same concept to measured data, is popular in medical imaging due to the small voxel sizes and large detector datasets typical in this problem space (Bruyant, 2002). Applying this concept to fast-neutron imaging and reconstruction without *a priori* source information or previously generated forward projections provides a strong need to limit the number of calculations performed in the MLEM process. While reconstruction of 3D source distributions was not considered, the 2D reconstructions performed are analogous to reconstructing a single slice of a 3D distribution,

and the same concepts of limiting the size of the source voxel array were applied, and could be extended to truly 3D imaging.

References

Accorsi, R. (2001, June). Design of Near-Field Coded Aperture Cameras for High-Resolution Medical and Industrial Gamma-Ray Imaging. Massachusetts Institute of Technology.

Agostinelli, S. (2003). GEANT4—a simulation toolkit. *Nuclear instruments and methods in physics research section A: Accelerators, Spectrometers, Detectors and Associated Equipment*.

Bouallegue, F. B., Crouzet, J., & Mariano-Goulart, D. (2013). A heuristic statistical stopping rule for iterative reconstruction in emission tomography. *Annals of Nuclear Medicine*(27), 84-95.

Brubaker, E. (2013). A Maximum Likelihood Expectation Maximization Iterative Image Reconstrution Technique for Mask/Anti-Mask Coded Aperture Data. *Nuclear Science Symposium and Medical Imaging Conference (NSS/MIC).* IEEE.

Bruyant, P. (2002, October). Analytic and Iterative Reconstruction Algorithms in SPECT. *Journal of Nuclear Medicine, 43*(10), 1343-1358.

Byrd, R., Moss, J., Priedhorsky, W., Pura, C., Richter, G., Saeger, K., . . . Scott, S. (2005, August). Nuclear Detection to Prevent or Defeat Clandestine Nuclear Attack. *IEEE Sensors Journal, 5*(4).

Caroli, E., Stephen, J., Di Cocco, G., Natalucci, L., & Spizzichino, A. (1987). Coded Aperture Imaging in X- and Gamma-Ray Astronomy. *Space Science Reviews*, 349-403.

Chen, S., Wu, Z., & Jin, Y. (2005). New Reconstruction and Analysis for Coded-aperture Imaging. *IEEE Nuclear Science Symposium.*

Chuang, K.-S., Jan, M.-L., Wu, J., Lu, J.-C., Chen, S., Hsu, C.-H., & Fu, Y.-K. (2005). A maximum likelihood expectation maximization algorithm. *Computerized Medical Imaging and Graphics, 29*, 571-578.

Fenimore, E., & Cannon, T. (1981, May 15). Uniformly Redundant Arrays: Digitial Reconstruction Methods. *Applied Optics, 20*(10), 8.

Gottesman, S. R., & Fenimore, E. (1989, October 15). New family of binary arrays for coded aperture imaging. *Applied Optics, 28*(20), 9.

Hagenauer, R., & Mayer, R. (1991). Methods for Nondestructive Assay Holdup Measurements in Shutdown Uranium Enrichment Facilities. *International Topical Conference on Facility Operations/Safeguards Interface.* Albuquerque, NM.

Hammersley, A. (1986). The Reconstruction of Coded-mask Data under Conditions Realistic to X-Ray Astronomy Observations. University of Birmingham.

Hausladen, P., & Blackston, M. (2009, August). Passive and Active Fast-Neutron Imaging in Support of AFCI Safegaurds Campaign. Oak Ridge, TN: Oak Ridge National Laboratory.

Hausladen, P., Blackston, M., & Newby, J. (2011). *Demonstration of Emitted-Neutron Computed Tomography to Quantify Nuclear Materials.* Oak Ridge National Laboratory, Nuclear Materials Detection and Characterization.

Hausladen, P., Blackston, M., & Newby, J. (2012). *Measurement Scenarios to Mimic Potential Uses of Passive Fast-Neutron Imaging for Quantifying Holdup at Fuel Cycle Facilities.* Oak Ridge: Oak Ridge National Laboratory.

Hausladen, P., Blackston, M., & Newby, R. (2010). *Position-Sensitive Fast-Neutron Detector Development in Support of Fuel-Cycle R&D MPACT Campaign.* Oak Ridge National Laboratory, Oak Ridge, TN.

Hausladen, P., Blackston, M., Brubaker, E., Chichester, D., Marleau, P., & Newby, R. (2012). Fast-Neutron Coded-Aperture Imaging of Special Nuclear Material Configurations. *INMM.*

Hausladen, P., Newby, J., Liang, F., & Blackston, M. (2013). *The Deployable Fast-Neutron Coded-Aperture Imager: Demonstration of Locating One or More Sources in Three Dimensions.* TM, Oak Ridge National Laboratory.

Horn, B., Lanza, R., Bell, J., & Koshe, G. (2010). Dynamic Reconstruction. *IEEE Transactions on Nuclear Science*.

IAEA. (n.d.). *Limits To The Safeguard System*. Retrieved 06 2014, from http://www.iaea.org/Publications/Booklets/Safeguards/pia3810.html

Ito, T., & Fujimura, S. (1996). Improvement on Depth Resolution and Reduction of Poisson Noise in Coded Aperture Emission CT. *IEEE International Conference On Image Processing*, *1.*

Iyengar, A., Beach, M., Newby, R., Fabris, L., Heilbronn, L., & Hayward, J. (2015). Systematic measurement of fast neutron background fluctuations in an urban area using a mobile detection system. *Nuclear Instruments and Methods A.*, 27-32.

Kowash, B. (2008). A Rotating Modulation Imager for the Orphan Source Search Problem. University of Michigan.

Kuhn, H., & Tucker, A. (1951). Nonlinear Programming. *Proceedings of the Second Berkeley Symposium on Mathematical Statistics and Probability* (pp. 481-492). Berkeley, CA: University of California Press.

Lawrence, C., Febbraro, M., Massey, T., Flaska, M., Becchetti, F., & Pozzi, S. (2014). Neutron response characterization for an EJ299-33 plastic scintillation detector. *Nuclear Instruments and Methods in Research A*, 7.

Lo Presti, C., Weier, D., Kouzes, R., & Schweppe, J. (2006). Baseline suppression of vehicle portal monitor gamma count profiles: A characterization study. *Nuclear Instruments and Methods in Physics Research A*, 281-297.

Luke, S., & Archer, D. (2000). Gamma Attribute Measurements - Pu-300, Pu600, Pu900. *Institute of Nuclear Materials Management.* New Orleans.

Marleau, P., Brenna, J., Brubaker, E., Gerling, M., Nowack, A., Schuster, P., & Steele, J. (2011). Time Encoded Fast Neutron/Gamma Imager for Large Standoff SNM Detection. *IEEE Nuclear Science Symposium*, (p. 5).

Mascarenhas, N., Brennan, J., Krenz, K., Lund, J., Marleau, P., Rasmussen, J., . . . Macri, J. (2006). Development of a Neutron Scatter Camera for Fission Neutrons. *IEEE Nuclear Science Symposium.*

Mu, Z., & Liu, Y.-H. (2006). Aperture Collimation Correction and Maximum-Likelihood Image Reconstruction for New-Field Coded Aperture Imaging of Single Photon Emission Computerized Tomography. *IEEE Transactions on Medical Imaging*, 701-711.

Newby, R., Hausladen, P., Blackston, M., & Liang, J. (2013). *Performance of Fast-Neutron Imaging Detectors Based on Plastic Scintillator EJ-299-34.* Oak Ridge National Laboratory, Nuclear Security and Isotope Technology Division, Oak Ridge, TN.

Nuclear Regulatory Commission. (2013, 05). *Frequently Asked Questions About Mixed Oxide Fuel*. Retrieved 06 2014, from http://www.nrc.gov/materials/fuel-cycle-fac/mox/faq.html

Oshawa, T., Horiguchi, T., & Mitsuhashi, M. (2000). Multimodal analysis of prompt neutron spectra for 238Pu (sf), 240Pu (sf), 242Pu (sf), and 239Pu(nth,f). *Nuclear Physics A*.

Pellaud, B. (2002). Proliferation aspects of plutonium recycling. *C.R. Physique 3*, 1079-1079.

Reilly, T. D. (2007). Nondestructive Assay of Holdup. In *PANDA.* Los Alamos National Laboratory.

Richardson, W. (1972). Bayesian-Based Iterative Method of Image Restoration. *Journal of the Optical Society of America*, 55-59.

Shepp, L., & Vardi, Y. (1982, October). Maximum Likelihood Reconstruction for Emission Tomography. *IEEE Transactions on Medical Imagign, M1-1*(2).

Sigg, R., Casella, V., Dewberry, R., & Moore, F. (n.d.). *Holdup Measurements for Visual Examination GLoveboxes at the Savannah River Site.* Savannah River National Laboratory, Aiken, SC.

Smith, A., Fields, P., & Roberts, J. (1957). Spontaneous Fission Neutron Spectrum of Cf252. *Physical Review*.

Swift, A. (2012). *Materials and Configuration from NMIS type Neutron Imaging and Gamma Spectroscopy.* Masters Thesis, University of Tennessee, Nuclear Engineering.

Vanier, P., Diosvegi, I., Salwen, C., & Forman, L. (2009). Directional Stand-Off Detection of Fast Neutrons and Gammas Using Angular Scattering Distributions. *IEEE Nuclear Science Symposium.* Orlando, FL.

Von Hippel, F. N. (2001, Sep 28). Plutonium and Reprocessing of Spent Nuclear Fuel. *Science, 293*(5539), 2397-2398.

Wagner, J. C., Peterson, J. L., Mueller, D. E., Gehin, J. C., Worrall, A., Taiwo, T., . . . Carter, J. T. (2012). *Categorization of Used Nuclear Fuel Invenstory in Support of a Comprehensive National Nuclear Fuel Cycle Strategy.* Oak Ridge National Laboratory.

Zaitseva, N., Rupert, B. L., PaweLczak, I., Glenn, A., Martinez, H. P., Carman, L., . . . Payne, S. (2012). Plastic scintillators with efficient neutron/gamma pulse shape discrimination. *Nuclear Instruments and Methods in Physics Research A, 668*(88).

Ziock, K., Blackston, M., & Van Vuure, T. (2011). 3D Millimeter Event Localization in Bulk Scintillator Crystals. *Nuclear Science Symposium and Medical Imaging Conference (NSS/MIC).* Valencia: IEEE.

Appendix

A. Geant4 Simulation

All simulations, unless otherwise noted, were performed on version geant4-09-06 on an Intel® Core™ i7-2640M CPU @ 2.8GHz.

Physics List

For all simulations, the following standard Geant4 physics lists were used:

- QGSP_BERT_HP

Source Distribution

Each source following a Cf-252 spontaneous fission energy spectrum was a General Particle Source with the following energy spectrum:

```
#            Energy (MeV)  Rel. Yield
#
/gps/hist/point  0.03791       32.71076
/gps/hist/point  0.08301       45.89684
/gps/hist/point  0.19830       59.07265
/gps/hist/point  0.34993       68.10622
/gps/hist/point  0.60544       74.34164
/gps/hist/point  0.81070       76.17980
/gps/hist/point  1.08555       73.89820
/gps/hist/point  1.55102       64.25226
/gps/hist/point  1.89664       55.40119
/gps/hist/point  2.39728       45.95365
/gps/hist/point  2.82949       37.80812
/gps/hist/point  3.50389       27.66813
/gps/hist/point  4.40363       17.72709
/gps/hist/point  5.04448       12.47039
/gps/hist/point  5.61632       8.97969
/gps/hist/point  6.24062       6.12068
/gps/hist/point  7.02125       3.73887
/gps/hist/point  8.84360       1.12916
#
/gps/hist/inter Lin
```

This source distribution was based on (Smith, Fields, & Roberts, 1957).

B. Experimental Design

While each source used was a Cf-252 source small enough in physical size to be equivalent to a point source, the intensity of the sources used ranged from combinations of 3.7 μCi sources to a single 74 μCi source. For demonstration of the ability to quantify one or multiple sources using the parallax imaging technique, each measurement used the P40 imager. Unless otherwise noted, the height of each source was at the center height of the detector pixel array component of the imager.

Distance Measurements

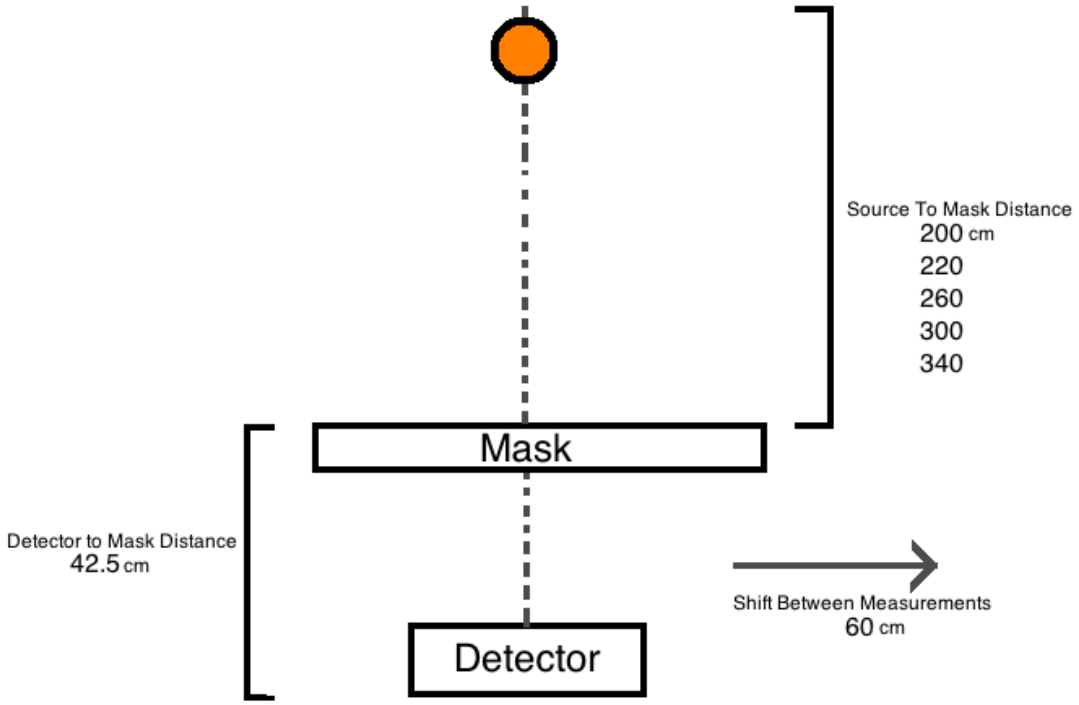

For each distance measurement, a single 74 µCi source was used, with a measurement time of 90 minutes for each mask orientation and detector position.

Measurement 1

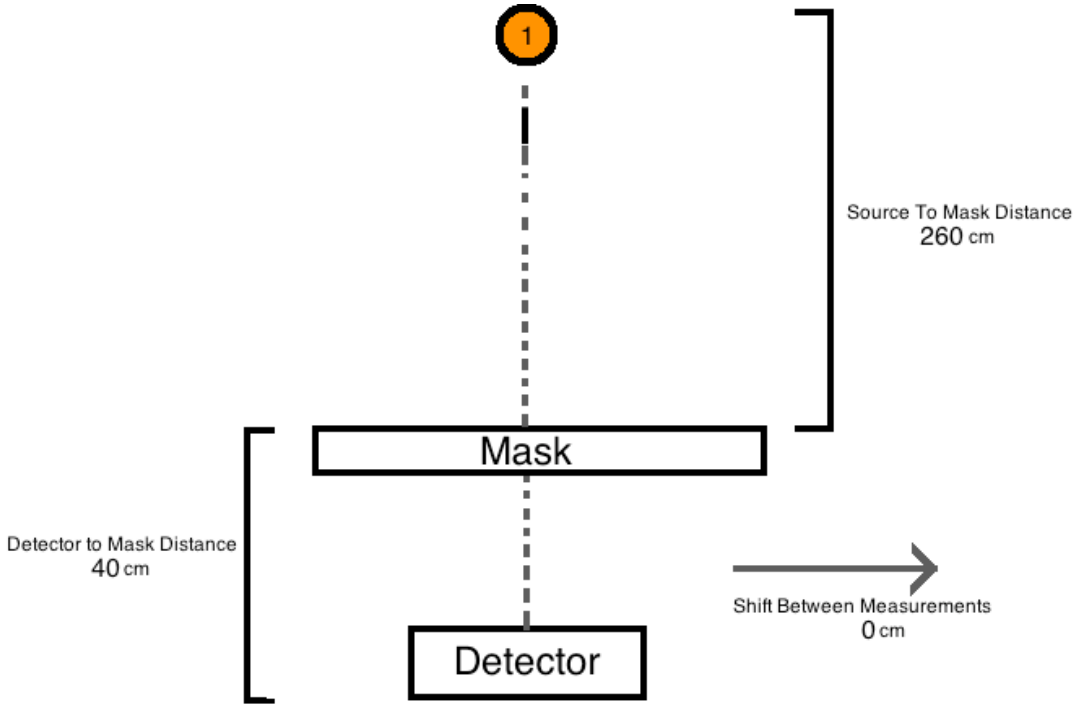

To demonstrate the poor distance resolution of coded aperture imaging without the parallax measurement technique, a single 3.706 µCi source was measured for 90 minutes with no second detector position.

Measurement 2

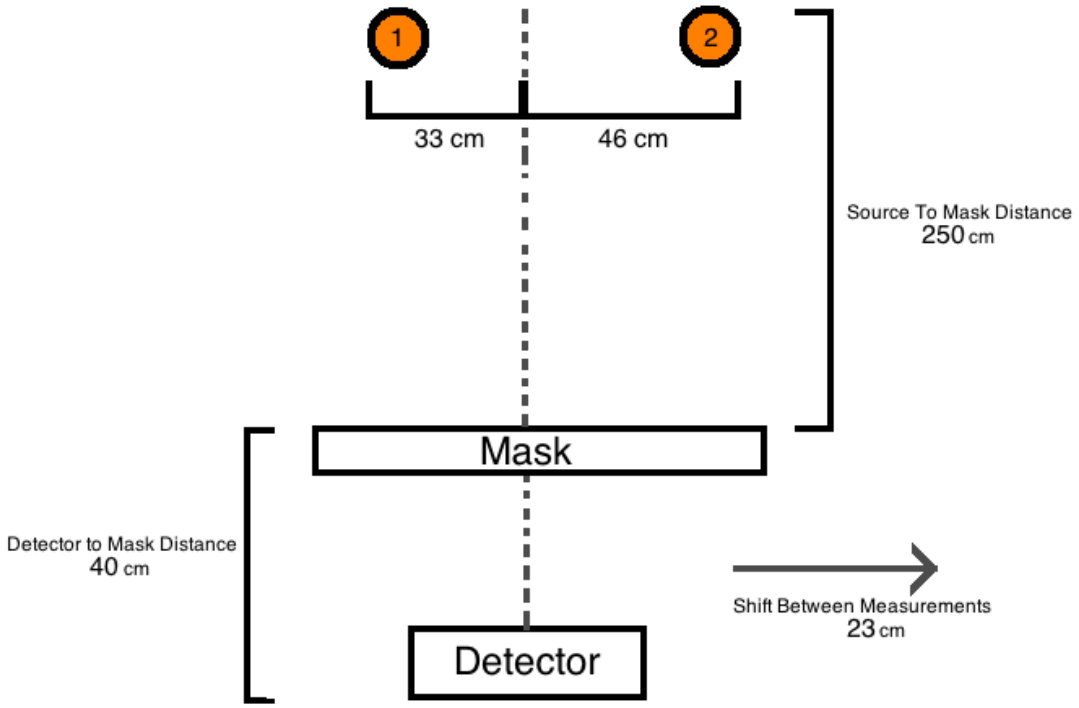

For each detector position, source 1 had an intensity of 74 µCi and source 2 had an intensity of 18.5 µCi. The measurement time at each mask orientation was 10 minutes.

Measurement 3

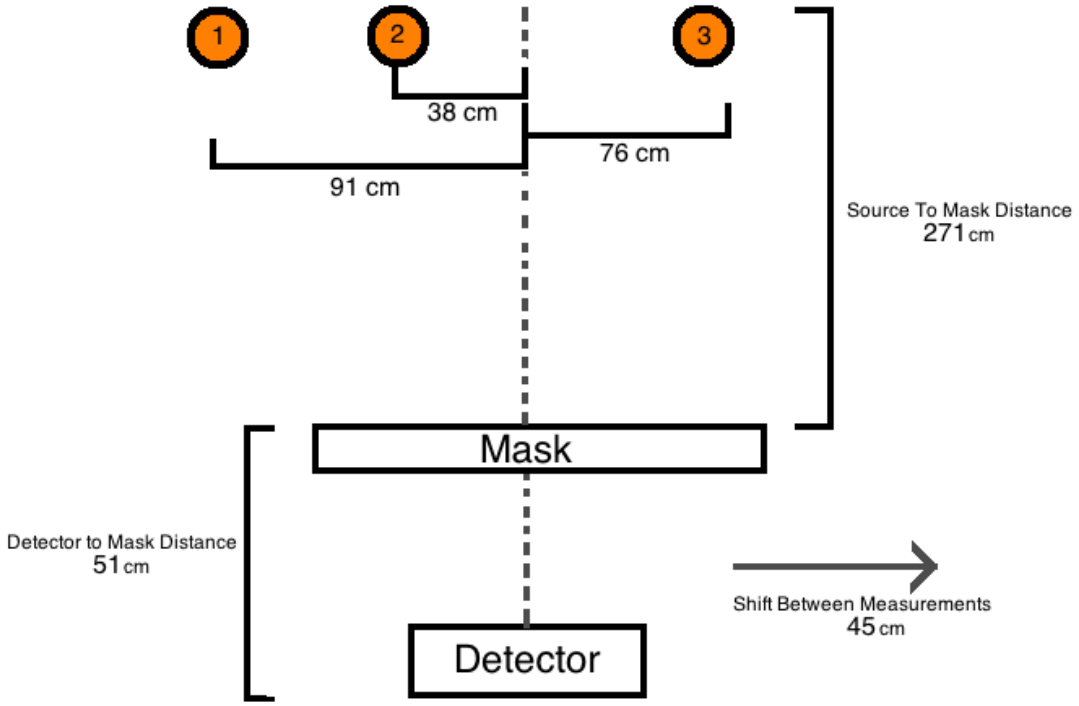

For each detector position, source 1 had an intensity of 7.4 µCi, source 2 had an intensity of 14.8 µCi, and source 3 had an intensity of 74 µCi. Each source was located at a different height relative to the floor of the measurement facility, with source 1 at a height of 118.4 cm, source 2 at a height of 63 cm, and source 3 at a height of 103.3 cm. The measurement time at each mask orientation was 60 minutes.

Measurement 4 & Measurement 5

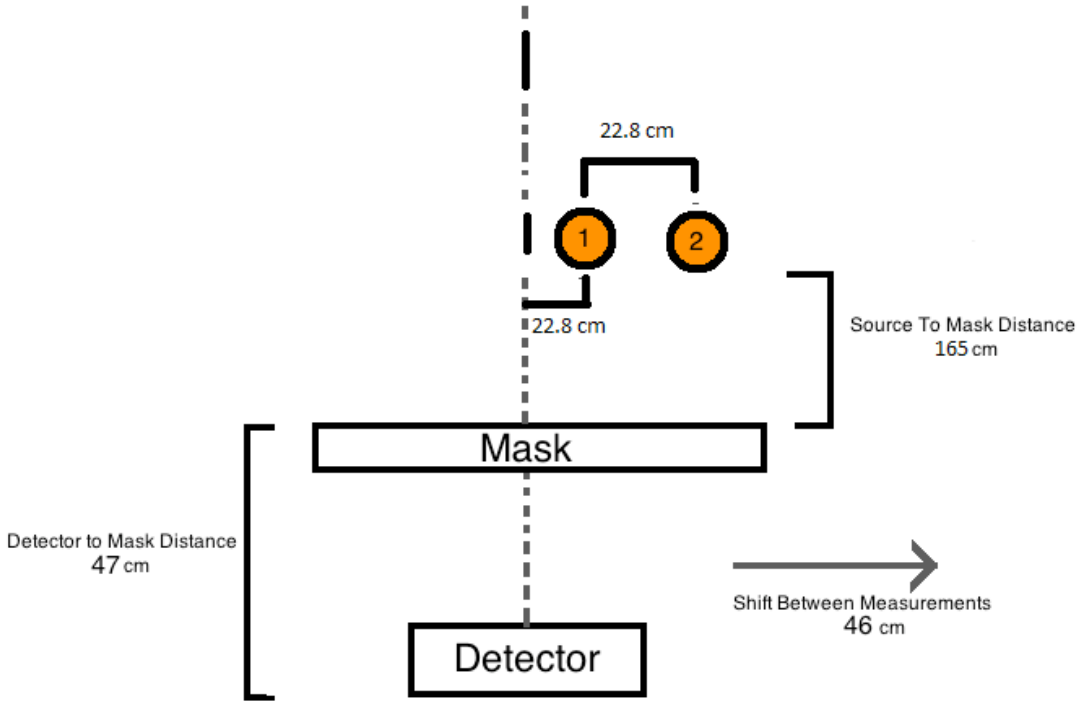

Both source 1 and source 2 had an intensity of 11.1 µCi. The measurement time for each mask orientation was 90 minutes.

Measurement 5 was identical to Measurement 4, with the exception that the shift between measurement positions was changed to 69 cm.

C. MLEM Derivation

While the true source distribution in a measurement is continuous, for reconstruction purposes the source distribution is discretized into voxels. Thus, each voxel, *b*, can be characterized by *λ(b)*, referring to the emission rate in that voxel. Statistical reconstruction consists of estimating *λ(b)* from the observed data *n*(d), d=1, …,D*, where *d* refers to the detector pixels. In the case of the MLEM reconstruction technique, this derives from a variety of frameworks, including the Expectation Maximization (EM) algorithm and as a result of Bayes' Theorem (Richardson, 1972), as shown in the following derivation.

The conditional probability of a voxel intensity given a detector pixel count is given by

$$\mathrm{P}(\lambda_b|\mathrm{n}^*{}_d) = \frac{P(\mathrm{n}^*{}_d|\lambda_b)P(\lambda_b)}{\sum_{bb}^{BB} P(\mathrm{n}^*{}_d|\lambda_{bb})P(\lambda_{bb})}; b = \{1, B\}, d = \{1, D\}$$

Considering that *n*(d)* is not dependent on just one source voxel, but all voxels, the probability of any given voxel is

$$\mathrm{P}(\lambda_b) = \sum_{d}^{D} P(\lambda_b|\mathrm{n}^*{}_d)P(\mathrm{n}^*{}_d)$$

Substituting the conditional probability into the summed probability yields

$$\mathrm{P}(\lambda_b) = \sum_{d}^{D} \frac{P(\mathrm{n}^*{}_d|\lambda_b)P(\lambda_b)P(\mathrm{n}^*{}_d)}{\sum_{bb}^{BB} P(\mathrm{n}^*{}_d|\lambda_{bb})P(\lambda_{bb})}$$

Note that both sides of the equation contain *P(λ(b))*, which is the desired solution. Since this is unknown in practice, an iterative procedure can be used by estimating *P(λ(b))*, with a new estimate being given by

$$\mathrm{P}_{r+1}(\lambda_b) = P_r(\lambda_b) \sum_{d}^{D} \frac{P(\mathrm{n}^*{}_d|\lambda_b)P(\mathrm{n}^*{}_d)}{\sum_{bb}^{BB} P(\mathrm{n}^*{}_d|\lambda_{bb})P_r(\lambda_{bb})}; r = \{0,1, \dots\}$$

Which starts with an initial estimate of $P_0(\lambda(b))$. The rate of convergence and behavior of convergence depends on the accuracy of $P_0(\lambda(b))$, and without *a priori* knowledge of the source

distribution is generally assumed to be a uniform distribution. Since in reconstruction, the number of counts measured by the detector is conserved, the probabilities can be normalized by

$$P(\lambda_b) = \frac{\lambda_b}{\sum_b^B \lambda_b}$$

$$P(\mathrm{n}^*{}_d) = \frac{\mathrm{n}^*{}_d}{\sum_d^D \mathrm{n}^*{}_d} = \frac{\mathrm{n}^*{}_d}{\sum_b^B \lambda_b}$$

Note that $P(n^*(d)|\ \lambda(b))$ is defined by the system model $p_{d,b}$, which is normalized to an 1 for each source voxel. The new estimate of the source probability then becomes

$$\frac{\lambda_{b,r+1}}{\sum_b^B \lambda_b} = \frac{\lambda_{b,r}}{\sum_b^B \lambda_b} \sum_d^D \frac{p_{d,b} \frac{\mathrm{n}^*{}_d}{\sum_b^B \lambda_b}}{\sum_{bb}^{BB} p_{d,b} \frac{\lambda_{b,r}}{\sum_b^B \lambda_b}}; r = \{0,1, \dots\}$$

Which condenses to

$$\lambda_{b,r+1} = \lambda_{b,r} \sum_d^D \frac{p_{d,b} \mathrm{n}^*{}_d}{\sum_{bb}^{BB} p_{d,bb} \lambda_{bb,r}}$$

Defining

$$S^{new}(b) = \lambda_{b,r+1}$$

$$S^{old}(b) = \lambda_{b,r}$$

$$\mathrm{P}^*{}_i = \mathrm{n}^*{}_d$$

The MLEM algorithm can be rewritten as

$$S^{new}(b) = S^{old}(b) \sum_{i=1}^m \frac{P^*{}_i\, p_{ib}}{\sum_{b'=0}^n S^{old}(b') p_{ib'}}$$

Which is the MLEM algorithm shown in Equation 17.

D. Mask Scattering Correction

Correcting for scattering within the mask consists of performing a pointwise operation with a transfer function on non-scattering data. The transfer function is generated through histogram equalization of Geant4 data. Histogram equalization and generation of the transfer function (transferFunc) is performed in HistogramEqualization, which calls CumulativeHistogramImage to create cumulative hisograms for image1 and image2.

```
TH1D* CumulativeHistogramImage(TH2D* hImage)
{
	TH1D* imageHist = new TH1D("imageHist","imageHist",5000,hImage->GetMinimum()/hImage->GetMaximum(),1);

	for (Int_t i=0;i<hImage->GetSize();i++)
	{
		if ((hImage->GetBinContent(i)!=0)||(imageHist->GetMaximum()!=256))
		{
			imageHist->Fill(hImage->GetBinContent(i)/hImage->GetMaximum());
		}
		else{;}
	}

	TH1D* cumulativeImageHist = (TH1D*)imageHist->Clone("cumulativeImageHist");
	double currentVal=0;
	for (int i=0;i<imageHist->GetSize();i++)
	{
		currentVal+=imageHist->GetBinContent(i);
		cumulativeImageHist->SetBinContent(i,currentVal);
	}
	return cumulativeImageHist;
}
TH2D* HistogramEqualization(TH2D* image1,TH2D*image2)
{
	TH2D* equalizedImage=(TH2D*)image1->Clone("equalizedImage");
	TObjArray* objArr = new TObjArray();
	TH1D* image1Hist = CumulativeHistogramImage(image1);
	TH1D* image2Hist = CumulativeHistogramImage(image2);

	TH1D* transferFunc = (TH1D*)image1Hist->Clone("transferFunc");
	for (int i=0;i<transferFunc->GetSize();i++)
	{
		int minBin = image2Hist->GetNbinsX();
		double separation = 10000;
		for (int j=0;j<image2Hist->GetSize();j++)
		{
			if ( TMath::Abs(image2Hist->GetBinContent(j)-image1Hist->GetBinContent(i)) <= separation)
			{
				minBin = j;
				separation = TMath::Abs(image2Hist->GetBinContent(j)-image1Hist->GetBinContent(i));
			}
			else{;}
		}
		transferFunc->SetBinContent(i,image2Hist->GetBinCenter(minBin));
```

```
	}
	for (int i=0;i<transferFunc->GetSize();i++)
	{
		if (transferFunc->GetBinContent(i)>image1Hist->GetMaximum())
		{
			transferFunc->SetBinContent(i,image1Hist->GetMaximum());
		}
		else{;}
	}
	transferFunc->Scale(1/transferFunc->GetMaximum());

	for (int i=0;i<equalizedImage->GetSize();i++)
	{
		equalizedImage->SetBinContent(i,image1->GetMaximum()*transferFunc->GetBinContent(transferFunc-
>FindBin(image1->GetBinContent(i)/image1->GetMaximum())));
	}

	objArr->Add(image1Hist);
	objArr->Add(image2Hist);
	objArr->Add(transferFunc);
	TFile* exitFile = new TFile("histogramFiles.root","RECREATE");
	objArr->Write();
	exitFile->Close();
	return equalizedImage;
}
```

E. Local Region Thresholding

Thresholding using the local region consists of setting the voxel histogram (sourceCountHist) bin value to zero if it does not meet a minimum threshold and the local region fails to meet certain criteria. The function NearestNeighborThreshold returns false if the voxel is rejected as a potential source voxel and thus zeroed.

```
bool MLEM::NearestNeighborThreshold(double binContent,double threshold,int binNumber)
{
	bool isSourceVoxel = true;
	double neighborThreshold = 1*threshold;

	if ((binContent <  threshold))
	{
		isSourceVoxel = false;
		double posX = oldSourceDistribution.at(binNumber).posX;
		double posZ = oldSourceDistribution.at(binNumber).posZ;
		// 4-connected neighbors
		//
		double downBin = sourceCountHist->GetBinContent(binNumber-sourceCountHist->GetNbinsX());
		double upBin = sourceCountHist->GetBinContent(binNumber+sourceCountHist->GetNbinsX());
		double leftBin = sourceCountHist->GetBinContent(sourceCountHist->FindBin(posX,posZ)-1);
		double rightBin = sourceCountHist->GetBinContent(sourceCountHist->FindBin(posX,posZ)+1);
		// 8-connected neighbors
		//
		double northEastBin = sourceCountHist->GetBinContent(binNumber+sourceCountHist->GetNbinsX()+1);
		double northWestBin = sourceCountHist->GetBinContent(binNumber+sourceCountHist->GetNbinsX()-1);
		double southEastBin = sourceCountHist->GetBinContent(binNumber-sourceCountHist->GetNbinsX()+1);
		double southWestBin = sourceCountHist->GetBinContent(binNumber-sourceCountHist->GetNbinsX()-1);

		int numNeighbors = 0;
		if (leftBin>neighborThreshold)
		{
			numNeighbors++;
		}
		else{;}
		if (rightBin>neighborThreshold)
		{
			numNeighbors++;
		}
		else{;}
		if (downBin>neighborThreshold)
		{
			numNeighbors++;
		}
		else{;}
		if (upBin>neighborThreshold)
		{
			numNeighbors++;
		}
		else{;}
		if (northEastBin>neighborThreshold)
		{
			numNeighbors++;
```

```
                }
                else{;}
                if (northWestBin>neighborThreshold)
                {
                        numNeighbors++;
                }
                else{;}
                if (southEastBin>neighborThreshold)
                {
                        numNeighbors++;
                }
                else{;}
                if (southWestBin>neighborThreshold)
                {
                        numNeighbors++;
                }
                else{;}

                if (numNeighbors>=2)
                {
                        isSourceVoxel = true;
                }
                else{;}
        }
        else{;}
        return isSourceVoxel;
}
```

F. Gamma-Ray Reconstruction

In contrast to fast-neutron measurements, the modulation of the gamma-ray distribution is poor, as shown in Figure 110.

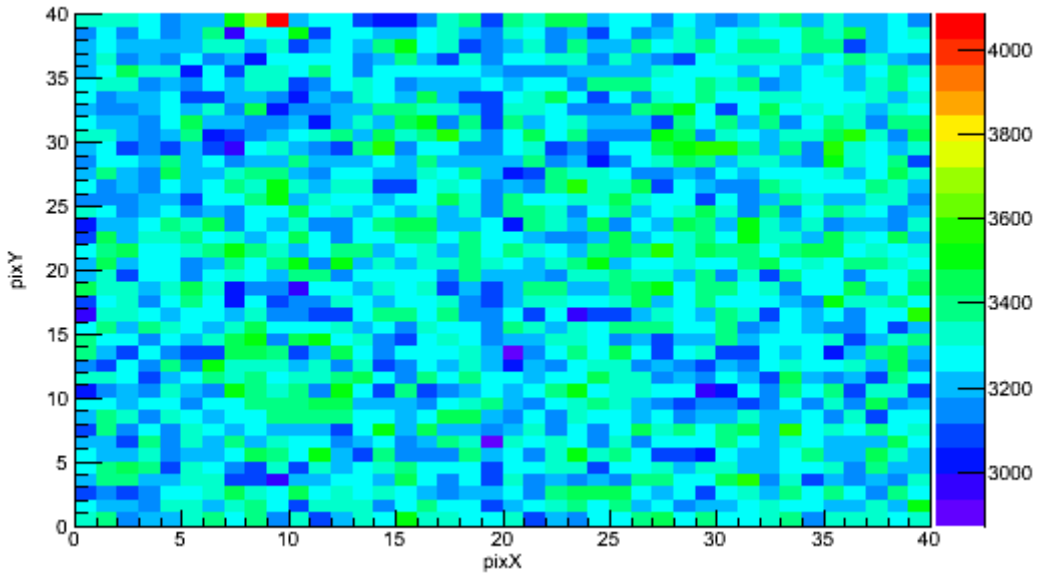

Figure 110. Gamma-ray measured spectrum for a 1-hour Cf-252 measurement at 205 cm distance.

While some mask features are visually apparent in Figure 110 to a trained eye, such as the decreased count rate due to the vertical moderator element at column 20, it is difficult to visually note mask features due to poor modulation of the gamma-ray distribution. Poor modulation of the gamma-ray distribution would be expected, since HDPE is not generally used as gamma-ray shielding, although some modulation does occur due to the presence of the mask. Since the cross-correlation reconstruction technique only requires an analytical

treatment of the measured data, it is possible to reconstruct a source from the gamma-ray data, as shown in Figure 111.

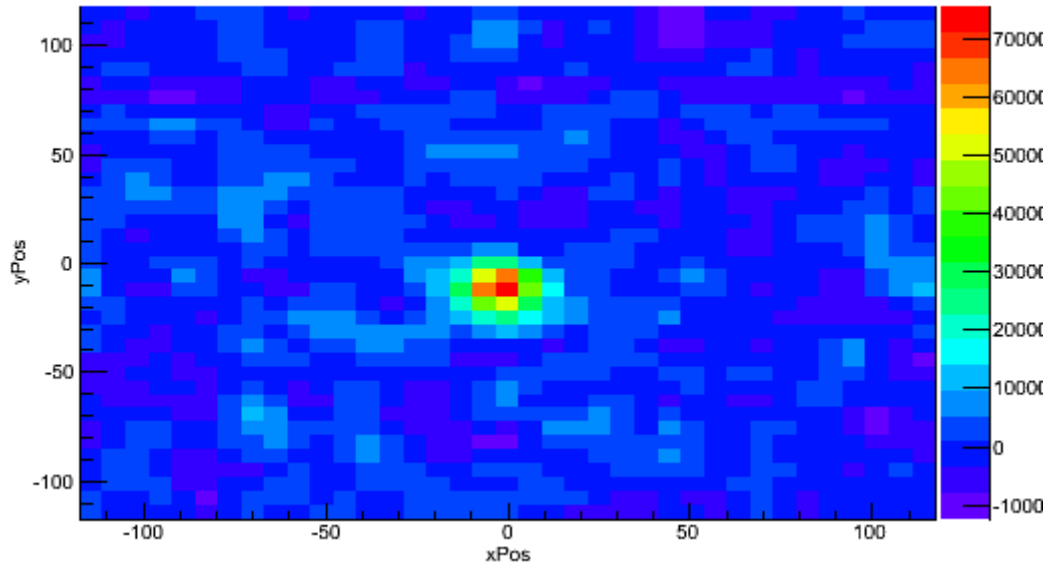

Figure 111. Cross-correlation reconstruction of Figure 110 at a distance of 250 cm.

Using the data from Figure 110, which consisted of a 60 minute measurement of a 0.04 mCi Cf-252 point source centered on one detector position and 40 cm shifted from the other detector position at a distance of 210 cm, this data was reconstructed using a MLEM reconstruction. Performing a MLEM reconstruction of this data using the system model developed for fast neutrons would in effect be reconstructing with an improper system model, with the added difficulty of poor contrast in the measured data.

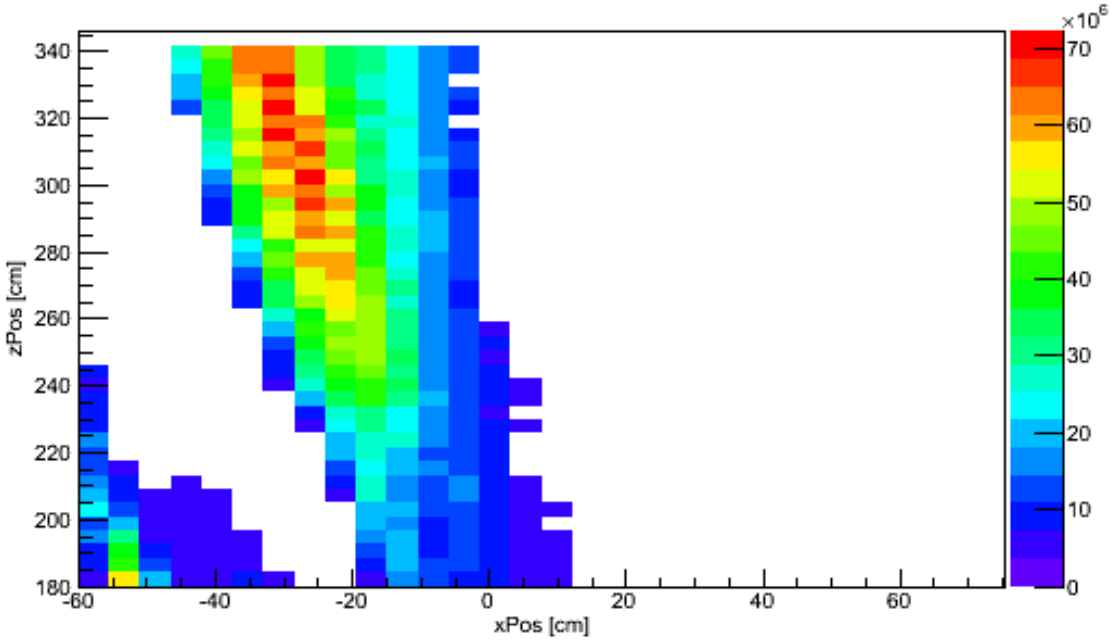

Figure 112. MLEM reconstruction of gamma-ray data from Cf-252 point source located at (0,210) on this figure.

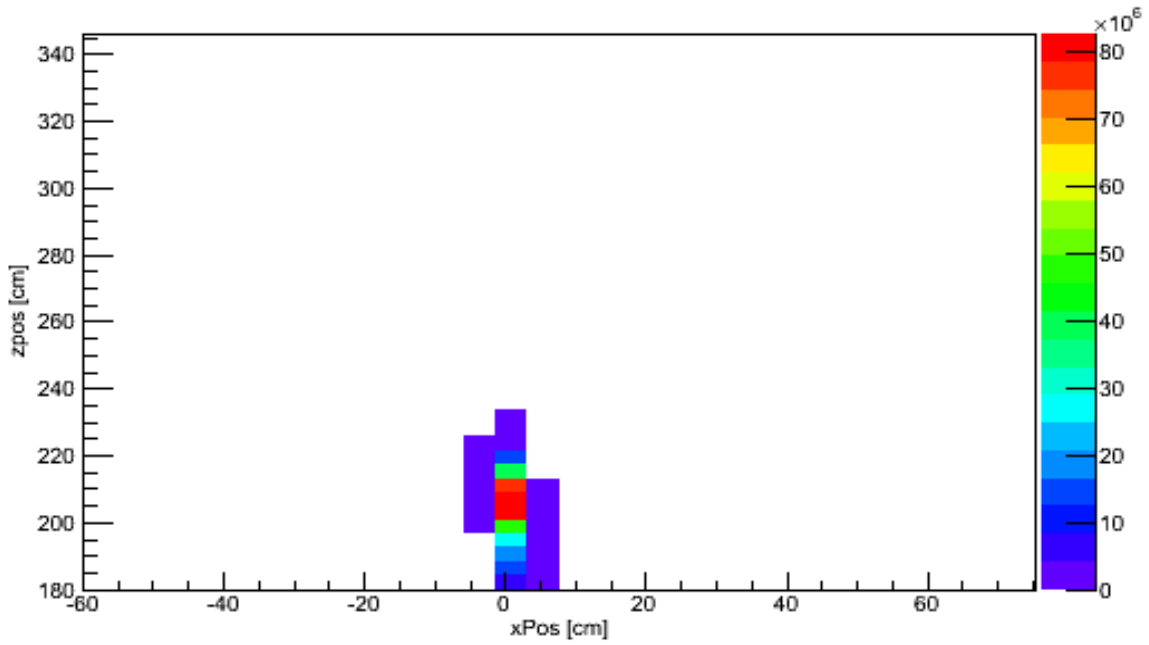

Figure 113. MLEM reconstruction of neutron data from Cf-252 point source located at (0,210) on this figure.

As shown in Figure 112 the gamma-ray component of the source is poorly reconstructed, with the reconstruction in the wrong position. This is in contrast to the neutron data, which properly reconstructs the source, as shown in Figure 113. Dual imaging, then, requires the development of both a neutron system model and a gamma-ray system model. Additional *a priori* information about the measurement geometry is needed to develop the gamma-ray model due to the increased effect of shielding for gamma-rays. Since the focus of this work is on fast-neutron imaging, development of a gamma-ray system model is outside the scope of this work, other than noting that the process to develop a gamma-ray system model would be identical to the process used to develop the neutron-response model.

G. Copyright Permissions

Technology Licensing Office

Massachusetts Institute of Technology
255 Main St., Kendall Square, Buidling NE18-501
Cambridge, Massachusetts 02142–1601

November 10, 2014

RE: Request to Use MIT-Copyrighted Material

Timothy D. Jackson
Oak Ridge National Laboratory
P.O. Box 2008 MS6010
Oak Ridge, TN 37831-6010

Dear Timothy,

In response to your November 2014 inquiry, the copyright notice corresponding to Figure 2.18 found in "Design of a near-field coded aperture cameras for high-resolution medical and industrial gamma-ray imaging" by Roberto Accorsi (2001) attributes ownership to the Massachusetts Institute of Technology ("MIT"). Accordingly, MIT hereby grants you permission to use the image in your thesis "Quantification of Fast-Neutron Sources with Coded Aperture Imaging" provided that any use of the image contains the proper acknowledgment of MIT's copyright and the author. This authorization to use the copyrighted figure also applies to any future editions, revisions, or translations (in whatever language published) and to mechanical and electronic storage on any carrier.

Sincerely,

Peter Bebergal
Associate Officer

ELSEVIER LICENSE
TERMS AND CONDITIONS

Nov 10, 2014

This is a License Agreement between Timothy Jackson ("You") and Elsevier ("Elsevier") provided by Copyright Clearance Center ("CCC"). The license consists of your order details, the terms and conditions provided by Elsevier, and the payment terms and conditions.

All payments must be made in full to CCC. For payment instructions, please see information listed at the bottom of this form.

Supplier	Elsevier Limited The Boulevard,Langford Lane Kidlington,Oxford,OX5 1GB,UK
Registered Company Number	1982084
Customer name	Timothy Jackson
Customer address	2000 Wilson Rd Apt 1248 KNOXVILLE, TN 37912
License number	3505551170769
License date	Nov 10, 2014
Licensed content publisher	Elsevier
Licensed content publication	Nuclear Physics A
Licensed content title	Multimodal analysis of prompt neutron spectra for 238Pu(sf), 240Pu(sf), 242Pu(sf) and 239Pu(nth,f)
Licensed content author	Takaaki Ohsawa,Tetsuo Horiguchi,Miki Mitsuhashi
Licensed content date	14 February 2000
Licensed content volume number	665
Licensed content issue number	1-2
Number of pages	10
Start Page	3
End Page	12
Type of Use	reuse in a thesis/dissertation
Portion	figures/tables/illustrations
Number of figures/tables/illustrations	1
Format	both print and electronic
Are you the author of this Elsevier article?	No
Will you be translating?	No

Thesis / Dissertation Reuse

The IEEE does not require individuals working on a thesis to obtain a formal reuse license, however, you may print out this statement to be used as a permission grant:

Requirements to be followed when using any portion (e.g., figure, graph, table, or textual material) of an IEEE copyrighted paper in a thesis:

1) In the case of textual material (e.g., using short quotes or referring to the work within these papers) users must give full credit to the original source (author, paper, publication) followed by the IEEE copyright line © 2011 IEEE.
2) In the case of illustrations or tabular material, we require that the copyright line © [Year of original publication] IEEE appear prominently with each reprinted figure and/or table.
3) If a substantial portion of the original paper is to be used, and if you are not the senior author, also obtain the senior author's approval.

Requirements to be followed when using an entire IEEE copyrighted paper in a thesis:

1) The following IEEE copyright/ credit notice should be placed prominently in the references: © [year of original publication] IEEE. Reprinted, with permission, from [author names, paper title, IEEE publication title, and month/year of publication]
2) Only the accepted version of an IEEE copyrighted paper can be used when posting the paper or your thesis on-line.
3) In placing the thesis on the author's university website, please display the following message in a prominent place on the website: In reference to IEEE copyrighted material which is used with permission in this thesis, the IEEE does not endorse any of [university/educational entity's name goes here]'s products or services. Internal or personal use of this material is permitted. If interested in reprinting/republishing IEEE copyrighted material for advertising or promotional purposes or for creating new collective works for resale or redistribution, please go to http://www.ieee.org/publications_standards/publications/rights/rights_link.html to learn how to obtain a License from RightsLink.

If applicable, University Microfilms and/or ProQuest Library, or the Archives of Canada may supply single copies of the dissertation.

BACK | CLOSE WINDOW

Title: Development of a Neutron Scatter Camera for Fission Neutrons

Conference Proceedings: Nuclear Science Symposium Conference Record, 2006. IEEE

Author: Mascarenhas, N.; Brennan, J.; Krenz, K.; Lund, J.; Marleau, P.; Rasmussen, J.; Ryan, J.; Macri, J.

Publisher: IEEE

Date: Oct. 29 2006-Nov. 1 2006

Thesis / Dissertation Reuse

The IEEE does not require individuals working on a thesis to obtain a formal reuse license, however, you may print out this statement to be used as a permission grant:

Requirements to be followed when using any portion (e.g., figure, graph, table, or textual material) of an IEEE copyrighted paper in a thesis:

1) In the case of textual material (e.g., using short quotes or referring to the work within these papers) users must give full credit to the original source (author, paper, publication) followed by the IEEE copyright line © 2011 IEEE.
2) In the case of illustrations or tabular material, we require that the copyright line © [Year of original publication] IEEE appear prominently with each reprinted figure and/or table.
3) If a substantial portion of the original paper is to be used, and if you are not the senior author, also obtain the senior author's approval.

Requirements to be followed when using an entire IEEE copyrighted paper in a thesis:

1) The following IEEE copyright/ credit notice should be placed prominently in the references: © [year of original publication] IEEE. Reprinted, with permission, from [author names, paper title, IEEE publication title, and month/year of publication]
2) Only the accepted version of an IEEE copyrighted paper can be used when posting the paper or your thesis on-line.
3) In placing the thesis on the author's university website, please display the following message in a prominent place on the website: In reference to IEEE copyrighted material which is used with permission in this thesis, the IEEE does not endorse any of [university/educational entity's name goes here]'s products or services. Internal or personal use of this material is permitted. If interested in reprinting/republishing IEEE copyrighted material for advertising or promotional purposes or for creating new collective works for resale or redistribution, please go to http://www.ieee.org/publications_standards/publications/rights/rights_link.html to learn how to obtain a License from RightsLink.

If applicable, University Microfilms and/or ProQuest Library, or the Archives of Canada may supply single copies of the dissertation.

Vita

Timothy Donald Jackson was born in Gettysburg, Pennsylvania on September 30, 1989. In May of 2011, he earned a Bachelor of Science degree in Nuclear Engineering from Rensselaer Polytechnic Institute. In 2009 he worked as a research assistant at the Lead Slowing Down Spectrometer, performing research in the area of experiment design for neutron interaction cross-section measurements. In 2010 and 2011 he participated in the Nuclear Engineering Science Laboratory Synthesis program at Oak Ridge National Laboratory, performing research in backscatter x-ray imaging of nuclear fuel and non-destructive quantification of the Plutonium content of spent nuclear fuel using analysis of the emitted x-ray spectrum and MCNP calculations. In August of 2011, he began graduate school at the University of Tennessee as an Energy Science & Engineering fellow in the Bredesen Center for Interdisciplinary Research and Graduate Education. Initially he worked on characterization of plastic scintillator materials capable of pule shape discrimination between neutrons and gamma-rays and Geant4 simulation of neutron block detectors for position sensitivity and timing resolution. With completion of that work, he began work on statistical reconstruction techniques for coded aperture fast-neutron imaging. The result of that work is presented in this dissertation.